ISSN 1980-9743

Soils and Rocks

Soils and Rocks

An International Journal of Geotechnical and Geoenvironmental Engineering

Volume 36, N. 2
May-August 2013

Soils and Rocks
Volume 36, N. 2
2013

SOILS and ROCKS

An International Journal of Geotechnical and Geoenvironmental Engineering

Editor André Pacheco de Assis - University of Brasilia, Brazil

Co-editor Manuel Matos Fernandes - University of Porto, Portugal

Soils and Rocks publishes papers in English in the broad fields of Geotechnical Engineering, Engineering Geology and Geo-environmental Engineering. The Journal is published in April, August and December. Subscription price is US$ 90.00 per year. The journal, with the name "Solos e Rochas", was first published in 1978 by the Graduate School of Engineering, Federal University of Rio de Janeiro (COPPE-UFRJ). In 1980 it became the official magazine of the Brazilian Association for Soil Mechanics and Geotechnical Engineering (ABMS), acquiring the national character that had been the intention of its founders. In 1986 it also became the official Journal of the Brazilian Association for Engineering Geology and the Environment (ABGE) and in 1999 became the Latin American Geotechnical Journal, following the support of Latin-American representatives gathered for the Pan-American Conference of Guadalajara (1996). In 2007 the journal acquired the status of an international journal under the name of Soils and Rocks, published by the Brazilian Association for Soil Mechanics and Geotechnical Engineering (ABMS), Brazilian Association for Engineering Geology and the Environment (ABGE) and Portuguese Geotechnical Society (SPG). In 2010, ABGE decided to publish its own journal and left the partnership.

Soils and Rocks

1978,	1 (1, 2)
1979,	1 (3), 2 (1,2)
1980-1983,	3-6 (1, 2, 3)
1984,	7 (single number)
1985-1987,	8-10 (1, 2, 3)
1988-1990,	11-13 (single number)
1991-1992,	14-15 (1, 2)
1993,	16 (1, 2, 3, 4)
1994-2010,	17-33 (1, 2, 3)
2011,	34 (1, 2, 3, 4)
2012,	35 (1, 2, 3)
2013,	**36 (1, 2,**

ISSN 1980-9743 CDU 624.131.1

ISSN 1980-9743

SOILS and ROCKS

An International Journal of Geotechnical and Geoenvironmental Engineering

Publication of

ABMS - Brazilian Association for Soil Mechanics and Geotechnical Engineering

SPG - Portuguese Geotechnical Society

Volume 36, N. 2, May-August 2013

Table of Contents

Manuel Rocha Lecture

Manuel Rocha (1913-1981) was honoured by the Portuguese Geotechnical Society with the establishment of the Lecture Series bearing his name in 1984.

Having completed the Civil Engineering Degree at the Technical University of Lisbon (1938) he did post-graduate training at MIT. He was the driving force behind the creation of the research team in Civil Engineering that would lead to the foundation of the National Laboratory for Civil Engineering (LNEC), in Lisbon. He was Head of LNEC from 1954 to 1974 and led it to the cutting edge of research in Civil Engineering.

His research work had great impact in the area of concrete dams and rock mechanics. He was the 1st President of the International Society for Rock Mechanics and organized its 1st Congress in Lisbon (1966). He did consultancy work in numerous countries. He was Honorary President of the Portuguese Geotechnical Society, having promoted with great commitment the cooperation between Portugal and Brazil in the area of Civil Engineering, and member of the National Academy of Sciences of the USA. Recognized as a brilliant researcher, scientist and professor, with a sharp, discerning intellect allied to a prodigious capacity for work and management, he was truly a man of many talents.

Prof. JOSÉ VIEIRA DE LEMOS is Senior Researcher at the National Laboratory for Civil Engineering (LNEC), in Lisbon, Portugal. He completed his Civil Engineering Degree at the University of Porto, Portugal, in 1978. His MSc and PhD were awarded by the University of Minnesota, Minneapolis, USA, where he conducted research on numerical modelling in rock mechanics. He was involved in the development of the discrete element codes UDEC and 3DEC, for Itasca Consulting Group. He has been a researcher at LNEC since 1989, where he led the division of numerical modelling applied to concrete dams and rock engineering, and served as Head of the Concrete Dams Department. He has taught post-graduate courses on rock mechanics and modelling. His current research interests include safety analysis of dam foundations, application of discrete element models in geomechanics, rock dynamics problems, and seismic analysis of historical masonry structures.

Soils and Rocks
v. 36, n. 2

Discontinuum Modelling in Rock Engineering

J.V. Lemos

Abstract. The evolution of numerical modelling in rock mechanics has made possible a more realistic representation of the behaviour of rock masses, and a more reliable prediction of the response of rock engineering structures. Discontinuum modelling techniques, namely the discrete element method, based on the explicit representation of the rock mass discontinuous structure, have progressively acquired a broader role. In this lecture, the essential concepts and main features of these numerical techniques are discussed, with reference to their historical development. The use of these idealizations is exemplified by two areas in which they proved very effective. On one hand, the analysis of practical rock engineering problems, intended, for example, for safety assessment or monitoring interpretation. This type of application is illustrated herein by dam foundation analyses based on deformable block models. A second level of discontinuum modelling involves research aimed at the understanding of the fundamental behaviour of rock and rock masses. An example of this approach is the analysis of fracture phenomena with particle models, primarily of laboratory specimens, but being extended to larger scales. Critical issues identified in the effective application of these modelling tools are examined, as well as some foreseeable evolution trends.

Keywords: rock mechanics, numerical modelling, discrete elements, block models, dam foundations, rock fracture.

1. Introduction

The development of Rock Mechanics as an independent discipline, with its own field of knowledge and methodologies, may be associated, to a large extent, with the progressive recognition of the role played by discontinuities in the behaviour rock masses. In 1964, in a well-known paper presented to the 8th ICOLD Congress in Edinburgh, Manuel Rocha stated that among the difficulties then facing Rock Mechanics should be mentioned "in first place, the consideration of families of joints and faults which turn rock masses into systems of more or less adjusted blocks" (Rocha, 1964a). Then, he questioned "how far such systems can be treated by extending to them the laws of behaviour applying to media assumed to be continuous or if it is necessary, at least in certain cases, to develop a mechanics of media divided by families of discontinuities". The examination of elementary systems, such as those depicted in Fig. 1, was a step towards the definition of appropriate conceptual models. In the same paper, Manuel Rocha recognized the limitations of the available analytical methods to deal with systems of such nature and complexity, pointing to physical experiments as a promising means to simulate discontinuous media and provide understanding about their mechanics.

In the late 1960s, numerical methods were advancing into the representation of systems cut by discontinuity surfaces, whether within the framework of the finite element methods, or in the newly developed discrete element method, a path that will be discussed in more detail in the following section. However, it would take a decade for the digital computing hardware to be able to handle large, complex 2D models, and perhaps two decades for 3D representations of problems of practical interest to be feasible. Today, we have the means to analyse problems with large sizes and intricate joint patterns. However, the hardware limits continue to be challenged, for example in the study of dynamic processes or coupled physics problems. In fact, the range of physical phenomena that modelling is called upon to simulate has significantly enlarged, with new requests arising in areas such as waste isolation, oil and gas exploration or CO_2 sequestration. Fluid flow has always been recognized as a major factor in rock engineering, namely in dam foundation problems, also being a problem in which discontinuities, and the way in which they are connected, play a dominant role. Transport and thermal phenomena have also to be addressed in some of the expanding fields. The need to consider the coupling between all of these processes adds to the difficulty in model development, and, more critically, in their validation for reliable application.

Rock masses display a discontinuous nature at various scales, with the singular planes or surfaces ranging in size from geologic faults to the micro-cracks in rock matrix grains. Modelling tools are increasingly employed to address all of these levels of analysis. Block models are more commonly used at the scale of engineering works, to represent the interplay between major features and joints from the various sets present at the site. At a larger scale, they have also been successful in providing insight into geologic processes. The interaction between experimental research and numerical analysis has intensified, with models becoming indispensable in the planning, preparation, and, particularly, in the interpretation of results of laboratory or field tests. From a research perspective, one of the clearest achievements of discontinuous idealizations is arguably the

J.V. Lemos , PhD, Laboratório Nacional de Engenharia Civil, Av. do Brasil 101, 1700-066 Lisboa, Portugal. e-mail: vlemos@lnec.pt.
Invited Lecture, No discussion.

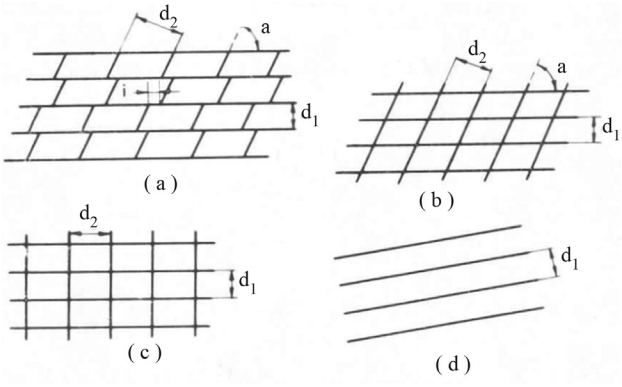

Figure 1 - Idealization of rock joint patterns (Rocha, 1964a).

role they assumed in the study of fracture phenomena. The need to examine fracture processes in rock based on a consistent analytical framework, while taking into consideration its specific aspects arising from heterogeneity and grain structure, has long been felt in rock mechanics (Fairhurst, 1972). The development of discrete element models based on circular or spherical particles has made numerical models a key ingredient in this important field. The power revealed in the analysis of laboratory test specimens is prompting their use at larger scales, which is again pushing the limits of computer technology.

The present lecture is aimed at the discussion of the essential issues that presently face the application of discontinuum models in rock engineering. The underlying conceptual models will be first examined. Then, it is instructive to look into the historical development and evolution of the numerical models, in particular those based on the discrete element method. Being impossible to cover all areas of rock mechanics, two fields of application were selected to discuss the use and capabilities of these models, one related to engineering practice, the other more research oriented. First, the problem of dam foundations in rock will be addressed, an application of block models at the engineering scale, which involves specific aspects such as hydromechanical analysis, seismic analysis and failure assessment methods. Secondly, the analysis of fracture processes by means of particle models is examined, in particular looking into the potential of these approaches for broader problems, as they begin to extend from the research environment to the engineering office. Finally, some concluding remarks are presented on the current trends and development needs of discontinuum modelling in rock engineering.

2. Conceptual Models in Rock Engineering. The Discontinuum Approach

2.1. Representation of a rock mass from an engineering perspective

An engineering model is necessarily a simplification of the physical reality, more often intended to answer a specific question, *e.g.* about safety or performance of a proposed design or an existing structure, rather than to provide a meticulous description of nature. The influence of the rock discontinuities on the overall response of the rock mass depends on the specific questions and behaviour traits being investigated. Therefore, a given geological condition may be idealized in different ways depending on the problem at hand. Whether the purpose of the analysis is preliminary or detailed design, whether the aim is the interpretation of monitoring data or the safety reassessment of an existing structure may have a strong influence on the choice of a conceptual model and its numerical implementation, as different geological or geomechanical traits assume more or less significance. It is also likely that the knowledge about the rock mass characteristics differs in each case, as well as the level of accuracy sought in the solution, or the time available to obtain the results. All of these may call for different ways to idealize the problem, giving more weight to the representation of the features recognized as dominant.

Two fundamental options exist for the representation of a jointed or fractured rock mass. The essential difference lies in the manner of representing the discontinuituies (faults, joints, fractures, interfaces) and their effects on rock mass behaviour. On one hand, we have the equivalent continuum approach, in which a continuum constitutive model is employed to represent in an average manner the effects of the discontinuities. The alternative is the discontinuum approach, in which the discontinuity surfaces are explicitly represented individually. The rock mass is then viewed as a jointed medium, or as an assembly of interacting blocks (or particles).

One of the basic criteria in deciding whether to use an equivalent continuum or blocky model is based on the scale of the jointing with respect to the size of the excavation or foundation under study, as illustrated by the classical scheme by Wittke (1990), reproduced in Fig. 2. Closely spaced joint sets are more appropriately included in the rock matrix behaviour, with explicit representation employed only for major, singular features. Major faults at known locations typically have to be considered individually. In practice, a range of representation options are possible combining continuum and discontinuum in the way that best fits the needs of the problem at hand. For example, in failure analysis, it may be sufficient to include a few joint planes of each set to represent the major potential mechanisms. However, the deformability of the block material, if it is important, should include the contribution of the joints not explicitly modelled.

The equivalent continuum option simplifies the geometric definition, but requires more complex material models. In some cases, when the loading is not expected to cause non-reversible effects, elastic models may be used, possibly with anisotropy to account for the joint orientation. Early no tension material models were

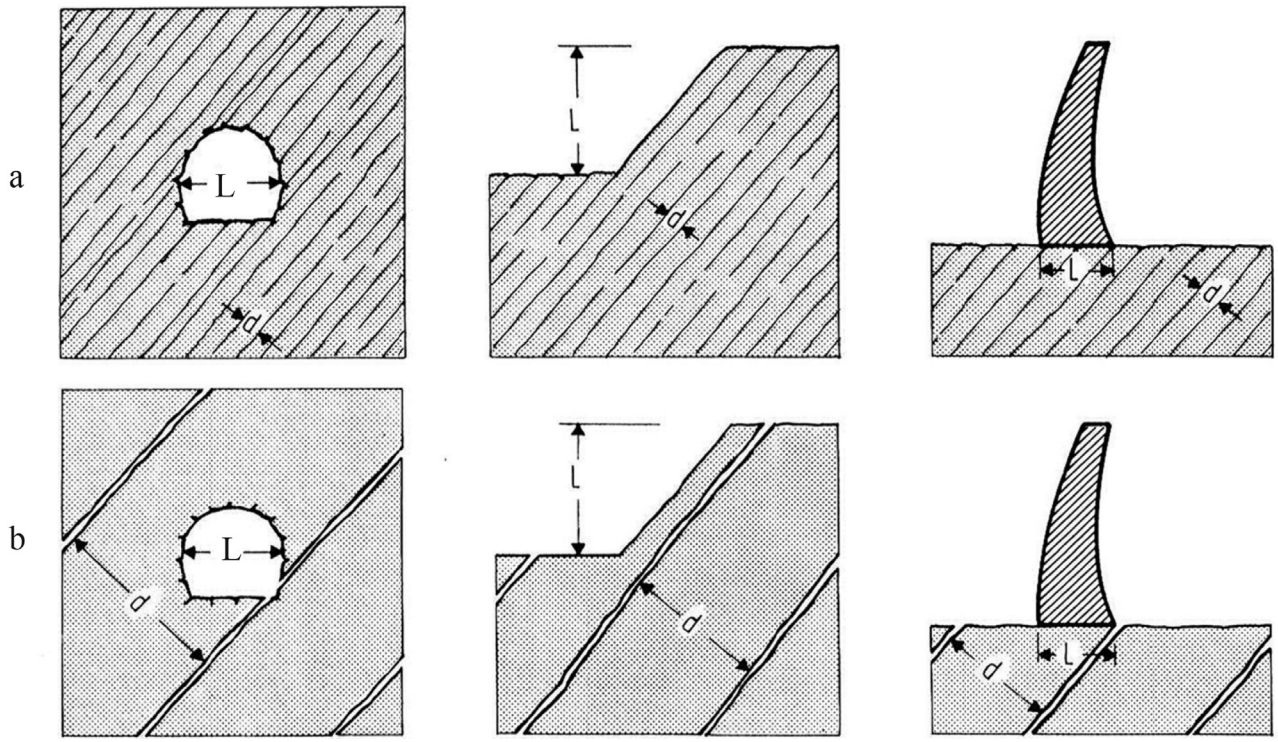

Figure 2 - Spacing of discontinuities in comparison with the engineering structure's dimensions: a) set of discontinuities d < < L; b) faults or set of discontinuities d ≥ L (Wittke, 1990).

followed by elasto-plastic and damage models (*e.g.*, for conditions of very fractured rock with statistical isotropy), and then by multilaminate or smeared crack models, capable of providing a directional variation of tensile and shear strength. In problems where the deformability of the rock mass is the main issue, or the profusion and complexity of joint patterns may be difficult to simulate by a block pattern, these continuum representations are a good option. The well-known discussion of the range of application of the Hoek-Brown failure criterion illustrates the continuum *vs.* discontinuum conceptual divide (Hoek & Brown, 1980).

The discontinuum option requires more geometric information, more detail, but it generally involves simpler constitutive laws. Jointed or blocky systems tend to represent more faithfully the types of experimental response observed in the field. However, given the natural uncertainty about jointing patterns, it may always be questioned whether a selected joint structure is representative. A relatively crude representation of the real jointing patterns in a discontinuum model may be justified if it addresses the essential impact it has on the response. The simple idealizations discussed by Rocha (1964a), shown in Fig. 1, illustrate key aspects that govern behaviour, such as orientation and persistence of each joint set or imbrication of cross-joints. Current research on discrete fracture networks is providing new tools to generate complex patterns, whenever there is statistical data to support them.

2.2. Discontinuum numerical models. The discrete element method

In the 1960s, the newly developed finite element (FE) method became an important tool in rock mechanics, as it allowed the stress analysis of complex geometries which were not addressable by the existing closed form solutions. FE models provided the means for the equivalent continuum representation of rock masses, initially based on linear elasticity, but soon afterwards extended to more elaborate non-elastic constitutive relations. The need of a truly discontinuous numerical representation, however, remained unanswered, particularly when failure mechanisms in jointed or blocky rock had to be assessed. The first solution to this problem was the joint element proposed by Goodman *et al.* (1968), which allowed the explicit representation of individual discontinuities in a FE model of a rock mass. This is a special type of finite element, which is assumed to have zero thickness and employs a joint constitutive model relating the joint normal and shear stresses with the differences in nodal displacements across the element, unlike the stress-strain laws of continuum elements. In the elastic range, therefore, the joint normal and shear stiffness parameters, as defined in rock mechanics, determine the element deformability. Non-linear behaviour in tension or shear was included from the outset, while extension to 3D posed no theoretical difficulties, only demanded more computer power.

Finite element models with joint elements were capable of actually representing a discontinuous medium, realizing the conceptual model of a continuum crossed by a few discontinuities where failure may take place. There were, however, some limitations when dealing with complex jointing patterns involving multiple sets leading to blocky systems. For example, failure mechanisms involving block rotational modes, with large movements, were not accounted for, and the small displacement assumption, prevalent in most codes, prevented changes in the system connectivity. In addition, the numerical methods of solution in use at the time, based on iterative methods using stiffness matrices, did not permit total block separation. These limitations were particularly obvious in slope stability analysis, and it was to address these problems that Cundall proposed a new numerical approach, designated as the 'Distinct (or discrete) element method' (DEM) (Cundall, 1971). This method viewed the rock mass as an assembly of distinct blocks or particles in mechanical interaction. These blocks could behave as rigid bodies, as often assumed by conceptual models of rock slope stability, a simplification that was not possible with the existing finite element models. Toppling failure was one of the first applications that illustrated the capabilities of the new method (Fig. 3).

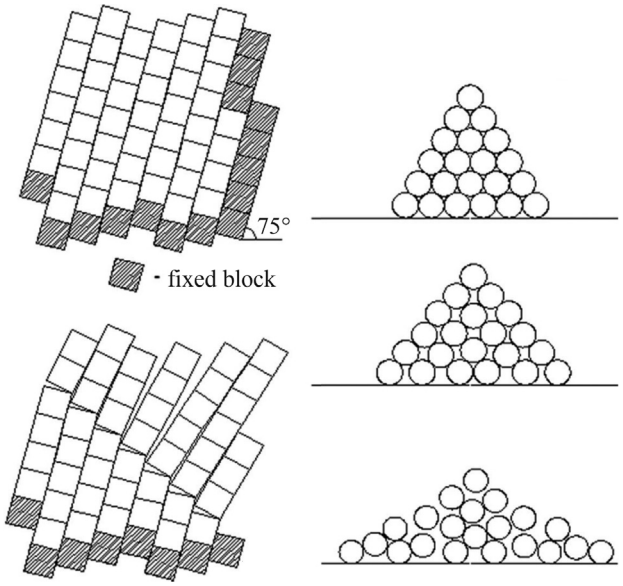

Figure 3 - Distinct element models: (left) rigid block model for analysis of toppling failure; (right) circular particle model (Cundall, 1971).

Earlier concepts of blocky systems, such as the "clastic mechanics" proposal of Trollope (1968), had a limited practical application given the shortcomings of the analytical framework. The key to the success of Cundall's DEM approach was the solution method chosen, which relied on the integration of the equations of the motion of the blocks using a time stepping explicit algorithm (Fig. 4). This type of solution method was well known in the finite difference community, as dynamic relaxation was one of the techniques employed to solve systems of linear equations before computers made direct solution feasible (*e.g.*, Otter, 1965). Physically it amounts to seeking the static solution of a mechanical system by means of artificially high damping. It is particularly suited for discrete systems undergoing large motions, for example, in the analysis of failure mechanisms, disaggregation processes or rock falls. Programming the contact detection and update algorithm in an efficient manner became a crucial component of discrete element codes, freeing the user from the need to define manually the initial system connectivity and the way it evolves during the analysis (*e.g.*, Cundall, 1988).

A distinctive feature of discrete element models is the representation of contact, based on sets of contact points. Rock joints are treated numerically as surfaces of interaction between neighbouring bodies, instead of being predefined as joint elements. This greatly enhances the flexibility of model generation and discretization, and also simplifies the consideration of large movements (*e.g.*, Lemos, 2008). Assigning representative contact areas to these contacts allows the standard rock joint constitutive models to be employed, such as the classical Mohr-Coulomb model, or more elaborate ones, such as Barton's joint model (Barton *et al.*, 1985).

In order to be applicable to wider problems, block deformability had to be considered. First, the assumption of uniform stress field in each block was adopted, but its limitations were evident, as complex deformation modes, such as bending, could not be represented. The alternative was to divide each block in an internal finite element mesh, which could be refined according to the stress analysis precision required. This approach to "deformable blocks", developed

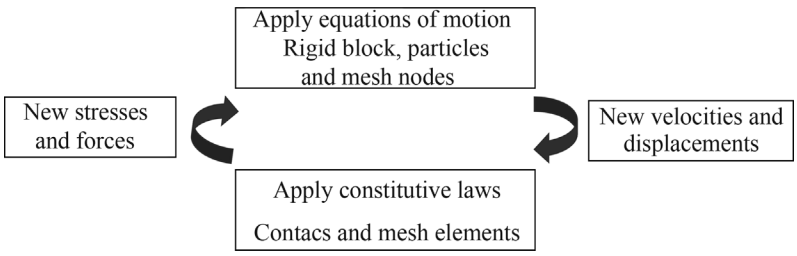

Figure 4 - Calculations performed at each step of an explicit algorithm.

in 1978, was used in the new UDEC code (Cundall, 1980), and its 3D counterpart 3DEC (Hart *et al.*, 1988). Similar schemes, sometimes designated as "discrete-finite elements", are now employed in various codes. In Cundall's codes, the solution method for deformable block models remains explicit, with the degrees of freedom of the system now being the displacement of the nodal points, instead of the rigid block displacements and rotations.

In the original 1971 paper, Cundall already included the circular particle models, treated numerically in the same way as rigid blocks. However, the geometric calculations involved in detecting and updating contact between circular (or spherical) particles are much simpler than between polygonal (or polyhedral) blocks. This implies that much larger systems can be simulated with reasonable run times, a major factor in the fast expansion of particle models. Initially proposed for micro-mechanical modelling of soils (Cundall & Strack, 1979), they became a choice tool for rock fracture studies.

Presently, many DEM codes, based either on block or particles, are routinely employed in rock mechanics research and practice, as well as other numerical methods that share some of its essential concepts for the representation of a discontinuum, including Discontinuous Deformation Analysis (DDA) (Shi & Goodman, 1988), Discrete-Finite Element Method (DFEM) (Munjiza, 2004), Non-Smooth Contact Dyanmics (NSCD) and others (*e.g.* Jing & Stephansson, 2007; Zhao *et al.*, 2012).

2.3. The use of discrete element models and codes

The ability to analyse systems of discrete bodies, in particular after the development of efficient techniques to cope with very large systems, has turned the discrete element method into a powerful instrument for detailed modelling in many fields of physics and engineering. Closer to rock mechanics are various applications involving geomaterials, such as soil, rockfill, masonry or concrete. Analysis of rock falls, mine caving and fragmentation processes are also problems for which DEM is particularly suited. A particularly intensive research effort has been directed towards addressing broader physical problems, for example involving thermo-hydro-mechanical and transport processes. This broad field of application has led to a multitude of formulations and software.

The variety and sophistication of the numerical techniques available, as well as the codes in which they are implemented, often present difficulties to the student or practitioner in the choice of the most effective tool for the problem at hand. A clear understanding of the underlying assumptions of a given code, in order to judge its capability to reproduce the conceptual mode adopted, is the first requirement for proficient use. The development of proper modelling methodologies of application of numerical models needs to receive more attention, particularly if we consider the natural tendency towards more complex models.

The amount of detail that may be included in a model is always limited by the experimental information available. Often, the choice of a continuum model is simply dictated by the preliminary nature of the study. Starfield & Cundall (1988) presented an influential discussion of analysis methodologies in rock mechanics which stresses the role of models in providing understanding about a given rock engineering problem. A numerical model may be viewed as a numerical laboratory in which to test different hypotheses of behaviour by comparison with the available knowledge, and to identify the critical factors, *e.g.*, those parameters that need reliable experimental evidence since they play a dominant role. Analysis of a given problem may proceed by a sequence of models intended to clarify specific aspects of behaviour. To address the entire range of issues with a single very detailed representation is often inefficient. Calibration of a multitude of parameters in a complex model based on a few known response features can be very misleading if the physical role of each one is not well understood.

The ability to automate model generation or output processing tasks increases the power of the simulation tools, but demands more expertise. Robust methodologies for model building and verification are essential for effective engineering analysis. Facilities to implement user-defined rock or joint constitutive models are being offered by advanced codes. In fact, versatility is a highly desirable quality in engineering software, allowing users to progress from elementary or occasional use to elaborate models, always building on the acquired expertise. In addition, it is of crucial importance to be proficient in the representation, processing and interpretation of the numerical results, so that as much knowledge as possible may be gained from the analysis.

3. Modelling Dam Foundations

3.1. Analysis needs and modelling choices

The design of concrete dams is subject to the fulfilment of general requirements of serviceability and safety shared by all engineering structures. The former imply that the structure should be able to perform its function satisfactorily, under the normal operating conditions. The latter require that the structure should not create unacceptable risks for those who use it or the public. In the case of dams, it is mandatory that, even in extreme conditions, uncontrolled loss of the retained water does not occur (Pedro, 1995).

The verification of the two types of requirements entails different analysis needs. For normal operating conditions, the aim is that the behaviour of structure and foundation remain essentially in the elastic, reversible domain. Therefore, equivalent continuum models are usually sufficient to represent the rock mass. The main requirement is to represent correctly the deformability of the various rock

mass zones, and possibly major singular features. These models are typically sufficient to predict structural displacements during normal operation, and may be validated and calibrated with monitoring data.

Safety assessment involves the analysis of the possible failure modes of the structure or foundation, considering extreme load conditions, including flood water levels and large earthquakes. Failure mechanisms involving the dam-rock interface and rock mass discontinuities need to be considered, for which discontinuum conceptual models are particularly appropriate. Rocha (1978) discusses the possible failure modes of gravity dams (Fig. 5), which in the simplest cases may be resolved by analytical calculations. Numerical models are now the best tools for these analyses, having no difficulty in addressing, for example, the case of failure surfaces with multiple segments.

The accident of Malpasset brought into attention the role of the hydraulic behaviour of the rock mass, and the importance of water pressures on rock discontinuities. In the 1960s, analytical and graphical methods were developed to assess the stability of rock wedges in arch dam abutments, including uplift forces, as shown in Fig. 6 (Londe, 1973).

Physical models were for a long time the main tool for stress analysis of arch dams, which only permitted the deformability of the foundation to be represented, and in a rather simplified manner (Rocha, 1964b). Experiments with blocky foundations were also carried out to simulate more complex rock mass conditions (Oberti & Fumagalli, 1963). Sliding failure mechanisms may also be analysed, as in the case of an arch dam studied at LNEC and depicted in Fig. 7 (Gomes, 2006). Numerical models gradually became the main analysis tool, but the contribution of physical models to their validation should not be overlooked. For the case of dynamic slip, shaking table tests remain an important source of data, given the complexity and variability of these phenomena.

Earlier numerical models were 2D representations or gravity dams adopting a continuous foundation. In spite of being limited by linear elastic assumptions, the numerical models had the means to include the spatial variability of deformability and anisotropy, a significant step forward from a practical point of view. Discontinuous finite element models using Goodman's joint model were soon applied to simulate major discontinuities. The discussion by Rocha (1978) of the analysis of Água Vermelha dam, in Brasil (Fig. 8), in which non-linear joint elements were used to represent a horizontal discontinuity in the foundation provides a clear example of the insight into the system behaviour that could be gained from a pertinent use of the new numerical techniques.

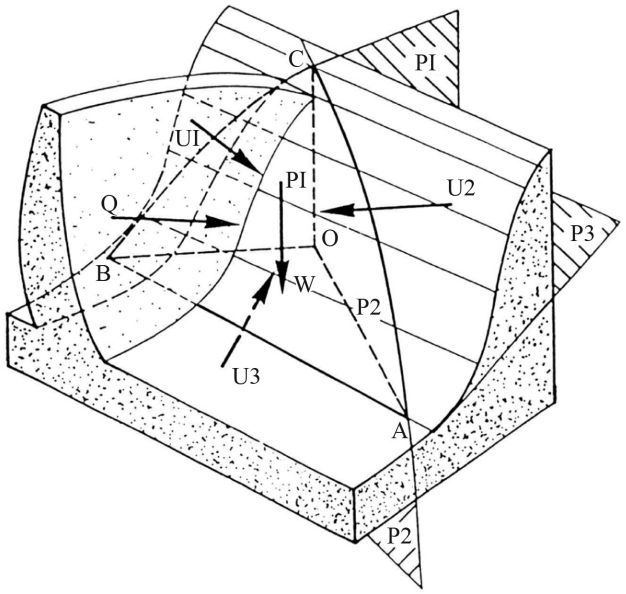

Figure 6 - Analysis of stability of rock wedge under arch dam abutment (Londe, 1973).

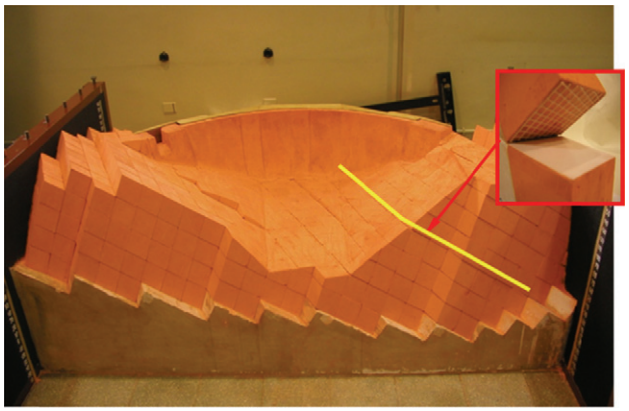

Figure 7 - Physical model of blocky foundation of an arch dam (Gomes, 2006).

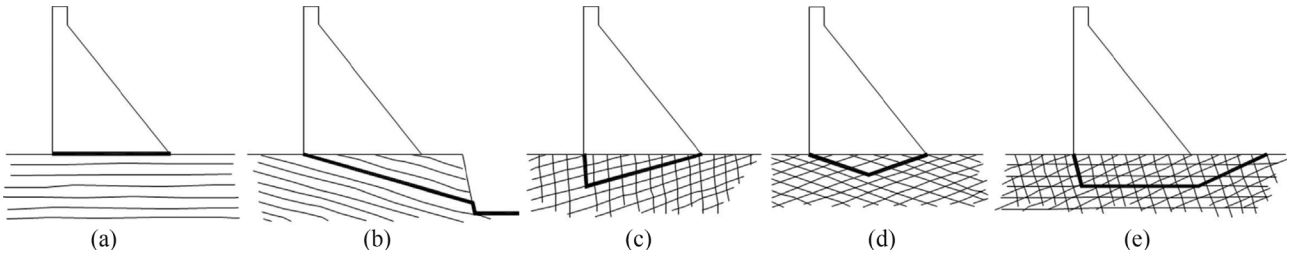

Figure 5 - Modes of failure involving the foundation of gravity dams (Rocha, 1978).

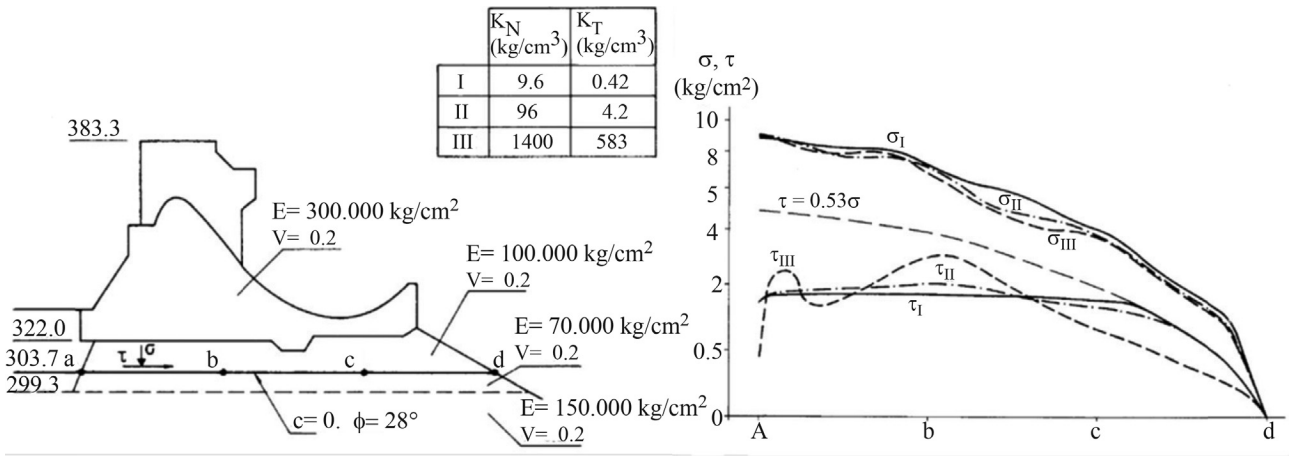

Figure 8 - Analysis of Água Vermelha dam, considering the non-elastic behaviour of horizontal discontinuity in the basaltic rock mass (Rocha, 1978).

The failure mechanisms illustrated in Figs. 4 and 5 may now be straightforwardly approached by DEM block models, which makes them a very helpful tool in dam design. As seepage and uplift pressures are of critical importance on performance and safety issues, they must be properly taken into account in the analyses.

3.2. Hydromechanical behaviour

The significance of uplift pressures for dam safety was recognized in the pioneering work of Lévy, following the accident of Bouzey dam in 1895, which made clear some inadequacies in traditional designs and the importance of drainage (*e.g.*, Bretas *et al.*, 2011). The failure of Malpasset Dam in 1959 at the completion of the first filling of the reservoir, as a result of sliding on a rock wedge under the left abutment, originated a great research effort aimed at a better understanding of the behaviour of rock foundations, in order to improve design practices (Duffaut, 2011). Londe's analysis stresses the influence of the jointing and deformation patterns on the rock mass permeability, which allowed high water pressures to be installed and favoured the sliding mechanism (Londe, 1987).

The analysis of the water flow and head distributions under dams was a challenge for a long time. Electrical analogs and other physical experiments were tried, before numerical solutions became the standard to study flow governed by Darcy's law. Finite-difference methods were initially used (*e.g.*, Serafim, 1968), followed by finite element models, first assuming uncoupled flow, and later coupled flow-stress analysis. Cases of gravity and arch dams are presented, for instance, in Wittke (1990). Multilaminate models were also used to account for the joint structure (Lamas & Sousa, 1993). The experimental study of flow in fractures by various researchers provided the background for discontinuum numerical representations, either using joint finite elements, or within a DEM framework (Damjanac & Fairhurst, 2000). Several authors have applied 2D fracture flow models to the study of the water flow under gravity (*e.g.*, Lemos, 1999; Gimenes & Fernández, 2006). Whether joint patterns are idealised, or some type of random generation is employed (Barla *et al.*, 2004; Fig. 9), the explicit inclusion of joints planes is particularly important for stability assessments.

While there is no question that flow in a rock mass is more realistically represented by fracture flow models, a number of difficulties often hinder the practical viability of this approach. First of all, fracture flow models require much more information than a continuum idealization. For the latter, the average permeability of the various foundation zones is sufficient, while a discontinuous representation of flow implies the specification of joint apertures, as well as realistic values of the joint normal stiffness since this parameter governs the stress-flow coupling. These data may not be available. The representation of the joint network also requires a good knowledge about the rock mass structure. For dams, the critical areas for flow are often at

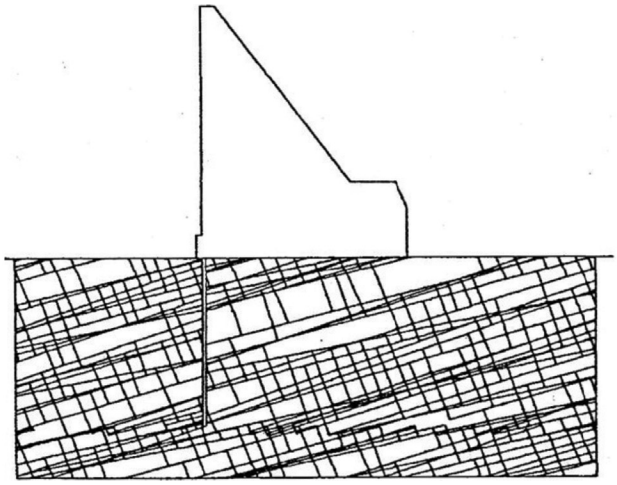

Figure 9 - Detail of DEM model for fracture flow analysis in gravity dam foundation (Barla *et al.*, 2004).

shallow depths below the dam, typically more disturbed and with higher variability. Furthermore, the representation of the grout curtain is also more problematic with a fracture flow model. A study of the hydraulic behaviour of Alqueva dam, involving packer tests to detect locations of water inflow into drainage boreholes, has clearly shown the importance of local conditions on the flow (Farinha *et al.*, 2011). A continuum flow model (Fig. 10), where the grout curtain and drainage systems were represented, was calibrated with the in situ tests data, but a detailed fracture flow model would not be viable, particularly at the design stage, when monitoring results were not yet available.

As discussed in the next section, discontinuum models are the ideal tool for failure analysis, given the dependence of the most likely collapse mechanisms on the rock mass features. In these safety assessment calculations, water pressure fields need to be specified in all discontinuities, so that the possibility of sliding is properly checked on the basis of effective stresses. However, these water pressures need not be the result of a fracture flow analysis, if there is not enough data to perform one. Either standard design hypotheses are assumed, or a less demanding continuum flow calculation may be performed, from which the water pressures can be transferred to the mechanical model for safety assessment. It should also be stressed that a fracture flow model requires a much finer representation of the jointing, in particular its connectivity, while for a stability analysis only the main discontinuities that may contribute to define a failure mechanism are necessary.

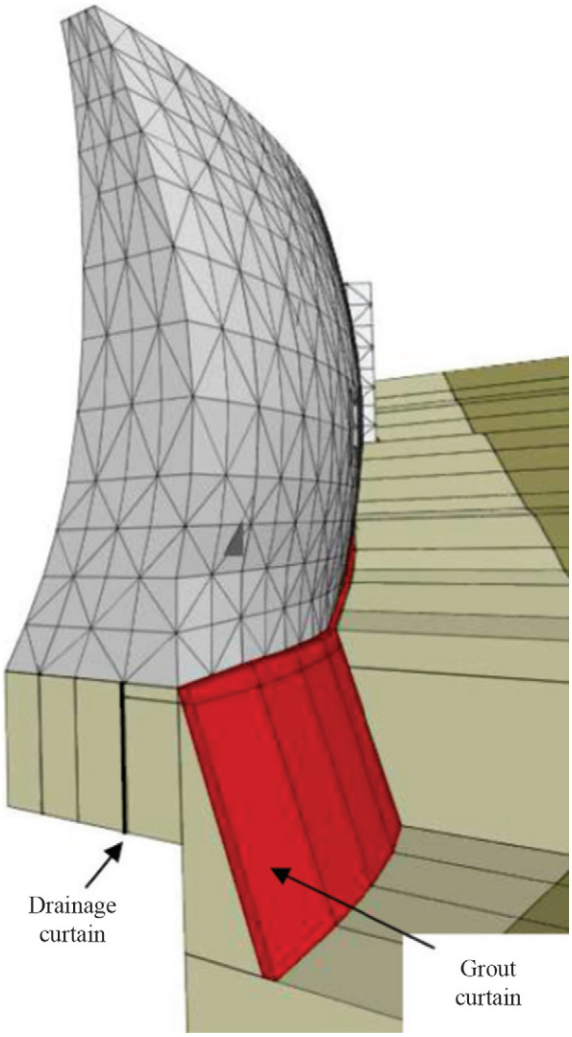

Figure 10 - Detail of model of Alqueva dam for analysis of water flow in the foundation (Farinha *et al.*, 2011).

3.3. Failure assessment

Analysis of failure of gravity dams has been traditionally performed by 2D models, as upstream-downstream sliding is the major concern. The dam-rock interface is the first location to be checked, followed by other mechanisms defined by the rock joints (Fig. 5). Sliding mechanisms involving multiple segments exceed the capabilities of the classical analytical calculations, so numerical models become the best option. Rock discontinuities have obviously a 3D structure, which may have to be considered in stability analysis, namely for blocks supported in the valley slopes (*e.g.*, Lombardi, 2007). The water pressure distribution is often the key parameter, stressing the importance of effective drainage. The strength properties of the concrete-rock interface encompass some uncertainty, so many code regulations require the consideration of a friction-only hypothesis (*e.g.*, ICOLD, 2004).

For arch dams, Londe's classical analysis (Fig. 6) illustrates the conceptual model of abutment failure. Numerical representation may be performed with finite element models with joint elements (*e.g.*, Wittke, 1990; Alonso *et al.*, 1994). At present, DEM codes provide the most flexible option to conduct this type of evaluation. Fig. 11 shows a model of Baixo Sabor dam, a 130 m high concrete arch in a wide valley in the North of Portugal (Matos & Paixão, 2007). The model, created with 3DEC (Itasca, 2007), may be used to exemplify the main issues posed by this type of analysis (Lemos, 2012b). All the blocks, in the dam and foundation, are deformable and assumed elastic. The dam is divided into cantilevers defined by the contraction joints, each one represented by means of higher order finite elements, with an accurate performance in bending. For the rock mass, deformable polyhedral blocks are employed, discretized in tetrahedral element internal meshes, which allow a proper consideration of the spatial variation of the rock mass deformability.

In this model, a very simplified representation of the rock mass discontinuities was chosen, focusing on the area of concern, the right abutment. First, the major faults were included at their known locations. Then, the block system was created by considering only a few joint planes of each of the 3 main sets of the granitic rock mass, in such a way that the various foreseeable failure modes could be generated. Away from this area of interest the model was ex-

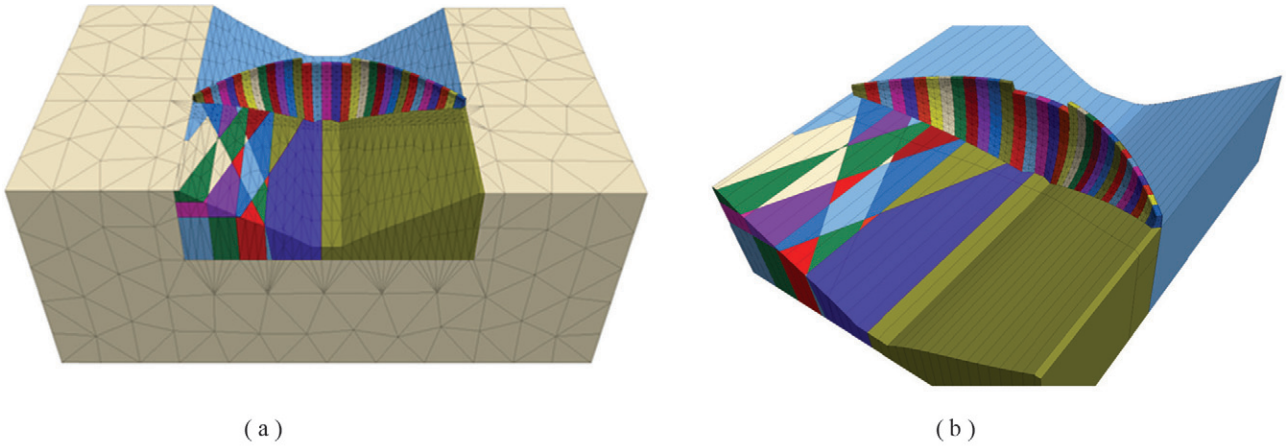

Figure 11 - DEM model of Baixo Sabor dam for analysis of right bank failure modes: (a) complete model; (b) detail view of rock block structure.

tended up to the boundaries by means of large elastic blocks. In the absence of detailed information to perform a flow analsys, conservative assumptions were considered to assign water pressure along the dam-rock interface and in all the rock joints. The safety quantification was performed by reducing the frictional strength in all discontinuities until a failure mechanism developed, as depicted in Fig. 12. The evolution of various displacement indicators throughout the strength reduction process, shown in Fig. 13, confirms the ample safety margin, as significant movements only take place for reduction factors above 2.

The question of how much complexity may be added to a workable model is certainly subjective, and different approaches are feasible. Some engineers prefer to use simpler models to study separately specific zones of concern. Different representations of the same dam may be employed, for example to study right and left bank stability, or different joint set locations or combinations. Others prefer to build a single large model in which all possible failure modes can be generated. This implies extra time in model preparation and verification, and the interpretation of the results may be less clear or straightforward. In fact, models have the power to provide insight into the traits of structural behaviour, which is sometimes more useful than yielding a safety factor number.

In the model shown above, the rock mass discontinuities were represented by extended planes, a justified assumption for the existing faults, but clearly conservative for the other rock joints needed to create a failure mode. In this case, a comfortable safety factor was achieved, even neglecting the effects of rock bridges. For other cases, this assumption may be too conservative, so a more elaborate

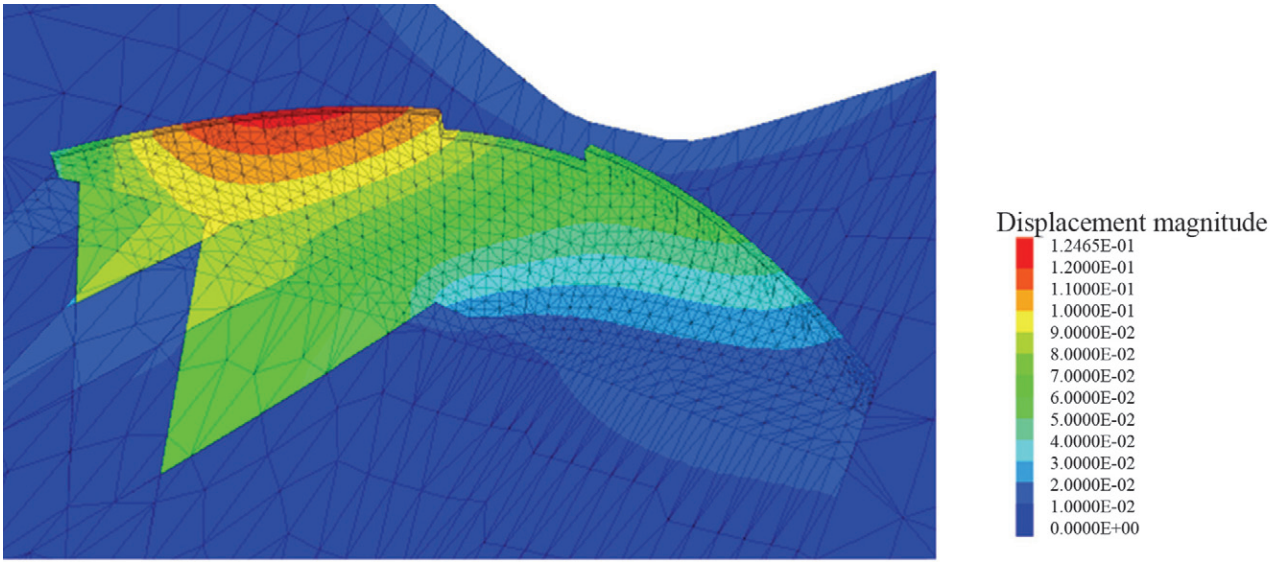

Figure 12 - Mode of failure through the rock mass discontinuities. Displacement magnitude contours for joint shear strength reduction factor F = 2.

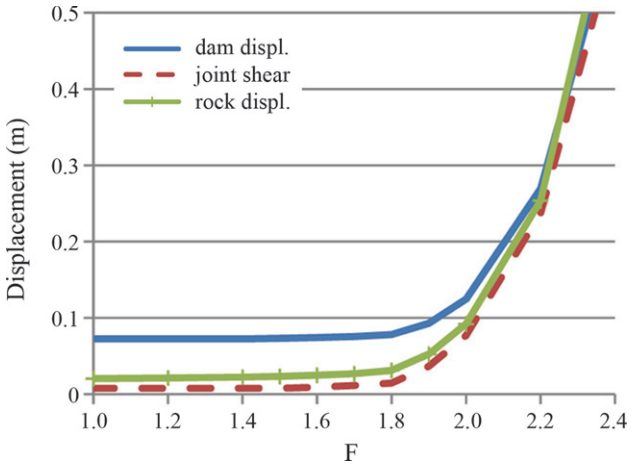

Figure 13 - Evolution of maximum dam and rock displacements and joint shear with the rock joint shear strength reduction factor.

representation of the jointing would be desirable. Generation of discrete fracture networks for use in stability analysis remains an important research topic, in order to improve the realism of rock mass representations, in agreement with its statistical descriptions derived from characterization studies (*e.g.*, Lorig, 2007). However, for analyses with non-persistent joints to be dependable, they need to take into account the possible breakage of the rock bridges and the progression of the failure surface. This issue will certainly gain from research on detailed fracture models, to be discussed below.

3.4. Seismic analysis

Seismic analysis of concrete dams traditionally concentrates on the response of the structure to assess the possible occurrence of cracking or collapse, with the rock mass being represented as an elastic continuum. For gravity dams, analysis of sliding on the foundation joint under seismic loading is now often performed for large design earthquakes, in order to provide estimates of permanent displacements. Oversimplified models in which the dam is represented as a single rigid block are not advisable, since the dam dynamic deformation alters the stress distribution on the foundation plane and thus the slip movements. Post-seismic stability analysis, considering possible damage to the dam-rock interface and to the grout curtain, with its potential implications in increased uplift diagrams, is also an important use of numerical models (*e.g.*, Aillard & Léger, 2008).

When non-linear behaviour of the rock foundation needs to be considered, more elaborate numerical setups are required, as the classical massless foundation hypothesis is no longer acceptable. The inertial and dissipation properties of the rock mass have to be included, with the appropriate non-reflecting and free-field boundary conditions (*e.g.*, Lemos, 1999). Seismic analysis of arch dam foundations is a topic that has been seldom addressed in the past, but the tools are now available to study the dynamic response of complex block systems. An example, using the model of the previous section, is shown in Fig. 14 (Lemos, 2012b). The permanent displacements after an earthquake with a peak ground acceleration of 0.5 *g*, depicted in the figure, are not expected to pose any risk to the dam integrity.

The transient dynamic water pressures that can be generated in a rock joint have been investigated experimentally (Javanmardi *et al.*, 2005), but their representation in numerical models still poses some difficulties. The simpler option is to disregard the transient pressure effects, keeping the hydrostatic water pressures unchanged, as it was done in the model of Fig. 13, which may be a conservative simplification in many cases (*e.g.*, Lemos, 1999). Given the uncertainties about these phenomena and the dispersion of estimates of dynamic slip that are usually obtained with numerical models, as well as shaking table tests, multiple analyses are always indispensable, varying the seismic input records and the less well-known properties.

4. Particle and Block Modelling at the Meso-Scale

4.1. Detailed DEM models

The discontinuous nature of geo-materials is evident at various scales, for each one being possible to identify different dominant phenomena and behaviour patterns. At the scale of engineering structures, when global stability is the main concern, the large block systems analysed in the previous section address the representation of the rock mass major features. Closer inspection would reveal a network of fissures which govern, for example, the patterns of fluid flow. Below that scale, the rock matrix may be described by the grain structure and its micro-cracks, either inter- or intra-granular. This is sometimes referred to as the meso-scale. Further down, we might consider the molecular scale, but that is beyond the scope of rock mechanics. While the definition of the entities and the modes in which they interact will vary, discrete elements are sufficiently versatile for the numerical treatment of all of these problems. Polygonal blocks are a natural representation of jointed rock. At the finer scales, a higher degree of idealization may be adopted, in terms of simpler particles shapes. Circular particles are especially efficient numerically, since the geometric resolution of the contact is straightforward, therefore allowing very large systems to be assembled. The representation of the behaviour of complex systems starting from elementary interactions is common to other scientific fields. In physics, the techniques of Molecular Dynamics (*e.g.*, Pöschel & Schwager, 2005) are based on concepts similar to the DEM. As computer power increases, the ability of these methods to address problems with practical interest has grown significantly, and their application has expanded.

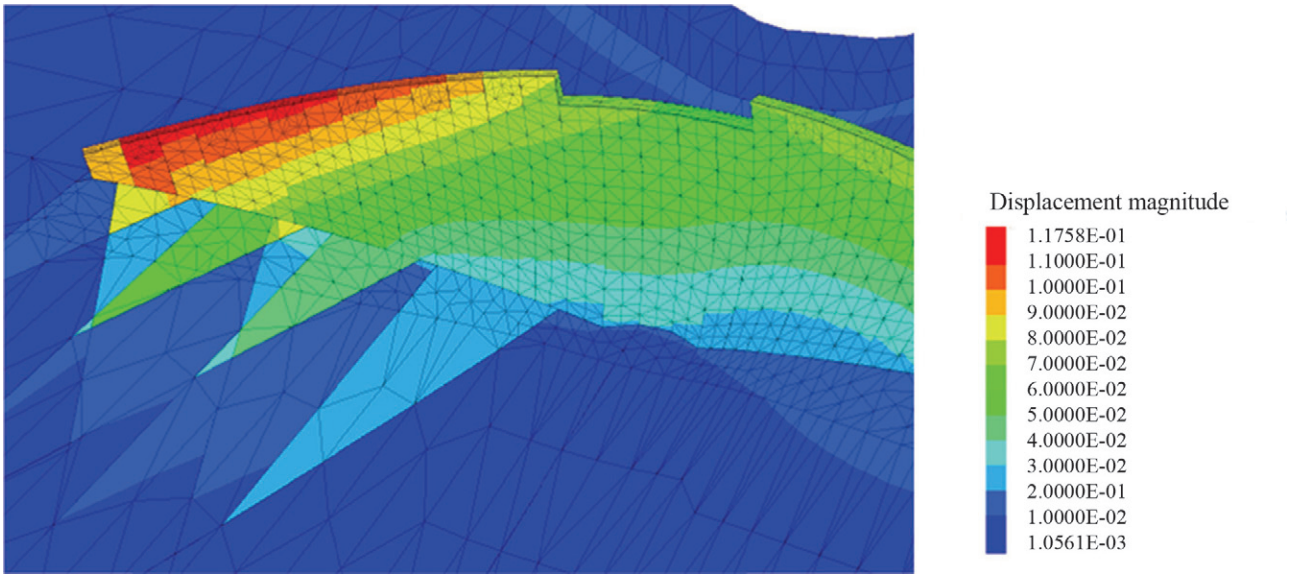

Figure 14 - Contours of permanent displacements after seismic action.

Cundall's original code (1971), already had circular particles in addition to blocks (Fig. 3), but the complete formulation of circular particle models was established by Cundall & Strack (1979). The leading motivation at the time was the micro-mechanical study of soils based on a conceptual representation of granular media as assemblies of rigid circular particles. DEM was employed to investigate the fundamental mechanical response of randomly generated assemblies of particles, as a tool to understand the underlying elementary phenomena, in order to allow the investigation and testing of constitutive assumptions, which could be then employed in continuum constitutive laws.

However, it is the study of rock fracture that has become the key application of circular particle models in rock mechanics. By connecting the particles with bonds, which are allowed to break according to specific failure criteria, the random assemblies of disks or spheres provide a powerful representation of the rock matrix, simulating the complexity of the fracture propagation paths. While circular particles have the advantage of simplicity and speed, polygonal blocks provide a more realistic representation of the interlocking grain structure, so they are increasingly resorted to in research work.

The next 3 sections will focus on the application of bonded particle models to represent, respectively, the rock matrix behaviour, rock joints, and, finally, the comprehensive response of rock mass.

4.2. Bonded particle models for the study of rock fracture

4.2.1. Essential concepts

The well-known paper by Potyondy & Cundall (2004) marked a decisive step in the numerical study of rock fracture by DEM, and is an excellent introduction to the designated Bonded Particle Models (BPM). The basic idea is to represent the rock material as an assembly of disks (in 2D) or spheres (in 3D), randomly generated according to some size distribution curve. These rigid particles are linked by breakable bonds. The system deformation derives from the inter-particle movements. Very few property parameters are necessary. The contact normal and shear stiffness govern the deformability of the unbroken system. Bond strength is described by the tensile strength and cohesion terms. After bond breakage the interaction between the particles becomes purely frictional. The bond formulation employed, known as parallel bonds, offers the capability to transmit moments, in addition to forces, between the particles.

This very simple set of assumptions allows very complex forms of behaviour to arise as the random particle assemblies are progressively loaded, which can be compared with experimental evidence. Fig. 15 shows results of 2 biaxial tests, the first with a low confining stress of 0.1 MPa, and the second with a high confining stress of 70 MPa. The expected axial splitting mode of failure is obtained in unconfined tests, while shear bands develop in the confined tests, with more distributed damage (represented by breakage of bonds) as the confining stresses increases. The transition from brittle to more ductile behaviour is thus simulated by the numerical model. However, this model does not reproduce correctly some aspects of experimental behaviour, namely the ratio of uniaxial tensile to compressive strength is too high, and the macroscopic friction angle, inferred from biaxial tests at different confining stresses, is too low. Clearly, the friction interlocking present in a real rock matrix is not being simulated. The various procedures

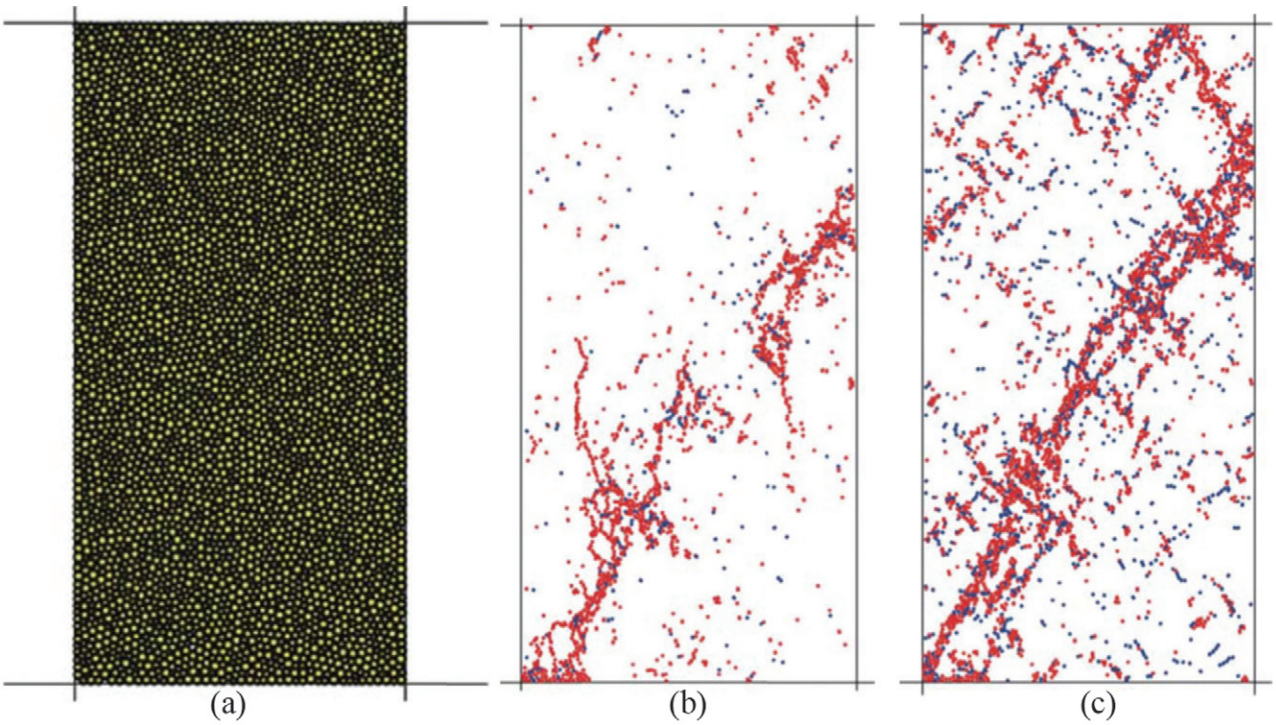

Figure 15 - Biaxial test of bonded-particle model. Particle assembly (a); Post-peak crack distribution for σ_3 = 0.1 MPa (b) and σ_3 = 70 MPa (c) (after Potyondy & Cundall, 2004).

since developed by various researchers to overcome these deficiencies will be discussed in the following section.

Several important aspects about this approach should be noted. First, the importance of the procedure to create the random assembly, discussed in detail by Potyondy & Cundall (2004), which is required to provide uniform, isotropic samples with the intended porosity and size distribution. Secondly, a major issue involved in this approach is the determination of the micro-properties, namely the bond stiffness and strength parameters, which in general cannot be directly related to the desired macroscopic properties. A procedure of calibration of the micro-parameters is necessary, in which these are varied in order to produce the experimental values of the sample Young's modulus, Poisson's ratio and macroscopic strength. This fact introduces some difficulty in the application of BPM, as a set of preliminary runs is always needed, before a given practical problem is solved. This may be facilitated by automated procedures to replicate the lab test setups, available, for example, in PFC (Itasca, 2008). Neural network techniques have also been used to identify the micro-properties that reproduce the deformability and strength of rock samples in uniaxial compression tests (Tawadrous *et al.*, 2009).

The analysis of the results of the simulation also requires tools unlike those in continuum modelling, for example, the definition of representative measures of strain and stress at various locations in the sample by means of measurement circles. Statistics of the evolution of performance indicators during the test, such as bond breakage in tension or shear, are also indispensable for a quantitative characterization of the response (*e.g.* Potyondy, 2012).

4.2.2. Modelling developments

The success of the BPM approach has promoted an active research effort in recent years, with many authors testing and enhancing the capabilities of particle models to reproduce more realistically the observed response of rock materials under the standard laboratory tests. The role of the numerical micro-parameters in modulating the various aspects of the physical response is now much better understood (*e.g.*, Schöpfer *et al.*, 2009).

In order to achieve a better match of the observed triaxial behaviour, Potyondy & Cundall (2004) had proposed that use of macro-particles composed of groups of circular particles joined together, therefore providing more interlocking in the assembly and enhanced frictional effects (Fig. 16). Subsequent work confirmed the success of this approach (Cho *et al.*, 2007; Yoon *et al.*, 2011; Potyondy, 2012). The ratio of uniaxial compressive strength to tensile strength in the numerical simulations, which was too low in the early models, also became easier to control. The macro-particles may behave as rigid bodies ("clumps"), or the bonds between the component particles may be allowed to break, therefore simulating the progression of intragranular cracks. These models essentially provided a way to discretize the grain structure in more detail, accomplishing more complex grain shapes and behaviour, naturally at the expense of increased computational effort.

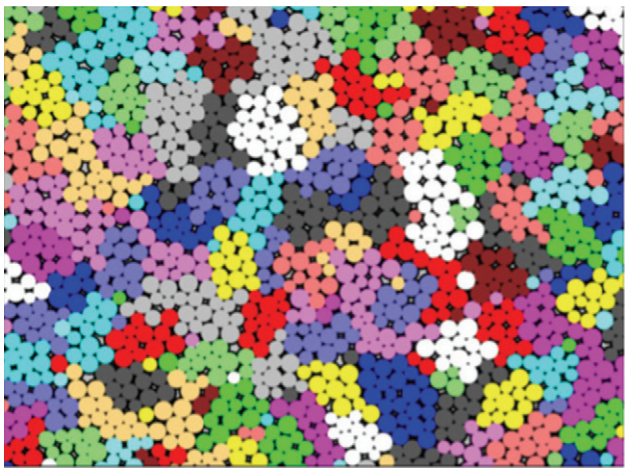

Figure 16 - Macro-particle ("clump") model for rock fracture analysis (after Cho *et al.*, 2007).

Polygonal block models resemble more closely the grain structure of many rocks. However, from a computational point of view, they are much more demanding, mainly because the geometric contact calculations between the edges and vertices of polygons involve many more operations than those needed for circular shapes. Models with elastic blocks had already been used to study the effect of random joint patterns on stress distributions (*e.g.*, Brady *et al.*, 1986). Very interesting results are now being attained in fracture analysis. Damjanac *et al.* (2007) studied the micro-mechanical behaviour of lithophysal tuff specimens with both particles and blocks. Lan *et al.* (2010) represented the microstructure of brittle rock by means of a deformable polygonal grain-like assembly, in order to study effect of heterogeneity of grain deformability properties on the behaviour under uniaxial compression (Fig. 17). Kazerani & Zhao (2011) used both Voronoi and Delaunay block assemblies to study the fracture propagation in uniaxial and Brazilian test specimens. Fracture of blocks is possible in some codes (*e.g.*, Munjiza, 2004; Eberhardt *et al.*, 2004), either through predefined potential crack paths, or by means of some form of internal remeshing. For this purpose, however, macro-particles formed by disks appear to be a more flexible and promising route, as they provide more freedom for the cracks to propagate with fewer numerical restraints.

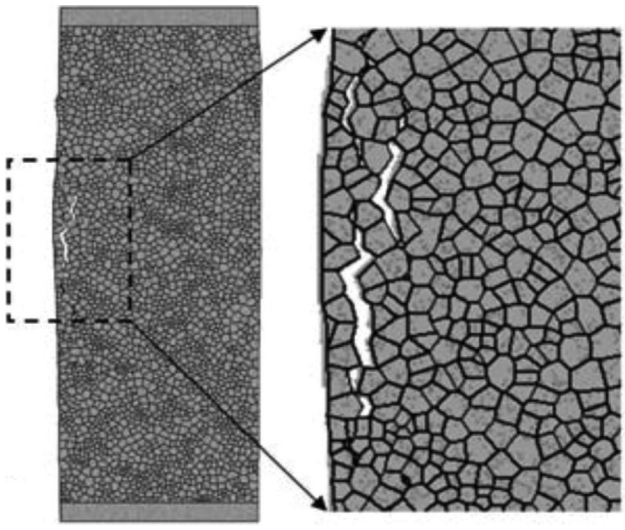

Figure 17 - Polygonal block model of uniaxial compression test (Lan *et al.*, 2010).

The main disadvantage of polygonal models is the computational effort, as contact detection and particle interaction calculations are much slower than for circular particles. This fact limits the size of assemblies that can be handled with reasonable run times, particularly in 3D, making it difficult to approach scales larger than those of lab specimens. The proposal of formulations based on multiple point contacts between two circular particles provided a way to achieve a response closer to that of polygonal models in a much more efficient way (Azevedo & Lemos, 2005). In this approach the contact between two disks is assumed to take place along a line segment, and it is discretized into several points, which may fail independently, allowing progressive cracking to develop. A more gradual response is obtained, in comparison with the instant breakage of a single rotational bond, while the use of contact models with softening also provides a less brittle post-peak response. Similar concepts underlie the "flat-joint model" proposed by Potyondy (2012). A 3D version of the multiple contact model was presented by Azevedo & Lemos (2013), using concentric rings of contact points (Fig. 18). In practice, five contact points appear sufficient to give good results. A key aspect addressed in this paper is the importance of the assembly compactness, which may be measured by the coordination number, defined as the average number of interactions for each particle (in this respect a multiple point contact counts as one interaction). For polyhedral block assemblies this number is higher than for spheres. Therefore, the authors proposed a new criterion to detect contact between spheres. A Voronoi-Laguerre diagram was superimposed on the sphere assembly, and two particles were allowed to interact if the corresponding polyhedra were adjacent, even if the spheres were not exactly touching. This increased the number of interactions, providing a response closer to the one obtained with a much more expensive polyhedral block model, namely capturing the experimental failure envelope of Lac du Bonnet granite (Fig. 19).

The aim to create larger model sizes has led research into more efficient formulations, such as Cundall's (2011) "lattice model", in which the finite-sized particles are replaced by point masses, and the contacts between particles are replaced by springs that may break. Assuming small displacements, this model achieves high computational efficiency because the interaction geometry (location and apparent stiffness of springs) can be pre-computed, eliminating contact detection as an overhead.

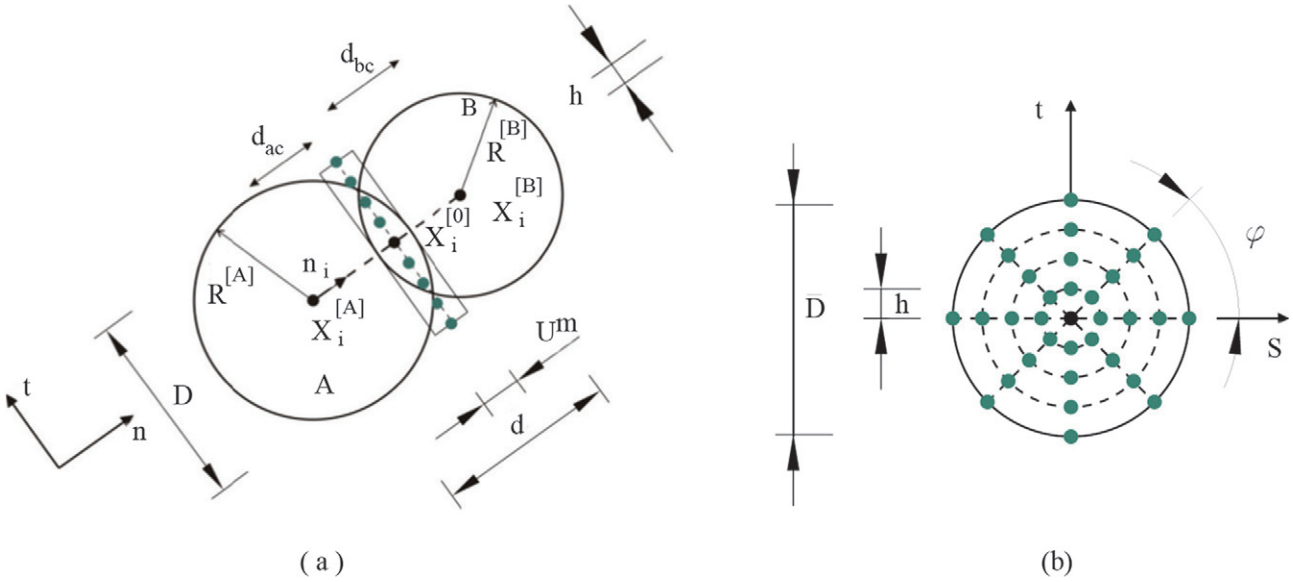

Figure 18 - Multiple point contact for particle models (Azevedo & Lemos, 2013).

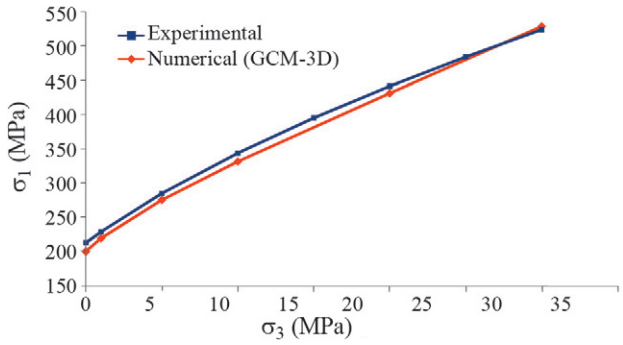

Figure 19 - Comparison of experimental and numerical envelopes in triaxial compression tests of Lac du Bonnet granite (after Azevedo & Lemos, 2013).

4.3. Rock joint representation

In addition to rock fracture, other aspects of fundamental rock behaviour are being approached by means of detailed models at the meso-level scale, mostly using particle representations. The mechanical response of rock joints in laboratory tests is a suitable application for these models, capable of reproducing the roughness of joint walls. Joint shearing was simulated with PFC by Cundall (2000) in 2D, while a 3D model was used by Park & Song (2009). The complex patterns of compressive and tensile contact forces creating by the uneven contact conditions are evident in these analyses. The development of cracks in the vicinity of the joint walls during shearing of the samples may also be followed in these simulations (Fig. 20).

The effect of discontinuities on stress waves was investigated by Resende *et al.* (2011) also with a particle model. A simplified procedure was developed to create a rough joint, with uneven contact conditions, and a contact constitutive model with variable stiffness was employed, leading to a global stress-dependent behaviour. The propagation of a plane wave across the discontinuity for various in situ stress levels was then simulated. The differences in the contact response for the different normal stresses induced complex velocity fields in the vicinity of the discontinuity, creating marked differences in the reflected and transmitted waves obtained (Fig. 21).

The detailed modelling of rock joints has motivated much interest, namely to investigate the hydromechanical behaviour, for which various techniques were used to replicate the joint roughness and aperture distributions, generally assuming joint walls to be rigid or elastic. DEM particle models have the potential to improve the analysis of joint wall behaviour, addressing the effects of roughness wear and cracking. This is a promising research field, even if the current particle models still have considerable difficulty to attain a realistic resolution of roughness profiles, as well as the processes that lead to the progressive damage to joint surfaces observed during normal or shear loading tests.

4.4. Rock mass modelling

The main practical challenge posed to particle models today lies in their extension to problems of larger size, necessary to jump from lab test analysis to the scale of engineering structures. The question of its feasibility seems to depend mostly on forecasts of computing power increases. A broader question is whether this objective is truly necessary, or, more precisely, in which circumstances will these finer representations be superior to the existing simplified engineering models. Cundall (2001) discussed the ongoing trend to discontinuous modelling in geomechanics. Continuum models of geomaterials rely on stress-strain

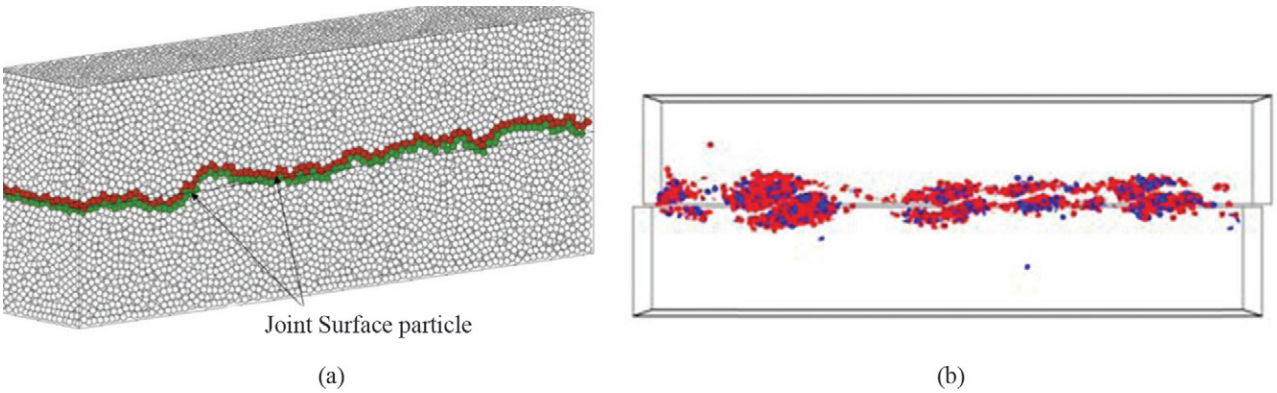

Figure 20 - Representation of rough joint with a particle model (a); micro-cracks in tension and shear (b) (after Park & Song, 2009).

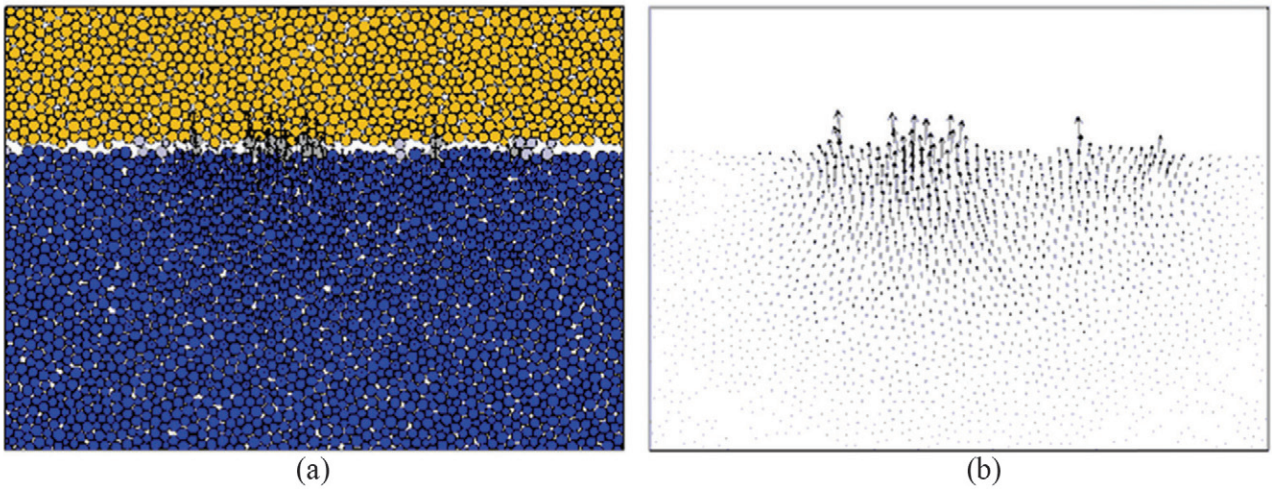

Figure 21 - Propagation of wave across rough fracture: detail of particle model (a); velocity field (b) (after Resende *et al.*, 2010).

laws to simulate their complex behaviour, which tend to become excessively complicated, and involve many parameters with obscure physical meaning. Besides, cracking and failure in rock processes are more naturally approached by discontinuum methods. In contrast, Cundall argued, assemblies of bonded discrete particles are capable of capturing the complicated behaviour of actual material with simple assumptions and few parameters at the micro level, with complex overall behaviour arising as an emergent property of the assembly.

There is no question that particle models are an indispensable research tool. However, in many practical engineering applications, simpler models appear sufficient for the purposes of safety assessment or prediction of global behaviour, as illustrated, for example, by the deformable block models presented above for dam foundation problems. After all, given the uncertainties involved in site characterisation, even these block models may challenge our capacity to provide reliable input parameters, so more refined representations may not be warranted.

One of the critical advantages of representing blocks as macro-particles composed of circular particles is the ease of considering block fracture, given the progresses discussed in the previous sections. The role of non-persistent discontinuities and the contribution of rock bridges to the strength of a rupture surface is an important aspect. Assumption of large extents for all joints is often overly conservative and contrary to geological information. The alternative to particle models is to adopt plasticity constitutive models for the block elements, which may be reasonable for global modes of response.

The Synthetic Rock Mass (SRM) concept proposes to extend the range of particle models to engineering scale, by considering the presence of the discontinuities (Mas Ivars *et al.*, 2011). A discrete fracture network (DFN) is overlaid on a particle assembly, thus partitioning it into a system of grains or blocks formed by bonded circular particles, as shown in Fig. 22. Different properties are assigned to the bonds of the contacts between particles belonging to the same block, representing the intact rock material, and to the contacts between adjacent blocks, representing the joint behaviour. Joint may be persistent or terminate within blocks, thus allowing progressive crack development processes.

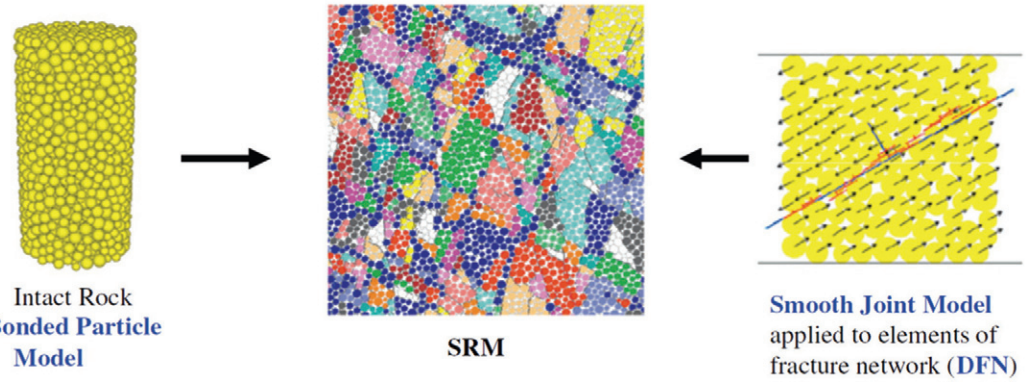

Figure 22 - Synthetic Rock Mass (SRM) model: random particle assembly; overlaid discrete fracture network; smooth-joint model representation of fractures (Mas Ivars *et al.*, 2011).

A major difficulty arises in the representation of sliding on the rough rock joints created in SRM models. The irregular shapes of the macro-particles, dependent on the size of the elementary disk or sphere components, imply excessive interlocking and dilation. From an engineering perspective, it would be desirable to assign a given friction angle, and controllable dilatant behaviour, to these surfaces. The solution to this problem lies in Cundall's Smooth Joint Model (SJM) concept, which is applied to the contacts between particles belonging to neighbouring blocks. Even if the interface is not an exact straight line, the SJM logic forces all these contacts to adopt a common normal, leading to a smooth sliding behaviour governed by the prescribed friction angle. Otherwise, sliding would imply riding over the particles, causing unrealistic dilation.

Successful applications of the SRM concept are starting to appear in the literature. Cundall (2007) presented a 2D model of a rock slope with a complex system of joint sets, which resulted in an assembly of about 330,000 particles. A detail of the model is shown in Fig. 23, displaying the contours of displacements triggered by the progressive excavation of the slope, which indicate the dominance of the toppling mechanism ensuing from the steeper dipping joints. A 3D SRM model based on the lattice formulation was applied by Cundall & Damjanac (2009) to the analysis of slopes with discontinuous joint sets, considering the fracture of the intact rock bridges. Mas Ivars *et al.* (2011)

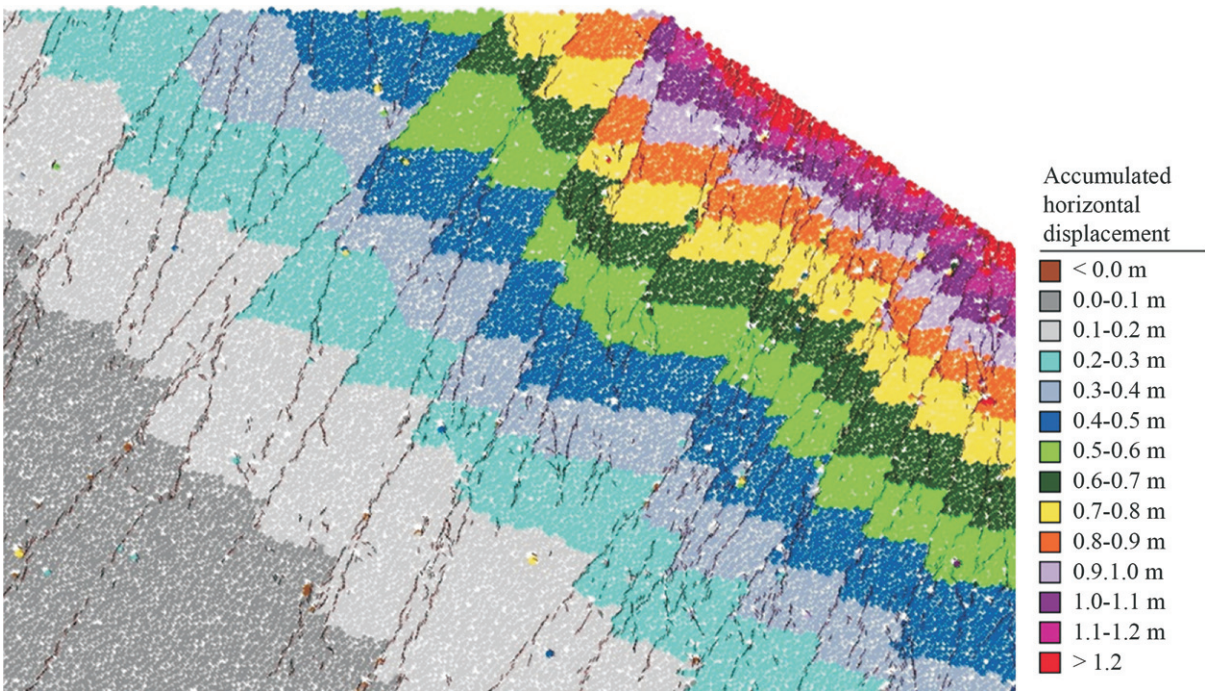

Figure 23 - Detail of SRM model of rock slope. Displacement contours illustrating the importance of the toppling mechanism (Cundall, 2007).

employed it to study scale effects in jointed rock masses. The anisotropic response and the trends in tensile and compressive strength variation were investigated by performing a series of numerical tests on samples of various sizes. Pierce & Fairhurst (2011) discuss the use of SRM models in the investigation of caving processing in underground mines. The complex problem of hydraulic fracturing is also being approached with these fracture models (Damjanac *et al.*, 2010).

The expansion of particle models to larger scales, mostly limited by the available computing resources, is inscribed in a natural tendency towards more complex simulations. Its effective use, however, depends on our ability to fulfil some essential requirements. First, it is necessary to generate realistic macro-particle assemblies, in conformity to the specific joint patterns at the site. Robust analysis methodologies have to be established, namely involving expedite procedures for calibration of micro-parameters, and multiple simulation schemes to account for the variability of the physical data. Finally, the interpretation of the numerical results of complex models needs to be based on sound and objective criteria, appropriate to specific aims, for example, the safety assessment of foundations or excavations.

5. Closing Remarks

The widening range of problems facing rock engineering continues to stimulate the development of new analysis tools. Stricter safety and environmental requirements, as well as technological and economic factors, challenge our capability to predict the integrated behaviour of rock masses subject to the demands of new structures or excavations. Numerical models based on the discontinuum paradigm are one of the essential instruments available today. The development and application of discrete element models has followed two distinct but complementary paths. On one hand, we have the more sophisticated models employed in research, aimed at the understanding of the fundamentals of rock and rock mass behaviour, in conjunction with laboratory and well-controlled in situ experiments. On the other, the simpler but more robust techniques that suit the needs of engineering design practice. As the more complex models are progressively validated against experimental evidence, while becoming more reliable and user-friendly, they are increasingly called to address practical goals.

The effective use of advanced numerical tools relies, first of all, on our ability to supply geologic and geomechanical information to characterize adequately the site conditions. Statistical description of jointing and expedite methods for generation of numerical fracture networks are a key issue. The adequate representation of network connectivity, joint persistence, or rock bridges remains an important goal, in order to avoid overly conservative assumptions. Extending the numerical models to encompass multi-physics phenomena is perhaps the greatest challenge, given the range of problems involving the time-dependent interactions between hydromechanical, thermal, transport and chemical processes in rock masses. Discontinnum models are also a key tool to address the problems of hydraulic fracturing, dynamic rupture and fragmentation processes. Computational developments, namely in parallel processing technologies, appear vital to make large 3D simulations more manageable.

At present, engineering is faced with ever greater demands for a more rigorous evaluation and management of risk, viewed in its full human and economic aspects. The achievement of these tasks, however, rests on our ability to understand the behaviour of rock masses and engineering materials, and to predict their performance. Numerical modelling tools play a key role in this endeavour, always keeping in mind that the development of new techniques has to be complemented by attention to proper modelling methodologies and effective training in their application.

Acknowledgments

The author greatly appreciates the invitation of the Portuguese Geotechnical Society (SPG) and the Association of Geotechnical Alumni of the Lisbon New University to present the XXIX Manuel Rocha Lecture. The author is indebted to all the colleagues who were involved in the works reported or made valuable contributions to this lecture and to Dr Luís Lamas for reading the manuscript.

References

Alliard, P.-M. & Léger, P. (2008) Earthquake safety evaluation of gravity dams considering aftershocks and reduced drainage efficiency. Journal of Engineering Mechanics - ASCE, v. 134:1, p. 12-22.

Alonso, E.E.; Gens, A.; Carol, I.; Prat, P. & Herrero, E. (1994) Three-dimensional failure mechanisms in arch dam abutments - A safety study. Proc. 18th ICOLD Congress, Durban, v. 1, pp. 471-484.

Azevedo, N.M. & Lemos, J.V. (2005) A generalized rigid particle contact model for fracture analysis. Int. J. Numerical and Analytical Methods in Geomechanics, v. 29:3, p. 269-285.

Azevedo, N.M. & Lemos, J.V. (2013) A 3D generalized rigid particle contact model for rock fracture. Engineering Computations, v. 30:2, p. 277-300.

Barla, G.; Bonini, M. & Cammarata, G. (2004) Stress and seepage analyses for a gravity dam on a jointed granitic rock mass. H. Konietzky (ed.) Numerical Modeling of Discrete Materials in Geotechnical Engineering. Balkema, Rotterdam, pp. 263-268.

Barton, N.; Bandis, S. & Bakhtar, K. (1985) Strength, deformation and conductivity coupling of rock joints. Int. J. Rock Mech. Min. Sci., v. 22:3, p. 121-140.

Brady, B.H.G.; Lemos, J.V. & Cundall, P.A. (1986) Stress measurement schemes for jointed and fractured rock.

Proc. Int. Symp. on Rock Stress, Stockholm, pp. 167-176.

Bretas, E.M.; Lemos, J.V. & Lourenço, P.B. (2012) Masonry dams: analysis of the historical profiles of Sazilly, Delocre, and Rankine. Int. J. Architectural Heritage, v. 6:1, p. 19-45.

Cho, N.; Martin, C.D. & Sego, D.C. (2007) A clumped particle model for rock, Int. J. Rock Mech. Min. Sci., v. 44:7, p. 997-1010.

Cundall, P.A. (1971) A computer model for simulating progressive large scale movements in blocky rock systems. Proc. Symp. Rock Fracture (ISRM), Nancy, v. 1, pp. II-8.

Cundall, P.A. & Strack, O.D.L. (1979) A discrete numerical model for granular assemblies. Geotechnique, v. 29:1, p. 47-65.

Cundall, P.A. (1980) UDEC - A generalized distinct element program for modelling jointed rock. Report PCAR-1-80, European Research Office, US Army, 80 pp.

Cundall, P.A. (1988) Formulation of a three-dimensional distinct element model - Part I: A scheme to detect and represent contacts in a system composed of many polyhedral blocks. Int. J. Rock Mech. Min. Sci., v. 25:3, p. 107-116.

Cundall, P.A. (2000) Numerical experiments on rough joints in shear using a bonded particle model. Lehner, F.K. & Urai, J.L. (eds.) Aspects of Tectonic Faulting (Festschrift in Honour of Georg Mandl). Springer-Verlag, Berlin, pp. 1-9.

Cundall, P.A. (2001) A discontinuous future for numerical modelling in geomechanics? Proc. Inst. Civil Engineers, Geotechnical Engineering, v. 149:1, p. 41-47.

Cundall, P.A. (2007) Synthesizing rock-mass behavior by combining a discrete fracture network with intact-rock fracture. E. Eberhardt et al. (eds.) 1st Canada-U.S. Rock Mech. Symp., Vancouver, Canada, p. 341-349.

Cundall, P.A. (2011) Lattice method for modeling brittle, jointed rock. Sainsbury, Hart, Detournay & Nelson (eds), Continuum and Distinct Element Numerical Modeling in Geomechanics – 2011, Paper 01-02, Itasca, Minneapolis.

Cundall, P.A. & Damjanac, B. (2009) A Comprehensive 3D Model for Rock Slopes Based on Micromechanics. Slope Stability 2009, Universidad de Los Andes, Santiago, Chile.

Damjanac, B. & Fairhurst, C. (2000) Ecoulement tridimensionnel d'eau sous pressions dans les milieux fracturés. Delage, H. & De Gennaro (eds) La Sécurité des Grands Ouvrages, Presses Ponts et Chaussées, Paris, pp. 5-16.

Damjanac, B.; Board, M.; Lin, M.; Kicker, D. & Leem, J. (2007) Mechanical degradation of emplacement drifts at Yucca Mountain - A modeling case study. Part II: Lithophysal rock, Int. J. Rock Mech. Min. Sci., v. 44, p. 368-399.

Damjanac, B.; Gil, I.; Pierce, M.; Sanchez, M.; Van As, A. & McLennan, J. (2010) A new approach to hydraulic fracturing modeling in naturally fractured reservoirs. Proc. 44th U.S. Rock Mechanics Symposium, ARMA, Alexandria, Virginia, Paper No. 10-400.

Duffaut, P. (2011) What modern rock mechanics owe to the Malpasset arch dam failure. Proc. 12th ISRM International Congress on Rock Mechanics, Beijing, CRC Press, Boca Raton, pp. 1889-1892.

Eberhardt, E.; Stead, D. & Coggan, J.S. (2004) Numerical analysis of initiation and progressive failure in natural rock slopes - The 1991 Randa rockslide. Int. J. Rock Mech. & Min. Sci., v. 41:1, p. 69-87.

Farinha, M.L.B.; Lemos, J.V. & Maranha das Neves, E. (2011) Numerical modelling of borehole water-inflow tests in the foundation of the Alqueva arch dam. Can. Geotech. J., v. 48:1, p. 72-88.

Fairhurst, C. (1972) Fundamental Considerations Relating to the Strength of Rock. Veröff. Inst. Bodenmechanik und Felsmechanik (Karlsruhe), v. 55:1, p. 1-56.

Gimenes, E. & Fernandez, G. (2006) Hydromechanical analysis of flow behavior in concrete gravity dam foundations. Can. Geotech. J., v. 43:3, p. 244-259.

Gomes, J.M.N.P. (2006) Experimental Analysis of Failure Scenarios of Concrete Dam Foundations - Static and Dynamic Tests. PhD Thesis, LNEC, Lisbon, pp. 278.

Goodman, R.E.; Taylor, R.L. & Brekke, T.L. (1968) A model for the mechanics of jointed rock. J. Soil Mech. Found. Div. ASCE, v. 94:SM3, p. 637-659.

Hart, R.D.; Cundall, P.A. & Lemos, J.V. (1988) Formulation of a three-dimensional distinct element model - Part II: Mechanical calculations for motion and interaction of a system composed of many polyhedral blocks. Int. J. Rock Mech. Min. Sci., v. 25:3, p. 117-125.

Hoek, E. & Brown, E.T. (1980) Empirical strength criterion for rock masses. J. Geotech. Eng. Div. ASCE, v. 106:GT9, p. 1013-1035.

ICOLD European Club (2004) Working Group on Sliding Safety of Existing Dams. G. Ruggeri (ed), Final Report, 111 pp.

Itasca (2007) 3DEC (3-Dimensional Distinct Element Code), Version 4.1. Minneapolis, Minnesota.

Itasca (2008) PFC2D (Particle Flow Code in 2 Dimensions), Version 4.0. Minneapolis, Minnesota.

Javanmardi, F.; Léger, P. & Tinawi, R. (2005) Seismic structural stability of concrete gravity dams considering transient uplift pressures in cracks. Engineering Structures, v. 27:4, p. 616-628.

Jing, L. & Stephansson, O. (2007) Fundamentals of Discrete Element Methods for Rock Engineering - Theory and Application. Elsevier, Amsterdam, 545 pp.

Kazerani, T. & Zhao, J. (2010) Micromechanical parameters in bonded particle method for modelling of brittle

material failure, Int. J. Numer. Anal. Meth. Geomech., v. 34:18, p. 1877-1895.

Lan, H.; Martin, C.D. & Hu, B. (2010) Effect of Heterogeneity of brittle rock on micromechanical extensile behaviour during compression loading. Journal of Geophysical Research, v. 115:1, p. 1-14.

Lamas, L.N. & Sousa, L.R. (1993) The use of a hydromechanical numerical model to understand the behaviour of pressure tunnels and shafts. Sousa L.R. & Grossman, N.F. (eds) Proc. EUROCK93. Balkema, Lisboa, pp. 961-968.

Lemos, J.V. (1999) Discrete element analysis of dam foundations. V.M. Sharma, K.R. Saxena & R.D. Woods (eds) Distinct Element Modelling in Geomechanics. Balkema, Rotterdam, pp. 89-115.

Lemos, J.V. (2008) Block modelling of rock masses - Concepts and application to dam foundations. European Journal of Environmental and Civil Engineering, v. 12:7-8, p. 915-949.

Lemos, J.V. (2012a) Explicit codes in geomechanics - FLAC, UDEC and PFC. Ribeiro e Sousa, L.; Vargas Jr., E.; Fernandes, M.M. & Azevedo, R. (eds) Innovative Numerical Modelling in Geomechanics. Taylor & Francis, London, pp. 299-315.

Lemos, J.V. (2012b) Modelling the failure modes of dams' rock foundations. G. Barla (ed.) MIR 2012 - Nuovi Metodi di Indagine, Monitoraggio e Modellazione Degli Amassi Rocciosi. Politecnico di Torino, Italy, 280 pp.

Lombardi, G. (2007) 3D analysis of gravity dams. Hydropower & Dams, Issue 1, p. 98-102.

Londe, P. (1973) Analysis of the stability of rock slopes. Q. Jl Engng Geol., v. 6:3, p. 93-127.

Londe P. (1987) The Malpasset Dam failure. Proc. Int. Workshop on Dam Failures, Purdue, Engineering Geology, v. 24:1-4, pp. 295-329.

Lorig, L.J. (2007) Using numbers from geology. Proc. 11th ISRM Congress, Lisbon, v. 3, pp. 1369-1377.

Mas Ivars, D.; Pierce, M.E.; Darcel, C.; Reyes-Montes, J.; Potyondy, D.O.; Paul Young, R. & Cundall P.A. (2011) The synthetic rock mass approach for jointed rock mass modelling. Int. J. Rock Mech. Min. Sci., v. 48:2, p. 219-244.

Matos, D.S.; Paixão, J. & Antunes, N. (2007) Arch design of the Baixo Sabor upstream scheme. Pina, C.; Portela, E. & Gomes, J.P. (eds) Proc. 5th Int. Conf. on Dam Engineering, LNEC, Lisbon, Portugal.

Munjiza A. (2004) The combined Finite-Discrete Element Method. John Wiley, Chichester, 352 pp.

Oberti, G. & Fumagalli, E. (1963) Geomechanical models for testing the statical behaviour of dams resting on highly deformable rock foundations. Felsmechanik und Ingenieurgeologie, v. 1-2, p. 97-103.

Otter, J.R.H. (1965) Dynamic Relaxation of Shell Theory Equations for Arch Dams. Rydzewski, J.R. (ed) Theory of Arch Dams. Pergamon, Oxford, pp. 313-328.

Park, J.-W. & Song. J.-J. (2009) Numerical Simulation of a direct shear test on a rock joint using a bonded-particle model. Int. J. Rock Mech. Min. Sci., v. 46:8, p. 1315-1328.

Pedro, J.O. (1995) Arch dams - Safety and performance evaluation. CISM Courses and Lectures no. 367, Springer, Wien, pp. 1-78.

Pierce, M.E. & Fairhurst, C. (2011) Synthetic rock mass applications in mass mining. Qian, Q. & Zouh, Y. (eds) Harmonizing Rock Engineering and the Environment. Proc. 12th ISRM Congress, Beijing, CRC Press, Boca Raton, pp. 109-114.

Pöschel, T. & Schwager, T. (2005) Computational Granular Dynamics: Models and Algorithms. Springer, Berlin, 322 pp.

Potyondy, D. & Cundall, P.A. (2004) A bonded-particle model for rock. Int J Rock Mech Min Sci, v. 41:8, p. 1329-1364.

Potyondy, D. (2012) The bonded-particle model as a tool for rock mechanics research and application: current trends and future directions. Proc. 7th Asian Rock Mechanics Symposium. Seoul, Korea, pp. 73-105.

Resende, R.; Lamas, L.; Lemos, J. & Calçada, R. (2010) Micro-mechanical modelling of stress waves in rock and rock fractures. Rock Mechanics and Rock Engineering, v. 43:6, p. 741-761.

Rocha, M. (1964a) Mechanical behaviour of rock foundations in concrete dams. Proc. 8th International Congress on Large Dams, Edinburgh, v. 1, pp. 785-831.

Rocha, M. (1964b) Statement of the physical problem of the arch dam. Theory of Arch Dams. Rydzewski, J.R. (ed) Pergamon, Oxford, pp. 3-22.

Rocha, M. (1978) Analysis and design of the foundation of concrete dams. Proc. ISRM International Symposium "Rock Mechanics Applied to Dam Foundations". Rio de Janeiro, Brazil, 1978.

Schöpfer, M.P.J.; Abe, S.; Childs, C. & Walsh, J.J. (2009) The impact of porosity and crack density on the elasticity, strength and friction of cohesive granular materials: Insights from DEM modelling. Int. J. Rock Mech. Min. Sci., v. 46:2, p. 250-261.

Serafim, J.L. (1968) Influence of interstitial water on the behaviour of rock masses. Stagg, K.G. & Zienkiewicz, O.C. (eds) Rock Mechanics in Engineering Practice, John Wiley, Chichester, pp. 55-97.

Shi, G.-H. & Goodman, R.E. (1988) Discontinuous deformation analysis - A new method for computing stress, strain and sliding of block systems. Cundall, Sterling & Starfield (eds) Key Questions in Rock Mechanics. Proc. 29th U.S. Symp., Balkema, Rotterdam, pp. 381-393.

Starfield, A.M. & Cundall, P.A. (1988) Towards a methodology for rock mechanics modelling. Int. J. Rock Mech. Min. Sci., v. 25:3, p. 93-106.

Tawadrous, A.S.; DeGagné, D.; Pierce, M. & Mas Ivars, D. (2009) Prediction of uniaxial compression PFC3D model micro-properties using artificial neural networks. Int. J. Numer. Analyt. Meth. Geomech., v. 33:18, p. 1953-1962.

Trollope, D.H. (1968) The mechanics of discontinua or clastic mechanics in rock problems. Stagg, K.G. & Zienkiewicz, O.C. (eds) Rock Mechanics in Engineering Practice. John Wiley, Chichester, pp. 275-320.

Wittke, W. (1990) Rock Mechanics - Theory and Applications with Case Histories. Springer-Verlag, Berlin, 1076 pp.

Yoon, J.S.; Jeon, S.; Zang, A. & Stephansson, O. (2011) Bonded particle model simulation of laboratory rock tests for granite using particle clumping and contact unbonding. Sainsbury, Hart, Detournay & Nelson (eds) Continuum and Distinct Element Numerical Modeling in Geomechanics 2011, Paper: 08-05.

Zhao, J.; Ohnishi, Y.; Zhao, G.-F. & Sasaki, T (eds) (2012) Advances in discontinuous numerical methods and applications in geomechanics and geoengineering. Proc. ICADD-10, Honolulu, 6-8 Dec. 2011, CRC Press, Boca Raton, pp. 428.

Articles

Soils and Rocks
v. 36, n. 2

An Efficient Model for Numerical Simulation of the Mechanical Behavior of Soils. Part 1: Theory and Numerical Algorithm

A.L. Braun, A.M. Awruch

Abstract. A numerical model to simulate the mechanical behavior of soils is presented in this first part of the present work. This paper reports some advances obtained in the first stage of an ongoing research, which aims to develop a robust and efficient algorithm for consolidation analyses of saturated/unsaturated soils. Hence, the present work is mainly concerned with basic issues, such as efficiency of the finite element formulation and accuracy of the constitutive formulation. Since geotechnical materials exhibit elastoplastic characteristics, the theory of plasticity is applied here by means of the critical state concept using the Cam-Clay formulation. The constitutive equation is integrated using an explicit algorithm where the strain increment is divided into a number of sub-steps defined automatically by the numerical scheme. Eight-node hexahedral finite elements with one-point quadrature are employed in the spatial discretization of the geometrical domain. In order to avoid excitation of spurious modes, an efficient hourglass control is utilized in conjunction with a corotational formulation, which also contributes to the treatment of geometrical and physical nonlinearities.

Keywords: critical state soil mechanics (CSSM), elastoplasticity, finite element method (FEM), one-point quadrature.

1. Introduction

The use of numerical models to simulate geotechnical problems has strongly increased in the last decades. This growth is mainly due to expressive advances obtained in constitutive modeling of soils and other granular materials and the great reliability achieved by present numerical methods, such as the Finite Element Method (FEM). Since the pioneering works of Coulomb (1776) and Rankine (1857), the theory of plasticity has been applied to describe analytically the mechanical behavior of soils, which is entirely justified considering experimental observations that suggest irreversible behavior for strains, yield phenomena and shear-induced dilatancy. In this sense, computational efforts to analyze such problems are usually high, owing to nonlinear characteristics referring to the material and kinematical descriptions of the problem. Therefore, robust low-order finite element formulations using the one-point quadrature technique are welcome.

One of the most popular constitutive formulations based on critical state soil mechanics (CSSM) is the Cam-Clay model. The original Cam-Clay formulation was presented by Roscoe & Schofield (1963) and Schofield & Wroth (1968) using an elastic-plastic constitutive framework. Later, Roscoe & Burland (1968) proposed the Modified Cam-Clay model, where some drawbacks of the original formulation were eliminated. The original Cam-Clay yield surface presents a discontinuity for isotropic compression stress states, which leads to numerical difficulties to determine strain increments when an associated flow rule is employed.

The Modified Cam-Clay model has been widely used as a constitutive model to describe essential mechanical properties of clays. The main advantages of the model are referred to its relative simplicity and ability to represent strength and deformation characteristics of clays realistically with a limited number of parameters to be defined. On the other hand, despite its great popularity, Cam-Clay formulation seems to be inadequate to reproduce very complex soil behavior. Shortcomings associated to the model are: (a) soils are assumed to be isotropic. It is well known that natural soils may be anisotropic due to the action of deposition; (b) time effect on soil deformation is not taken into account (viscoelastic/plastic behavior is neglected); (c) failure stress states to the left of the critical state line are overestimated due to the form adopted for the yield surface; (d) shear strains are not well predicted within the yield surface because either the shear modulus or the Poisson's ratio is assumed to be constant; (e) the behavior of sands cannot be precisely predicted because sands do not follow exactly the principle of normality and experimental data show that the critical state point lies to the left of the peak of the yield locus; (f) soils under cyclic loading is another problematic subject because Cam-Clay models estimate large plastic strains for primary loading but for the remaining unload-reload cycles within the yield surface only purely elastic strains are obtained. Experimental evidences show that all unload-reload cycles result in hysteretic behavior.

A.L. Braun, DSc, Programa de Pós Graduação Engenharia Civil, Universidade Federal do Rio Grande do Sul, 90035-190 Porto Alegre, RS, Brasil. e-mail: allbraun@ig.com.br.
A.M. Awruch, DSc, Programa de Pós Graduação Engenharia Civil, Universidade Federal do Rio Grande do Sul, 90035-190 Porto Alegre, RS, Brasil. e-mail: amawruch@ufrgs.br.
Submitted on March 29, 2011; Final Acceptance on July 30, 2013; Discussion open until December 31, 2013.

Nevertheless, most of the basic features referring to mechanical behavior of soils can be covered using the Cam-Clay model, such as increasing stiffness while the material undergoes compression, hardening/softening and compaction/dilatancy behaviors, and a tendency to reach the critical state eventually. Moreover, the Basic Barcelona Model (BBM) by Alonso *et al.* (1990) utilizes the Cam-Clay formulation to develop a mathematical model to analyze unsaturated soil behavior, which is the final goal of the present research. Some other important critical state models may be found in Zienkiewicz & Naylor (1973), Carter *et al.* (1982), Naylor (1985), Gens & Potts (1988), Pastor & Zienkiewicz (1990), Crouch *et al.* (1994), Collins & Houlsby (1997), Yu (1998), Sheng *et al.* (2000) and Zhao *et al.* (2005).

Numerical procedures to simulate three-dimensional nonlinear problems lead usually to very time-consuming algorithms because an iterative process is required in order to satisfy the mechanical equilibrium. The stiffness matrix as well as the internal and external force vectors must be updated regularly and a numerical scheme is needed to integrate the incremental constitutive equation. As models based on the FEM utilize quadrature techniques to evaluate element matrices and force vectors numerically, the computational work for each iterative step is multiplied by the number of quadrature points to perform the numerical integration. Therefore, element formulations with full integration have been frequently replaced by one-point quadrature elements in order to obtain more efficient schemes for quadrature computations. In this case, hourglass control techniques are required to avoid excitation of spurious modes (hourglass modes). A hexahedral element formulation using one-point quadrature and a corotational coordinate system with hourglass control was presented by Hu & Nagy (1997). More recently, Duarte Filho & Awruch (2004) extended that formulation to geometrically nonlinear analysis using the model proposed by Liu *et al.* (1998) and uniform reduced integration. Numerical investigations based on the numerical model introduced by Duarte Filho & Awruch (2004) may be found in Andrade *et al.* (2007), Braun & Awruch (2008) and Braun & Awruch (2009). An application of three-dimensional low-order finite elements on soil mechanics was previously performed by de Borst & Groen (1999), but without dealing with reduced integration techniques.

In a finite element analysis where nonlinear materials are considered, stress updates are obtained from numerical integration of the constitutive equation, which is performed using implicit or explicit algorithms. The main difference between implicit and explicit integration schemes lies on how variables are evaluated: at known stress states for explicit integration methods or at unknown stress states for implicit ones. From previous investigations (see, for instance, Gens & Potts, 1988; Potts & Ganendra, 1994; Sloan *et al.*, 2001; Zhao *et al.*, 2005), one verifies that explicit algorithms are more indicated to reproduce complex stress-strain relations, such as those observed for critical state models.

In this first part of the present work, the numerical model presented by Duarte Filho & Awruch (2004) is extended to cover problems with elastic-plastic constitutive models, particularly the Modified Cam-Clay model. The critical state theory for soil mechanics is briefly explained using the elastoplastic framework to introduce the constitutive relations and a corotational reference system is presented in order to describe kinematically the motion of the continuum. A finite element formulation based on reduced integration for the eight-node hexahedral element is described, where stabilization is performed using hourglass control techniques to avoid numerical instabilities such as volumetric locking and shear locking. In addition, an explicit integration scheme, similar to that presented by Sloan *et al.* (2001), is adopted in order to update stress states at the center of the finite elements.

2. Analytical Model for Critical State Soil Mechanics

Soil materials present a very complex nature where a multiphase system is usually considered to describe the mechanical behavior of the soil mass (see Fredlund & Rahardjo, 1993). The phases observed within the soil volume are the soil skeleton, or the solid phase, and the pores or void spaces, which may be filled with gaseous (air and/or other chemical species) and/or liquid (water and/or other chemical species) matter. In order to describe the soil behavior using the theory of continuum mechanics, all phases are assumed to be continuous and linear such that all elements may be considered together by superposition. Momentum, mass and energy balance equations must be satisfied and a constitutive equation that relates energetically conjugated stress and strain measures must be also defined. In soil mechanics, the momentum balance for each infinitesimal element is described in terms of effective stresses and in the absence of temperature changes, the energy conserving equation may be disregarded. A measure for the stress tensor must be chosen such that the stress-strain relation maintains its objectivity in the nonlinear range. In this work, the Cauchy stress tensor and the small strain tensor are utilized, which will be defined in a corotational reference system.

2.1. Stress-strain relations

In this work, a nonlinear hypoelastic constitutive equation is considered to relate strain and stress measures in the elastic regime using a rate form as follows:

$$\dot{\sigma}_{ij} = D^{e}_{ijkl}\,\dot{\varepsilon}_{kl} \quad (i, j, k, l = 1, 2, 3) \tag{1}$$

with:

$$D^{e}_{ijkl} = 2G\delta_{ik}\delta_{jl} + \left(K - \frac{2}{3}G\right)\delta_{ij}\delta_{kl} \quad (2)$$

where σ_{ij} and ε_{ij} are components of the Cauchy stress tensor $\boldsymbol{\sigma}$ and small strain tensor $\boldsymbol{\varepsilon}$, D^{e}_{ijkl} represents components of the elastic constitutive matrix $\mathbf{D}^{e}$ and K and G are the bulk and shear moduli, respectively. For critical state models, the tangential form of these moduli is usually assumed to be dependent on the effective mean normal stress p, which are usually expressed as:

$$K = \frac{\partial p}{\partial \varepsilon^{e}_{v}} = \frac{1+e_0}{k}p = \frac{v_s p}{k} \quad (3)$$

$$G = \frac{1}{2}\frac{\partial p}{\partial \varepsilon^{e}_{d}} = \frac{3(1-2\nu)}{2(1+\nu)}K \quad (4)$$

where ε^{e}_{v} and ε^{e}_{d} are the volumetric and deviatoric parts of the elastic strain tensor $\boldsymbol{\varepsilon}^{e}$, q is the deviatoric stress, e_0 is the initial voids ratio, v_s is the specific volume, ν is the Poisson's ratio and k is the slope of the unloading-reloading lines (URL) on a ln p-v plane (see Schofield & Wroth, 1968 for additional information). It is worth to notice that the stress dependence on K and G leads to a nonlinear elastic constitutive matrix $\mathbf{D}^{e}$. The secant forms of Eqs. 3 and 4 are obtained by integrating Eq. 3, which yields:

$$\overline{K} = \frac{p_0}{\Delta\varepsilon^{e}_{v}}\left[\exp^{\left(\frac{v_s \Delta\varepsilon^{e}_{v}}{k}\right)} - 1\right] \quad (5)$$

and, consequently:

$$G = \frac{3(1-2\nu)}{2(1+\nu)}\overline{K} \quad (6)$$

where p_0 is the effective normal stress at the beginning of the volumetric strain increment $\Delta\varepsilon^{e}_{v}$.

In the elastoplastic range, a yield function f, a plastic potential g, a flow rule and a hardening law must be introduced in order to define the elastoplastic formulation (see Owen & Hinton, 1980). The yield function for the Modified Cam-Clay model may be written as:

$$f = q^2 - M^2(pp_c - p^2) \quad (7)$$

where M is the slope of the critical state line and p_c is the preconsolidation pressure, which is related to the maximum effective pressure experienced by the soil mass. Hence, if a stress state leads to $f < 0$, it is assumed to be elastic and if a stress state leads to $f \geq 0$, it is assumed to be plastic (see also Fig. 1).

Critical state models usually describe rate relations of volumetric plastic strains and the preconsolidation pressure according to:

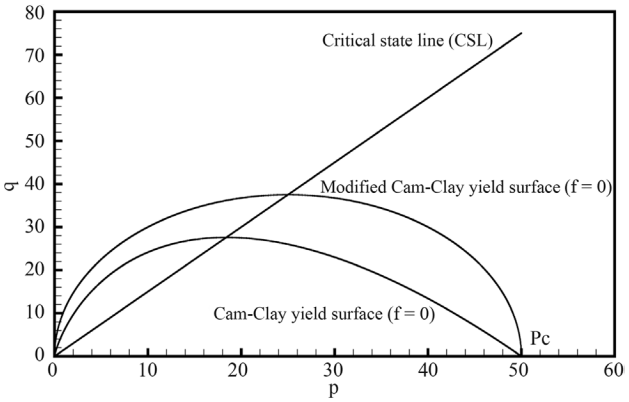

Figure 1 - Critical state line (CSL) and Cam-Clay yield surfaces represented on the pxq stress plane.

$$dp_c = \frac{v_s p_c}{\lambda - k}d\varepsilon^{p}_{v} = \frac{v_s p_c}{\lambda - k}d\lambda\frac{\partial g}{\partial p} \quad (8)$$

where λ is the slope of the normal compression lines (NCL) on a ln p-v plane (see Schofield & Wroth, 1968 for additional information) and $d\lambda$ is the plastic multiplier of the flow rule, which is defined according to the principle of normality.

The incremental stress-strain equation in the elastoplatic range may be written as follows:

$$d\boldsymbol{\sigma} = \mathbf{D}^{ep}d\boldsymbol{\varepsilon} \quad (9)$$

where:

$$\mathbf{D}^{ep} = \mathbf{D}^{e} - \frac{\mathbf{D}^{e}\mathbf{a}_g\mathbf{a}_f^{T}\mathbf{D}^{e}}{A + \mathbf{a}_f^{T}\mathbf{D}^{e}\mathbf{a}_g}d\boldsymbol{\varepsilon} \quad (10)$$

and:

$$A = -\frac{\partial f}{\partial p_c}\frac{\partial p_c}{\partial \varepsilon^{p}_{v}}\frac{\partial g}{\partial p};\ \ \mathbf{a}_f = \frac{\partial f}{\partial \boldsymbol{\varepsilon}};\ \ \mathbf{a}_g = \frac{\partial g}{\partial \boldsymbol{\sigma}} \quad (11)$$

where A is a hardening parameter and $\mathbf{a}_f$ and $\mathbf{a}_g$ are the flow vectors based on the yield function f and plastic potential g, respectively. The flow vectors are evaluated using the generalized formulation presented by Nayak & Zienkiewicz (1972). By assuming an associative flow rule, where $f \equiv g$, $\mathbf{a}_g$ and $\mathbf{a}_f$ lead to the same result.

2.2. Motion description in the corotational reference system

For elastoplastic formulations, strain increments are imposed taking into account the last incremental displacement field obtained from the solution of the equilibrium equation, considering a generic iterative step. At each iterative step, the respective stress updates are obtained according to the material behavior, using either Eq. 1 in the elastic range or Eq. 9 in the plastic range. Since any motion of a continuous medium may be decomposed into rigid body

and deformation motions, assuming that the finite element discretization is fine enough, the pure deformation portion of the motion is a small quantity compared with the element dimensions if the motion decomposition is performed in a corotational coordinate system. Consequently, the small strain hypothesis can be considered appropriately.

In order to update strains in the corotational system, the following expression is adopted:

$$\hat{\varepsilon}^{n+1} = \hat{\varepsilon}^{n} + \Delta\hat{\varepsilon} \tag{12}$$

where $n + 1$ and n indicate initial and final positions of the time interval $[t_n, t_{n+1}]$ and $\hat{\varepsilon}$ is the strain tensor calculated in the corotational system. The strain increment $\Delta\hat{\varepsilon}$ is obtained using the mid-point integration of the strain rate tensor as follows:

$$\Delta\hat{\varepsilon} = \int_{n}^{n+1} \hat{\dot{\varepsilon}}\, d\tau \doteq \frac{1}{2}\left[\frac{\partial \Delta\hat{\mathbf{u}}^{\,def}}{\partial \hat{\mathbf{x}}_{n+1/2}} + \left(\frac{\partial \Delta\hat{\mathbf{u}}^{\,def}}{\partial \hat{\mathbf{x}}_{n+1/2}}\right)^{T}\right] \tag{13}$$

where $\hat{\mathbf{x}}_{n+1/2}$ is the geometric configuration of the finite element in the corotational system at the mid-point of the time interval $[t_n, t_{n+1}]$ and $\Delta\hat{\mathbf{u}}^{\,def}$ is referred to the deformation part of the total displacement increment $\Delta\hat{\mathbf{u}}$ in the corotational system. The total displacement increment $\Delta\hat{\mathbf{u}}$ is decomposed into a part owing to pure deformation $\Delta\hat{\mathbf{u}}^{\,def}$ and a part owing to pure rotation $\Delta\hat{\mathbf{u}}^{\,rot}$, such that $\Delta\hat{\mathbf{u}} = \Delta\hat{\mathbf{u}}^{\,def} + \Delta\hat{\mathbf{u}}^{\,rot}$.

The increment of deformation displacements in the corotational system is obtained using:

$$\Delta\hat{\mathbf{u}}^{\,def} = \hat{\mathbf{x}}_{n+1} - \hat{\mathbf{x}}_{n} \tag{14}$$

where $\hat{\mathbf{x}}_n$ and $\hat{\mathbf{x}}_{n+1}$ are geometric configurations of the finite element in the corotational system at t_n and t_{n+1}, respectively (see Fig. 2). The geometric configurations $\hat{\mathbf{x}}_n$, $\hat{\mathbf{x}}_{n+1/2}$ and $\hat{\mathbf{x}}_{n+1}$ are obtained from the following transformations:

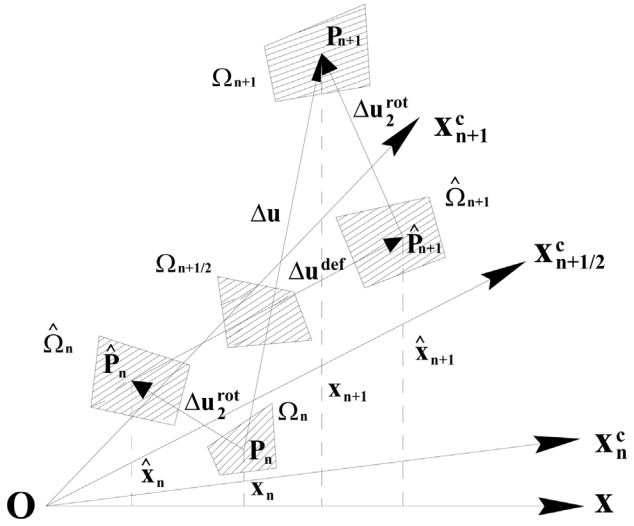

Figure 2 - Decomposition of the incremental displacement field in the corotational system.

$$\begin{aligned}
\hat{\mathbf{x}}_{n} &= \mathbf{R}_{n}\mathbf{X}_{n};\\
\hat{\mathbf{x}}_{n+1/2} &= \mathbf{R}_{n+1/2}\mathbf{X}_{n+1/2};\\
\hat{\mathbf{x}}_{n+1} &= \mathbf{R}_{n+1}\mathbf{X}_{n+1}
\end{aligned} \tag{15}$$

where $\mathbf{R}_n$, $\mathbf{R}_{n+1/2}$ and $\mathbf{R}_{n+1}$ are orthogonal transformation matrices, performing rotations from the global coordinate system to the corotational coordinate system, and $\mathbf{x}_n$, $\mathbf{x}_{n+1/2}$ and $\mathbf{x}_{n+1}$ are geometric configurations defined in the global coordinate system. The subscripts n, n + 1/2 and n + 1 denote positions in the time interval $[t_n, t_{n+1}]$.

The components of the transformation matrix $\mathbf{R}$ are given by:

$$\begin{aligned}
\mathbf{R}_{1j} &= \frac{\mathbf{r}_{1j}}{\mathbf{r}_1^{T}\mathbf{r}_1};\\
\mathbf{R}_{2j} &= \frac{(\mathbf{r}_{2j} + \mathbf{r}_{cj})}{(\mathbf{r}_{2j} + \mathbf{r}_{cj})^{T}(\mathbf{r}_{2j} + \mathbf{r}_{cj})};\\
\mathbf{R}_{3j} &= \frac{\mathbf{r}_{3j}}{\mathbf{r}_3^{T}\mathbf{r}_3}
\end{aligned} \tag{16}$$

with:

$$\begin{aligned}
&\mathbf{r}_{1j} = \boldsymbol{\xi}^{T}\mathbf{x}_j; \qquad \mathbf{r}_{2j} = \boldsymbol{\eta}^{T}\mathbf{x}_j;\\
&\mathbf{r}_{cj} = -\frac{\mathbf{r}_{1j}^{T}\mathbf{r}_{2j}}{\mathbf{r}_{1j}^{T}\mathbf{r}_{1j}}\mathbf{r}_{1j}; \qquad \mathbf{r}_{3j} = \mathbf{r}_{1j} \times (\mathbf{r}_{2j} + \mathbf{r}_{cj})
\end{aligned} \tag{17}$$

where $\boldsymbol{\xi}$, $\boldsymbol{\eta}$ and $\mathbf{x}_j$ are vectors containing local nodal coordinates and global nodal coordinates associated to the eight-node hexahedral element (see Fig. 3), respectively.

Since the local coordinate system rotate attached to each element in a corotational coordinate system, stress measures are not affected by rigid motions (objectivity). Therefore, the Cauchy stress tensor is employed in this work to calculate stress values in the corotational system. The Cauchy stress tensor in the global system is obtained from an objective tensor transformation as follows:

$$\boldsymbol{\sigma} = \mathbf{R}^{T}\hat{\boldsymbol{\sigma}}\mathbf{R} \tag{18}$$

where $\boldsymbol{\sigma}$ and $\hat{\boldsymbol{\sigma}}$ are the Cauchy stress tensor evaluated in the global and corotational coordinate systems, respectively.

On the other hand, stress rate measures are performed in this work using the Truesdell rate tensor in order to maintain objectivity of the stress updates in the corotational system:

$$d\hat{\boldsymbol{\sigma}}^{TR} = d\hat{\boldsymbol{\sigma}} - \mathbf{L}\hat{\boldsymbol{\sigma}} - \hat{\boldsymbol{\sigma}}\mathbf{L}^{T} + \hat{\boldsymbol{\sigma}}\hat{\dot{\varepsilon}}\mathbf{I} \tag{19}$$

where $\mathbf{I}$ is the unit tensor and

$$\mathbf{L} = \hat{\dot{\varepsilon}} + \hat{\omega} \tag{20}$$

where $\hat{\dot{\varepsilon}}$ and $\hat{\omega}$ are the strain rate tensor and the spin tensor, respectively, which are evaluated in the corotational system.

$$\mathbf{x}_1^T = \mathbf{x}^T = [x_1, x_2, x_3, x_4, x_5, x_6, x_7, x_8] \qquad \xi_1^T = \xi^T = [-1,+1,+1,-1,-1,+1,+1,-1]$$
$$\mathbf{x}_2^T = \mathbf{y}^T = [y_1, y_2, y_3, y_4, y_5, y_6, y_7, y_8] \qquad \xi_2^T = \eta^T = [-1,-1,+1,+1,-1,-1,+1,+1]$$
$$\mathbf{x}_3^T = \mathbf{z}^T = [z_1, z_2, z_3, z_4, z_5, z_6, z_7, z_8] \qquad \xi_3^T = \zeta^T = [-1,-1,-1,-1,+1,+1,+1,+1]$$

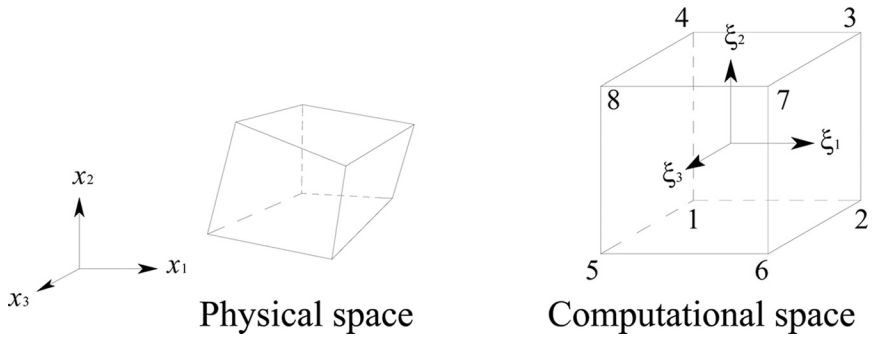

Figure 3 - Reference systems for the hexahedral finite element.

It is worth to notice that all geometrical configurations defined above should be referred to the undeformed configuration of the structure for geometrically linear problems.

3. The Numerical Model

3.1. Finite element formulation

The principle of the virtual displacements may be expressed as:

$$\int_{\Omega_E} (\nabla \delta \mathbf{u})^T \boldsymbol{\sigma} d\Omega_E = \int_{\Omega_E} \delta \mathbf{u}^T \mathbf{b} d\Omega_E + \int_{\Gamma_E} \delta \mathbf{u}^T \mathbf{t} d\Gamma_E \quad (21)$$

where $\mathbf{t}$ is the traction vector, Ω_E is the volume referred to element E and Γ_E represents its boundary surfaces, both considered in the FEM context.

Spatial coordinates and displacements are approximated at element level using the eight-node hexahedral finite element formulation, which may be expressed as:

$$\mathbf{x} = \mathbf{N}\mathbf{x}_E; \quad \delta\mathbf{u} = \mathbf{N}\delta\mathbf{u}_E; \quad \mathbf{u} = \mathbf{N}\mathbf{u}_E \quad (22)$$

where $\mathbf{x}$, $\delta\mathbf{u}$ and $\mathbf{u}$ are the coordinate, virtual displacement and displacement vectors evaluated within the element domain and $\mathbf{x}_E$, $\delta\mathbf{u}_E$ and $\mathbf{u}_E$ are their respective nodal values. The column matrix $\mathbf{N}$ contains the shape functions of the eight-node hexahedral element, which is usually presented as (see also Fig. 3):

$$N = [N_j]; \; N_j(\xi, \eta, \zeta) = \frac{1}{8}(1+\xi_j \xi)(1+\eta_j \eta)(1+\zeta_j \zeta), \; (j = 1, 2, \ldots, 8) \quad (23)$$

where ξ, η and ζ represent the axis directions of the local coordinate system (corotational system) and j denotes the local node numbers of the hexahedral element.

The equilibrium equation (Eq. 21) must be iteratively satisfied using the incremental approach, where the stiffness matrix and the internal force vector are considered as functions of the current element configuration as well as the current stress state. The Newton-Raphson method is employed in order to linearize all nonlinearities of the model. Consequently, the internal force vector is submitted to a Taylor series expansion within the time interval $[t_n, t_{n+1}]$, which gives:

$$\mathbf{f}^{int}_{n+1,\,i} = \mathbf{f}^{int}_{n+1,\,i-1} + \frac{\partial \mathbf{f}^{int}_{n+1,\,i-1}}{\partial \mathbf{u}_{n+1}} \Delta\mathbf{u} = \mathbf{f}^{int}_{n+1,\,i-1} + \mathbf{K}^{tan}_{n+1,\,i-1} \Delta\mathbf{u} \quad (24)$$

where i and i-1 indicate current and previous iterative steps within the time interval $[t_n, t_{n+1}]$ and $\mathbf{K}^{tan}_{n+1,\,i-1}$ represents the tangent stiffness matrix.

The tangent stiffness matrix and the internal force vector are evaluated in the corotational coordinate system at time instant t and iteration i as follows:

$$\hat{\mathbf{K}}^{tan}_{n,\,i} = \int_{\hat{\Omega}_E} \hat{\mathbf{B}}^T (\mathbf{D} + \mathbf{T}) \hat{\mathbf{B}} d\hat{\Omega}_E; \quad \hat{\mathbf{f}}_{n,\,i} = \int_{\hat{\Omega}_E} \hat{\mathbf{B}}^T \hat{\boldsymbol{\sigma}}_i \, d\hat{\Omega}_E \quad (25)$$

where the gradient matrix $\hat{\mathbf{B}}$ and $\hat{\Omega}_E$ are referred to the current element configuration in the corotational system, $\mathbf{D}$ and $\mathbf{T}$ are fourth order tensors related to the elastic constitutive equation and Truesdell rate terms, repectively, and $\boldsymbol{\sigma}_i$ is the corotational Cauchy stress tensor evaluated at the iterative step i (see Braun & Awruch, 2008; Duarte Filho & Awruch, 2004 for further details). It is important to notice that $\mathbf{T}$ vanishes for geometrically linear problems as well as $\mathbf{D}$ becomes $\mathbf{D}^e$ for elastic materials and $\mathbf{D}^{ep}$ for elastoplastic materials.

In order to solve the equilibrium equation, the tangent stiffness matrix and the internal force vector are brought back to the global coordinate system using the following objective transformations:

$$\mathbf{K}^{tan} = \mathbf{R}^T \hat{\mathbf{K}}^{tan} \mathbf{R}; \quad \mathbf{f}^{int} = \mathbf{R}^T \hat{\mathbf{f}}^{int} \quad (26)$$

where **R** is the transformation matrix defined in Eqs. 16 and 17.

The final matrix format of Eq. 21 in the global system, considering the incremental approach, is given as follows:

$$\mathbf{K}^{\tan}_{n+1,\,i\,-1}(\mathbf{u},\boldsymbol{\sigma})\Delta\mathbf{u}_{n+1,\,i}=\mathbf{f}^{\text{ext}}_{n+1}-\mathbf{f}^{\text{int}}_{n+1,\,i\,-1}(\mathbf{u},\boldsymbol{\sigma}) \tag{27}$$

where subscripts n+1 denote current position in the time marching with i and i-1 indicating current and previous iterative steps in the Newton-Raphson method. The vector of external forces $\mathbf{f}^{\text{ext}}$ represents the right-hand side terms of Eq. 21.

3.2. Reduced integration and element stabilization

Element formulations based on reduced integration must be stabilized using hourglass control techniques in order to avoid numerical instabilities. Volumetric locking, for instance, is remedied using reduced selective integration, where the gradient matrix **B** is decomposed as follows:

$$\mathbf{B}(\xi,\eta,\zeta)=\overline{\mathbf{B}}(0)+\tilde{\mathbf{B}}(\xi,\eta,\zeta) \tag{28}$$

where $\overline{\mathbf{B}}(0)$ corresponds to volumetric terms of the strain tensor, which is evaluated at the center of the element ($\xi = 0$, $\eta = 0$, $\zeta = 0$), and $\tilde{\mathbf{B}}(\xi,\eta,\zeta)$ is referred to deviatoric terms of the strain tensor.

In addition, $\tilde{\mathbf{B}}(\xi,\eta,\zeta)$ must be expanded using Taylor series at the center of the element up to bilinear terms. Consequently, Eq. 28 can be re-written as:

$$\begin{aligned}\mathbf{B}(\xi,\eta,\zeta)=\mathbf{B}(0)+\tilde{\mathbf{B}}_{,\xi}(0)\xi+\tilde{\mathbf{B}}_{,\eta}(0)\eta+\tilde{\mathbf{B}}_{,\zeta}(0)\zeta+\\ 2\tilde{\mathbf{B}}_{,\xi\eta}(0)\xi\eta+2\tilde{\mathbf{B}}_{,\eta\zeta}(0)\eta\zeta+2\tilde{\mathbf{B}}_{,\xi\zeta}(0)\xi,\zeta\end{aligned} \tag{29}$$

where **B**(0) is a sum of the volumetric and deviatoric parts of the gradient matrix, both obtained from one-point quadrature.

The vector representation of the stress tensor $\boldsymbol{\sigma}$ is also submitted to a Taylor series expansion over the center of the element, which leads to:

$$\begin{aligned}\boldsymbol{\sigma}(\xi,\eta,\zeta)=\boldsymbol{\sigma}(0)+\tilde{\boldsymbol{\sigma}}_{,\xi}(0)\xi+\tilde{\boldsymbol{\sigma}}_{,\eta}(0)\eta+\tilde{\boldsymbol{\sigma}}_{,\zeta}(0)\zeta+\\ 2\tilde{\boldsymbol{\sigma}}_{,\xi\eta}(0)\xi\eta+2\tilde{\boldsymbol{\sigma}}_{,\eta\zeta}(0)\eta\zeta+2\tilde{\boldsymbol{\sigma}}_{,\xi\zeta}(0)\xi,\zeta\end{aligned} \tag{30}$$

where all the terms above have similar interpretations to those described in Eq. 29.

By substituting Eqs. 29 and 30 into the left-hand side term of Eq. 21, considering the relation between strain and displacement components and the decomposition performed in Eq. 28, the internal force vector must be re-written as follows:

$$\mathbf{f}^{\text{int}}=\mathbf{f}^{\text{int},0}+\mathbf{f}^{\text{int, hg}} \tag{31}$$

where $\mathbf{f}^{\text{int},0}$ and $\mathbf{f}^{\text{int,hg}}$ are the one-point quadrature and hourglass control parts of the internal force vector, respectively, which may be expressed as:

$$\mathbf{f}^{\text{int}}=\mathbf{K}^{\tan}\mathbf{u}=\left(\int_{\Omega_E}\mathbf{B}^{\mathrm{T}}(\mathbf{D}+\mathbf{T})\mathbf{B}\,d\hat{\Omega}_E\right)\mathbf{u} \tag{32}$$

$$\begin{aligned}\mathbf{f}^{\text{int, hg}}=\mathbf{K}^{\text{stab}}\mathbf{u}=\Big[&\frac{1}{3}\tilde{\mathbf{B}}^{\mathrm{T}}_{,\xi}\tilde{\boldsymbol{\sigma}}_{,\xi}(0)+\frac{1}{3}\tilde{\mathbf{B}}^{\mathrm{T}}_{,\eta}\tilde{\boldsymbol{\sigma}}_{,\eta}(0)+\\ &\frac{1}{3}\tilde{\mathbf{B}}^{\mathrm{T}}_{,\zeta}\tilde{\boldsymbol{\sigma}}_{,\zeta}(0)+\frac{1}{9}\tilde{\mathbf{B}}^{\mathrm{T}}_{,\xi\eta}\tilde{\boldsymbol{\sigma}}_{,\xi\eta}(0)+\frac{1}{9}\tilde{\mathbf{B}}^{\mathrm{T}}_{,\eta\zeta}\tilde{\boldsymbol{\sigma}}_{,\eta\zeta}(0)+\\ &\frac{1}{9}\tilde{\mathbf{B}}^{\mathrm{T}}_{,\xi\zeta}\tilde{\boldsymbol{\sigma}}_{,\xi\zeta}(0)\Big]\Omega_E\end{aligned} \tag{33}$$

where $\mathbf{K}^{\text{stab}}$ is the element stabilization stiffness matrix and Ω_E is the volume of the element. Derivatives of the stress vector are obtained employing the stabilization matrix **E** proposed by Hu & Nagy (1997), which leads to a constitutive-like relation between stress and strain derivatives (see Duarte Filho & Awruch, 2004; Braun & Awruch, 2008). For elastoplastic behavior, Reese (2005) proposed a modified stabilization matrix constituted by an optimized stabilization parameter μ. In this work, the following procedure is adopted:

$$\begin{aligned}&\mu=G\ \text{(elastic range)};\\ &\mu=G\,\frac{A_0}{3K(1-2\nu)+A_0}\ \text{(plastic range)}\end{aligned} \tag{34}$$

where A_0 is the hardening parameter given by Eq. 11 and evaluated only at the first yielding of the respective element. The stabilization matrix **E** is obtained using the stabilization parameter μ as follows:

$$\mathbf{E}=\begin{bmatrix}\mathbf{e}&\mathbf{0}\\ \mathbf{0}&\mathbf{e}\end{bmatrix};\quad \mathbf{e}=\begin{pmatrix}2\mu&0&0\\ 0&2\mu&0\\ 0&0&2\mu\end{pmatrix} \tag{35}$$

Shear locking is removed describing the shear components of the strain tensor in an orthogonal corotational coordinate system. In addition, all shear components are linearly interpolated in a single direction of the reference system as follows:

$$\begin{aligned}&\varepsilon_{xy}(\xi,\eta,\zeta)=\varepsilon_{xy}(0)+\tilde{\varepsilon}_{xy,\zeta}(0)\zeta\\ &\varepsilon_{yz}(\xi,\eta,\zeta)=\varepsilon_{yz}(0)+\tilde{\varepsilon}_{yz,\xi}(0)\xi\\ &\varepsilon_{xz}(\xi,\eta,\zeta)=\varepsilon_{xz}(0)+\tilde{\varepsilon}_{xz,\eta}(0)\eta\end{aligned} \tag{36}$$

which leads to:

$$\begin{aligned}&\tilde{B}_{xy,\xi}(0)=\tilde{B}_{xy,\eta}(0)=\tilde{B}_{xy,\xi\eta}(0)=\tilde{B}_{xy,\eta\zeta}(0)=\tilde{B}_{xy,\xi\zeta}(0)=0\\ &\tilde{B}_{yz,\eta}(0)=\tilde{B}_{yz,\zeta}(0)=\tilde{B}_{yz,\xi\eta}(0)=\tilde{B}_{yz,\eta\zeta}(0)=\tilde{B}_{yz,\xi\zeta}(0)=0\\ &\tilde{B}_{xz,\xi}(0)=\tilde{B}_{xz,\zeta}(0)=\tilde{B}_{xz,\xi\eta}(0)=\tilde{B}_{xz,\eta\zeta}(0)=\tilde{B}_{xz,\xi\zeta}(0)=0\end{aligned} \tag{37}$$

The internal force vector is not well evaluated for distorted elements if one-point quadrature is used. In order to correct this deficiency the gradient matrix obtained with reduced integration **B**(0) must be replaced by uniform gradi-

ent submatrices $\mathbf{B}'_a(0)$ defined by Flanagan & Belytschko (1981):

$$\mathbf{B}'_a(0) = \frac{1}{\Omega_E}\int_{\Omega_E} \mathbf{B}_a(\xi,\eta,\zeta)\mathrm{d}\Omega_E \tag{38}$$

where the subscript a corresponds to the local node number of the element.

It is worth to notice that all equations presented in this section are implicitly referred to the corotational coordinate system, although the symbol ^ adopted previously has been omitted in the respective expressions.

3.3. Integration of the stress-strain relation

In elastoplastic analysis, strain increments are imposed at element level based on the incremental solution obtained from the equilibrium equation. On the other hand, stress increments are dependent on the material behavior. A trial elastic stress increment is usually considered as an initial estimative for the new stress state. If this new stress state does not lead to plastic yielding, the corresponding stress increment is taken as true. However, if plastic yielding is observed, the following system of ordinary differential equations must be solved:

$$\frac{\mathrm{d}\boldsymbol{\sigma}}{\mathrm{d}T} = \mathbf{D}^{ep}\Delta\varepsilon;\quad \frac{\mathrm{d}\kappa}{\mathrm{d}T} = \Delta\lambda B \tag{39}$$

with:

$$\begin{aligned} T &= \frac{t-t_0}{\Delta t};\quad \Delta\lambda = \frac{\mathbf{a}_f^{\mathrm{T}}\mathbf{D}^e}{A+\mathbf{a}_f^{\mathrm{T}}\mathbf{D}^e\mathbf{a}_g}\Delta\varepsilon; \\ B &= -\frac{A}{\partial f/\partial\kappa} = \frac{v_s p_c}{\lambda-k}\frac{\partial g}{\partial p} \end{aligned} \tag{40}$$

where T is the artificial time, which is defined in the range $0 \le T \le 1$, t_0 is the time at the starting point of the load increment (Δt), t is the time in a position within the load increment (Δt) and B is a hardening parameter.

In the remainder of the present section, numerical procedures to solve the elastoplastic problem are briefly described. A step-by-step algorithm of the present numerical model may be found in Appendix A.

(a) Determination of the elastic trial stress increment

Considering a strain increment $\Delta\varepsilon$ obtained from the incremental solution $\Delta\mathbf{u}_{n+1,i}$ of the equilibrium equation (Eq. 27) at iteration i, the elastic trial stress increment $\Delta\overline{\boldsymbol{\sigma}}^e$ is calculated from:

$$\Delta\overline{\boldsymbol{\sigma}}^e = \overline{\mathbf{D}}^e(\overline{K},\overline{G})\Delta\varepsilon \tag{41}$$

where $\overline{\mathbf{D}}^e$ is the secant constitutive matrix, which is defined using $\overline{K}$ and $\overline{G}$ (see Eqs. 5 and 6) owing to the nonlinear elastic behavior observed in critical state models. It is important to notice that $\overline{K}$ and $\overline{G}$ are evaluated using the stress state at the starting point of the current strain increment ($\boldsymbol{\sigma}_0$) and the total volumetric strain increment $\Delta\varepsilon_v$. For conventional constitutive models, such as the Mohr-Coulomb yield criterion, these parameters are linear elastic constants evaluated using classical elastic relations, which leads to the tangent form of the constitutive matrix $\mathbf{D}^e$. In this case, $\overline{\mathbf{D}}^e$ must be replaced by $\mathbf{D}^e$ in Eq. 41 and hereafter.

(b) Determination of the elastic fraction of the stress increment

The elastic trial stress increment $\Delta\overline{\boldsymbol{\sigma}}^e$ is now utilized to check the yield function (Eq. 7) with the corresponding trial stress state ($\boldsymbol{\sigma}_0 + \Delta\overline{\boldsymbol{\sigma}}^e$). If no plastic yielding occurs ($f(\boldsymbol{\sigma}_0 + \Delta\overline{\boldsymbol{\sigma}}^e, \kappa_0) < 0$), the stress state is updated according to the trial stress state. On the other hand, if the trial stress state causes plastic yielding, the following alternatives must be considered (see also Fig. 4):

1) if $f(\boldsymbol{\sigma}_0, \kappa_0) < 0$ and $f(\boldsymbol{\sigma}_0 + \Delta\overline{\boldsymbol{\sigma}}^e, \kappa_0) > 0$: the stress state has changed from elastic to plastic. The elastic fraction of the total strain increment $\Delta\varepsilon$ must be determined in order to advance the initial stress state $\boldsymbol{\sigma}_0$ to the stress state on the yield surface $\boldsymbol{\sigma}_{yld}$;
2) if $f(\boldsymbol{\sigma}_0, \kappa_0) = 0$ and $f(\boldsymbol{\sigma}_0 + \Delta\overline{\boldsymbol{\sigma}}^e, \kappa_0) > 0$: the stress state is initially lying on the yield surface and the trial stress state causes plastic yielding. In this case, elastoplastic unloading may occur, which is observed if the angle θ between the flow vector $\mathbf{a}_0$ and the tangential elastic increment $\Delta\boldsymbol{\sigma}^e(K,G)$ is larger than 90º. The angle θ may be calculated using:

$$\cos\theta = \frac{\mathbf{a}_0^{\mathrm{T}}\Delta\boldsymbol{\sigma}^e}{\left\|\mathbf{a}_0\right\|\left\|\Delta\boldsymbol{\sigma}^e\right\|} \tag{42}$$

where $\mathbf{a}_0$ is evaluated at the initial stress state $\boldsymbol{\sigma}_0$ and $\Delta\boldsymbol{\sigma}^e$ is evaluated using the incremental form of Eq. 1. If no elastoplastic unloading occurs, the strain increment $\Delta\varepsilon$ is assumed to be totally plastic. Nevertheless, if the elastoplastic unloading conditions are satisfied, the elastic fraction of the total strain increment $\Delta\varepsilon$ must be determined.

The stress state on the yield surface $\boldsymbol{\sigma}_{yld}$ may be determined considering the following nonlinear equation:

$$f(\boldsymbol{\sigma}_0 + \alpha\overline{\mathbf{D}}^e\Delta\varepsilon, \kappa_0) = 0 \tag{43}$$

where α is a scalar to be determined in order to satisfy Eq. 43. The secant constitutive matrix $\overline{\mathbf{D}}^e$ is evaluated using the initial stress $\boldsymbol{\sigma}_0$ and the strain increment $\alpha\Delta\varepsilon$. If $\alpha = 0$, the strain increment $\Delta\varepsilon$ is assumed to be totally plastic and if $\alpha = 1$, the strain increment $\Delta\varepsilon$ is assumed to be totally elastic. Elastic to plastic transition is characterized by $0 < \alpha < 1$, where the elastic fraction of the total strain increment $\Delta\varepsilon$ is given by $\alpha\Delta\varepsilon$. In order to solve Eq. 43, the Pegasus algorithm introduced by Dowell & Jarratt (1972) is

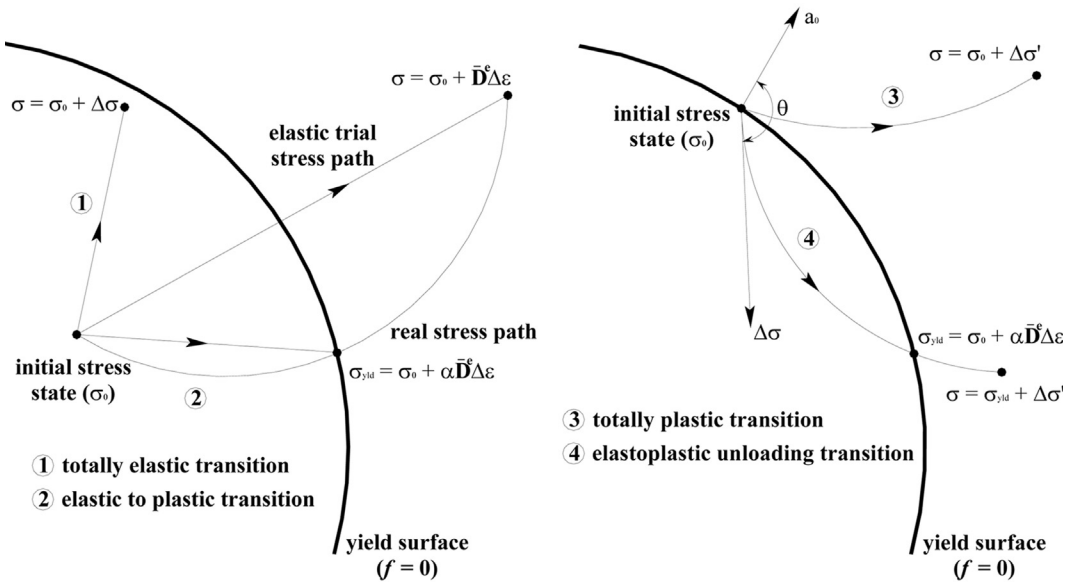

Figure 4 - Possible transitions for the stress state during an elastoplastic analysis.

adopted in the present work (see Appendix B for a detailed description).

(c) Integration of the stress-strain equation:

Once the elastic fraction of the stress increment is obtained from the Pegasus algorithm, the plastic fraction of the strain increment $\Delta\varepsilon'$ is determined using:

$$\Delta\varepsilon' = (1-\alpha)\Delta\varepsilon \tag{44}$$

In order to define initial conditions for the system of equations described by Eq. 39, the stress state $\boldsymbol{\sigma}_0$ is updated to the stress state at the onset of the plastic yielding $\boldsymbol{\sigma}_{yld}$ and the hardening parameter κ_0 is considered at the start of the strain increment $\Delta\varepsilon'$ where $T = 0$ and $t = t_0$. By using the explicit Euler method, a substepping technique, as proposed by Sloan *et al.* (2001), is performed over the strain increment $\Delta\varepsilon'$ to find the stress state and the hardening parameter at the end of $\Delta\varepsilon'$, where $T = 1$. Subincrements of $\Delta\varepsilon'$ are defined according to the artificial time increment ΔT, which is calculated taking into account a local error measure obtained by the difference between a second order accurate modified Euler solution and a first order accurate Euler solution. Consequently, the size of the subincrements is automatically modified along the integration process.

In the explicit Euler method, stress state $\boldsymbol{\sigma}_n$ and hardening parameter κ_n at the end of an artificial time increment ΔT_n are obtained as follows:

$$\boldsymbol{\sigma}_n = \boldsymbol{\sigma}_{n-1} - \Delta\boldsymbol{\sigma}_1; \quad \kappa_n = \kappa_{n-1} - \Delta\kappa_1 \tag{45}$$

with:

$$\Delta\boldsymbol{\sigma}_1 = \mathbf{D}^e(\boldsymbol{\sigma}_{n-1}, \kappa_{n-1})\Delta\varepsilon'_n \tag{46}$$

$$\Delta\kappa_1 = \Delta\lambda(\boldsymbol{\sigma}_{n-1}, \kappa_{n-1}, \Delta\varepsilon'_n)B(\boldsymbol{\sigma}_{n-1}) \tag{47}$$

$$\Delta\varepsilon'_n = \Delta T_n \Delta\varepsilon' \ (0 \le \Delta T_n \le 1) \tag{48}$$

where n-1 and n are referred to previous and current artificial time positions T_{n-1} and T_n, respectively, such that $T_n = T_{n-1} + \Delta T_n$.

In the modified Euler method, stress state $\boldsymbol{\sigma}_n$ and hardening parameter κ_n at the end of an artificial time increment ΔT_n are obtained as follows:

$$\boldsymbol{\sigma}_n = \boldsymbol{\sigma}_{n-1} + \frac{1}{2}(\Delta\boldsymbol{\sigma}_1 + \Delta\boldsymbol{\sigma}_2); \ \kappa_n = \kappa_{n-1} + \frac{1}{2}(\Delta\kappa_1 + \Delta\kappa_2) \tag{49}$$

where $\Delta\boldsymbol{\sigma}_1$ and $\Delta\kappa_1$ are calculated with Eqs. 46 and 47 and:

$$\Delta\boldsymbol{\sigma}_2 = \mathbf{D}^e(\boldsymbol{\sigma}_{n-1} + \Delta\boldsymbol{\sigma}_1, \kappa_{n-1} + \Delta\kappa_1)\Delta\varepsilon'_n \tag{50}$$

$$\Delta\kappa_2 = \Delta\lambda(\boldsymbol{\sigma}_{n-1} + \Delta\boldsymbol{\sigma}_1, \kappa_{n-1} + \Delta\kappa_1, \Delta\varepsilon'_n)\cdot B(\boldsymbol{\sigma}_{n-1} + \Delta\boldsymbol{\sigma}_1) \tag{51}$$

The relative local error measures over $\boldsymbol{\sigma}_n$ and κ_n are estimated from:

$$E_n^\sigma = \frac{1}{2}\left(\frac{\|\Delta\boldsymbol{\sigma}_2 - \Delta\boldsymbol{\sigma}_1\|}{\|\boldsymbol{\sigma}_n\|}\right); \ E_n^\kappa = \frac{1}{2}\left(\frac{|\Delta\kappa_2 - \Delta\kappa_1|}{|\kappa_n|}\right) \tag{52}$$

where the Euclidian norm $\|\boldsymbol{\sigma}_n\|$ and the absolute value $|\kappa_n|$ are calculated using Eq. 49.

The current subincrement $\Delta\varepsilon'$ is accepted if both the errors given by Eq. 52 are less than a prescribed tolerance value. The next artificial time increment ΔT_{n+1} is obtained taking into account the relative errors of the current artificial time T_n, which permits the size of the subincrements to vary during the integration process. At the end of each subincrement, corrections in the stress state and hardening parameter may be needed in order to satisfy the yield condi-

tion accurately and avoid yield surface drift. The integration process is carried on until the plastic increment $\Delta\varepsilon'$ is completely applied, *i.e.* $T_n = 1$. Suitable tolerance values for all the iterative procedures utilized in the present scheme are found in Sloan *et al.* (2001), where a sensitive analysis is presented in order to investigate the influence of the tolerance values over the numerical predictions.

For a complete description of the numerical model adopted in this work, readers are addressed to the algorithm presented in Appendix A.

4. Conclusions

A numerical model based on one-point quadrature and critical state formulation was proposed in this work to simulate the mechanical behavior of soils. The critical state formulation was briefly described using a classical elastoplastic approach where the Modified Cam-Clay model was emphasized. The finite element implementation of the analytical model was performed using the eight-node hexahedral element formulation and reduced integration techniques. A corotational reference system was utilized to stabilize the element formulation as well as to describe stress-strain relations and motion, especially for geometrically nonlinear analysis. The constitutive equation was integrated in this paper using an explicit algorithm with an automatic procedure to split the strain increment into a number of subincrements. Numerical algorithms to determine the yield intersection point, to handle elastoplastic unloading and to restore uncorrected stresses to the yield surface were also presented. One can observe that the formulation presented here leads to a highly efficient numerical model, especially for nonlinear analysis, where the computational effort is substantially reduced when compared to other formulations employing standard approaches. In future works, following this on-going research, the present formulation will be extended to analyze the mechanical behavior of saturated/unsaturated soils.

Appendix A

All numerical procedures adopted in this work may be summarized according to the following algorithm:

Initialization procedures

– Read input data (algorithmic parameters, physical constants and mesh configuration)
– Evaluate the transformation matrix **R** and the gradient matrix **B** at element level considering the initial geometric configuration in the corotational system. For geometrically linear problems, those matrices will be maintained throughout the analysis.
– Evaluate the internal force vector $\mathbf{f}^{int}$ considering the imposed initial stress state.

Time loop: $t_{n+1} = t_n + \Delta t$ (where Δt defines the load step)

– Evaluate the external force vector $\mathbf{f}^{ext}$ at the current time t_{n+1}: $\mathbf{f}^{ext}_{n+1} = \mathbf{f}^{ext}_{n} = \Delta\mathbf{f}^{ext}$.

Iterative loop: i = i + 1

1) For geometrically nonlinear problems, update the gradient matrix **B** and the transformation matrix **R** at element level considering the current geometric configuration in the corotational system and evaluate the Truesdell rate tensor **T**, which must be added to the constitutive matrix **D**.
2) Evaluate the tangent constitutive matrix **D**: in the elastic regime, consider $\mathbf{D} = \mathbf{D}^e$; in the plastic regime, consider $\mathbf{D} = \mathbf{D}^{ep}$.
3) Evaluate the tangent stiffness matrix $\mathbf{K}^{tan}$ in the corotational system including the element stabilization terms.
4) Solve the equilibrium equation in the global system: $\mathbf{K}^{tan}_{n+1,\,i-1}(\mathbf{u}, \boldsymbol{\sigma})\Delta\mathbf{u}_{n+1,\,i} = \mathbf{f}^{ext}_{n+1} - \mathbf{f}^{int}_{n+1,\,i-1}(\mathbf{u}, \boldsymbol{\sigma})$.
5) For geometrically nonlinear problems, determine the intermediate geometric configuration $\mathbf{x}_{n+1/2}$ based on the last incremental solution $\Delta\mathbf{u}_{n+1,\,i}$.
6) Determine the strain increment $\Delta\varepsilon$ in the corotational system using the incremental solution $\Delta\mathbf{u}_{n+1,\,i}$. For geometrically nonlinear problems, the transformation matrix **R** and the gradient matrix **B** adopted in the evaluation of the strain increment must be updated considering the intermediate geometric configuration $\mathbf{x}_{n+1/2}$ in the corotational system.
7) Determine the trial stress state using the elastic trial stress increment:
$\Delta\overline{\boldsymbol{\sigma}}^e = \overline{\mathbf{D}}^e(\overline{K}, \overline{G})\Delta\varepsilon \Rightarrow \boldsymbol{\sigma}^e = \boldsymbol{\sigma}_0 + \Delta\overline{\boldsymbol{\sigma}}^e$
8) Check the yield function: $f(\boldsymbol{\sigma}^e, \kappa_0)$
9) If $f(\boldsymbol{\sigma}^e, \kappa_0) < 0 \Rightarrow$ totally elastic stress state transition: set $\boldsymbol{\sigma} = \boldsymbol{\sigma}^e$ and go to step 11.
If $f(\boldsymbol{\sigma}^e, \kappa_0) \geq 0 \Rightarrow$ verify the following alternatives:
   - If $f(\boldsymbol{\sigma}_0, \kappa_0) < 0$ and $f(\boldsymbol{\sigma}^e, \kappa_0) \geq 0$: elastic to plastic transition; determine the elastic fraction of $\Delta\varepsilon$ using the Pegasus scheme.
   - If $f(\boldsymbol{\sigma}_0, \kappa_0) = 0$ and $f(\boldsymbol{\sigma}^e, \kappa_0) > 0$: check if elastoplastic unloading occurs by computing $\cos\theta = \dfrac{\mathbf{a}_0^T \Delta\boldsymbol{\sigma}_e}{\|\mathbf{a}_0\|\|\Delta\boldsymbol{\sigma}_e\|}$. For $\cos\theta \geq 0$, the stress increment is totally plastic; otherwise, determine the elastic fraction of $\Delta\varepsilon$ using the Pegasus scheme for elastoplastic unloading.
10) Update the stress state $\boldsymbol{\sigma}_0$ to the stress state at the onset of the plastic yielding $\boldsymbol{\sigma}_{yld}$; determine the plastic fraction of the strain increment using $\Delta\varepsilon' = (1-\alpha)\Delta\varepsilon$.

Substepping loop: $T_n = T_{n-1} + \Delta T_n$

a) Compute the increments of stress and hardening parameter employing: $\Delta\boldsymbol{\sigma}_1 = \mathbf{D}^{ep}(\boldsymbol{\sigma}_{n-1}, \kappa_{n-1})\Delta\varepsilon'_n$; $\Delta\kappa_1 = \Delta\lambda(\boldsymbol{\sigma}_{n-1}, \kappa_{n-1}, \Delta\varepsilon'_n)B(\boldsymbol{\sigma}_{n-1})$.
b) Update the stress state and the hardening parameter using the explicit Euler method.

c) Compute the increments of stress and hardening parameter employing:

$\Delta\boldsymbol{\sigma}_2 = \mathbf{D}^{ep}(\boldsymbol{\sigma}_{n-1} + \Delta\boldsymbol{\sigma}_1, \kappa_{n-1} + \Delta\kappa_1)\Delta\boldsymbol{\varepsilon}'_n$ and

$\Delta\kappa_2 = \Delta\lambda(\boldsymbol{\sigma}_{n-1} + \Delta\boldsymbol{\sigma}_1, \kappa_{n-1} + \Delta\kappa_1, \Delta\boldsymbol{\varepsilon}'_n)B(\boldsymbol{\sigma}_{n-1} + \Delta\boldsymbol{\sigma}_1)$.

d) Update the stress state and the hardening parameter using the modified Euler method.

e) Compute the relative errors over $\boldsymbol{\sigma}_n$ and κ_n and decide if the current subincrement is successful or not.

f) For accepted subincrements, check the yield function: if $f(\boldsymbol{\sigma}_n, \kappa_n) \neq 0$ then correct the stress state and the hardening parameter to satisfy the yield condition precisely.

End of substepping loop ($T_n = 1$)

11) Update the stress state and the hardening parameter at the end of the strain increment $\Delta\varepsilon$.

12) For geometrically nonlinear problems, determine the final geometric configuration $\mathbf{x}_{n+1}$ based on the last incremental solution $\Delta\mathbf{u}_{n+1,i}$ and update the gradient matrix **B** and the transformation matrix **R** at element level considering $\mathbf{x}_{n+1}$ in the corotational system.

13) Compute the internal force vector considering the last updated stress state.

14) Verify convergence of the current load step.

End of iterative loop

End of time loop

Appendix B

The Pegasus algorithm utilized in this work may be described as follows:

1) Retain the stress state $\boldsymbol{\sigma}_0$ and the hardening parameter κ_0 evaluated at the start of the strain increment $\Delta\varepsilon$.

2) Set $\alpha_0 = 0$ and $\alpha_1 = 1$.

3) Determine an elastic trial stress increment using $\Delta\boldsymbol{\sigma}^e = \alpha_1 \mathbf{D}^e \Delta\varepsilon$, where $\overline{\mathbf{D}}^e = \overline{\mathbf{D}}^e(\boldsymbol{\sigma}_0, \alpha_1, \Delta\varepsilon_v)$.

4) Evaluate the yield function at the start and the end of the trial stress increment as follows: $F_0 = f(\boldsymbol{\sigma}_0, \kappa_0)$ and $F_1 = f(\boldsymbol{\sigma}_0 + \Delta\overline{\boldsymbol{\sigma}}^e, \kappa_0)$.

Iterative loop: i = i + 1

a) Calculate $\alpha = \alpha_1 - F_1 \dfrac{\alpha_1 - \alpha_0}{F_1 - F_0}$.

b) Determine a new elastic trial stress increment using $\Delta\overline{\boldsymbol{\sigma}}^e = \alpha\overline{\mathbf{D}}^e\Delta\varepsilon$, where $\overline{\mathbf{D}}^e = \overline{\mathbf{D}}^e(\boldsymbol{\sigma}_0, \alpha\Delta\varepsilon_v)$.

c) Evaluate the yield function based on the last trial stress increment as follows: $\mathbf{F}_N = f(\boldsymbol{\sigma}_0 + \Delta\overline{\boldsymbol{\sigma}}^e, \kappa_0)$.

d) If $|\mathbf{F}_N| \leq$ TOL then leave the iterative loop retaining the last evaluation of α, else go to the next step of the iterative loop. TOL is referred to a tolerance criterion adopted to define the convergence of the numerical procedure.

e) If F_N presents an opposite sign to F_0, set $\alpha_1 = \alpha$ and $F_1 = F_N$, otherwise update F_1 using $F_1 = \dfrac{F_1 F_0}{F_N F_0}$ and set $\alpha_0 = \alpha$ with $F_0 = F_N$.

End of iterative loop

Exit with α.

For elastoplastic unloading, different values must be considered for α_0 and α_1 to initiate the iterative procedure in order to ensure that the Pegasus algorithm finds the intersection point on the yield surface precisely. Therefore, α_0 and α_1 should satisfy the following conditions:

$f(\boldsymbol{\sigma}_0 + \alpha_0\overline{\mathbf{D}}^e\Delta\varepsilon, \kappa_0) < -$TOL and

$f(\boldsymbol{\sigma}_0 + \alpha_1\overline{\mathbf{D}}^e\Delta\varepsilon, \kappa_0) >$ TOL.

References

Alonso, E.E.; Gens, A. & Josa, A. (1990) A constitutive model for partially saturated soils. Géotechnique, v. 40:3, p. 405-430.

Andrade, L.G.; Awruch, A.M. & Morsch, I.B. (2007) Geometrically nonlinear analysis of laminate composite plates and shells using the eight-node hexahedral element with one point integration. Composite Structures, v. 79:4, p. 571-580.

Braun, A.L. & Awruch, A.M. (2008) Geometrically nonlinear analysis in elastodynamics using the eight-node finite element with one-point quadrature and the generalized-alpha method. Latin American Journal of Solids and Structures, v. 5:1, p. 17-45.

Braun, A.L. & Awruch A.M. (2009) A partitioned model for fluid-structure interaction problems using hexahedral finite elements with one-point quadrature. International Journal for Numerical Methods in Engineering, v. 79:5, p. 505-549.

Carter, J.P.; Booker, J.R. & Wroth, C.P. (1982) A critical state model for cyclic loading. Pande and Zienkiewicz (eds) Soil Mechanics - Transient and Cyclic Loads, Wiley, Chichester, p. 219-252.

Collins, I.F. & Houlsby, G.T. (1997) Application of thermomechanical priciples to the modeling of geotechnical materials. Proc. Royal Society of London, v. A/453, p. 1975-2001.

Coulomb, C.A. (1776) Essai sur une application des règles de maxims et minims à quelques problèmes de statique, relatifs à l'architecture. Mèm. Acad. R. Sci., v. 7:1, p. 343-382.

Crouch, R.S.; Wolf, J.P. & Dafalias, Y.F. (1994) Unified critical state bounding surface plasticity model for soil. Journal of Engineering Mechanics, ASCE, v. 120:11, p. 2251-2270.

de Borst, R. & Groen, A.E. (1999) Towards efficient and robust elements for 3D-soil plasticity. Computers and Structures, v. 70:1, p. 23-34.

Dowell, M. & Jarrat, P. (1972) The Pegasus method for computing the root of an equation. BIT, v. 12:4, p. 503-508.

Duarte Filho, L.A. & Awruch, A.M. (2004) Geometrically nonlinear static and dynamic analysis of shells and plates using the eight-node hexahedral element with one-point quadrature. Finite Elements in Analysis and Design, v. 40:1, p. 1297-1315.

Flanagan, D.P. & Belytschko, T. (1981) A uniform strain hexahedron and quadrilateral with orthogonal hourglass control. International Journal of Numerical Methods in Engineering, v. 17:5, p. 679-706.

Fredlund, D.G. & Rahardjo, H. (1993) Soil Mechanics for Unsaturated Soils. John Wiley & Sons, New York, 517 pp.

Gens, A. & Potts, D.M. (1988) Critical state models in computational geomechanics. Engineering Computations, v. 5:3, p. 178-197.

Hu, Y.K. & Nagy, L.I. (1997) A one-point quadrature eight-node brick element with hourglass control. Computers and Structures, v. 65:6, p. 893-902.

Liu, W.K.; Guo, Y.; Tang, S. & Belytschko, T. (1998) A multiple-quadrature eight-node hexahedral finite element for large deformation elastoplastic analysis. Computer Methods in Applied Mechanics and Engineering, v. 154:1-2, p. 69-132.

Nayak, G.C. & Zienkiewicz, O.C. (1972) Elasto-plastic stress analysis. A generalization for various constitutive relations including strain softening. International Journal for Numerical Methods in Engineering, v. 5:1, p. 113-135.

Naylor, D.J. (1985) A continuous plasticity version of the critical state model. International Journal for Numerical Methods in Engineering, v. 21:7, p. 1187-1204.

Owen, D.R.J. & Hinton, E. (1980) Finite Elements in Plasticity: Theory and Pratice, Pineridge Press, Swansea, 594 pp.

Pastor, M. & Zienkiewicz, O.C. (1990) Generalized plasticity and modeling of soil behaviour. International Journal for Analytical and Numerical Methods in Geomechanics, v. 14:3, p. 151-190.

Potts, D.M. & Ganendra, D. (1994) An evaluation of substepping and implicit stress point algorithms. Computer Methods in Applied Mechanics and Engineering, v. 119:3-4, p. 341-354.

Rankine, W.J.M. (1857) On the stability of loose earth. Phil. Trans. R. Soc., v. 147:2, p. 9-27.

Reese S. (2005) On a physically stabilized one point finite element formulation for three-dimensional finite elasto-plasticity. Computer Methods in Applied Mechanics and Engineering, v. 194:45-47, p. 4685-4715.

Roscoe, K.H. & Schofield, A.N. (1963) Mechanical behaviour of an idealized "wet" clay. Proc. 2nd European Conference on Solid Mechanics & Foundation Engineering, Wiesbaden, v. 1, pp. 47-54.

Roscoe, K.H. & Burland, J.B. (1968) On the generalized stress-strain behaviour of "wet" clay. Engineering Plasticity. Cambridge University Press, Cambridge, pp. 535-560.

Schofield, A.N. & Wroth, C.P. (1968) Critical State Soil Mechanics, McGraw-Hill, London, 310 p.

Sheng, D.; Sloan, S.W. & Yu, H.S. (2000) Aspects of finite element implementation of critical state models. Computational Mechanics, v. 26:2, p. 185-196.

Sloan, S.W.; Abbo, A.J. & Sheng, D. (2001) Refined explicit integration of elastoplastic models with automatic error control. Engineering Computations, v. 18:1-2, p. 121-154.

Yu, H.S. (1998) CASM: A unified state parameter model for clay and sand. International Journal for Numerical and Analytical Methods in Geomechanics, v. 22:8, p. 621-653.

Zhao, J.; Sheng, D.; Rouainia, M. & Sloan, S.W. (2005) Explicit Integration of complex soil models. International Journal for Numerical and Analytical Methods in Geomechanics, v. 29:12, p. 1209-1229.

Zienkiewicz, O.C. & Naylor, D.J. (1973) Finite element studies of soils and porous media. Oden and de Arantes (eds) Lecturer Finite Elements in Continuum Mechanics. UAH Press, Huntsville, Alabama, pp. 459-493.

An Efficient Model for Numerical Simulation of the Mechanical Behavior of Soils. Part 2: Applications

A.L. Braun, A.M. Awruch

Abstract. A numerical model to simulate the mechanical behavior of soils was introduced in Part 1 of this paper (also published in this issue). Detailed information about the analytical model were presented, where the critical state theory for soil mechanics was considered in the context of the elastoplastic formulation. Moreover, an efficient numerical formulation to deal with nonlinear applications was also presented, featuring important characteristics such as reduced integration techniques, explicit integration of the constitutive equation and a corotational formulation for the kinematical description of the continuum. In this second part of the present work, the numerical model proposed in the previous paper is applied to some classical examples of soil mechanics to demonstrate the applicability of the present formulation. Effects of a geometrically nonlinear approach over the numerical predictions are investigated and comparisons are performed taking into account results obtained by using a geometrically linear model. In addition, some comparisons are also carried out considering evaluations performed with different constitutive formulations in order to observe the mechanical behavior of the soil mass under different constitutive assumptions.

Keywords: critical state soil mechanics (CSSM), elastoplasticity, finite element method (FEM), One-point quadrature.

1. Introduction

In the first part of the present work (Braun & Awruch, 2013) a numerical model to simulate the mechanical behavior of soil masses was presented. An analytical model based on critical state soil mechanics (CSSM) was formulated utilizing the elastoplastic framework, which is entirely justified by experimental evidences. A corotational formulation was also presented in order to improve the kinematical description of the continuum. In addition, a finite element model was developed considering eight-node hexahedral elements with one-point quadrature and special techniques for the integration procedure of the constitutive equation. It was observed that the formulation presented previously leads to a highly efficient numerical model, especially for nonlinear analysis, where the computational effort is significantly reduced when compared with other formulations employing standard approaches.

In the present paper some classical problems, including three-dimensional examples, are numerically simulated to demonstrate the applicability of the present formulation when geotechnical analyses are carried out. Effects of a geometrically nonlinear approach over the numerical predictions are investigated considering comparisons performed with respect to results obtained by using a geometrically linear approach for the numerical model proposed here. Furthermore, investigations are also performed taking into account different constitutive formulations in order to compare responses obtained under different constitutive assumptions for the applications analyzed in this work. Whenever possible, predictions obtained here are compared to results obtained by other authors.

2. Numerical Applications

2.1. One element triaxial test

A triaxial compression test is numerically simulated here using a single hexahedral element in order to perform a simple and reliable verification over numerical routines of the present model referring to elastoplastic analysis and Cam-Clay formulation. Information about geometrical parameters and boundary conditions employed in the present analysis are shown in Fig. 1 and material properties related to Cam-Clay characterization of the soil mass are found in Table 1. In order to reproduce the experimental procedure, vertical displacements are imposed gradually at the top of the element and horizontal forces are applied on the vertical faces and calculated based on an initial hydrostatic stress state. The initial conditions are mainly characterized according to the overconsolidation ratio (OCR), which may be defined as follows:

$$\mathrm{OCR} = \frac{p_{c\,0}}{p_0} \tag{1}$$

where p_0 and p_{c0} are initial values for effective normal stress p and preconsolidation pressure p_c. Two different initial conditions are analyzed here: a lightly overconsolidated state, characterized by OCR = 1.2, and a strongly overconsolidated state, characterized by OCR = 6.0. In addition, comparisons between the geometrically linear and geomet-

A.L. Braun, DSc, Programa de Pós Graduação Engenharia Civil, Universidade Federal do Rio Grande do Sul, 90035-190 Porto Alegre, RS, Brasil. e-mail: allbraun@ig.com.br.
A.M. Awruch, DSc, Programa de Pós Graduação Engenharia Civil, Universidade Federal do Rio Grande do Sul, 90035-190 Porto Alegre, RS, Brasil. e-mail: amawruch@ufrgs.br.
Submitted on March 29, 2011; Final Acceptance on July 30, 2013; Discussion open until December 31, 2013.

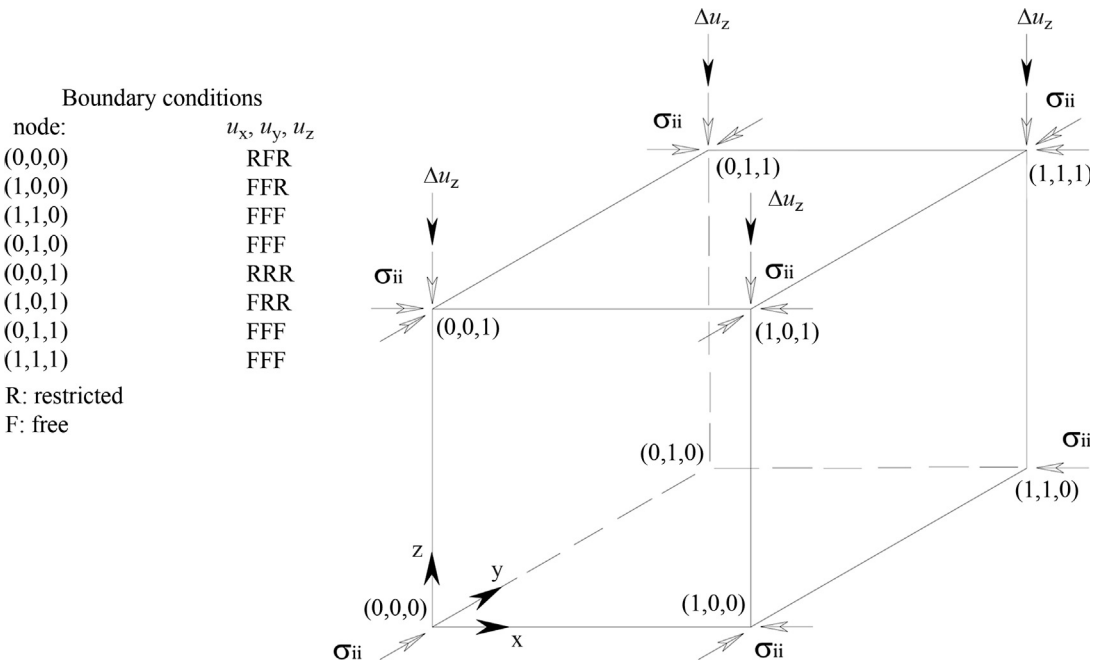

Figure 1 - Geometrical characteristics and boundary conditions employed in the triaxial test.

rically nonlinear approaches are also performed to determine effects of geometrical nonlinearities over the computed results.

Results obtained in this work are presented in Fig. 2 and compared with numerical predictions performed by Sheng *et al.* (2000). A good agreement can be observed between the reference work and predictions carried out with the geometrically linear approach. Hardening and softening behaviors are clearly reproduced, where hardening is associated to the lightly overconsolidated state as well as softening is related to the strongly overconsolidated state. For the lightly overconsolidated state, the stress path intersects the yield surface and then returns towards the critical state line following approximately the same path. The critical state is obtained at $\varepsilon_a \cong 20\%$ and $\varepsilon_a \cong 50\%$ for OCR = 6.0 and OCR = 1.2, respectively, which is in accordance with the reference results. On the other hand, when the geometrically nonlinear model is utilized, the critical state is not obtained. The stress path related to the lightly overconsolidated state returns from the point of intersection on the yield surface using a little different path, which follows an asymptotic curve towards the critical state line (CSL). The same behavior is observed for the strongly overconsolidated state after yielding. That particular behavior leads to a continuous increase of the deviator stress, which violates one of the basic critical state assumptions. However, it is worth to mention that geometrically nonlinear models tend to increase stiffness when deformation takes place, which is originated from stress rate terms added to the elastic constitutive matrix (Braun & Awruch, 2013 - Eq. 25) and changes in the reference configuration.

Table 1 - Material parameters utilized in the triaxial test.

Slope of CSL - M		1.2
Slope of NCL - λ		0.2
Slope of URL - k		0.02
Poisson's ratio - ν		0.3
Preconsolidation pressure - p_{c0} [N/m^2]		60.0
Initial void ratio - e_0	OCR = 1.2	1.5
	OCR = 6.0	1.53
Initial stress state - σ_{ii} [N/m^2] (σ_{ij} = 0.00)	OCR = 1.2	50.0
	OCR = 6.0	10.0

2.2. Embankment analysis

An embankment under the action of gravity is analyzed in this section. In order to verify the present numerical scheme, the Mohr-Coulomb constitutive model is first considered to compare results with numerical predictions performed by Zienkiewicz *et al.* (1978). Simulations are then carried out considering the Cam-Clay formulation utilized in this paper and a geometrically linear model, whose results are then compared with the previous predictions.

Geometrical characteristics of the computational domain employed in this example are shown in Fig. 3, where boundary conditions for the displacement field are also illustrated. Displacements in the orthogonal direction (axis z) are locked to reproduce the plane strain condition. The physical parameters adopted in the present simulations are found in Table 2 and all analyses are performed using a finite element mesh with 459 eight-node hexahedral elements. It is important to notice that material properties for

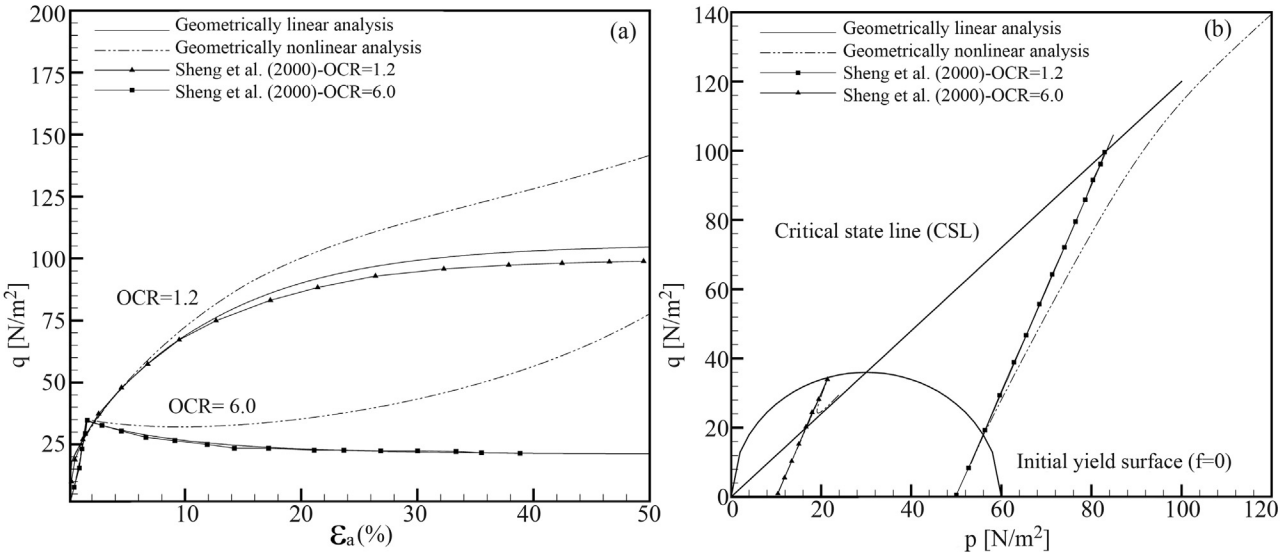

Figure 2 - Results for triaxial compression tests: (a) axial strain x deviator stress; (b) effective normal stress x deviator stress.

Table 2 - Physical constants utilized in the embankment analysis.

Constitutive model	Parameter	Value
Mohr-Coulomb	Young's modulus - E [kN/m^2]	2 x 10^5
	Angle of friction - ϕ [°]	20
	Cohesion - c [kN/m^2]	10 20 and 30
	Poisson's ratio - ν	0.25
	Specific weight - γ [kN/m^3]	20
Modified Cam-Clay	Slope of CSL - M	0.898
	Slope of NCL - λ	0.25
	Slope of URL - k	0.05
	Initial void ratio - e_0	1.6
	Poisson's ratio - ν	0.25
	Specific weight - γ [kN/m^3]	20

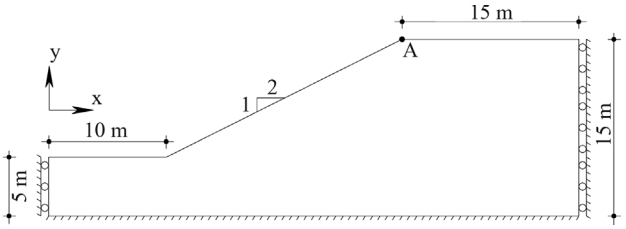

Figure 3 - Geometrical characteristics and boundary conditions considered in the embankment analysis.

the Cam-Clay constitutive model are not available in the reference work. Therefore, a set of physical constants usually employed by other authors to characterize a Cam-Clay modeling of the soil is considered here. In order to reproduce stiffness characteristics of the Mohr-Coulomb simulations, a hydrostatic stress state p is imposed over the computational domain, which is calculated using Eq. 3 from the first part of the present work (see Braun & Awruch, 2013) and the classical elastic relation:

$$K = \frac{E}{3(1-2\nu)} \tag{2}$$

where E is the Young's modulus, K is the compressibility modulus and ν is the Poisson's ratio. Consequently, the preconsolidation pressure can be defined based on the overconsolidation ratio OCR (see Eq. 1), which assumes the following values in this study: OCR = 1.025, OCR = 1.05, OCR = 1.075, OCR = 1.1 and OCR = 2.0.

All results obtained in the present work are summarized in Table 3 together with predictions presented by Zienkiewicz *et al.* (1978), where comparisons in terms of vertical (u_y) and horizontal displacements (u_x) measured at point A (see Fig. 3) are performed. In addition, these results are plotted against load ratio Qn/Qt in Fig. 4, where Qn and Qt are the current and total load applied on the embankment, respectively. All simulations carried out using the Mohr-Coulomb constitutive model resulted in predictions very similar to those obtained by Zienkiewicz *et al.* (1978). By using the Modified Cam-Clay formulation, a reasonable agreement with the Mohr-Coulomb results can be observed for analyses performed with OCR ≥ 1.075, for which identical predictions are produced owing to the fully elastic state established in this range of overconsolidation ratios. On the other hand, as OCR decreases the horizontal displacements u_x tend to follow a distinct curve when compared with that provided by using the Mohr-Coulomb formulation with smaller cohesion values, where negative

Table 3 - Results for the embankment analysis.

Model		u_x [mm]	u_y [mm]
Mohr-Coulomb	c = 10 [kN/m^2]	0.358	-9.263
	c = 20 [kN/m^2]	0.603	-8.749
	c = 30 [kN/m^2]	0.645	-8.558
Modified Cam-Clay	OCR = 1.025	2.350	-12.107
	OCR = 1.050	1.015	-8.942
	OCR = 1.075	0.608	-8.392
	OCR = 1.100	0.608	-8.392
	OCR = 2.000	0.608	-8.392
Zienkiewicz *et al.* (1978)	c = 10 [kN/m^2]	0.337	-9.256
	c = 20 [kN/m^2]	0.651	-8.744
	c = 30 [kN/m^2]	0.706	-8.512

displacements are observed if c < 7 kN/m^2 is considered. Nevertheless, all curves referring to vertical displacements u_y obtained with the present Cam-Clay model and decreasing OCR values show a similar trend to that verified in the Mohr-Coulomb simulations when the cohesion is reduced.

In Fig. 5, final patterns of flow vectors and stress fields obtained from the Mohr-Coulomb and Modified Cam-Clay models are presented. In order to confront simulations performed with different constitutive models but with similar characteristics, comparisons are carried out considering that responses obtained with the Cam-Clay formulation are referred to OCR = 1.075 and responses obtained with the Mohr-Coulomb model are referred to c = 20 kN/m^2. As can be noticed, a good agreement can be verified in all comparisons performed here. It is worth to mention that stress measures from the Cam-Clay responses are referred to sign conventions usually adopted in soil mechanics, where compression is considered as positive as well as tension is taken as negative. Moreover, Cam-Clay axial stresses σ_{xx} and σ_{zz} are shifted by an initial value related to the hydrostatic stress state imposed at the start of the simulation.

2.3. Two-dimensional analysis of a rigid strip footing

A two-dimensional analysis of a rigid strip footing resting on a soil layer is carried out in this section. Footing tests have been extensively used to validate numerical algorithms based on elastoplastic formulations applied to soil mechanics. This problem may be considered as a very difficult task for most of the numerical schemes due to strong rotations verified in the principal stresses and the singularity observed near the edge of the footing.

All simulations are performed using the Modified Cam-Clay model and results are compared with numerical predictions obtained by Sheng *et al.* (2000), who also utilized a Cam-Clay formulation. Comparisons are also carried out with respect to the geometrically linear and nonlinear approaches adopted in this problem. Geometry and boundary conditions utilized in the present study are shown in Fig. 6 and material parameters adopted in the Cam-Clay characterization of the soil mass are listed in Table 4. The computational domain is divided into 2703 eight-node hexahedral elements and the plane strain condition is imposed by displacement restrictions applied in the orthogonal direction (axis z). In order to simulate the action of the rigid foundation on the soil mass, uniform vertical displacements are imposed along the footing-soil interface. It is important to notice that critical state models cannot mobilize any strength if the effective normal stress *p* is zero or under tensile stress. Therefore, a compressive initial stress state must be established over the soil, which is accomplished in this example by considering a hydrostatic stress state generated from the soil specific weight. Moreover, the soil is assumed to be overconsolidated to 50 kPa at the ground surface, which implies that, at the ground surface, the preconsolidation pressure is 50 kPa.

The load-displacement curves obtained in this work are presented in Fig. 7, where a prediction computed by Sheng *et al.* (2000) is also shown. Displacements and footing loads are measured at point A underneath the footing, as indicated in Fig. 6. A good agreement is verified when predictions provided by the geometrically linear model is taken into account. On the other hand, results obtained us-

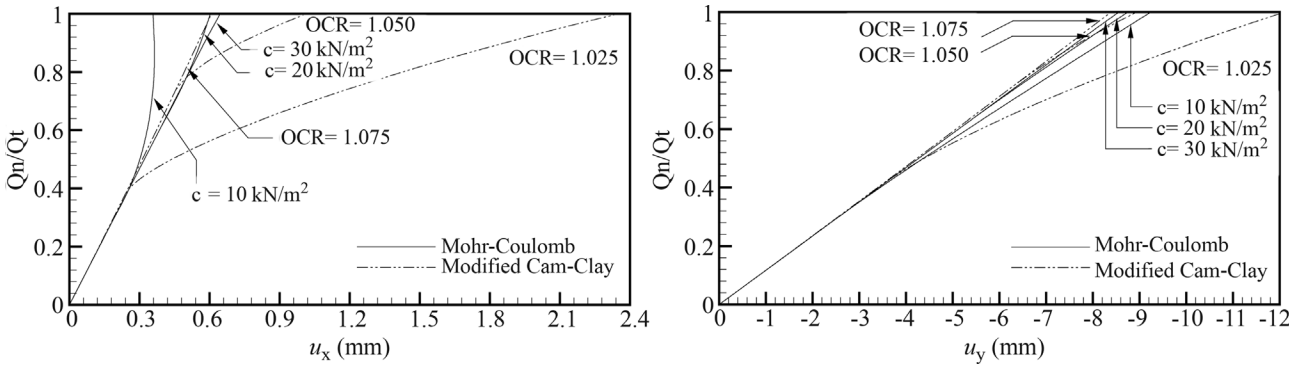

Figure 4 - Displacement-load curves obtained in the embankment analysis.

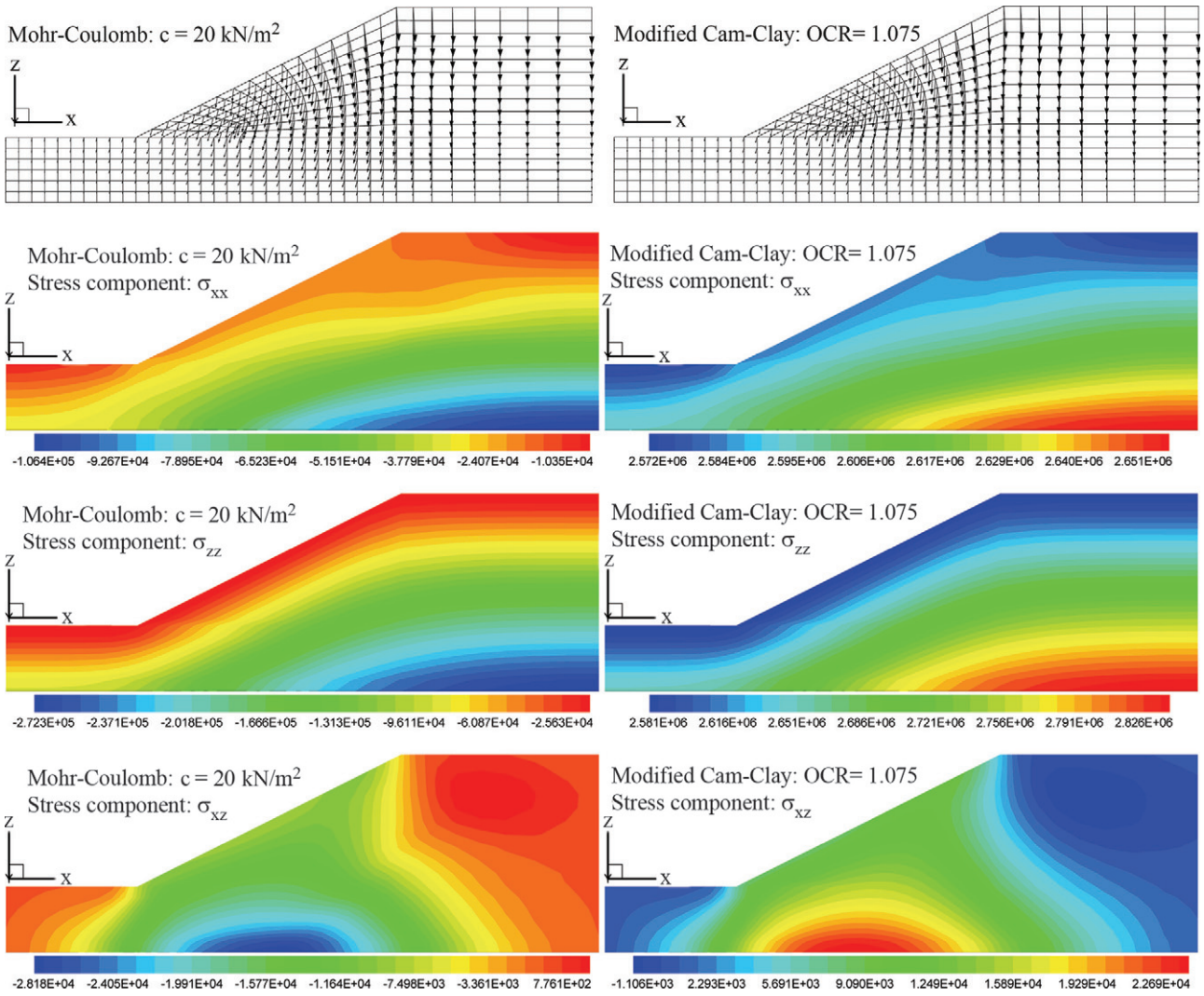

Figure 5 - Flow vectors and stress fields obtained in the embankment analysis.

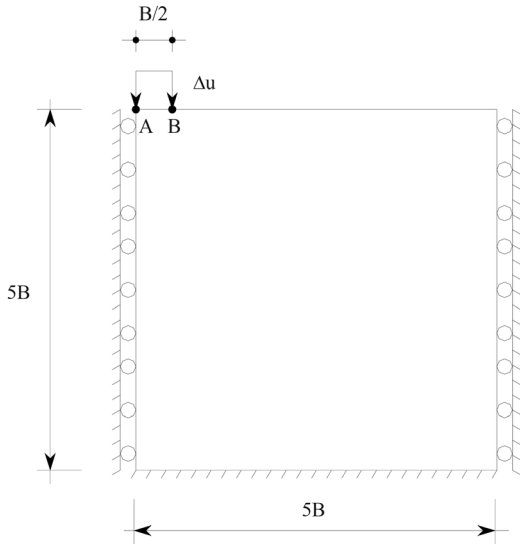

Figure 6 - Geometry and boundary conditions utilized in the two-dimensional rigid footing analysis.

ing the geometrically nonlinear approach lead to an overestimation of loads owing to an increase of stiffness, which is a characteristic usually observed in geometrically nonlinear models. Yielding can be observed in all predictions when the imposed displacements reach almost 20% of the footing width.

Stress paths computed at points A and B underneath the footing (see Fig. 6) are found in Fig. 8, where compari-

Table 4 - Physical parameters adopted in the rigid footing analysis.

Slope of CSL - M	0.898
Slope of NCL - λ	0.25
Slope of URL - k	0.05
Poisson's ratio - ν	0.3
Specific weight - γ [kN/m^3]	6
Initial void ratio - e_0	1.6

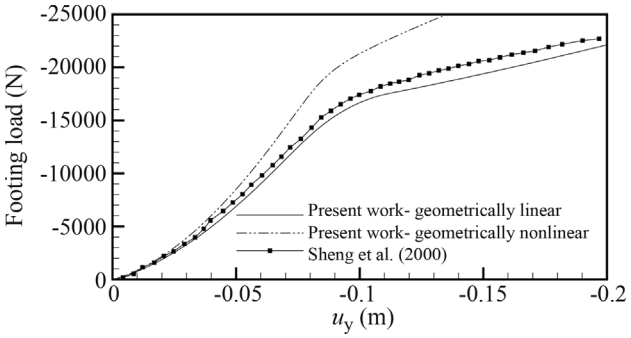

Figure 7 - Load-displacement curves obtained in the rigid footing analysis.

sons are performed with results presented by Sheng *et al.* (2000). In the present work, those points are referred to the Gauss points of elements localized underneath the footing borders. A good correlation can be observed when both the linear and nonlinear responses obtained at point A are compared with the respective result presented by the reference work. As can be noticed, predictions obtained with geometrical linear and nonlinear models lead to very similar stress paths in the elastic range. However, some mayor differences between linear and nonlinear responses can be observed after yielding. At point B, a reasonable agreement is verified between the geometrically linear stress path obtained here and the corresponding stress path predicted by Sheng *et al.* (2000), which is not verified when the geometrically nonlinear response is considered after the onset of the plastic yielding. Unlike point A, where the stress distribution is more regular, the stress distribution near point B presents strong gradients, which demands a precise localization of the measure point. Since the measure points are not precisely defined in the reference work, the measure points utilized in this work are probably localized at different positions if compared with those adopted by Sheng *et al.* (2000).

In Fig. 9, mesh configurations and stress distributions over the computational domain are shown, which are referred to the final configuration of the footing settlement. Comparisons are performed with respect to predictions obtained using the geometrically linear and geometrically nonlinear approaches, where a reasonable agreement is verified for σ_{zz}.

2.4. Two-dimensional analysis of flexible strip footings

In the present analysis, numerical simulations of soil layers under the action of two-dimensional flexible strip footings are performed, where two distinct configurations referred to load and geometrical characteristics adopted in the numerical modeling are considered. Flexible strip footings may be represented applying uniform vertical loads along the footing-soil interface. The first configuration considered here is analyzed using the Mohr-Coulomb and Modified Cam-Clay models in order to compare predictions performed by Zienkiewicz *et al.* (1978), who utilized the Mohr-Coulomb formulation to determine settlements for a strip load on a soil layer with an ideal weightless material. The second configuration was proposed by Borja & Tamagnini (1998) to verify their critical state formulation, which is based on an alternative Cam-Clay model. In this second problem, comparisons of results obtained with the geometrically linear and nonlinear approaches utilized in the present scheme are also carried out.

Geometrical characteristics referring to the configurations employed in the present study are found in Fig. 10, where boundary conditions are also shown. Physical properties of the soil are presented in Table 5 according to the constitutive models and configurations utilized here. The computational domain is divided into 480 and 540 eight-node hexahedral elements, considering the first and second configurations respectively. For simulations referred to the first configuration, an initial hydrostatic stress state p_0 is imposed over the computational domain using the same procedure adopted in Section 2.2, whereas physical constants must be utilized based on the properties indicated in Table 5. Just as in the previous analysis, the initial stress state for the second configuration is generated using the soil specific weight. Plane strain conditions are imposed for both configurations.

Load-displacement curves computed in the present work are presented in Fig. 11 considering both configurations simulated here, where results obtained from the reference authors are also shown. Several overconsolidation

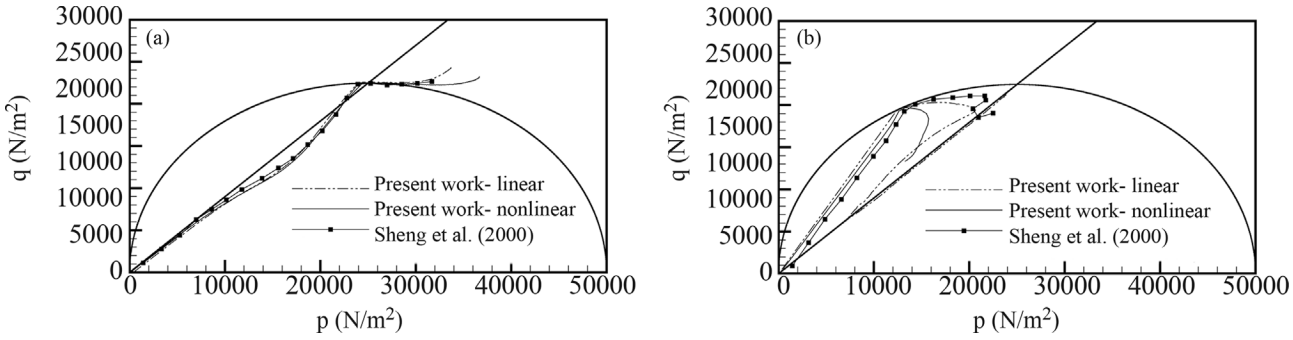

Figure 8 - Stress paths measured underneath the footing location: (a) point A; (b) point B.

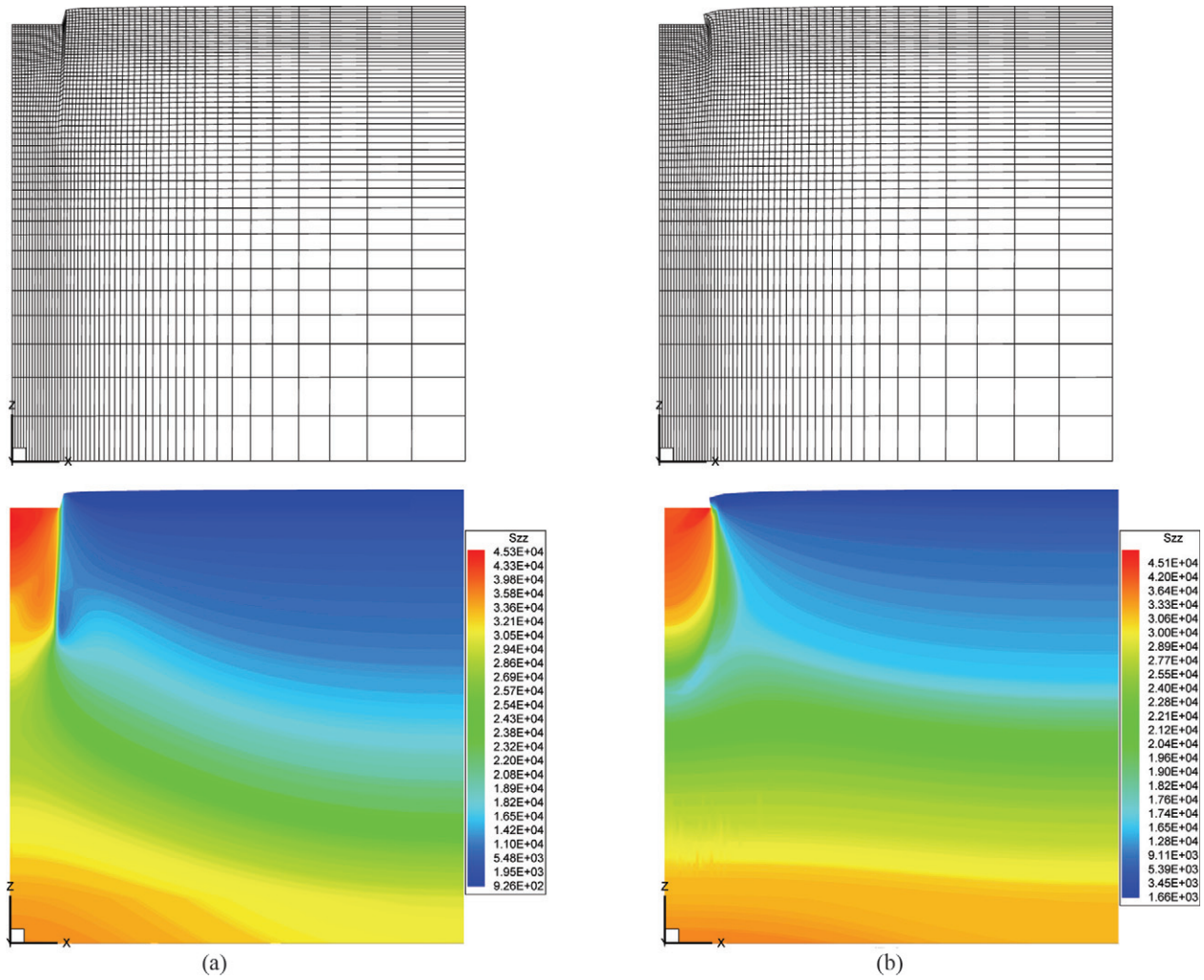

Figure 9 - Final mesh configurations and stress distributions obtained in the rigid footing analysis: (a) geometrically linear model; (b) geometrically nonlinear model.

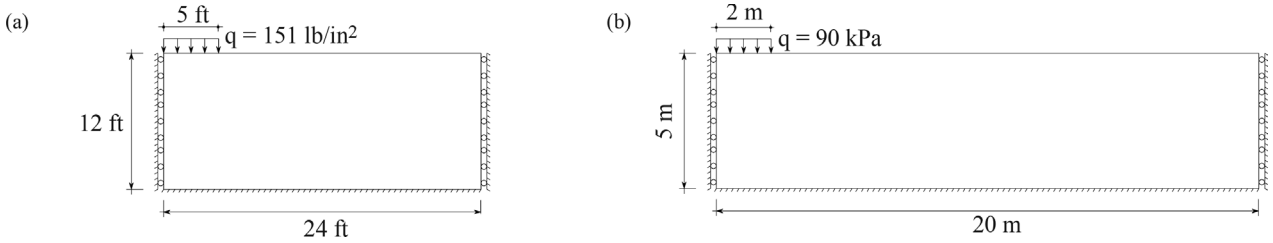

Figure 10 - Geometry and boundary conditions utilized in the flexible footing analyses: (a) first configuration; (b) second configuration.

ratios (OCR = p_{c0}/p_0) are simulated here in order to reproduce the reference predictions and investigate its influence over the mechanical response. All displacements are measured at a point corresponding to the point of contact between the soil layer and the intermediate point underneath the footing, which correspond to the top left node of the computational domain.

Results obtained for the first configuration show that simulations with a conventional Mohr-Coulomb formulation cannot converge in this problem. It is worth to notice that Zienkiewicz *et al.* (1978) only obtained a stable solution by using an alternative Mohr-Coulomb model. Comparisons are also performed using the Modified Cam-Clay model with various OCR's, where the elastic responses are well correlated to the Mohr-Coulomb results. Nevertheless, the plastic response is quite different, as expected, since each formulation considers different assumptions to describe the plastic phenomena. Even so, some simulations

Table 5 - Physical parameters adopted for the flexible footing analyses.

Geometrical model	Constitutive model	Parameter	Value
First configuration	Mohr-Coulomb	Young's modulus - E [lb/in^2]	30x10^3
		Angle of friction - ϕ [º]	20.0
		Cohesion - c [lb/in^2]	10.0
		Poisson's ratio - ν	0.3
		Specific weight - γ [lb/in^3]	0
	Modified Cam-Clay	Slope of CSL - M	0.898
		Slope of NCL - λ	0.25
		Slope of URL - k	0.05
		Initial void ratio - e_0	1.6
		Poisson's ratio - ν	0.3
		Specific weight - γ [kN/m^3]	0
Second configuration	Modified Cam-Clay	Slope of CSL - M	1.05
		Slope of NCL - λ	0.13
		Slope of URL - k	0.018
		Initial void ratio - e_0	1.6
		Poisson's ratio - ν	0.25
		Specific weight - γ [kN/m^3]	10.0

approximated the Mohr-Coulomb responses, such as the curves referred to OCR = 1.1 and OCR = 1.2. Regarding results obtained for the second configuration, the best agreements between the reference work and simulations carried out here are referred to OCR = 2.5 and OCR = 2.25, although the plastic behavior immediately after the onset of the plastic yielding in these cases are distinct to that predicted by Borja & Tamagnini (1998), which is explained by some particular characteristics observed in the constitutive model adopted in the reference work. All simulations performed here reproduced well the mechanical response in the elastic range, but only that referred to OCR = 1.5 obtained the yielding load indicated by the reference result. As expected, the prediction obtained with the geometrically nonlinear model resulted in smaller vertical displacements when compared with that obtained with the linear model.

Final mesh configurations and stress components computed with the numerical simulation carried out over the second configuration are presented in Fig. 12, where comparisons are performed taking into account results obtained with the geometrically linear and nonlinear models and OCR = 2.5. The mesh deformation referred to the nonlinear analysis is clearly smaller than that obtained with the linear model, although both predictions show expressive lateral displacements in the region beneath the footing location.

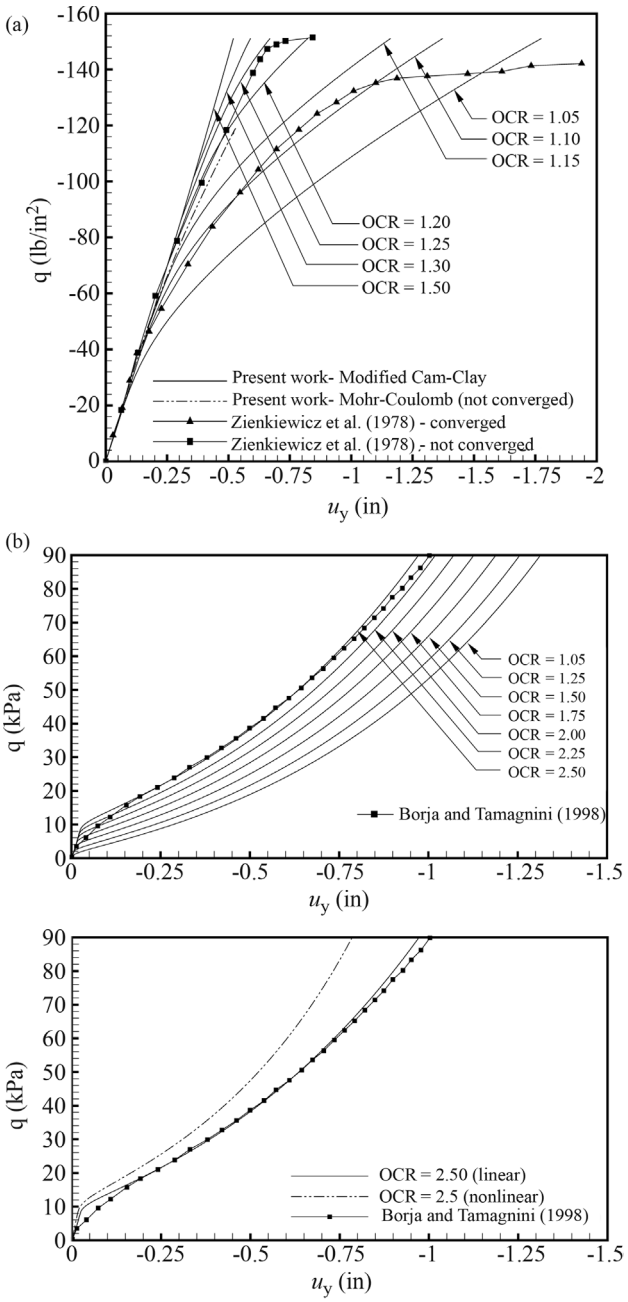

Figure 11 - Load-displacement curves obtained in the flexible footing analyses: (a) first configuration; (b) second configuration.

2.5. Three-dimensional analysis of compaction and footing problems

The numerical model proposed in this work is verified in this section using numerical tests that demonstrate its ability to predict results for three-dimensional stress states. Two different problems are analyzed here, which are characterized with different geometrical properties and distinct load characteristics. The first problem is based on the footing test performed by Lee *et al.* (2005), where a cubical model under the action of a flexible square footing is inves-

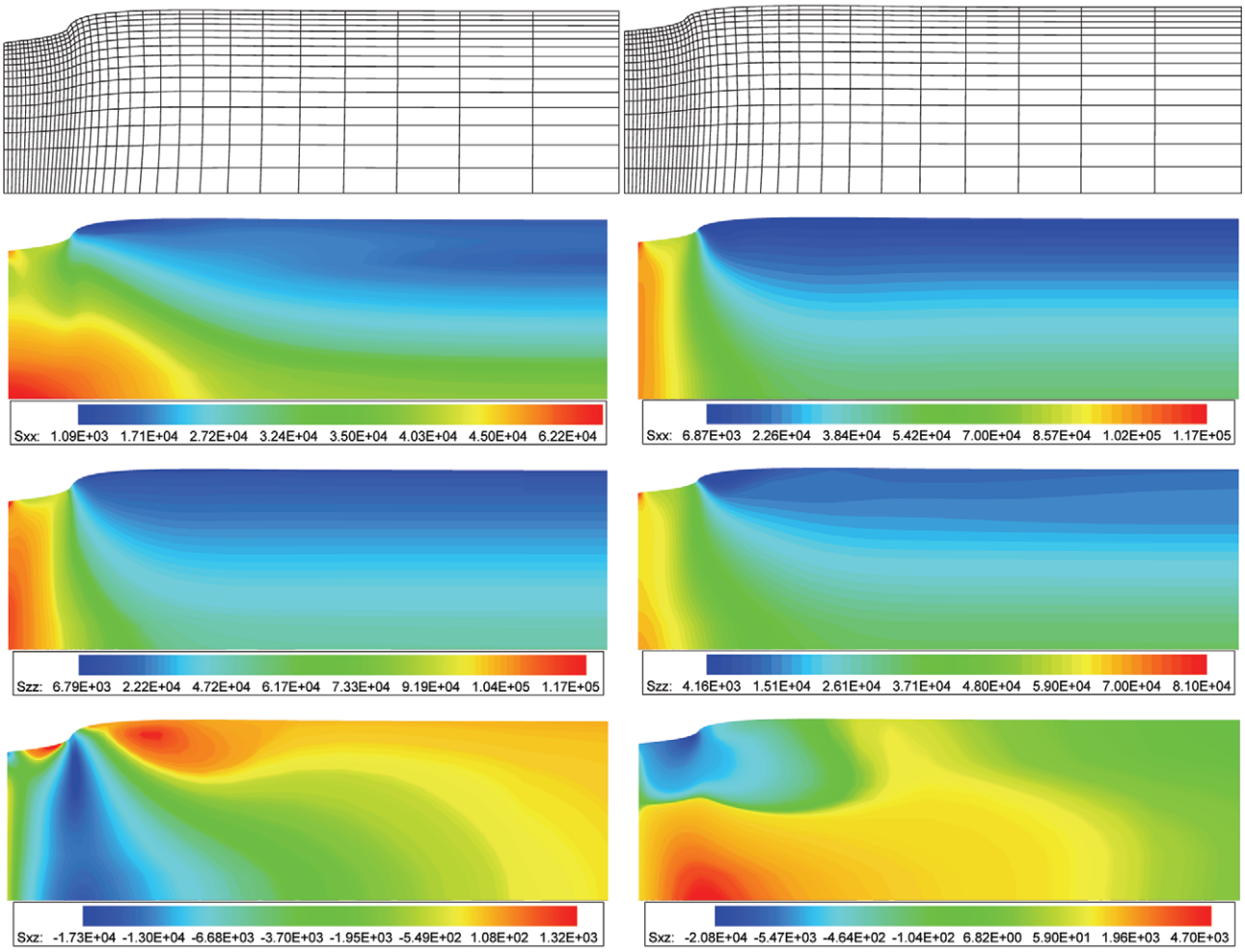

Figure 12 - Final mesh configurations and final stress distributions obtained in the flexible footing analysis referred to the second configuration: (a) geometrically linear analysis; (b) geometrically nonlinear analysis.

tigated. The second problem is referred to the compaction test proposed by Xia & Masud (2009), who analyzed spatial density changes induced during compaction of a three-dimensional soil model. The Modified Cam-Clay formulation proposed in this work is utilized in both the problems analyzed here. A comparison between results obtained with the geometrically linear and nonlinear models is carried out for the compaction test.

Geometrical and load characteristics related to the problems studied in this section are shown in Fig. 13. For both geometrical models, symmetry boundary conditions are imposed on the planes defined by (x, y, z) = (0, 0, 0). The computational domain is composed of 24x24x14 and 14x14x8 eight-node hexahedral elements, considering the footing and compaction tests, respectively. Physical constants adopted in the present simulations are listed in Table 6. Gravity and external loads are applied simultaneously in the footing test and initial stress states utilized in both analyses carried out here are based on the procedure explained in Section 2.2, using the Young's modulus indicated in the respective reference works and other physical constants presented in Table 6.

Load-settlement curves obtained in the present simulations are shown in Fig. 14 together with predictions taken from the respective reference works, where displacements are measured at (x,y,z) = (0,0,2) and (x,y,z) = (0,0,11) for the footing and compaction test, respectively. In the elastic range, the response obtained in the footing test with the present formulation agrees very well with the numerical predictions observed in Lee *et al.* (2005). On the other hand, after plastic yielding a slightly different response is verified, although a reasonable agreement is still observed. For the compaction test, several overconsolidation ratios (OCR) were analyzed. Results show that when OCR = 3.0 is considered, a very good agreement is verified in the range $0 \leq q \leq 16$ between the present predictions and those referred to Xia & Masud (2009). However, the plastic behavior is quite different in this case as well as in the remaining cases studied here. It is worth to mention that Xia & Masud

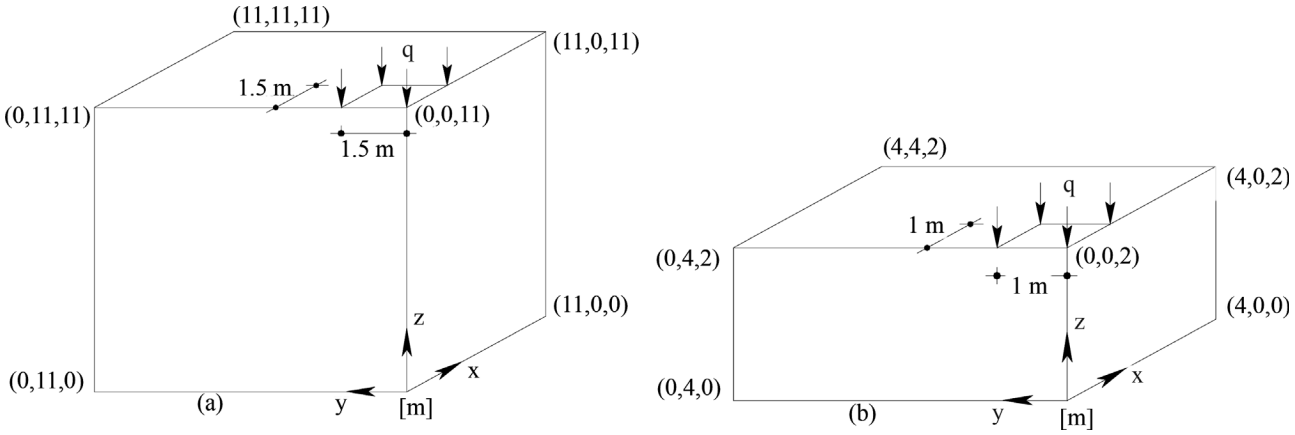

Figure 13 - Geometrical characteristics and boundary conditions considered in the three-dimensional analyses: (a) footing test; (b) compaction test.

(2009) adopted a constitutive formulation based on the smooth surface cap model. In the comparison performed with respect to the influence of geometrical nonlinearity, predictions obtained with the geometrically nonlinear model and OCR = 3.0 indicate an anticipation of the yielding load and a modification of the mechanical response in the plastic range when compared with the geometrically linear response under the same conditions.

Figure 15 illustrates the final mesh configuration and final stress distribution of σ_{zz} over the computational domain referred to the footing test. An intermediate stress distribution of σ_{zz} and the corresponding mesh related to the compaction test at the fictitious time t = 60% are also

Table 6 - Physical parameters adopted in the three-dimensional analyses.

Geometrical model	Parameter	Value
Footing test	Young's modulus - E (MPa)	80.0
	Slope of CSL - M	0.898
	Slope of NCL - λ	0.25
	Slope of URL - k	0.05
	Initial void ratio - e_0	1.6
	Poisson's ratio - ν	0.25
	Specific weight - γ [kN/m^3]	20.0
Compaction test	Young's modulus - E (MPa)	0.5
	Slope of CSL - M	0.898
	Slope of NCL - λ	0.25
	Slope of URL - k	0.05
	Initial void ratio - e_0	1.6
	Poisson's ratio - ν	0.3
	Specific weight - γ [kN/m^3]	20.0

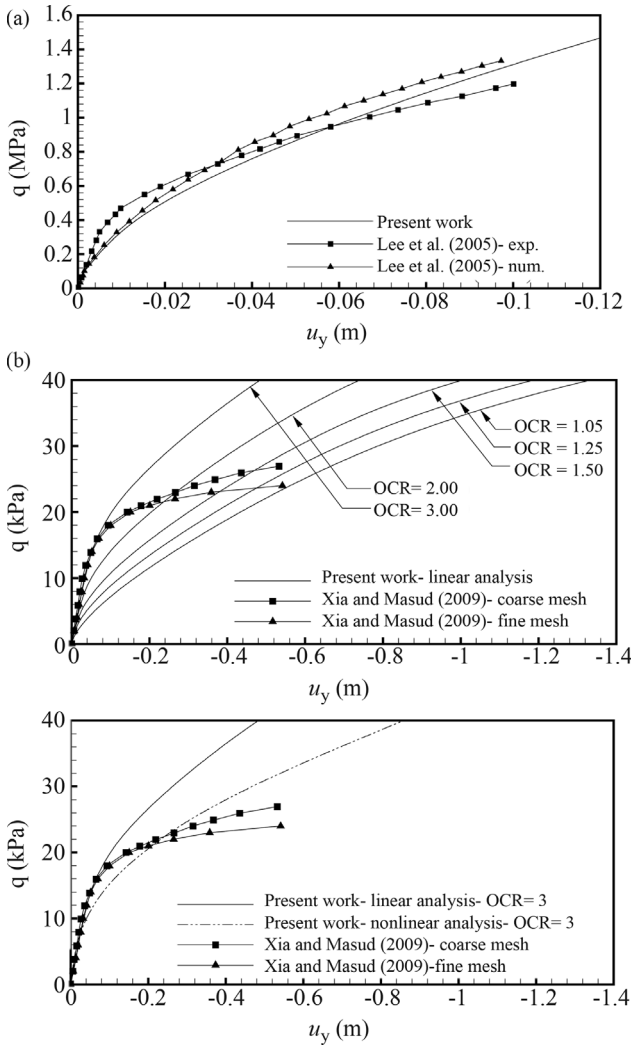

Figure 14 - Load-settlement curves obtained in the three-dimensional analyses: (a) footing test; (b) compaction test.

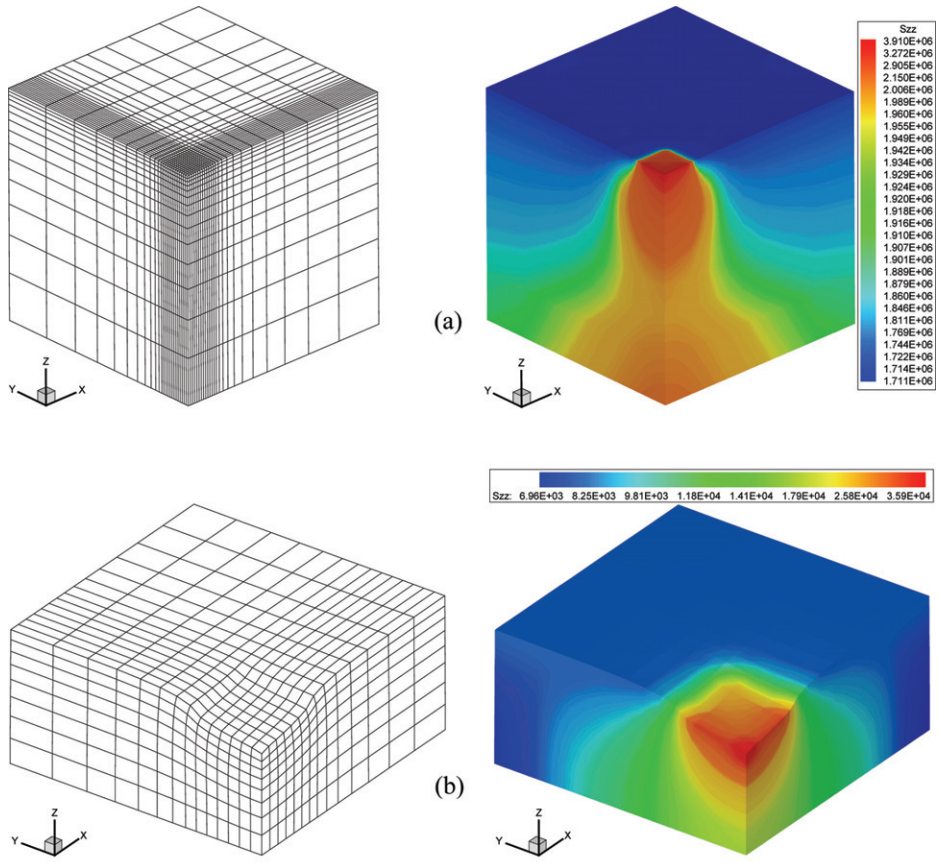

Figure 15 - Final mesh configuration and final stress distributions: (a) footing test; (b) compaction test (at t = 60%).

shown. As expected, the characteristic compression bulb under the load area is easily identified in the stress field σ_{zz} for both results. The stress distribution and the mesh configuration obtained in the compaction test show a good agreement with the corresponding results obtained by Xia & Masud (2009).

5. Conclusions

A numerical model based on one-point quadrature and critical state formulation was proposed in a previous paper to simulate the mechanical behavior of soil masses. Results obtained here demonstrated good agreement with the reference works whenever comparisons were possible to be made, considering that experimental predictions obtained by other authors were also included. Investigations performed with respect to geometrical nonlinearity showed that an approach considering large displacements and rotations may be not important for the cases analyzed here. On the other hand, it is well known that many geotechnical problems are characterized by large strains in the plastic range. Comparisons considering different constitutive models were also carried out, where responses with different behavior were demonstrated. Although results concerning the numerical efficiency of the present formulation were not presented here, simulations indicated that the stress integration scheme utilized in this work presents high sensibility to the tolerance values adopted in the iterative procedures. These conclusions are similar to those obtained by Sloan *et al.* (2001) and, therefore, tolerance values should be chosen carefully (see Sloan *et al.*, 2001 for suitable tolerance values). In order to improve the present model a finite strain formulation to solve problems involving large deformation should be implemented in future works. An alternative to be considered may be found in Nazem *et al.* (2008), where an arbitrary Lagranian-Eulerian algorithm is proposed.

References

Borja, R.I. & Tamagnini, C. (1998) Cam-Clay plasticity. Part III: Extension of the infinitesimal model to include finite strains. Computer Methods in Applied Mechanics and Engineering, v. 155:1-2, p. 73-95.

Braun, A.L. & Awruch, A.M. (2013) An efficient model for numerical simulation of the mechanical behavior of soils. Part 1: theory and numerical algorithm. Soils and Rocks, v. 36:2, p. 149-159.

Lee, J.; Salgado, R. & Kim, S. (2005) Bearing capacity of circular footings under surcharge using state-dependent finite element analysis. Computers and Geotechnics, v. 32:6, p. 445-457.

Nazem, M.; Sheng, D. Carter, J.P. & Sloan S.W. (2008) Arbitrary Lagrangian-Eulerian methods for large-strain consolidation problems. International Journal for Numerical and Analytical Methods in Geomechanics, v. 32:9, p. 1023-1050.

Sheng, D.; Sloan, S.W. & Yu, H.S. (2000) Aspects of finite element implementation of critical state models. Computational Mechanics, v. 26:2, p. 185-196.

Sloan, S.W.; Abbo, A.J. & Sheng, D. (2001) Refined explicit integration of elastoplastic models with automatic error control. Engineering Computations, v. 18:1-2, p. 121-154.

Xia, K. & Masud, A. (2009) A stabilized finite element formulation for finite deformation elastoplasticity in geomechanics. Computers and Geotechnics, v. 36:3, p. 396-405.

Zienkiewicz, O.C.; Norris, V.A.; Winnicki, L.A.; Naylor, D.J. & Lewis, R.W. (1978) A unified approach to the soil mechanics problems of offshore foundations. Zienkiewicz, Lewis and Stagg (eds) Numerical Methods in Offshore Engineering. John Wiley & Sons, Chichester, Chapter 12, pp. 361-411.

Volume Change Behavior due to Water Content Variation in an Expansive Soil from the Semiarid Region of Pernambuco - Brazil

S.R.M. Ferreira, L.M. Costa, L.J.N. Guimarães, I.D.S. Pontes Filho

Abstract. One of the most important morphological characteristics of expansive soil is contracting and fissuring during drying and swelling during wetting. Soils that change volume when inundated with water require extra care, whether they are used in agriculture, engineering or both. In this paper, conventional and suction-controlled oedometric tests were used to evaluate the changes in volume and swelling pressure caused by changes in water content in an expansive soil from Petrolândia-PE. A coupled hydro-mechanical formulation, implemented in the computational code CODE_BRIGHT, was applied to simulate the tests performed with this soil. The constitutive model used was the double structure generalized plasticity model proposed by Sanchez *et al.* (2005). The results show that soil expansion, contraction and collapse depend on the initial water content and the external load applied. The conclusion is that volume changes due to water content variation are associated with the initial conditions of the soil and the load applied to the soil. The experimental data and simulation results are in good agreement, showing that the model and computer code are able to accurately represent the hydro-mechanical behavior of expansive soils.

Keywords: expansive soil, double structure model, hydro-mechanical coupled analysis.

1. Introduction

Expansive soils are characterized by their tendency to contract and fissure during drying and swell during wetting. The volumetric instability (contraction and expansion or collapse) of unsaturated soils upon inundation has complex causes and is affected by various factors. The instability depends on the type of soil (origin and formation), the presence of climatic determinants, the stresses affecting the soil and other factors. The use of expansive soils in construction projects can cause serious damage (fissures, ruptures and cracks) to the buildings when the soils are not adequately analyzed during the project and construction phases.

Several types of soils are subject to the phenomenon of swelling. These types include soils derived from igneous rocks, primarily basalt, diabase, gabbro, pyroxene and feldspar, and soils derived from sedimentary rocks with the clay mineral montmorillonite, such as shales, marls and limestones, which disintegrate easily.

In Brazil, expansive soils are found in various regions of the country. In the Northeast, Vargas (1985) identified regions that appear in layers of Cretaceous formations, from the north of Bahia to Pernambuco and Ceará. Costa Nunes *et al.* (1982) highlighted the expansive soil in the large metropolitan region of Recife, Maria Farinha Formation, of the Barreiras Group. Ferreira (1988) studied expansive soils in several municipalities of Pernambuco. Gusmão Filho & Silva (1991) and subsequently Jucá *et al.* (1992), used laboratory tests and field instruments to study the behavior of expansive clay in a metropolitan area of Recife. The expansive soil of Recôncavo was the focus of studies by various researchers: Sobral (1956), Simões & Costa Filho (1981), etc. In the Central South and South, expansive soils were found in superficial layers of the podzolic formations in Passa Dois and Tubarão Group in São Paulo, Parana and Santa Catarina, and also in the Santa Maria Formation in Rio Grande do Sul. Expansive soils are also found in Maranhão, Rio Grande do Norte, Alagoas, Sergipe, Mato Grosso. The geotechnical characteristics and the volume change response caused by wetting in the expansive soils of Brazil were analyzed by Ferreira (2008).

In expansive soils, volume changes caused by applied stress or suction are governed by various phenomena occurring at the microstructural level due to the interactions of individual clay particles with their surroundings. Gens & Alonso (1992) presented a conceptual basis for modeling expansive soil, in which two different levels are considered: the microstructural level, at which swelling of active minerals occurs, and the macrostructural level, which is responsible for major structural rearrangements.

S.R.M. Ferreira, DSc, Departamento de Engenharia Civil, Universidade de Pernambuco e Universidade Católica de Pernambuco, Av. Acadêmico Hélio Ramos s/n, 50740-530 Recife, PE, Brazil. e-mail: sr.mf@hotmail.com.
L.M. Costa, DSc, Departamento de Engenharia Civil, UFPE, Av. Acadêmico Hélio Ramos s/n, 50740-530 Recife, PE, Brazil. e-mail: licia@ufpe.br.
L.J.N. Guimarães, D.Sc., Departamento de Engenharia Civil, Universidade Federal de Pernambuco, Av. Acadêmico Hélio Ramos s/n, 50740-530 Recife, PE, Brazil. e-mail: leonardo@ufpe.br.
I.D.S. Pontes Filho, DSc, Departamento de Engenharia Civil, Universidade Federal de Pernambuco, Av. Acadêmico Hélio Ramos s/n, 50740-530, Recife, PE, Brazil. e-mail: ivaldo@ufpe.br.
Submitted on August 24, 2011; Final Acceptance on January 31, 2013; Discussion open until December 31, 2013.

This paper analyzes the characteristics of volume variations due to changes in water content of an expansive soil from Petrolândia in Pernambuco, in the northeast of Brazil (520 km from Recife). The study site is located in Jatobá Basin. The local geology is represented by sediments of the Aliança Formation, which is composed of siltstones, shales and limestones of brown and reddish colors. The soil from this formation has clay or silt features, with dark colors that usually range from dark grey to reddish (Melo, 1980). In the field, desiccation cracks have been observed. This paper also utilizes a double structure model based on the work of Gens & Alonso (1992), which is implemented in a computer program to analyze the volume changes caused by changes in water content.

2. Materials and Methods

2.1. Geotechnical investigation program

The geotechnical investigation program was divided in two parts. In the situ part, undisturbed and disturbed samples were examined, and physical indices of the soil were measured. In the laboratory part, physical characterization tests were conducted in natural soil according to the methods of the Brazilian Association of Technical Standards (ABNT, 1984a; ABNT, 1984b; ABNT, 1984c; ABNT, 1984d), characteristic curve, microstructure (O-optic) and chemical analysis have been performed.

The volume changes associated with variations in the stress state and water content were analyzed through simple and conventional oedometer tests with controlled suction. Undisturbed samples with constant water content were statically loaded to a pre-determined stress level and then suction was progressively reduced.

In single oedometric tests, the applied vertical stresses were increased with the ratio $\Delta\sigma/\sigma = 1$. An initial stress of 10 kPa was used, and the stress was varied up to 1280 kPa. The time of each step was such that the deformation between consecutive time intervals ($\Delta t/t = 1$) was less than 5% of the total deformation that occurred up to the previous recorded time. The vertical deformations caused by inundation were measured at 0, 0.10, 0.25, 1, 2, 4, 8, 15, 30, 60, 120, 480 and 1440 minutes.

The swelling pressure was determined using three different methods: 1 - Loading after expansion with different vertical consolidation stresses, 2 - Expansion and collapse under stress, 3 - Constant stress (Justo *et al.*, 1984, and Ferreira, 1995).

Oedometric tests conducted with controlled suction had two stress paths. First, the undisturbed soil with natural water content was loaded until a certain vertical consolidation stress was reached (pressures of 10, 20, 40, 80, 160, 320, 640 and 1280 kPa were successively applied). In the second path, after stabilization of the deformation caused by vertical stress, the suction of the soil was reduced in stages (5.0, 2.5, 1.0, 0.5, 0.2 and 0.0 MPa), and the expansion deformation of the soil was measured. We sought to distinguish the vertical deformation caused by stress from that caused by reduced soil moisture (suction).

To analyze the pre-wetting and drying effects, undisturbed samples were molded in rings with a diameter of 101 mm and a height of 30 mm. The samples were placed in desiccators with different concentrations of sodium chloride or sulfuric acid for 10 months, and they were molded in rings with a diameter of 71.40 mm and a height of 20.0 mm for the simple oedometer test. To analyze the effect of desiccation on stress, undisturbed samples were molded and loaded to a pre-determined stress level, and the water content was allowed to decrease under stress at room temperature until the deformation stabilized, which occurred between 60 and 70 days.

2.2. Constitutive model

The constitutive model adopted in this paper is the double structure generalized plasticity model proposed by Sanchez *et al.* (2005), which is based on the general framework proposed by Gens & Alonso (1992) and incorporates improvements suggested by Alonso *et al.* (1999). Two levels of structure are considered. The macrostructural behavior is described by the Barcelona Basic Model (BBM), developed by Alonso *et al.* (1990). Other mechanisms not included in the BBM that occur in the microstructure at the clay particle level can occur in expansive soils and induce plastic strains. Thus, the double structure formulation includes the definitions of laws for the macrostructural level, the microstructure level and the interactions between both structural levels.

2.2.1. Macrostructural model

The BBM considers two independent stress variables, the net stress, $(\sigma_{ij} - p_a\delta_{ij})$, and the matric suction, $s = (p_a - p_w)$. It is an elastoplastic strain-hardening model, which extends the concept of a critical state for saturated soils to unsaturated conditions, including the dependence of the yield surface on matric suction. The yield surface is expressed by

$$f(p, q, s, p_0^*) = q^2 - M^2(p + p_s)(p_0 - p) = 0 \qquad (1)$$

with

$$p = \sigma_m - \max(p_a, p_w);\ \ \sigma_m = \frac{\sigma_1 + \sigma_2 + \sigma_3}{3} \qquad (2)$$

$$q = \sigma_1 - \sigma_3 \qquad (3)$$

$$p_s = ks \qquad (4)$$

where σ_1, σ_2 and σ_3 are the total principal stress, M is the slope of the critical state line, p_0 is the apparent unsaturated isotropic preconsolidation stress for suction s, p_0* is the saturated preconsolidation stress and k describes the increase of the apparent cohesion with suction. The net mean stress p is defined as indicated in Eq. 2 to facilitate the transition

from unsaturated to saturated states, σ_m is the mean stress, p_a is the air pressure and p_w is the water pressure.

For isotropic conditions, the yield states associated with suction are described using a yield function defined in the space (p, s), which is named Loading-Collapse (LC). This yield function explains the collapse that occurs upon wetting and the increase in apparent pre-consolidation stress p_0 caused by suction. The relationship is expressed as

$$\frac{p_0}{p^c} = \left(\frac{p_0^*}{p^c} \right)^{\frac{\lambda(0)-\kappa}{\lambda(s)-\kappa}} \tag{5}$$

where κ is the elastic stiffness parameter against changes in p, $\lambda(0)$ is the slope of the virgin compression line for saturated isotropic loading, p^c is a reference stress and $\lambda(s)$ is the slope of the virgin compression line for isotropic loading at a constant suction s. The slope $\lambda(s)$ is defined as

$$\lambda(s) = \lambda(0)[(1-r)\exp(-\beta s) + r] \tag{6}$$

where β controls the rate of stiffness increase with suction, and r is a limiting value of soil stiffness for very high suction.

A non-associated plastic potential is defined by

$$g(p, q, s, p_0^*) = \alpha q^2 - M^2 (p + p_s)(p_0 - p) \tag{7}$$

where α is established in such a way that under K_0 loading, lateral strains are zero.

The hardening parameter p_0* depends on the rate of volumetric plastic strain. The hardening law is given by

$$\frac{dp_0^*}{p_0^*} = \frac{(1+e)}{\lambda(0)-\kappa} d\varepsilon^p \tag{8}$$

where e is the void ratio.

Elastic strains are induced by changes in net mean stress, deviatory stress and suction according to the expression

$$d\varepsilon^p = \frac{\kappa}{(1+e)} \frac{dp}{p} + \frac{1}{3G} dq + \frac{\kappa_s}{(1+e)} \frac{ds}{(s + p_{atm})} \tag{9}$$

where G is the shear modulus, κ_s is the elastic stiffness parameter against changes in suction and p_{atm} is the atmospheric pressure.

2.2.2. Microstructural model

The microstructural behavior is assumed to be elastic and volumetric. The microstructural volumetric strain depends on a microstructural effective stress ($\hat{p}$), defined by

$$\hat{p} = p + \chi s \tag{10}$$

where χ is a constant, defined by the slope of the neutral line.

Another assumption made in this formulation is the hydraulic equilibrium between microstructure and macrostructure. Therefore, only one suction variable should be considered.

In the (p, s) plane, a line corresponding to a constant microstructural effective stresses is called the neutral line (NL) because no microstructural strain occurs along it. The neutral line divides the (p, s) plane into two parts, defining the microstructural stress paths indicated in Fig. 1.

The increment of the microstructural elastic strain is expressed as a function of the increment of the microstructural effective stress:

$$\dot{\varepsilon}_{vm} = \frac{\dot{\hat{p}}}{K_m} = \frac{\dot{p}}{K_m} + \chi \frac{\dot{s}}{K_m} \tag{11}$$

In this equation, the subscript m refers to the microstructural level, the subscript v refers to the volumetric component, and K_m is the microstructural bulk modulus. We compute K_m by the following law

$$K_m = \frac{e^{-\alpha_m \hat{p}}}{\beta_m} \tag{12}$$

2.2.3. Interactions between structural levels

Microstructural effects induce irreversible macrostructural deformations, which are considered proportional to microstructural strain, as described by certain interaction functions.

Two interaction functions are defined: f_c for microstructural compression paths and f_s for microstructural swelling paths. For isotropic loading, the interaction functions depend on the ratio p/p_0.

The ratio p/p_0 indicates the degree of openness of the macrostructure relative to the applied stress state. When this ratio is low, it indicates a dense packing of the material, and it is expected that microstructural swelling induces large macrostructural plastic strains.

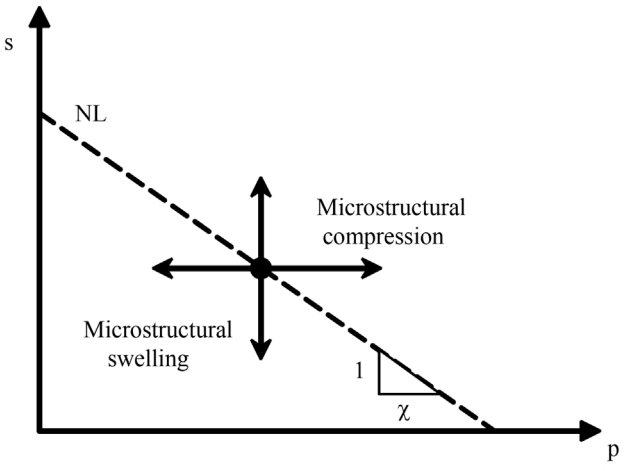

Figure 1 - Definition of microstructural swelling and contraction paths.

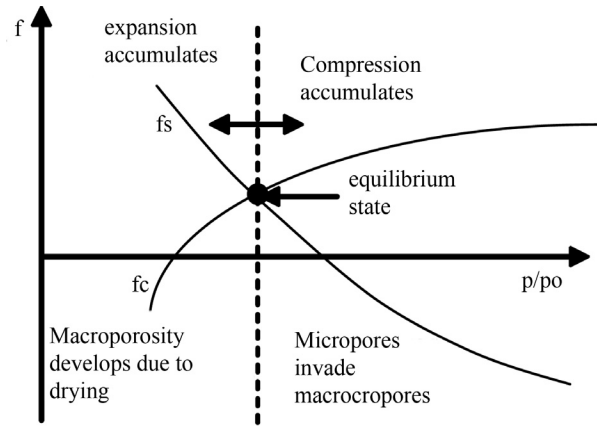

Figure 2 - Interaction mechanisms between micropores and macropores.

According to Alonso *et al.* (1999) any suitable function for f_s and f_c that is consistent with the physical ideas presented in Fig. 2 can be adopted.

This paper adopted the interaction functions proposed by Alonso *et al.* (1999):

$$f_c = f_{c0} + f_{c1}\left(\frac{p}{p_0}\right)^{n_c} \quad (13)$$

$$f_s = f_{s0} + f_{s1}\left(1-\frac{p}{p_0}\right)^{n_s} \quad (14)$$

3. Results and Analysis

The expansive soil of Petrolândia shows discrete variations in composition along its profile. Clay composes more than 54% of the soil, and sand represents less than 9%. The ratio of silt to clay decreases with depth, indicating that there is a translation of the thinner material from the surface to the sub-superficial horizons. The thinner material is carried by water and seepage through fissures. The soil has the following characteristics: w_L = 60%, PI = 30%, w_c = 19%, w = 17.41% and γ_d = 15.05 kN/m^3. The initial degree of saturation was 59.24%, which corresponds to a suction of 5.0 MPa.

The expansive soil matrix is characterized by a fine textured, compact, predominantly silicate clay permeated by micritic calcite crystals that comprise much of the silt and fine sand. Shaped lamellar particles were found, most likely originating from the filling of flattened channels and pores. These particles destroyed and compressed the soil matrix due to the action of the high activity clay (Ta) that occurs in this soil (Fig. 3a). Calcitic nodules are typical, and calcium carbonate ($CaCO_3$) commonly precipitates on the pore walls (Fig. 3b).

In the dry period, it has been observed that fissures in the soil surface have thicknesses that vary by only a few millimeters around a thickness of 120 mm. The thickness decreases with depth, and the extension reaches 2.0 m (observed in the inspection shaft). For water penetration, large fissures have a greater effect than a large number of narrow fissures because as the water content increases, the soil expands, and the slimmest fissures are progressively restricted, while the largest ones can remain open for a longer period of time. In the beginning of the wetting process, the fissure intensity is as important as the width and depth of the individual fissures. As rain occurs, the soil absorbs water from the surface and from the interior of the fissures, and the clay particles expand as micro-reliefs appear. The surface is composed of blocks of soils of irregular shapes, which are detected in an area of 100 m^2 chosen randomly in the field. The area represents approximately 190 blocks, each with an average area of 0.53 m^2 (Fig. 4a). It has also been observed that rain is sufficient to make some superficial fissures disappear completely (Fig. 4b). In this soil, free calcium carbonate predominated over sodium (Ferreira, 1995), thus presenting

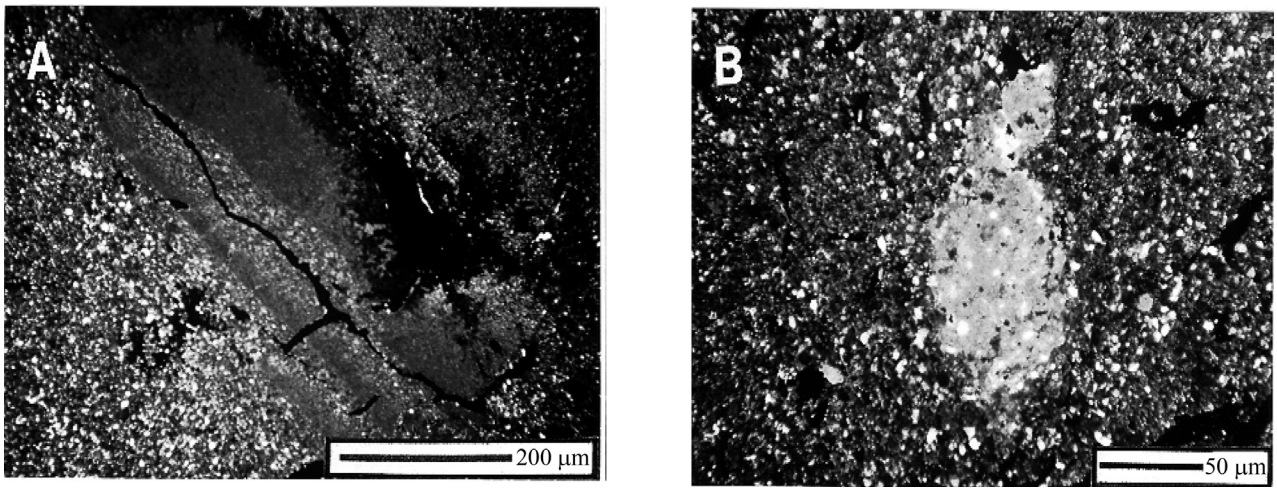

Figure 3 - a) Micrograph of fractures and flattened pores. b) Micrograph of calcitic nodule.

a smaller number of cracks with increased bandwidth, confirming the observations of Ahmad (1983).

The soil water content, measured from the surface to a depth of 3.50 m, changes in the rainy period from 42% to 20.90%, and in the dry period it changes from 14.54% to 21.03% (Fig. 4c). Beyond a depth of 2.50 m, no significant variation in water content between the dry and rainy periods was observed during the two years of observation, which indicates that this is the active zone of change in water content.

The soil swelling pressure obtained by the constant volume method increases with depth in the rainy period, and in the dry period it decreases until a depth of 2.5 m; from this depth onward it remains basically constant (Fig. 4d). In the same way, swelling pressure and effective stress have been found to vary with depth (Fig. 4e). Up to 2.5 m depth, there is considerable influence of the climatic conditions on water content, swelling pressure and fissure depth. In the field, fissures were observed at up to 2.0 m depth, in the dry period.

The volume change that occurs due to inundation was analyzed by considering the influence of vertical stress at inundation, along with the swelling pressure, the initial water content and the drying that occurred under stress.

3.1. Influence of consolidation vertical stress

Strain was plotted as a function of time after inundation in simple oedometer tests, as shown in Fig. 5. Expansion and collapse can sometimes occur simultaneously. Therefore, what is measured is the net deformation, which is a function of vertical stress, void ratio and water content (state of stress) in the soil before it is inundated. At some pre-determined state of stress, the deformation due to inundation is equal to expansion due to stress at 160 kPa, or expansion and collapse in the range of 240 to 400 kPa (initially, the soil compresses for 8 min, then it expands until 240 min and compresses until deformations stabilize). Collapse is caused at stress greater than 640 kPa.

The deformation process of expansion or collapse caused by inundation can be divided into three phases:

i) Initial - From time zero to one minute, in which small deformations are observed and the water only moistens the periphery.

ii) Primary - From 1 minute to 300 min, the water percolates from the periphery to the center, moistening the soil progressively (as a function of hydraulic conductivity). Deformations occur with higher intensity.

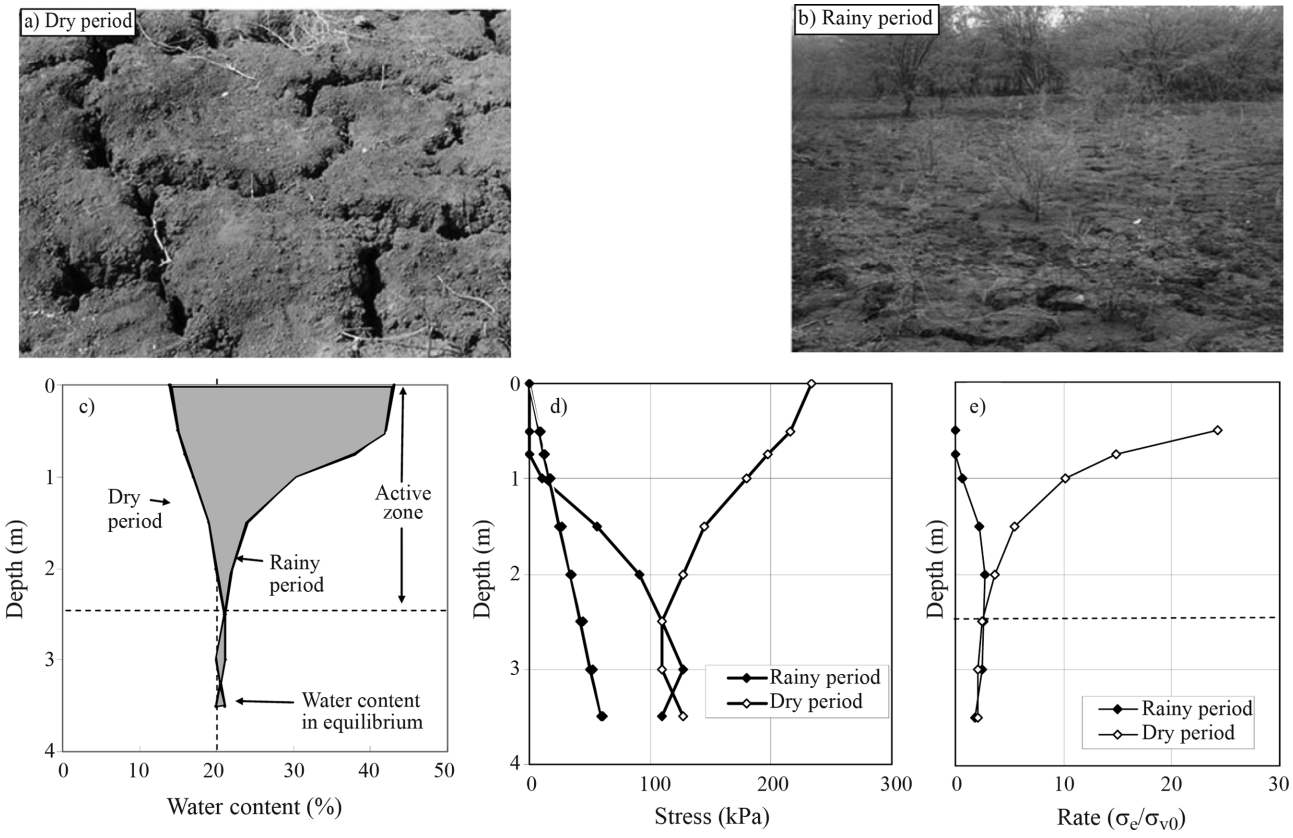

Figure 4 - a) Fissures and micro-reliefs in the dry period. b) Fissures and micro-reliefs in the rainy period, c) Active zone. d) In situ stress and expansion stress. e) Ratio between in situ stress and expansion stress in an expansive soil from Petrolândia.

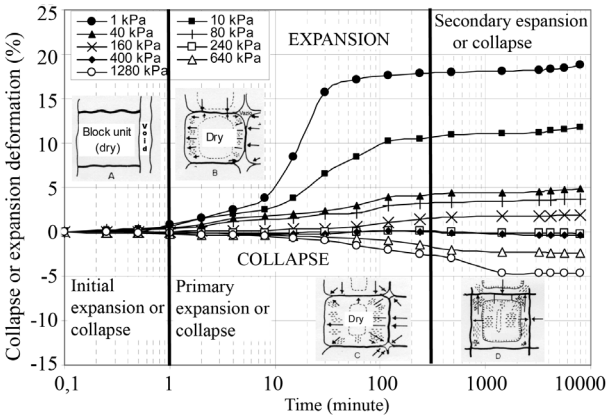

Figure 5 - Deformation as a function of time during the advance of the wetting front. (a) Small alteration in the soil water content; (b) Change in water content of the soil periphery; (c) Only the central nucleus maintains the initial water content; (d) Change in the water content of the whole soil.

iii) Secondary - Beyond 300 minutes, the water moistens the central nucleus, and the empty spaces are almost completely filled with water. The deformation velocity decreases (Fig. 5). Roo (2006) suggests that the initial deformations are associated with the microstructure, whereas the primary and secondary deformations are associated with the macrostructure.

The variation of expansion or collapse potential, as a function of consolidation vertical stress, void ratio or degree of saturation before soil inundation, is shown in Fig. 6.

For stresses lower than 312 kPa (Fig. 6a), void ratios higher than 0.745 (Fig. 6b) and saturation degrees less than 63.90% (Fig. 6c), Petrolândia soil expands when there is an increase in soil water content, characterizing the expansion region. For stresses greater than 312 kPa (Fig. 6a), void ratios less than 0.745 (Fig. 6b) and saturation degrees greater than 63.90% (Fig. 6c), Petrolândia soil collapses when water content increases, characterizing the collapse region. There are values of stress (σ_{crit} = 312 kPa), void ratio (e_{crit} = 0.745) and degree of saturation (Sr_{crit} = 63.90%) that are critical. At these values, the soil volume does not change when inundated (Fig. 6).

3.2. Influence of initial water content

The "free" expansion variation increases (approximately linearly) with the decrease in initial water content (increasing suction) and with the decrease in vertical stress of consolidation before inundation (Fig. 7a).

The "free" expansion of the expansive soil under study, at a water content of 17.41%, has high expansivity according to the Vijayvergiya & Ghazzaly (1973) criteria, which assume a consolidation stress of 10 kPa.

The values of swelling pressure and physical indices for samples that were previously wetted or dried before being inundated were determined by the loading methods after expansion, after consolidation and expansion under vertical stress (Method 1) and after collapse under stress (Method 2) with initial water contents of 22.58%, 20.80%, 17.41% and 7.76% (Table 1). The highest expansion stress values were obtained at the lowest water content values (7.76%), saturation degree values (35.22%) and void ratio values (0.57), and at higher suction values (117 MPa) and higher dry apparent specific weights (16.96 kN/m^3). The previous wetting process of the soil causes reduction in swelling pressure, whereas desiccation causes an increase.

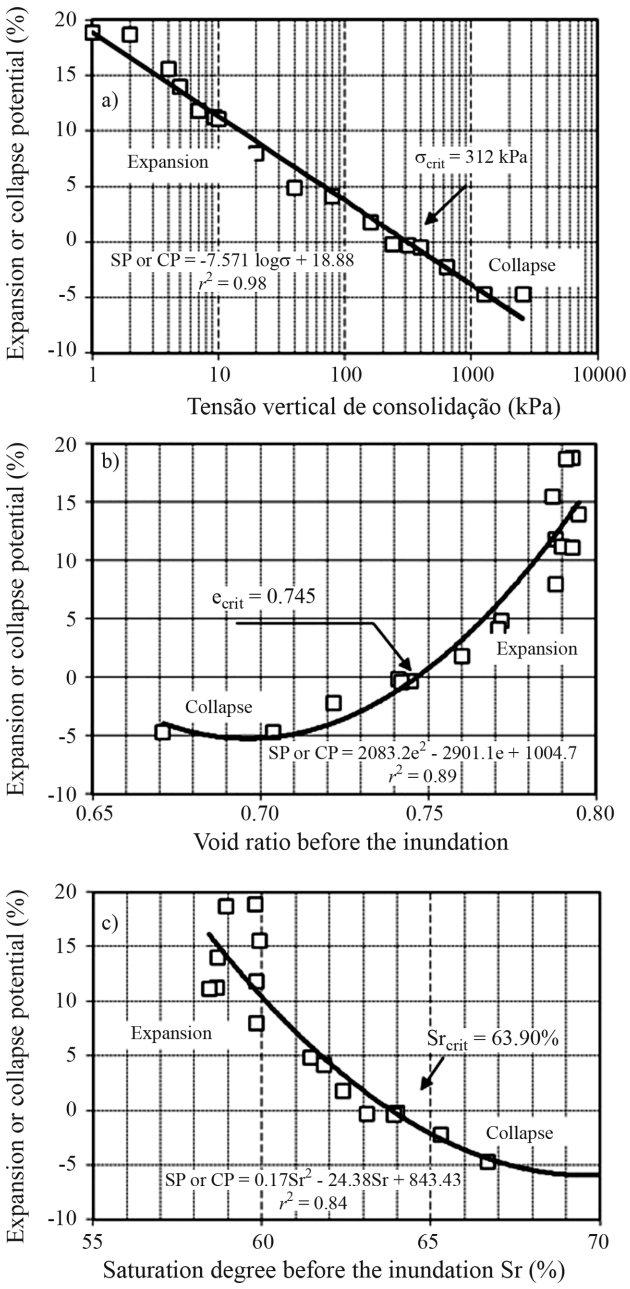

Figure 6 - Difference between expansion potential and collapse potential measured in simple oedometer tests. a) with consolidation vertical stress; b) with void ratio before inundation; c) with saturation degree before inundation.

This shows that, in the field, the climate conditioning factors have considerable influence on soil expansion stress.

The specific volumetric deformation curves that are observed under soil consolidation vertical stress (ε_v *vs.* σ - log) at different initial water content levels, and under stresses of 10 kPa and 160 kPa, are presented in Fig. 7b. At the same initial water content, the expansion due to inundation decreases with increasing consolidation vertical stress.

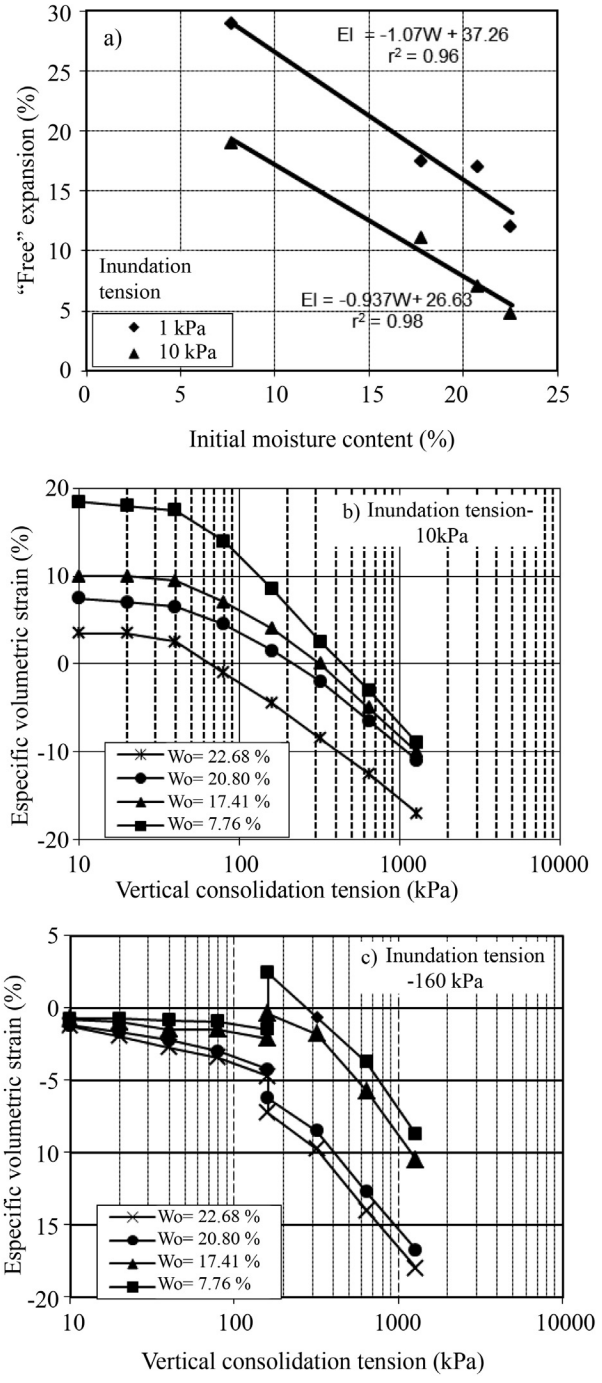

Figure 7 - Influence of initial water content: a) in "free" expansion; b) in compression; c) in expansion or collapse under stress.

At the same level of consolidation vertical stress, soil expansion is reduced as initial water content increases (Fig. 7b) because the previous wetting causes expansion before loading. Under a consolidation vertical stress of 160 kPa, soil inundation causes collapse at initial water content of 22.58% or 20.80%, and expansion at initial water content of 17.41% or 7.76% (Fig. 7c). A similar behavior was observed by Presa (1982) in soil with approximately the same void ratio and different initial water content, which was consolidated under a stress of 200 kPa. The initial water content and stress greatly affect the volume change observed when the soil is inundated.

3.3. Drying

The process of soil deformation due to desiccation is much slower than deformation during wetting. This is due to the way the water is transferred. During inundation, it is processed in the liquid phase, but in desiccation it is partially processed in the vapor phase.

The effect of desiccation on the total deformation of the soil is greater at lower stress than at higher stress (Fig. 8a). The deformations measured during desiccation result from the addition of three components: immediate compression, deformation due to vertical stress and retrac-

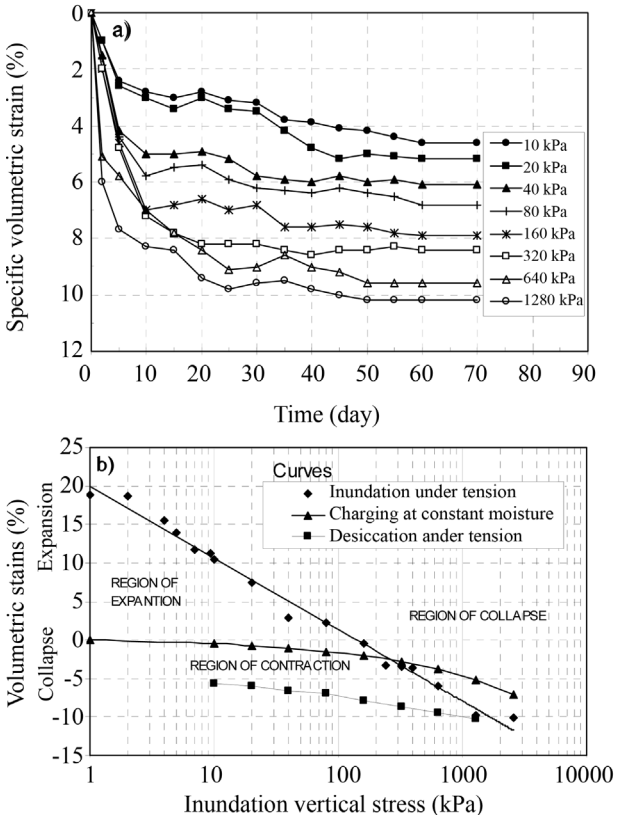

Figure 8 - Volumetric deformation with the addition of stress, desiccation and inundation: a) volumetric deformation with the simultaneous addition of stress and desiccation; b) expansion, collapse and contraction regions.

Table 1 - Influence of initial water content in deformation and stress of expansion.

W (%)	Initial suction (kPa)	e_o	ρ_d (kN/m^3)	Sr (%)	Relationship of expansion deformation and stress		Expansion stress (kPa)	
					εs (%)	σ (kPa)	Method 1	Method 2
7.76	117.000	0.597	16.96	35.22	εs = -11.82 logσ + 29.73	r^2 = 0.99	456	328
17.41	5.000	0.801	15.05	59.24	εs = -7.84 logσ + 18.66	r^2 = 0.99	333	239
20.70	700	0.885	14.37	63.39	εs = -8.62 logσ + 16.64	r^2 = 0.99	153	83
22.60	200	0.936	14.00	65.43	εs = -6.36 logσ + 11.60	r^2 = 099	85	67

W - initial water content in the dry period; e_o - void ratio; Sr - degree of saturation of water; εs - expansion deformation (εs = 100 $\Delta H/H_i$, where ΔH is the body's height variation due to inundation, and H_i is the specimen's height before inundation); σ - stress; ρd- dry apparent specific weight; r^2 - correlation coefficient; Method 1 - loading after expansion with different consolidation vertical stress; Method 2 - expansion and collapse under stress.

tion. At stresses less than 40 kPa, the time required for 50% of deformations to occur is at least 8 days, but for stresses greater than 320 kPa it is at most 2 days. This is explained by the fact that, at consolidation stresses less than 40 kPa, the immediate compressions and the compressions due to the stress effect are reduced with time compared to the ones caused by desiccation, and they prevail over the compressions caused by retraction, which are slower. At stresses greater than 320 kPa, the immediate compressions and the ones due to the stress magnitude effect have greater importance and occur more quickly than the compressions caused by desiccation. The region between the loading curves, with constant water content, and the curves of desiccation under stress limit the contraction. (Fig. 8b).

The curves describing volume changes due to changes in water content under stress and those describing volume changes due to loading at constant water content define two regions: a region of expansion at stress lower than 277 kPa and a region of collapse at stress greater than 277 kPa (Fig. 8b). The area formed by the curves describing volume variation due to water content change under stress, volume change due to loading at constant water content and desiccation under stress constitutes an important piece of information about the influence of the stress path on the behavior of volume variation due to change in soil water content. These curves define the limits of the regions of expansion, collapse and contraction.

3.4. Numerical simulation

Three suction-controlled oedometric tests involving inundation at different stress levels were conducted. In the first simulation, the specimen was flooded at 10 kPa. In the second test, the inundation occurred at 160 kPa. In the third test, the sample was inundated under a vertical pressure of 640 kPa. Laboratory results are presented in Fig. 9.

The model described above was implemented in the Finite Element program CODE_BRIGHT (Olivella *et al.*, 1996; Sanchez *et al.*, 2005), which was used to simulate the suction-controlled oedometric tests.

The parameters used in the simulation were obtained from tests results and are listed in Table 2.

Laboratory data and numerical simulation results are presented in Fig. 9.

In Test 1, the sample was flooded under low vertical stress (10 kPa), and swelling deformation was measured. A volumetric strain of 10% was registered. In Test 2, inundation occurred under a higher vertical stress (160 kPa), and the swelling volumetric strain was lower (approximately 2%). For Test 3, inundation occurred when the vertical stress was 640 kPa. At this stress level, the sample collapses.

The simulation results show very good agreement with the experimental data. The loading observed under controlled suction and the swelling observed as a result of suction reduction under a determined level of vertical stress were reproduced very well. The collapse at higher stress levels was also in agreement with experimental results.

Simulation results also allow us to analyze the volume change behavior of microstructural and macrostructural levels separately, as illustrated for void ratio variation in Fig. 10.

According to the constitutive model used, a decrease in suction implies a microstructural swelling (Fig. 1), which was observed in the three tests (Fig. 10).

Table 2 - Parameters used in simulation.

Parameters defining BBM for the macrostructural level
$\kappa = 0.009$ $\kappa_s = 0.002$ $\lambda(0) = 0.10$ $r = 0.50$ β (MPa^{-1}) = 1.0
p_0*(MPa) = 0.22 p^c (MPa) = 0.10
Parameters defining the laws for the microstructural level
$\chi = 1.0$ α_m (MPa^{-1}) = 0.006 β_m (MPa^{-1}) = 0.012
Interaction functions
$f_{c0} = -0.10$ $f_{c1} = 1.5$ $n_c = 0.50$ $f_{s0} = -1.50$ $f_{s1} = 3.70$ $n_s = 2.0$
$e_{macro} = 0.80$ $e_{micro} = 0.30$

Changes in the microstructural void ratio are not greatly influenced by the stress level, whereas the macrostructural void ratio is greatly affected by stress.

In Test 1, when inundation occurs under a vertical stress of 10 kPa, both the microstructure and macrostructure expand. The BBM model can reproduce some of the expansion at low stress levels. Moreover, the ratio p/p_0 is low, and the f_s interaction value is positive. The induced microstructural strains are due to expansion.

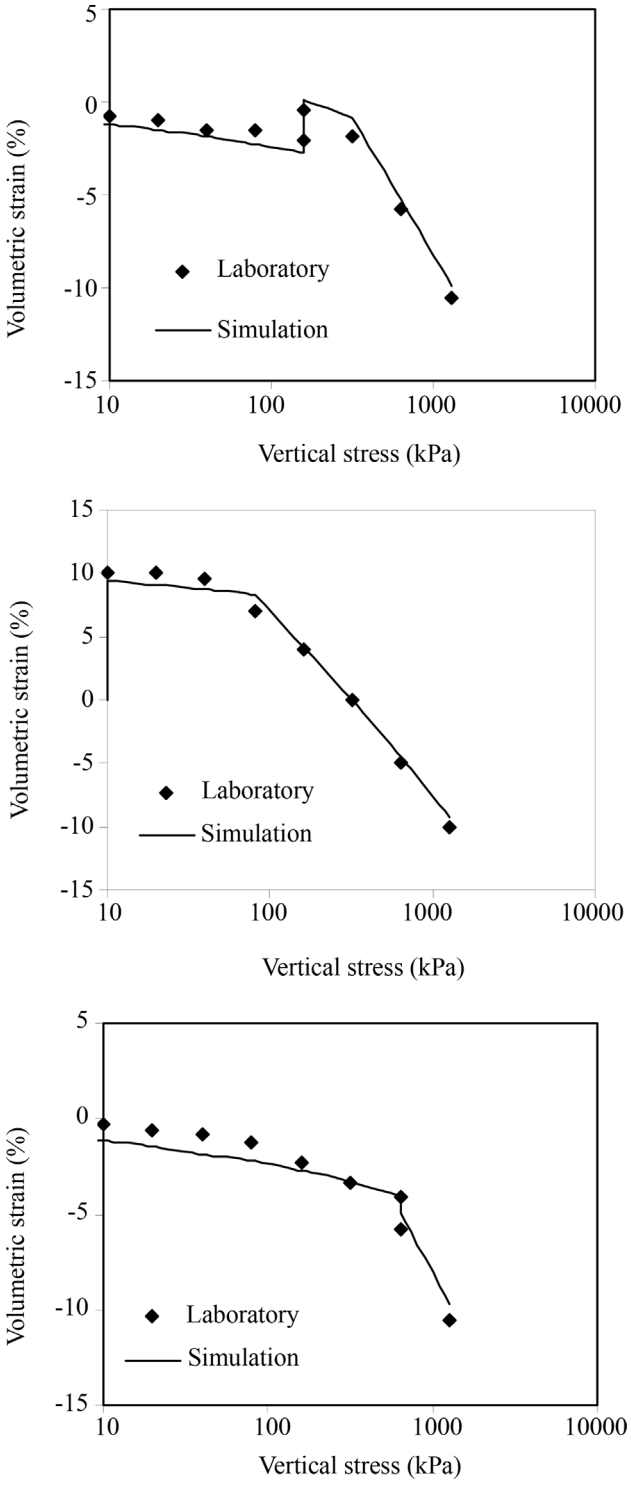

Figure 9 - Comparison between laboratory data and simulation results for Tests 1, 2 and 3.

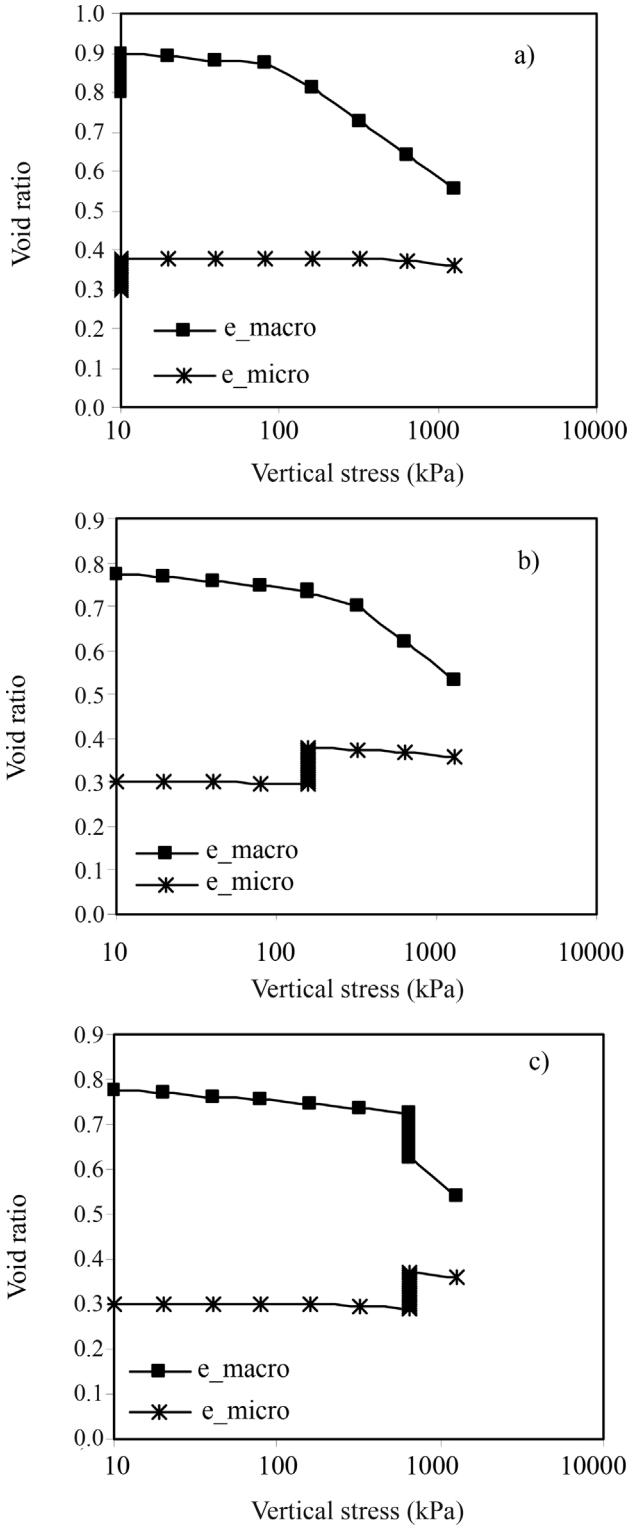

Figure 10 - Simulation results of macro and micro void ratio variation for a) Test 1; b) Test 2; c) Test 3.

As the inundation stress level increases to 160 kPa (Test 2), expansion is observed only in the microstructure. Because the ratio p/p_0 is greater than in Test 1, the f_s interaction value decreases, and the induced macrostructural strains of expansion are smaller.

When the sample is inundated at a higher stress level, such as in Test 3, the macrostructure collapses. The influence of microstructural strain is minimal.

4. Conclusions

We conclude that soils with lower initial water content and higher exterior applied vertical stress exhibit greater expansion due to their increased water content.

The order in which the soil is subjected to stress or inundation affects the expansion stress value. The inundation leads to soil volume increase (expansion) or decrease (collapse) depending on the initial moisture and the vertical stress applied to the soil.

The numerical results demonstrate that the double structure generalized plasticity model proposed by Sanchez *et al.* (2005) is able to reproduce the experimental behavior of expansive soils.

Finally, the factors that limit the regions of expansion, collapse and contraction are the curves of inundation, the changing or constant humidity and the desiccation under stress.

Acknowledgments

We thank Prof. Mauro C. dos Santos from UFRPE, who made possible the identification and microstructural analysis of soils. The investigation described above was performed with the support of the Foundation for Support of Science and Technology of the State Pernambuco (FACEPE).

The authors also wish to acknowledge the financial support provided by CNPq/Brazil.

References

Ahmad, N. (1983) Vertisoils. Wildiny, L.P.; Smeck, N.E. & Hall, G.F. (eds) Pedogenesis and Soil Taxonomy. Elsevier, Amsterdam, pp. 91-123.

Alonso, E.E.; Gens, A. & Josa, A. (1990) A constitutive model for partially saturated soils. Geotechnique, v. 40:3, p. 405-430.

Alonso, E.; Vaunat, J. & Gens, A. (1999) Modelling the mechanical behaviour of expansive clays.Engineering Geology, v. 54, p. 173-183.

ABNT (1984a) Soil – Grain-size Distribution Analyses - NBR 7181. Rio de Janeiro, 13 pp (In Portuguese).

ABNT (1984b) Soil – GrainsPassinigtheSieve 4,8 mm – DeterminationofSolidsDensity NBR 6508. Rio de Janeiro, 8 pp (In Portuguese).

ABNT (1984c) Soil – Determination of the Liquit Limit - NBR 6459.Rio de Janeiro6 pp (In Portuguese).

ABNT (1984d) Soil – Determinationof the Plastict Limit - NBR 7180. Rio de Janeiro pp 6 pp (In Portuguese).

Ferreira, S.R.M. (1988) Solos Especiais: Colapsíveis, Dispersivos e Expansivos: Relatório de Pesquisa - CNPq. Recife, 144 pp.

Ferreira, S.R.M. (1995) Collapse and Expansion of Natural Unsaturated Soils Due to Wetting. Doctoral Thesis, Federal University of Rio de Janeiro, Rio de Janeiro, 379 pp (In Portuguese).

Ferreira, S.R.M. (2008) Collapsible and expansive soils: A panoramic vision in Brazil. Proc.VI Brazilian Symposium on Unsaturated Soils, Salvador v. 2, p. 593-618 (In Portuguese).

Gens, A. & Alonso, E.E. (1992) A framework for the behaviour of unsaturated expansive clays. Canadian Geotechnical Journal, v. 29, pp. 1013-1032.

GusmãoFilho, J.A. & Silva, J.M.J. (1991) Field instrumentation as related to a expansive soil. Proc. 9th Panamerican Conference on Soil Mechanics and Foundation Engineering, Viña Del Mar, v. 1, pp. 76-86.

Jucá, J.F.T.; Gusmão Filho, J.A. & Justino da Silva, J.M. (1992) Laboratory and field tests on an expansive soil in Brazil. Proc. 7th International Conference on Expansive Soils, Dallas/Texas, v. 1, pp. 337-342.

Justo, J.L.A.; Delgado, A. & Ruiz, J. (1984) The influence of stress-path in the collapse - swelling of soils at the laboratory. Proc. 5th International Conference on Expansive Soils, Adelaide, p. 67-71.

Melo, J.G. (1980) Estudo Hidrológico da Bacia Sedimentar do Jatobá (PE). Recursos Exploráveis e Dispositivos de Captação. Dissertação de Mestrado, Universidade Federal de Pernambuco, Recife, 332 pp.

Nunes, A.J.C.; Vasconcelos, E.M. & Pandolfi, R.L.M. (1982) Occurrence of engineering of soil in the area of greater Recife. Proc. 7th Brazilian Congress on Soil Mechanics Foundation Engineerimg, Recife/Olinda, v. 5, pp. 193-209 (In Portuguese).

Olivella, S.; Gens, A.; Carrera, J. & Alonso, E.E. (1996) Numerical formulation for a simulator (CODE-BRIGHT) for the coupled analysis of saline media. Engineering Computations, v. 13:7, p. 87-112.

Presa, E.P. (1982) Deformabilidad de las argillas expansivas bajo succión controlada. Tesi Doctoral, Universidad Politécnicade Madrid, Madrid, 663 pp.

Roo, S.M. (2006) Identification and classification of expansive soils. Al-Rams, A.A. & Goosen, M.F.A. (eds) Taylor & Francis / Balkema, London, pp. 15-24.

Sanchez, M.; Gens, A.; Guimarães, L.N. & Olivella, S. (2005) A double structure generalized plasticity model for expansive materials. International Journal for Numerical and Analisis Methods in Geomechanics, v. 29, p. 751-787.

Simões, P.R.M. & Costa Filho, L.M. (1981) Mineralogical characteristics of expansive soils of the Recôncavo

Baiano. Proc. Brazilian Symposiumon Tropical Soils, Rio de Janeiro, pp. 569-588.

Sobral, H.S. (1956) Contribuição ao Estudo do Massapê como Solo para Construção. Tese de Concurso para Cadeira de Materiais de Construção, Escola de Belas Artes, Universidade Federal da Bahia, Salvador.

Vargas, M. (1985) The concept of Tropical Soils. Proc. 1st International Conference Geomechanics in Tropical Lateritic and Saprolitic Soils, Brasília, v. 3, pp. 101-134.

Vijayvergiya, V.N. & Ghazzaly, O.I. (1973) Prediction of swelling potential for natural clays. Proc. 3rd International Conference on Expansive Soils, Hayfa, v. 1, pp. 227-236.

Observational Method applied to the Rio Grande Port Breakwater

F. Schnaid, L.G. Mello, S.S. Sandroni

Abstract. A case study describing the experience in modeling and designing the process of construction of the Rio Grande Breakwater on soft clay deposits is summarized in this paper. Field performance during and after embankment construction was monitored with inclinometers, magnetometers and electrical piezometers providing the necessary information to check the design hypothesis, to evaluate the uncertainties related to the natural ground variability and to ensure that the work conformed with acceptable limits of behaviour. The importance of modeling the construction by finite element analysis as an interactive process supported by observations collected from the construction phases is highlighted. The successful completion of the work stimulates the use of the Observational Method in geotechnical practice and, for this reason, guidance is provided for future work.

Keywords: observational method, soft clay, instrumentation, numerical analysis.

1. Observational Method: Design Principles

As reported by Peck (1969) "observational methods have always been used by engineers working in the fields now included in applied soil mechanics, but the observational method – OM is a term having a specific restricted meaning". The systematization of the OM is associated by Peck to Terzaghi (1961), who reports that the between 1912 and 1922 the Swedish State Railroads was using the observational procedure on a large scale in earthworks. Terzaghi (1961) presents some of his works conceived to follow this procedure. In every case reported by Terzaghi the OM was used to compensate for the uncertainties associated to the interpretation of subsoil exploration.

Peck (1969) quotes an early version of the introduction to the book Soil Mechanics in Engineering Practice, in which Terzaghi (1948) wrote "the results of computations are not more than working hypothesis, subject to confirmation or modification during construction. Soil mechanics as we understand it today, provides a method which would be called the experimental method". Reference is made to the practical application of the learn-as-you-go method, closing the gap in knowledge and, if necessary, leading to modifications of the design during construction.

There is little doubt that Peck (1969) framed the ideas and concepts being used, inclusive by Terzaghi, proposing that "the complete application on the method embodies the following ingredients:

- Exploration sufficient to establish at least the general nature, pattern and properties of the deposits, but not necessarily in detail;
- Assessment of the most probable conditions and the most unfavourable conceivable deviations from these conditions. In this assessment geology often plays a major role;
- Establishment of the design based on a working hypothesis of the behaviour anticipated under the most probable conditions;
- Selection of quantities to be observed as construction proceeds and calculation of their anticipated values on the basis of the working hypothesis;
- Calculation of values of the same quantities under the most unfavourable conditions compatible with the available data concerning the subsurface conditions;
- Selection in advance of a course of action or modification of design for every foreseeable significant deviation of the observational findings from those predicted on the basis of the working hypothesis;
- Measurement of quantities to be observed and evaluation of factual conditions;
- Modification of design to suit actual conditions".

In the conclusion of his Rankine Lecture, Peck (1969) mentions that the successful use of the OM is associated to the possibility of optimizing/altering the design during construction, as well as the necessity of having contracts that allow for these changes, without burdening either party involved in an unbalanced way.

Lambe (1973) in his Rankine Lecture focuses on discussing predictions in geotechnical engineering. In his proposal, a classification of predictions as related to when and based on what data was available at this time, named Type B prediction as "made during the construction and would have available data obtained during the initial parts of the construction, such as measurements made during excava-

F. Schnaid, PhD, Associate Professor, Departamento de Engenharia Civil, Universidade Federal do Rio Grande do Sul, Porto Alegre, RS, Brazil. e-mail: fernando@ufrgs.br.
L.G. Mello, Senior Engineer, Vecttor Design, São Paulo, SP, Brazil. e-mail: lgmello@vecttor.com.
S.S. Sandroni, Director, Geoprojetos Engineering, Associate Research Professor, Pontifícia Universidade Católica do Rio de Janeiro, Rio de Janeiro, RJ, Brazil. e-mail: sandro@geoprojetos.com.br.
Submitted on July 10, 2012; Final Acceptance on July 30, 2013; Discussion open until December 31, 2013.

tion, foundation construction, etc.", with the outcome of the event being predicted still unknown.

There is a clear link of Lambe's concerns of accuracy of predictions with the concepts of the OM, as "the evaluation of a prediction consists of an examination and interpretation of the prediction in the light of the known outcome of the predicted event, it is built round a comparison of the predicted performance with the measured performance". Specific mention is done to the fact that an engineer "makes decisions and takes actions on the basis of his re-examinations. The Terzaghi-Peck OM depends on an evaluation of predictions" is presented.

Numerous authors have worked within these concepts and developed parallel thoughts from then on, and the OM has also been recognised as a design method in codes like Eurocode 7 (1997). Design review during construction is specifically mentioned.

Requirements to be met are postulated in this Code as reproduced below:

- Acceptable limits of behaviours are established;
- The range of possible behaviour is assessed and is documented that there is an acceptable probability that the actual performance will be within the acceptable limits;
- A monitoring program is devised to document the actual performance. The monitoring program shall document the accepted performance early in the construction process, with data acquisition at sufficiently short intervals as to allow for prompt contingency actions to be undertaken successfully;
- The response time of the instruments and the procedures for analysing the results shall be sufficiently rapid in relation to the possible evolution of the system;
- A plan of contingency actions shall be prepared, to be adopted if the monitoring reveals behaviour outside acceptable limits.

In 1999, Nicholson et al. published a relevant contribution to the theme, updating it to modern society's concerns and requirements, mainly aiming at responding to cost savings, increase in safety and team co-operation as embodied in modern contract types. Their definition is: "the OM is a process in which acceptable limits of structural and geotechnical behaviour are established. In addition, performance predictions, monitoring, review and modification plans, and emergency plans, are fully prepared**.** The design is checked for robustness before construction starts. During (and after) construction, the results from the monitoring are reviewed against the predictions and robust modifications are introduced where appropriate".

To illustrate these points, a flow chart of the OM is presented and reproduced herewith (Fig. 1). Risk management, in its technical aspects, is intrinsically linked with and part of the OM. The definition of the O M that encompass these ideas is properly summarized as: "a continuous, managed, integrated, process of design, construction control, monitoring and review that enables previously defined modifications to be incorporated during or after construction, as appropriate" (Nicholson *et al.*, 1999). The authors would add the need of previously also approve the modifications to eventually incorporate in design.

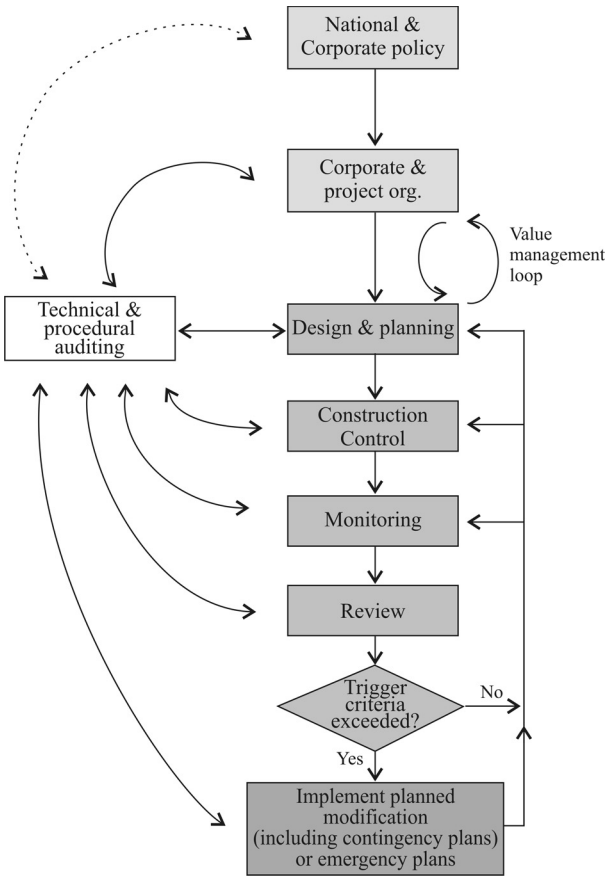

Figure 1 - Observational Method Flow Chart, apud Nicholson *et al.*, 1999.

As monitoring is an important item of the OM, the postulation of trigger criteria is also implicitly important, to start implementation of planned modifications and/or of the contingency plan if an emergency situation is foreseen.

The postulation of values of forces/stresses and/or movements/displacements, leading to the calculation of velocity of changes and many other techniques of assessing and interpreting the behaviour of a structure, require that all the correct possible models of collapse that a structure in a certain subsoil stratigraphy may undergo are properly identified, that all the geomechanical properties of the distinct material layers are properly determined, and that design calculations, from which the trigger values are derived, are developed with models that correctly simulate the field reality in time/stress/time path.

Numerous Symposiums, Specialty Sessions, Work Groups etc were organized to discuss and present case histories where the OM was used, leading to the existence of quite a number of published technical papers on the topic.

The identification of existing risks in any project, their mitigation during design, and their monitoring throughout construction, has become part of most important works.

Patel *et al.* (2007) refer to a publication by the GeoTechNet (2002) which showed that the implementation of the OM in Eurocode EC7 had shortcomings, as there was a general lack of understanding of the principles of use of the OM, its use within contractual framework on an engineering project and the important responsibilities incumbent on all parties involved, the client, the designer and the contracting teams when implementing the OM approach to a project.

The important discussion that, while in traditional ground engineering projects, monitoring plays a passive role to check original predictions and provide confidence to third party checkers, in the OM monitoring plays a very much proactive role in both design and constructing, allowing pre-planned modifications to be carried out within an agreed contractual framework.

The approach to the application of the OM has developed and matured since Peck (1969), as discussed by Nicholson *et al.* (1999). Peck had adopted the most probable design, evolving to reduced moderately conservative design parameters if and when triggers in the monitoring program were exceeded. Nicholson et al. propose a safer approach to design adopting a progressive modification of the design starting based on moderately conservative parameters and then, backed by monitoring, developing to most probable conditions. In this modern approach, risk analysis and risk management became a must, especially with lump sum contracting. Managing geotechnical risks is the focus of many professionals and applied in most important heavy infrastructure projects (*e.g.* Clayton, 2001).

In parallel, the collapse of the Heathrow tunnel and the consequential investigation by the British authorities triggered the incorporation of a Code of Practice (2006) agreed with the risk takers, the Insurance industry, to identify and mitigate risks during design and construction of tunnels, an important area of civil engineering works which uses the OM method approach applied to tunnelling practice, mainly in the New Austrian Tunnelling Method – NATM.

The modification of moderately conservative predefined design to the most probable situation reduces the uncertainties and, therefore, greater site controls are necessary, balanced by rigorous monitoring and existence of proper contingency plans fully discussed previously to works commencement.

Flexibility is required at the work fronts in order to accommodate changes in design and programme. The stakeholders need to be fully tuned with the technical and commercial risks linked to any contingency materializing.

Monitoring becomes a crucial item in the whole construction planning and development. A competent regime has to be set in place, checking, reviewing and responding to any result in a short time.

The possibility of having brittle behaviour in the structure or rapid uncontrollable deterioration in the materials which does not allow sufficient warning to implement planned modifications have to be excluded by design decisions, as stated by de Mello (1977).

Finally, the authors consider valid to comment the recent use of a modern terminology for the OM: the Interactive Design. In our understanding it is the OM as discussed by Peck (1969) adapted to the third millennium societies' terminologies and needs. Many other designations have been used since Peck presented his Rankine lecture, like Experimental Method and Design-as-you-Go (Ladd, 1991; Staversen, 2006; Negro *et al.*, 2008).

The present paper aims at sharing knowledge of the current OM state-of-practice based on a critical overview of the Rio Grande Port breakwater construction case study. Fundamental concepts that frame the OM - introduced above - have been fully implemented given room to highlight advantages, limitations and perspectives of this type of approach in geotechnical practice regarding ultimate limit states.

2. Rio Grande Port Breakwater: Case Study

The case study describes the stage construction of an extension of a 20 m high marine breakwater laying over a thick soft sedimentary deposit at the Rio Grande Port in southern Brazil. The Western and Eastern breakwaters are 700 m and 370 m long extensions of existing facilities constructed in 1910 by *Compagnie Française du Port Rio Grande* (Fig. 2). The construction completed in March 2011 deepened the existing navigation channel from -14 m to -18 m in order to allow access for larger ships.

Breakwater design was an engineering challenge due to the combination of difficult geotechnical and environmental conditions in the region, with strong currents from the lagoon system, severe winds and large waves. The crest level is relatively low, namely TAW + 5 m, leading to large overtopping during storms. Designed to withstand the im-

Figure 2 - Eastern breakwater at the Rio Grande Port, Brazil.

pact of overtopping waves, the breakwater was constructed in a 1V:1.5H embankment slope, protected by an armour layer and underwater equilibrium berms for slope stability (Fig. 3).

Construction of the extension of the breakwaters was completed in 4 stages: (i) placing a first mattresses layer up to TAW -11.0 m, (b) construction by ships and barges up to TAW -5.0 m, (c) land construction up to TAW +3.0 m and (d) finishing at TAW + 5.0 m during placement of armor layer and tetrapods.

3. Site Characterization and Instrumentation

A preliminary site investigation was carried out at an early design stage and included SPT's boreholes, vane tests and undisturbed soil samples from 4" Shelby samplers. A complementary, comprehensive offshore site investigation campaign was performed from a submergible unit. A series of piezocone tests were carried out along the eastern and western breakwater plan area and undisturbed sampling were retrieved for laboratory triaxial and oedometer tests (e.g. Schnaid, 2009). Characteristic features of a continuous profile from CPTU data are shown in Fig. 4, revealing a sedimentary deposit with a 3 m sandy-clay layer overlain a 12 m thick soft clay layer. A superficial thin silty-clay layer, recently deposited, is frequently observed along the site. A representative profile of the Eastern breakwater is shown in Fig. 5. Design parameters assessed from laboratory and in situ testing are summarized in Table 1.

Given the challenges arisen by adverse geotechnical conditions, the breakwater construction was instrumented and the OM approach fully implemented. Seven open-ended 0.8 m diameter steel casing instrument towers were deployed on the seabed, adjacent to the projected breakwater toe contour and embedded into the equilibrium berms. Four towers were located along the Western side (MO01, MO02, MO03 e MO04) and three along the Eastern side (ML01, ML02 e ML03) as shown in the aerial photograph and plan view in Fig. 6. These instrumented towers enabled the instrumentation to be installed and provided protection to the instruments during construction. Instrumentation

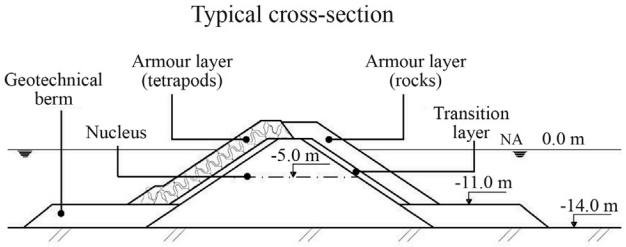

Figure 3 - Layout of a typical cross-section of the Rio Grande breakwater.

Table 1 - Material properties.

Material	Thickness (m)	e_o	C_c	ϕ'
Rockfill	22	incompressible		45°
Very soft silty-clay	4	3.6	1.6	33°
Loose sand	6	2.0	1.0	45°
Soft clay	11	1.0	0.5	26°
Very dense sand	∞	incompressible		45°

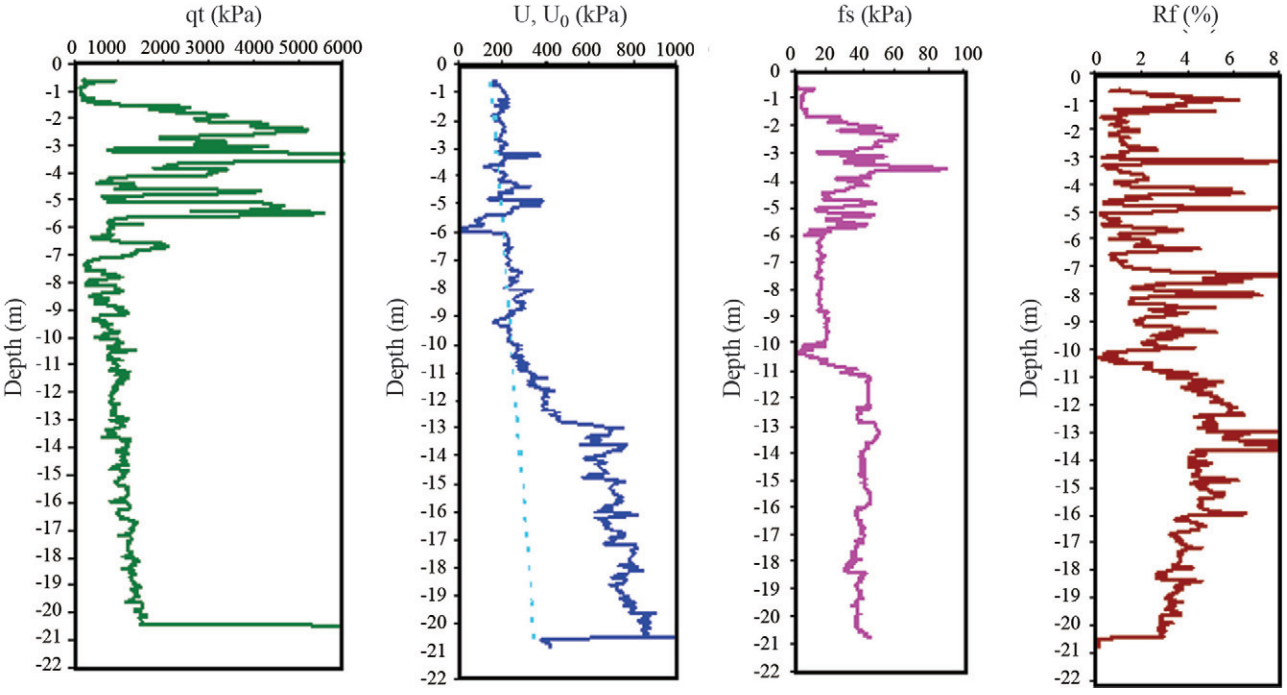

Figure 4 - CPTU testing data at the Eastern Breakwater.

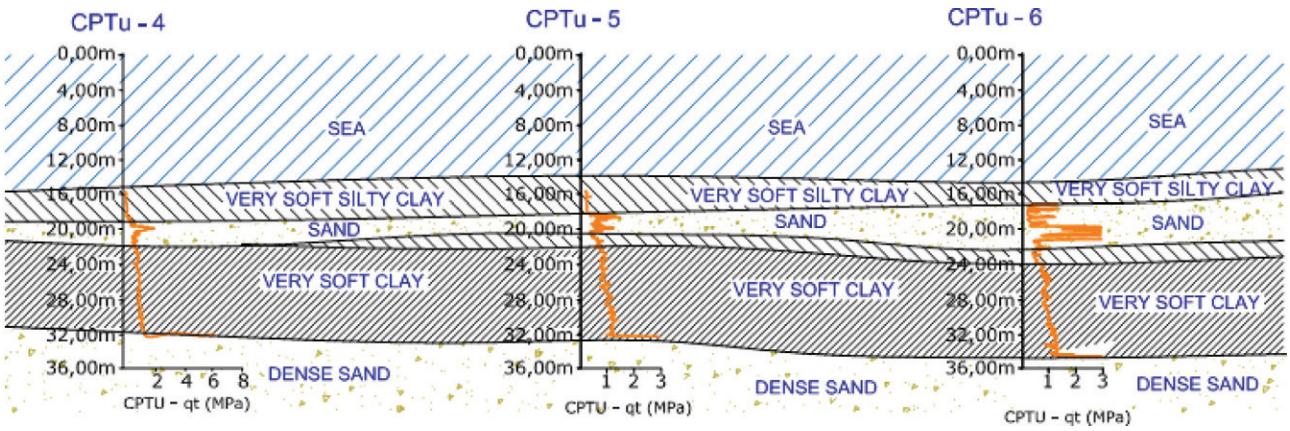

Figure 5 - Soil profile of the Eastern Breakwater.

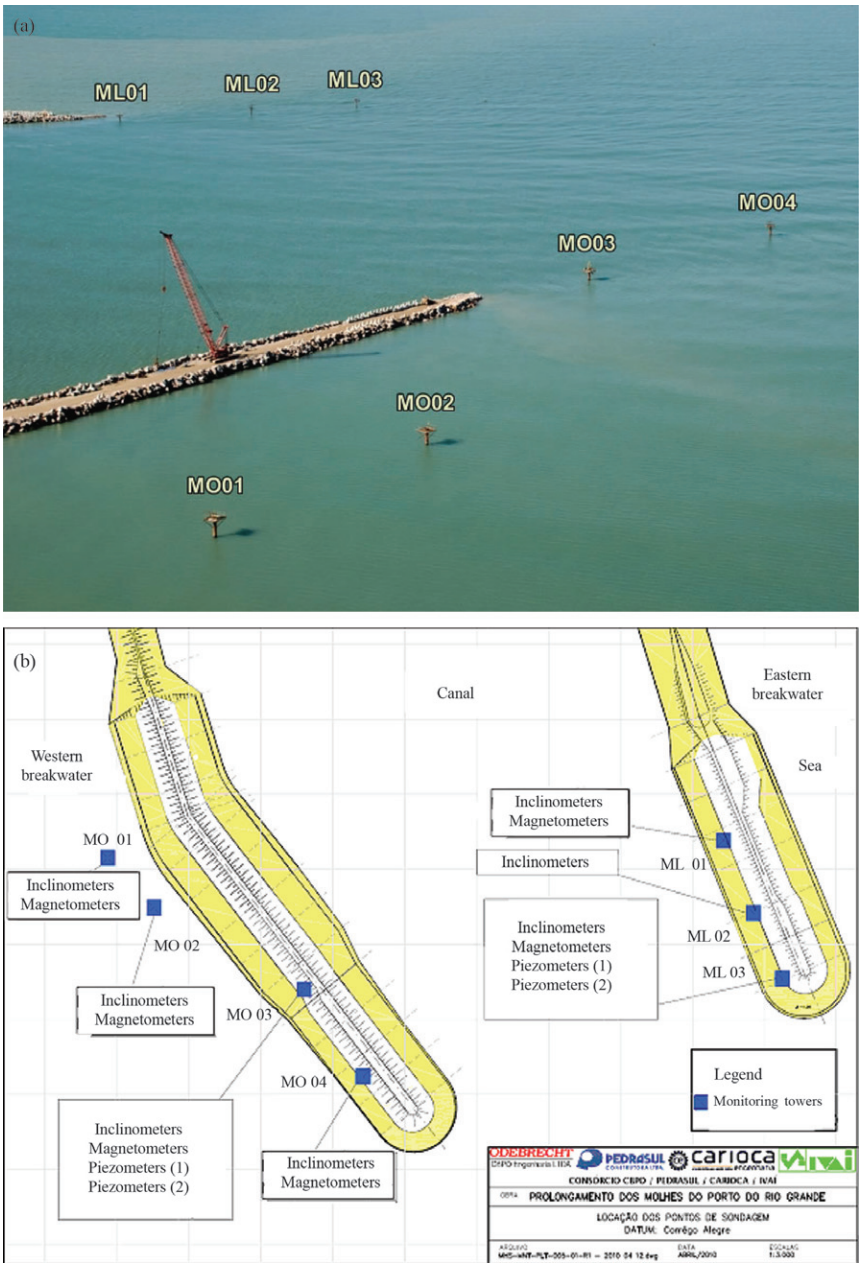

Figure 6 - Location of instrumented sections (a) aerial photograph and (b) plan view.

comprises inclinometers, settlement detection devices (magnetometers) and electrical piezometers. A detailed description of instruments and installation procedures has been reported by Rabassa (2010).

In general, all instrumented towers produced the same qualitative information and, therefore, results from a single instrumented location (MO03) are used to evaluate the measured performance of the breakwater construction. Representative of the overall measured behavior and devised as part of a detailed monitoring scheme, these results are analyzed on the basis of acceptable limits and contingency action plans. For example, horizontal displacement *versus* depth curves measured at an axis perpendicular to the breakwater for a number of load increments are show in Fig. 7. Maximum horizontal displacement measured at a depth around 24 m to 28 m reached 140 mm.

The results as presented in Figs. 8 and 9 show the vertical deviation θ and variation of vertical deviation with time ($V_\delta = \Delta\theta_v/\Delta t$) for a depth of 27 m (depth of large observed displacements). The vertical deviation is defined as the increment in horizontal displacement $\Delta\delta_h$ divided by the distance between the measured points Δz, that is $\theta_v = \Delta\delta_h/\Delta z$. The evolution of θ_v and V_δ with time and cumulative load (ton) reveals aspects of behavior that deserve close consideration. By increasing the elevation of the breakwater in the vicinity of the inclinometer location, both θ_v and V_d increase considerably as comprehensively reported in the literature for embankments constructed close to undrained conditions (e.g Ladd 1991; Almeida 1996; Brugger *et al.*, 1999; Almeida *et al.*, 2010). The onset of increasing displacements in August 2009 shown in the figure gives a threshold point in a plane of maximum shear strains at the depth associated to the potential failure surface (see Fig. 9). However, at a constant load, the consolidation process starts and produces a further increase in θ_v and a continuous reduction in V_d. Clearly vertical deviation reflects the displacement path produced by both undrained shear and consolidation and for this reason it cannot be used alone to define reference acceptable limits of performance in cases where load increments are superimposed to some consolidation (as often observed in practice).

Results from the variation of pore-pressure measurements with time are illustrated in Fig. 10. Recorded measurements show fluctuations of the order of 5 kPa, corresponding to tide and wave oscillations of about 1 m of water column. Within the clay layer, pore water pressures increased significantly during August and September 2009, a period that corresponds to breakwater elevation from -11 m to -5 m below average sea level. In the remaining time, there are periods of pore pressure increments (construction stages from -5 m to +5 m) followed by pressure decrease due to consolidation.

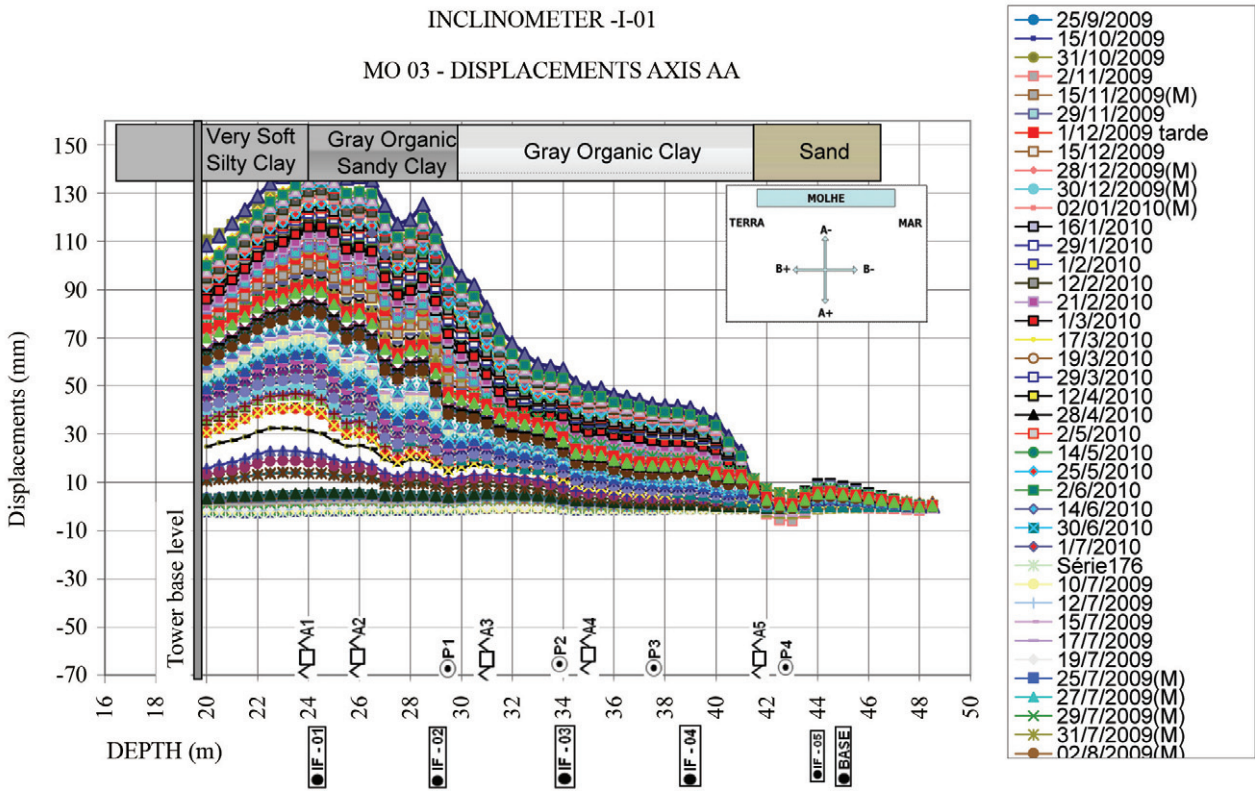

Figure 7 - Inclinometer data for toe embankment position MO03.

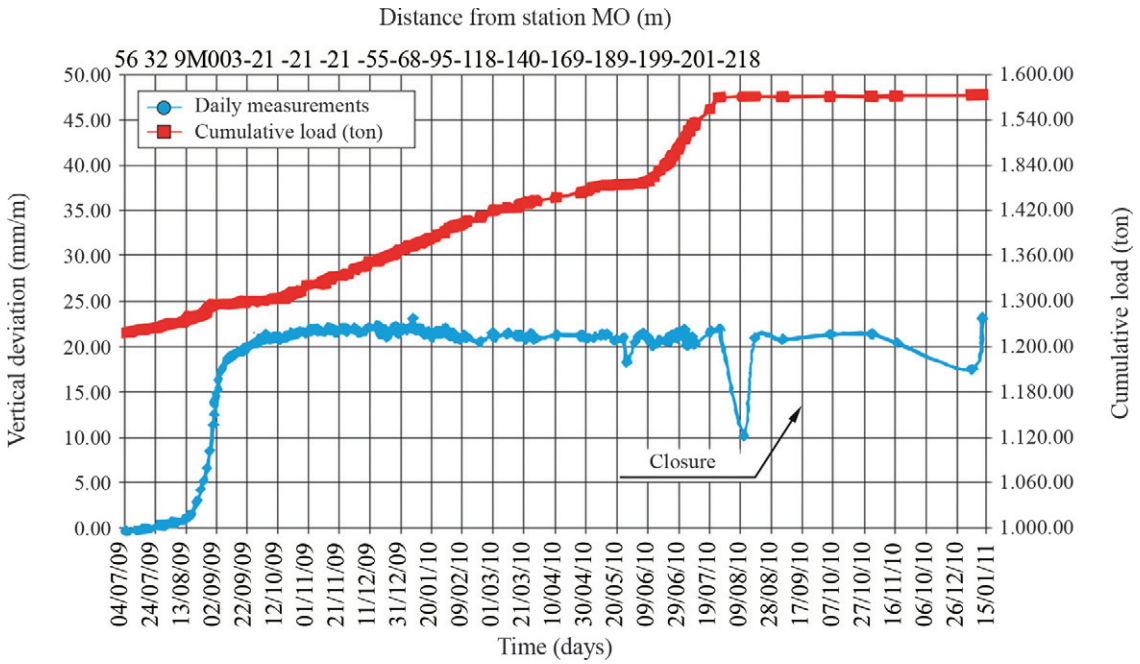

Figure 8 - Vertical deviation and embankment cumulative load plotted against time at a depth of 27 m.

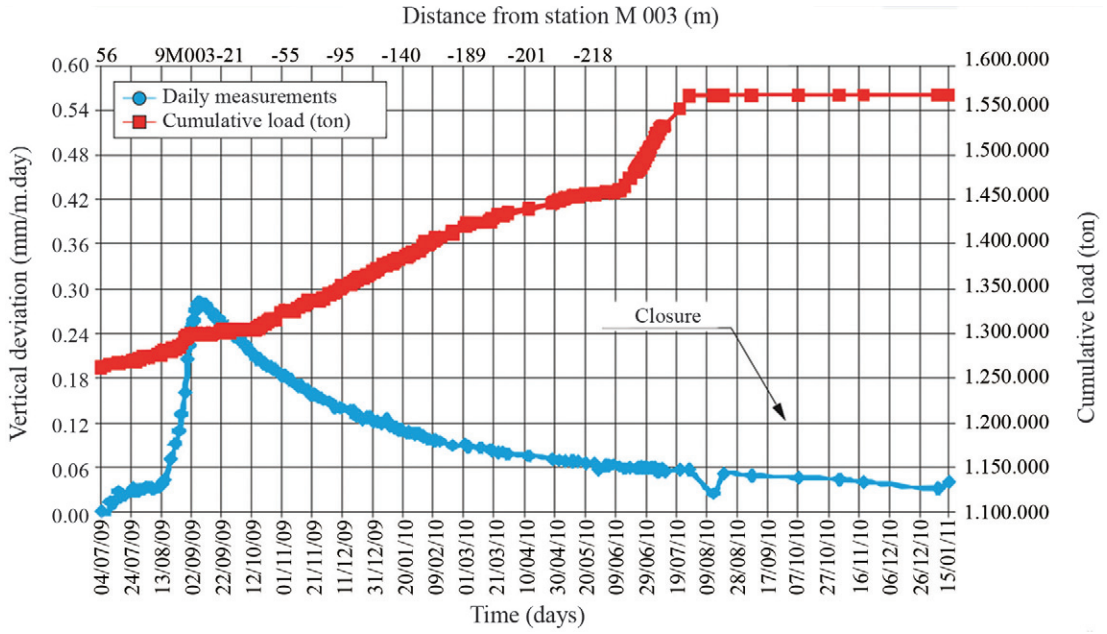

Figure 9 - Variation of vertical deviation and embankment cumulative load at a depth of 27 m.

Acceptable limits of behavior for stage construction close to undrained conditions were defined from results of numerical analyses of representative cross-sections (later summarized by Dienstmann, 2011). Limits conceived to increase rate of monitoring and prepared to implement contingency were defined from both experience (Almeida 1996; Brugger *et al.*, 1999; Almeida *et al.*, 2010) and numerical (Dienstmann, 2011) analyses: (a) vertical deviation θ greater than 15 mm/m.day and (b) variation of vertical deviation greater than 20 mm/m. Contingency actions planned to be triggered when monitoring values were outside acceptable limits comprised reducing construction rate, stopping construction and even modifying the layout of the designed cross-section. Whereas the two previous recommendations were implemented, the original design proved to be acceptable and there has been no need to reinforce the designed cross section throughout construction.

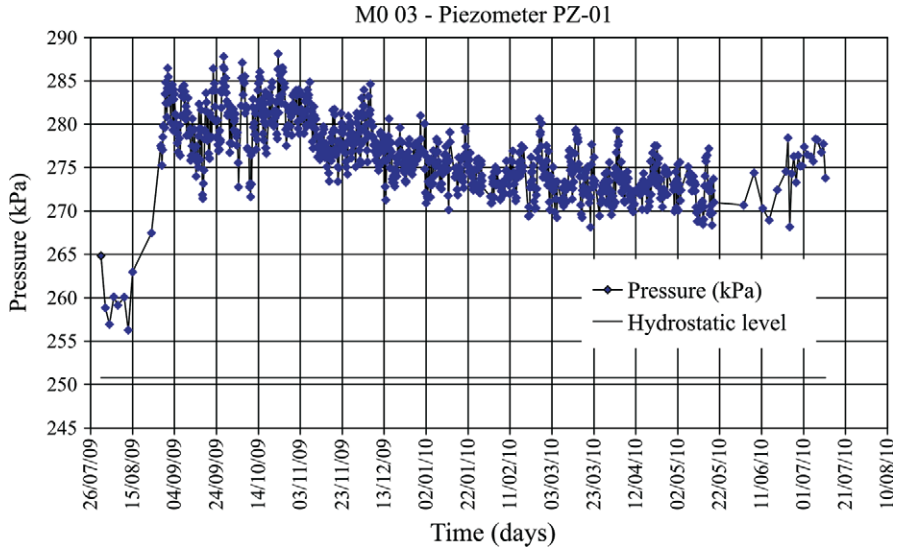

Figure 10 - Variation in pore water pressure with time.

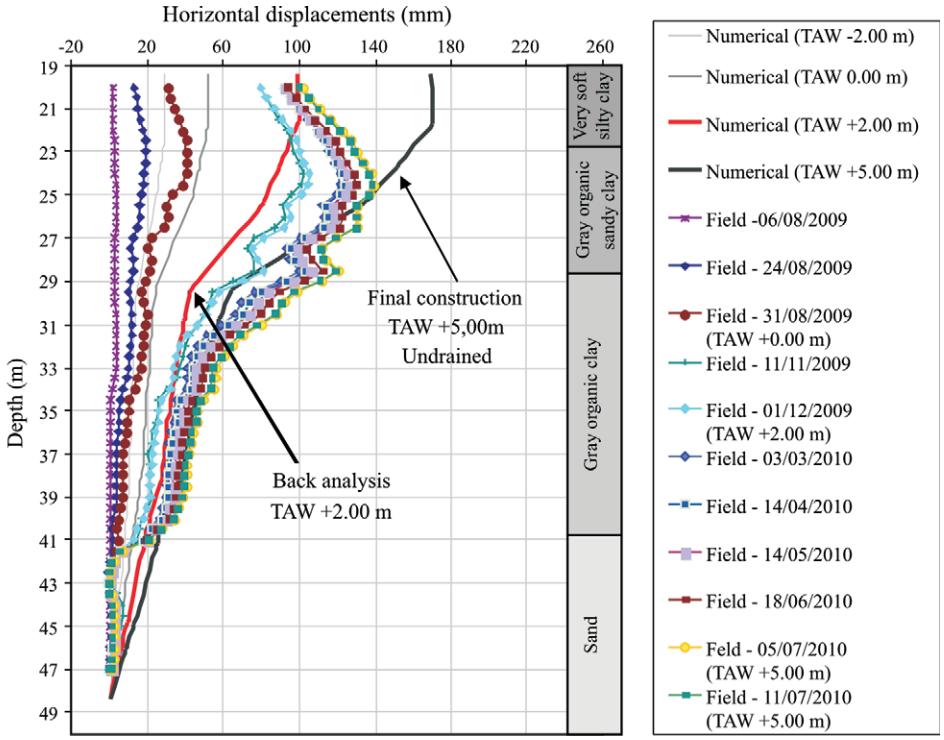

Figure 11 - Measured and predicted horizontal displacements.

Finally it is worth mentioning that last readings showed that the rates of displacements have decreased substantially and hence the settlement monitoring program was terminated in May 2012. Minor secondary settlements will occur in the future.

4. Numerical Simulation

Up to this point, the implementation of the observational method has been discussed on more empirical bases and previous experience of the authors, i.e. selection of quantities to be observed during construction and comparisons to their anticipated values on the basis of the working hypothesis. However, in parallel to the described procedure as postulated by Peck (1969), an interactive analysis (this time with numerical tools) conceived to support the decision-making process was performed to evaluate the influence of partial drainage paths in the measured behavior. The numerical simulation was carried out in plane-strain

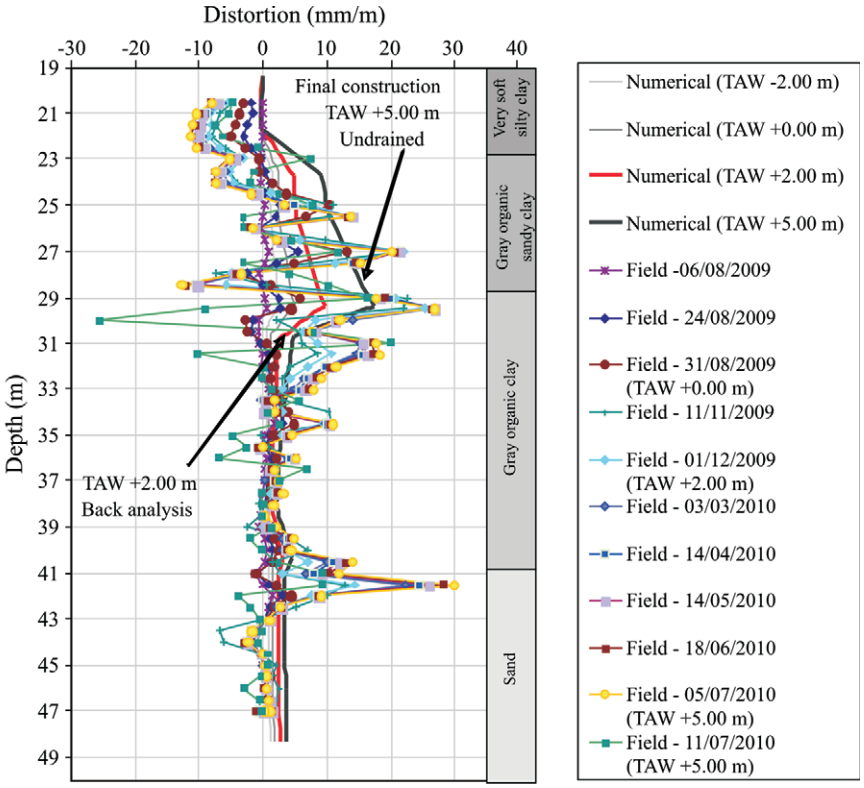

Figure 12 - Measured and predicted vertical deviation with depth.

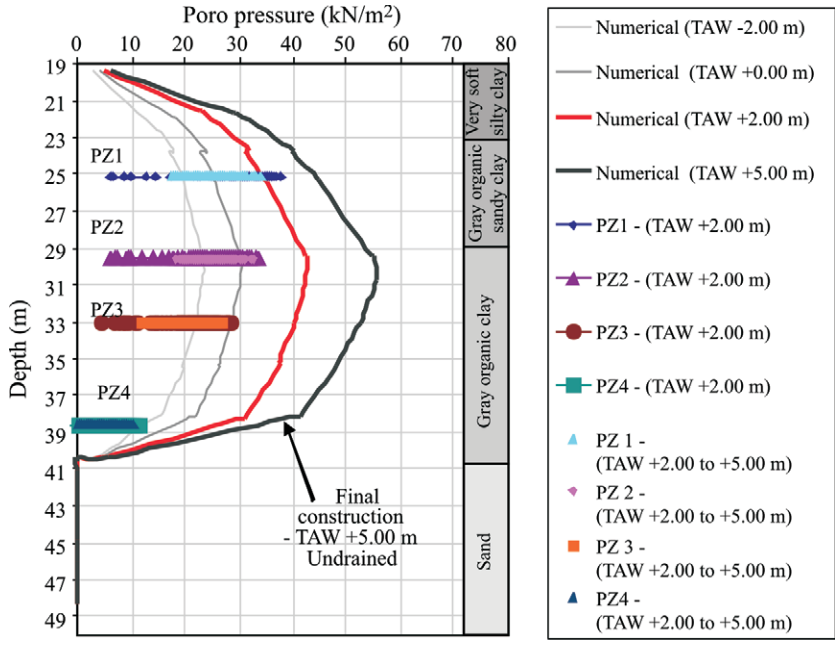

Figure 13 - Measured and predicted pore pressure with depth.

conditions using the modified Cam-Clay model, and the Biot theory for consolidation. After a throughout calibration of the program to local conditions (Dienstmann, 2011), displacements and excess pore water pressure dissipation during and after construction were predicted.

Finite element calculations enabled the back analysis of available measured data recorded from previous construction stages to be performed before predicting future embankment response. Numerical analysis becomes an interactive curve fitting process of displacement and pore

pressure *versus* time data, designed to refine the constitutive parameters on the basis of information generated in the interactive analysis cycle. Once the set of design parameters and boundary conditions are refined, a subsequent analysis is performed and used to guide the next stage of construction and final stability checks.

Figure 11 shows a plot of the computed horizontal displacements (elevation up to +2.0 m and to +5.0 m), using the finite element solution, along with the experimental data. The first analysis (or back analysis) at TAW +2.00 m was made as a prior evaluation of model and drained conditions, showing qualitative agreement with the experimental data, displaying a physical variation of lateral movements with depth that coincides with field measurements (maximum displacement around 100 mm). Since predicted displacements show promising overall agreement with experiment data, the analysis was extrapolated to predicting the behavior of the breakwater for elevation +5.0 m. Results presented in the same figure show field measurements on the final construction stage (TAW +5.00 m): maximum displacements at the seabed coincide with measured values (of the order of 140 mm) at the depth of about 25 m.

Similarly variations of vertical deviation and pore pressures with depth are presented in Figs. 12 and13, respectively. Two construction phases are illustrated: back analysis at +2.00 TAW and final construction at +5.00 TAW. Although both vertical deviation and pore pressures show a general good agreement with the field performance, a close inspection of the data reveals that vertical deviations are underpredicted and pore pressures overpredicted.

The numerical work was particular useful in demonstrating that there were no signs of failure in any of the construction stages. Additional work was essential to separate out the effects of drained and undrained loading on predicted and observed measurements of displacements. Consider the example illustrated in Fig. 14, in which vertical deviation is plotted against the rate of vertical deviation for measurements recorded at Station MO03 at the depth of 29.40 m. Numerical predictions for undrained loading up to failure are confronted to undrained loading followed by consolidation of the breakwater at an elevation of +5 m (predictions that correspond to observed field performance). In both cases the vertical deviation increases continuously to fairly high values of the order of 5% irrespectively to the drained path indicating that measures of vertical deviation alone cannot be adopted as risk analysis criterion. On the other hand, the rate of vertical deviation seems to be a good predictor of instability given the fact that it increases considerably during undrained loading and reduces during consolidation. The combined analysis of vertical deviation and rate of vertical deviation gives the best approach to risk assessment irrespectively to the need of cross correlating displacements to pore pressure measurements to depict signs of drainage.

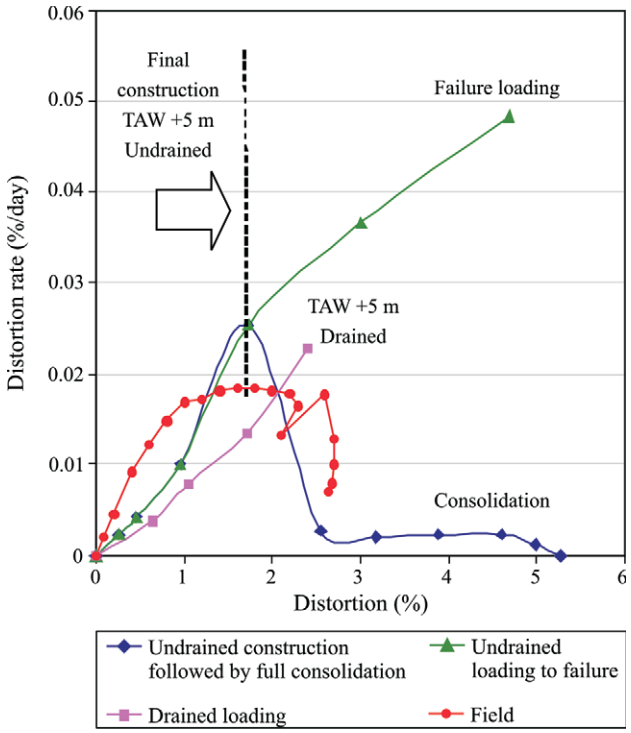

Figure 14 - Vertical deviation versus rate of vertical deviation at 29.38 m depth (Station MO03).

Finally is it worth emphasizing that a computational *risk assessment* approach *for breakwaters cannot rely on pre-established* reference acceptable limits of performance; acceptable limits have to be *adjusted* according to soil and loading conditions as well as the geometric representation of the structure to be constructed.

5. Discussion

From the years since Terzaghi and Peck first conceived and started working with the Observational Method to today, its use has been generalized, discussed in conferences and seminars, criticized, new names have been used to address it. But, has anything essential really changed from the early period?

It is the authors' opinion that important contribution for using the OM in an efficient and accurate way, in order to respond to todays' societies demands, came with the technological developments introduced in monitoring the behavior of structures and earthworks, as well as the tremendous potential of analysis brought by numerical simulations. But, the essence behind the driving force to use the OM as a decision tool comes from Society, investigating, questioning and judging the performance of infrastructure works, in their interface with people and their products.

In all predictions of future behavior, even when based in back-analysis of data and parameters derived from previous stages of construction, the engineer is faced with an inevitable scatter of results derived from the best methods

available. This scatter may be minimized when a well planned site investigation, in tune with the geological-geomechanical model of the site, supports the elaboration of a sound and solid physical model of anticipated behaviors, which in turn helps choosing mathematical models to better represent them.

Determinism, and deterministically derived prediction behavior values, cannot be seen as a realistic tool when the variability of geomechanical and hydraulic parameters, the representativeness of constitutive models and of the numerical simulations are incorporated in the decision making process. Use of mathematical models that well represent the anticipated physical model transmits reliability to the risks management process, intrinsically linked with the confirmation that the observed behaviour of the structure is within the anticipated range.

Table 2 shows a comparison between the general principles of application of the OM and the specific ways in which the method has been applied at the Rio Grande breakwater project. By doing so it is possible to summarize the key issues raised throughout the paper, highlighting the concepts that are deeply involved with the OM: that of robust design, safety case and contract flexibility. The British Institute of Structural Eng. (IStructE, 1990) and the Health and Safety Executive (HSE, 1996) both discuss the need of robustness in structures, which Burland (2006, 2008) defines as "the ability of absorbing damage without collapse", which is broader than the concept of ductility, "the ability

Table 2 - Comparison of general conditions for application of the OM with the specificities of the Rio Grande Breakwater.

Conditions for application of the observational method		Application of the method in the rio grande breakwaters
Investigation	Sufficient geotechnical investigation must be available.	Boreholes, field tests (SPT, vane, undisturbed samples, piezocone) and laboratory tests. A horizontal continuous soft soil layer has been identified as the main object of attention.
Robustness	The system constituted by the structure and the terrain must be robust, meaning that it shall not be liable to an abrupt and unpredictable change from a stable to an unstable condition.	Soft soil is not highly sensitive and is in a normally consolidated condition during the most critical phase of construction. Therefore, ductile behavior.
Risk	Possible malfunction mechanisms must be identified and understood.	Identified risks: foundation shear failure during construction and excessive settlement after completion. Risk of acceleration and failure due to terciary creep considered low because of low sensitivity of clay and of precedents in the Rio Grande area.
Monitoring	Instrumentation must cover all identified forms of risk materialization.	Horizontal displacements (inclinometers), vertical displacements in various depths (magnetometers) and pore pressures (piezometers) have been used.
Stages	Stage construction or velocity of construction must be smaller than the time required to interpret the monitoring data and to implement changes if necessary.	Rio Grande breakwaters constructed in four stages (-10 m, -5 m, +2 m and +5 m). In each stage, the increase of loading was gradual and could be interrupted.
Criteria	Criteria and procedures to confirm that the behavior is inside the anticipated range must be defined.	As far as the shear failure risk was concerned, the evolution of horizontal displacements and distortions based on limits from previous experience was the first criterion. Finite element analyses with parameters adjusted from one stage to the next where carried out in parallel. The long range settlements have been estimated from settlement plates installed in the top of the breakwaters.
Changes	Design must allow for changes in velocity of loading, intensity of load or construction procedures.	Loading could be stoped (as, in fact, happened once) and the design could be modified (wich was not necessary)
Agility	Well defined decision hierarchy and management conditions to rapidly impose the changes considered necessary.	Direct contact between Consultant and Contractor with the proactive participation of the Owner allowed quick enforcement of decisions.
Flexibility	Contracts must be flexible in order to accommodate eventual changes in the construction period, loads or procedures.	Eventual interruptions in loading have been anticipated (and concretized in one occasion). If there was the need to change the design (which did not happened) contractual terms between the Contractor and the Owner would have to be renegotiated.

of undergo inelastic deformations without significant loss of strength". Robustness is usually also provided by identifying the hazards and risks and by checking that the design proposed is able to adequately withstand them.

Nicholson *et al.* (1999) postulate that "risk control measures must be an explicit part of the safety management system required by regulations", like the UK Construction Design and Management Regulations established by Health and Safety Commission (1994), and in this context define a safety case as "a systematic and, where possible, quantified demonstration that an installation or system meets specific safety criteria".

Sound judgment is required, and the careful analysis and interpretation of tendencies of behavior becomes a powerful tool. A previously defined hierarchy of decision taking at the jobsite is required to allow the rapid implementation of any action as shown by the monitoring program and its interpretation. For these reasons contracts must be flexible to accommodate the necessary changes in construction geometry, time and procedures.

6. Conclusions

A review of the early works on Observational Design as revealed through the extraordinary contributions from Terzaghi, Peck, Lambe, de Mello and others demonstrated the strength of the pioneering ideas embraced by conceptual Soil Mechanics, as well as their links to geotechnical engineering practice. These early concepts do not contrast with the outcome of some modern soil mechanics research, and yet the proposed framework of OM has not been entirely incorporated to current ground engineering projects. Consequences are that optimized cost-benefit design is not always achieved and identification of the hazards and risks are not entirely accounted for, especially in large structures subjected to adverse geo-environmental conditions.

The Rio Grande breakwater design and construction offered a unique opportunity for a critical appraisal of the OM approach where a complete application of the method was necessary given the extreme adverse geotechnical and hidrogeological conditions of the site. It comprised a comprehensive soil investigation, the setting of working hypothesis of soil behaviour described by a synthetic physical and mathematical model and a monitoring program devised to document the breakwater performance. Results have been confronted to acceptable limits of behaviour which triggered pre-established contingency actions conceived to ensure the successful completion of the work under the principles of the Observational Method.

Acknowledgments

The authors would like to express their gratitude to the Consortium *CBPO, Carioca, Pedrasul e Ivaí* for permission to use the test data and collaboration throughout the work. Thanks are extended to Mr. Marcos Pitanguy , Manager Director of the Project, and Camila Rabassa and Gracieli Dienstmann for their research contributions as MSc Students at Federal University of Rio Grande do Sul.

References

Almeida, M.S.S. (1996) Aterros Sobre Solos Moles: Da Concepção à Avaliação do Desempenho. UFRJ, Rio de Janeiro, 1.215 pp .

Almeida, M.S.S.; Marques, M.E.S. & Lima, B.T. (2010) Overview of Brazilian construction practice over soft soils. Conf. New Techniques on Soft Soils, v. 1, p. 205-225.

Brugger, P.J.; Almeida, M.S.S.; Sandroni, S.S. & Lacerda, W.A. (1999) Numerical analysis of the breakwater construction of Sergipe Harbour. Canadian Geotechnical Journal, v. 35:5, p. 1018-1031.

Burland, J.B. (2006) Interaction between structural and geotechnical engineers. Annual Joint Meeting IStructE / ICE, London, v. 84:8, p 29-37.

Burland, J.B. (2008) Reflections on Victor de Mello, Friend, Engineer and Philosopher. Soils and Rocks, v. 31:3, p. 111-123.

Clayton, C.R.I. (2001) Managing Geotechnical Risk. DETR Partners in Technology Programme for the Institution of Civil Engineers. ICE, London, 80 pp.

Dienstmann, G. (2011) Interactive Design of the Rio Grande Breakwater. MSc Thesis, Federal University of Rio Grande do Sul, 179 pp.

Eurocode 7 (1997) British Standard EN 1997-1:2004 Geotechnical Design - Part 1 - General Rules. 174 pp.

De Mello, V.F.B. (1977) Reflections on design decisions of practical significance to embankment dams. Seventeenth Rankine Lecture, Geotechnique, v. 27:3, p. 279-355.

GeoTechNet Project GTC2-2000-33033 (2000) WP3: Innovation Design Tools in Geotechnics – Observational Method and Finite Element Method. Noel Huybrechts, editor, BBRI, 31 pp.

Hanna, T.H. (1985) Field Instrumentation in Geotechnical Engineering. Trans. Tech., New York, 843 pp.

Health and Safety Commission (1994) Managing Construction for Health and Safety, Construction Design and Management Regulations. Approved Code of Practice. HSE Books, Suffolk, 106 pp.

ITIG (2006) A Code of Practice for Risk Management of Tunnel Works. International Tunnelling Insurance Group, London, 28 pp.

Ladd, C.C. (1991) Stability evaluation during staged constructions: The twenty-second Terzaghi lecture. Journal of Geotechnical Engineering, ASCE, v. 117:4, p. 540-615.

Lambe, T.W. (1973) Predictions in Soil Mechanics. Thirteenth Rankine Lecture, Geotechnique, v. 23:2, p. 149-202.

Negro, A.; Karlsrud, K.; Ervin, M.; Srihar, S. & Vorster, E. (2008) Prediction, Monitoring and Evaluation of Per-

formance of Geotechnical Structures. State of the Art Report, Proceedings of ICSMGE Cairo, Egypt, v. 4, p. 2930-3005.

Nicholson, D.; Tse, C.M. & Penny, C. (1999) The Observational method in Ground Engineering: Principles and Applications. CIRIA Report 185, London, 217 pp.

Patel, D.; Nicholson, D.; Huybrechts, N. & Maertens, J. (2007) The observational method in geotechnics. Proc. 14th European Conference on Soil Mechanics and Geotechnical Engineering, Madrid 2007, pp. 371-380.

Peck, R.B. (1969) The advantages and limitations of the observational method in applied soil mechanics. Ninth Rankine Lecture, Geotechnique, v. 19:2, p. 171-187.

Rabassa, C.M. (2010) Geotechnical Monitoring of the Rio Grande Breakwaterl. Msc Thesis, Federal University of Rio Grande do Sul, 125 pp.

Staversen, M. (2006) Uncertainty and Ground Conditions, a Risk Management Approach. Elsevier, Oxford, 305 pp.

Schnaid, F. (2009) In Situ Testing In Geomechanics - The Main Tests. Taylor & Francis, London, 352 pp.

Terzaghi, K. (1961) Past and future of applied soil mechanics. Journal of the Boston Society of Civil Engineers, Contributions to Soil Mechanics, April 1961, pp. 400-429.

Terzaghi, K. & Peck, R.B. (1948) Soil Mechanics in Engineering Practice. Wiley & Sons, New York, 729 pp.

Influence of Exposure Conditions on the Values of Strength and Absorption in the Soil Stabilized with Lime and Rice Husk Ash

M.A.M. Alcantara, L.L. Fernandes, J.A. Lollo, D.C. Lima

Abstract. The article presents a study on the influence of exposure conditions on strength and absorption in soil stabilized with lime and rice husk ash. A soil classified as A-4 and CL, known as Red-Yellow Podzol, a hydrated lime and a crystal-type burnt rice husk ashes were used throughout the study. The laboratory testing program encompassed compaction of specimens of soil and its mixtures with lime content of 8% enriched with ash contents of 5% and 10% of the soil dry weight in the Normal Proctor Energy. The specimens were moist-cured for 28 days and then subjected to different exposure conditions, including curing in kiln oven, fully exposed and immersed in water. After curing the specimens were subjected to compressive strength tests with and without previous 24 h immersion in water, and also to absorption tests. Results showed the advantages of using ash as an auxiliary additive in soil-lime mixtures to promote mechanical strength increase and its long-term maintenance, as well as reducing the influence of saturation on compressive strength. Water immersion promoted the best mechanical strength increase, and water absorption increased with the increasing percentage of ash and with the curing time of the mixtures.

Keywords: stabilized soil, soil-lime, soli-lime-ash, mechanical strength, water absorption, soil mixtures cure.

1. Introduction

Of the stabilization mechanisms in the soil-lime mixtures, the pozzolanic reactions stand out among the solubilized mineral elements of soil and lime,which normally result in increased soil mechanical strength. According to Alcântara (1995), the addition of pozzolans can improve the stabilization effectiveness of soils with lime. Sharma *et al.* (2012) present chaos were the UCS value increased to 105 kPa and the CBR value increased to 5,7% by addition of 20% ash and 8,5% of lime. Still according Saeid *et al.* (2012) the additions could improve the mechanical properties of soils such as strength, swelling, plasticity index and compressibility; and, the obtained results indicated that for a progressing in soil properties the combination of lime and ash might be more effective than use of only lime or ash.

Among these there is rice husk ash, which according to chemical and mineral analysis, present a high silica content as mineral element after firing, which may be in amorphous or crystalline forms. The pozzolanic activity of rice husk ash can be seen in Cincotto & Kaupatez (1984), Barbosa (2006), Silva (2009) and Alcântara *et al.* (2010). Within this context, experiments were conducted using rice husk ash as an additive for soil stabilization, together with lime. According to Alcântara *et al.* (2010), the addition of 5% and 10% of crystalline rice husk ash to a A-4 soil (Red-Yellow Argisol), stabilized with 8% hydrated lime and compacted in the normal Proctor test energy, produced compressive strength gains of 16.6% and 57%, respectively, at 90 days of curing.

Thus, with the aforementioned technological aspects, the importance of this type of materials for engineering solutions is taken into account, with the durability aspect comprising an important aspect for the reliability of such materials. Alcântara *et al.* (2011) report results of a study that produced soil-lime-ash bricks using crystalline rice husk in a hand press, compressed to approximately 95% of maximum dry specific weight as determined by Alcântara *et al.* (2010), according to NBR 10832 (ABNT, 1989). This study obtained higher mechanical strength values of 3.6 MPa and 3.4 MPa, for 90 days of curing in a humid chamber and in a kiln oven, respectively, because the minimum required by NBR 8491 (ABNT, 1984a), and NBR 8492 (ABNT, 1984b) is of 2 MPa. However, these authors reported that the mechanical strength values of the bricks experienced a gradual decrease when considering curing times of 28 to 90 days, observing a decrease in strength of about 13% and 25% for humid chamber curing and kiln oven curing, respectively. On the other hand, the absorption values increased by 4% for humid chamber curing and 1% for kiln oven curing. In experiments conducted by Akasaki & Silva (2001) and Milani (2005), it was reported that when

M.A.M. Alcantara, PhD, Faculdade de Engenharia de Ilha Solteira, Universidade Estadual Paulista "Júlio de Mesquita Filho", Ilha Solteira, SP, Brazil. e-mail: alcantar@dec.feis.unesp.br
L.L. Fernandes, Civil Engineer, Faculdade de Engenharia de Ilha Solteira, Universidade Estadual Paulista "Júlio de Mesquita Filho", Ilha Solteira, SP, Brazil.
J.A. Lollo, PhD, Faculdade de Engenharia de Ilha Solteira, Universidade Estadual Paulista "Júlio de Mesquita Filho", Ilha Solteira, SP, Brazil.
D.C. Lima, PhD, Universidade Federal de Viçosa, Viçosa, MG, Brazil.
Submitted on November 9, 2011; Final Acceptance on July 31, 2013; Discussion open until December 31, 2013.

using rice husk soil-cement-ash, and with the same degree of compaction, there was a mechanical strength decrease and increased absorption in stressed conditions, with the lowest degree of compression as the cause for the increased water absorption.

The ensuing actions of changing exposure conditions, resulting in different absorption and drying and expansion and contraction cycles, due to temperature variations throughout the day, such as weathering agents, which influence soil durability stabilized with lime, and which can be influenced by the degree of compression are discussed in Alcântara *et al.* (1996). However, Alcântara *et al.* (2011) draw attention to the presence of ash in the absorption processes and discuss the rupture test procedure, when the material is immersed prior to the test, and which may interfere in the mechanical strength values due to water absorption resulting from its hygroscopic and porosity nature and also its internal permeability condition, which can be another microcracking indicator.

2. Materials and Methods

This study verifies the durability of engineering parameters of specimens of soil and soil-lime-rice husk ash mixtures compacted in the mini-Proctor test. The work of Alcântara *et al.* (2010) was used as a basis in the production of the specimens for the soil and mixes, using optimum compaction parameters determined in the compaction energy of the standard Proctor test, according to NBR 7182 (ABNT, 1986), using a lime content of 8% and calcined and ground crystalline rice husk ash contents of 5% and 10%, in relation to the dry soil weight.

The grinding and characterization of rice husk ash were performed in the Civil Engineering CESP Laboratory of Ilha Solteira, using the equipment of the Civil Engineering Laboratory of Ilha Solteira - UNESP for the production, curing, mechanical resistance and absorption tests of the specimens of soil and mixtures.

In order to check the durability of the soil-lime-ash mixture with different exposure conditions, samples with ash contents of 5% and 10% were prepared based on the results by Alcântara *et al.* (2010). Besides the soil-lime-ash sample specimens, soil samples and their mixture with 8% of hydrated lime were prepared, and these results were used as the comparative performance basis for the soil-lime-ash mixtures.

2.1. Materials

The crystalline rice husk ash used in the tests was from the region of Pelotas, Rio Grande do Sul, Brazil, which was ground in a ball mill for 30 minutes, similar to that used for cement production in the Civil Engineering CESP Laboratory of Ilha Solteira. Figures 1 and 2 show the aspect of the ground ash, ready to use and sieved, and Table 1 shows the data of the physical and chemical characteristics of this material.

In the experiment, the water supply of the city of Ilha Solteira, São Paulo, Brazil was used, and in the mixtures CH-III-type hydrated lime was used, with physical, chemi-

Table 1 - Physico-chemical characteristics of crystalline rice husk ash.

Sample		Crystalline Rice Husk Ash	NBR-12653 (Pozzolanic material)	
			Min	Max
Apparent density (kN/m^3)		6.0	-	-
Absolute density (kN/m^3)		21.4	-	-
Grain diameter (micra)		20.13	-	-
Moisture of sample (%)		1.08	-	3.0
Chemical analysis (%)	Fire loss	7.95	-	6.0
	SiO_2		-	-
	Fe_2O_3		-	-
	Al_2O_3		-	-
	CaO		-	-
	MgO		-	-
	SO_3		-	5.0
	Al_2O_3+Fe_2O_3		-	-
	SiO_2+Al_2O_3+Fe_2O_3		70.0	-
	Equiv. Alc. in Na_2O (disp.)		-	-
	Na_2O		-	-
	K_2O		-	-

Figure 1 - Ground rice husk ash.

Figure 2 - Sieved soil.

cal and mechanical properties that met the requirements of NBR 7175 (ABNT, 1984c). The soil used was classified as A-4, according to the Transportation Research Board Soil Classification System - TRB (DNIT, 2006), as CL, according to the Unified Soil Classification - USC (DNIT, 2006) and as Red-Yellow Argisol, according to the pedological classification (EMBRAPA, 2006). Figure 2 shows the aspect of the soil collected after sieving, Table 2 shows the test characterization results and geotechnical classifications of the soil (Alcântara, 1995) and Table 3 shows the results of the compression test performed on the soil and on the soil-lime (8%), soil-lime (8%)-ash (5%) and soil-lime (8%)-ash (10%) mixtures.

The results obtained in the compression tests clearly show the optimum moisture content increase and the maximum dry density decrease in the following order: natural soil, soil-lime, soil-lime-ash (5%) and soil-lime-ash (10%). The DNER-ME 228-94 standard was followed for the production of the specimens. All test specimens were first cured packed in plastic bags and placed in a moist chamber for 28 days, and for 1/3 of them the last curing was performed in a kiln oven, 1/3 were exposed to the external environment and 1/3 were cured by water immersion in the humid chamber.

Table 2 - Soil geotechnical characterization and geotechnical classification test results.

Parameters	Soil
Liquid limit (%)	26
Plasticity index (%)	10
Specific particle weight (kN/m^3)	27.4
Particle size:	
$\Phi < 0.005$ mm (%)	31
$0.005 \leq \Phi < 0.05$ mm (%)	12
$0.05 < \Phi \leq 0.48$ mm (%)	57
Soil classification:	
TRB	A-4
USC	CL

Table 3 - Residual mature soil compaction parameters: optimum moisture content ($W_{ót}$) and maximum dry weight (γ_{dmax}).

Materials	Wot (%)	γ_{max} (kN/m^3)
Soil	12.37	19.2
Soil + 8% lime	13.71	18.8
Soil + 8% lime + 5% ash	13.67	18.4
Soil + 8% lime + 10% ash	14.42	18.1

2.2. Methods

After collecting the soil sample in the borrow area, it was exposed to air near the Civil Engineering Laboratory of Ilha Solteira Engineering School - UNESP, to achieve hygroscopic equilibrium with the environment, after being sifted and stored in plastic bags.

To produce the four kind of test specimens, namely: soil (S), soil with 8% lime (S-8), soil with 8% lime and 5% rice husk ash (S-8-5) and soil with 8% lime and 10% ash (S-8-10), the following steps were followed: (i) separating the soil to produce the specimens of approximately 200 g; (ii) calculating the quantities of ash and lime to be added to the soil in relation to its hygroscopic equilibrium weight with the environment, and; (iii) mixing and homogenizing soil-lime and soil-lime-ash in a plastic bag to prevent loss of moisture to the environment. First, the soil was mixed with lime, then the ash was added, when applicable. These materials were homogenized, and then after mixing, the water was added with additional homogenization; and (iv) the amount of mixture to be placed in the mini-Proctor compression cylinder was calculated to mold the 50 mm (height) specimens, considering a permissible deviation of 1 mm, compression degree of 100% and permitted deviation of 1%. Any test specimen that did not meet the required compression degree or height characteristics was discarded.

Of the 72 test specimens produced with the required characteristics, 18 were prepared with soil without additions, 18 with soil mixture plus 8% lime, 18 with soil mixture with 8% lime and 5% ash, and 18 with soil mixture with 8% lime and 10% ash. After the test specimens were prepared, identified and packaged in plastic bags, they were kept in a moist chamber for 28 days, after which a part was cured under total exposure to air, another part in a kiln oven and another part cured under water immersion. Thus, after the first 28 days of curing, the test specimens were unpacked and submitted to the respective three curing modalities. Figures 3 and 4 illustrate the test specimens already packed and ready to be taken to the humid chamber and the test specimens stored in a moist chamber.

Figure 5 shows the test specimens that were kept under immersion and cured in a water tray.

The test specimens in the kiln oven were placed on a tray and wrapped in a plastic bag, at the Laboratory of the Civil Engineering School of Ilha Solteira, so as not to be exposed to the direct action of weathering, as illustrated in Fig. 6.

Figure 7 shows the test specimens under total exposure and placed on perforated trays to prevent water accumulation, and exposed to weathering action in the external courtyard of the Laboratory of the School of Civil Engineering of Ilha Solteira.

Next, after the exposure period under different curing conditions, the specimens underwent the unconfined compression and water absorption tests, according to NBR 8492 (ABNT, 1984). The compressive strength tests were carried out by immersion, as well as without immersion, in water for 24 h prior to failure; the procedure was performed on the test specimens of the mixtures subjected to all cure types, except those consisting only of soil, due to the great strength loss, which exhibited a high degree of cracks for the exposed curing, or breaking up for the immersed curing. Immersion was performed in a 24-h period, one day prior to the compressive strength test. This procedure was carried out to analyze the saturation influence on the strength of various types of mixing and curing modes.

Figure 3 - Test specimens already packed, ready to go to a moist chamber.

Figure 4 - Test specimens stored in a moist chamber.

Figure 5 - Test specimens immersed cured.

Figure 6 - Test specimens cured in a kiln oven.

Figure 7 - Fully exposed cured test specimens.

The water absorption tests were performed on all test specimens, except for those constituted only of soil due to the aforementioned reasons. The purpose of these tests was to relate the absorption increase to the higher internal cracking, causing a compressive strength drop in the test specimens. The absorption tests were conducted after the immersion of the specimens for a 24 h period in order to obtain the wet mass and then oven dried at 105 °C until constant weight to determine dry weight. The percentage difference between the dry and saturated masses corresponded to the total capacity value of water absorption, calculated on a dry basis.

3. Results

For the soil without additives, due to their damage effects, it was not possible to present the compressive strength and water absorption results of the soil specimens subjected to the immersed curing, the exposed curing and after water immersion for 24 h. Figure 8 shows the broken soil specimens.

Figure 9 illustrates the fully exposed cured test specimens with cracks so intense they could not undergo simple compressive strength tests.

For the mixtures with additives, the test specimens showed no curing problems, which were tested normally, measuring the water absorption and compressive strength without previous immersion and after immersion for 24 h before failure. Tables 4 to 6 show the mean strength of the test specimens cured under the three exposure conditions and tested after 28, 60 and 90 days of exposure, as well as the standard deviation, which considered failure under the same curing conditions and age, with and without immersion for 24 h before failure.

Table 7 shows the absorption test results carried out for all conditions and curing times of the mixtures tested, with the mean absorption and standard deviation of the specimens.

Figure 8 - Soil test specimens after immersion.

Figure 9 - Soil test specimens cured under full exposure.

4. Discussions

As for the compressive strength values, the soil specimens without additives broke apart when subjected to wa-

Table 4 - Mean compressive strength (μ) and standard deviation (σ), after curing in kiln oven.

Curing strength in kiln oven (without 24 h immersion)							
Mixture	Cure time (days)	28		60		90	
		μ	σ	μ	σ	μ	σ
S-8	Mean compressive strength (kN/m^2)	1033.03	33.43	1852.48	46.29	1541.61	75.51
S-8-5		1048.33	33.93	2135.89	53.37	2665.45	119.64
S-8-10		1212.10	39.23	2168.25	54.18	2887.08	87.28
Curing strength in kiln oven (with 24 h immersion)							
Mixture	Cure time (days)	28		60		90	
		μ	σ	μ	σ	μ	σ
S-8	Mean compressive strength (kN/m^2)	563.88	118.66	935.55	80.41	873.77	87.28
S-8-5		549.17	89.24	1393.52	45.11	1564.16	78.45
S-8-10		775.71	31.38	1486.69	69.63	2041.74	56.88

Table 5 - Mean compressive strength and standard deviation (σ), after full exposure.

Fully exposed curing strength (without 24 h immersion)							
Mixture	Cure time (days)	28		60		90	
		μ	σ	μ	σ	μ	σ
S-8	Mean compressive strength (kN/m^2)	994.39	87.28	1524.93	96.11	1443.54	50.99
S-8-5		1341.55	127.49	1774.02	75.51	2185.90	70.61
S-8-10		1515.03	89.93	2333.00	47.07	2793.91	109.83
Fully exposed curing strength (with 24 h immersion)							
Mixture	Cure time (days)	28		60		90	
		μ	σ	μ	σ	μ	σ
S-8	Mean compressive strength (kN/m^2)	383.44	75.51	887.50	188.29	742.36	43.15
S-8-5		394.23	614.99	1323.90	191.23	1608.29	81.40
S-8-10		672.74	183.38	1296.44	205.94	1609.27	94.14

Table 6 - Mean compressive strength and standard deviation (σ), after water immersion cure.

Curing strength with water immersion (without 24 h immersion)							
Mixture	Cure time (days)	28		60		90	
		μ	σ	μ	σ	μ	σ
S-8	Mean compressive strength (kN/m^2)	1187.59	80.41	1943.68	20.59	2011.34	102.97
S-8-5		1574.95	79.43	2570.32	63.74	3103.80	90.22
S-8-10		1788.73	64.72	2814.51	107.54	3433.31	52.96
Curing strength with water immersion (with 24 h immersion)							
Mixture	Cure time (days)	28		60		90	
		μ	σ	μ	σ	μ	σ
S-8	Mean compressive strength (kN/m^2)	726.67	96.11	954.19	86.30	1071.87	107.87
S-8-5		526.62	100.03	1426.87	49.03	1834.82	129.45
S-8-10		709.02	77.47	1840.71	120.62	2526.19	146.12

ter immersion and showed strong cracking when cured in the sun, to the point of ruling out the strength compression test. Therefore, the experimental protocols that had been proposed were not applied. However, this behavior was not observed for the specimens molded with the soil-lime and soil-lime-ash mixtures, probably because of the pozzolanic effect due to the presence of lime in the mixture. This is in agreement with Abiko (1984), which distinguishes the behavior of the soil with chemical additives for the soil without additives. The compressive strength test results show more clearly the effect of the presence of ash on the mixture, particularly for older ages, such as 60 and 90 days. The results in Tables 4 to 6 show the mechanical strength increase of the mixtures during the curing period for all the types of cure analyzed, except for the data obtained for the kiln curing conditions and the fully exposed cure conditions of the soil-lime mixture, for curing times of 60 and 90 days, which showed a slight strength decrease.

Figures 10, 11 and 12 illustrate the results presented in Tables 4 to 6, for all types of mixtures and curing conditions. The soil-lime mixture (8%) was considered as a reference composition. Thus, Table 8 presents the percentage relationship between the strength reached by the soil-lime samples (8%), rice-husk ashes (5%) and soil-lime (8%), rice-husk ash (10%) compared to the strength reached by the soil-lime mixture (8%).

For the lime-soil mixture, in all types of curing, the occurrence of a maximum strength peak was observed at 60 days of curing, which stands out for soil-lime-ash mixtures, where a continuous mechanical strength increase is observed with time and with the ash content incorporated. The results indicate, as an advantage, that the maximum point is for the older ages for the percentages of ash in the mix. The growth rates are, for practical purposes, the same for 8 and 10% of ash incorporated.

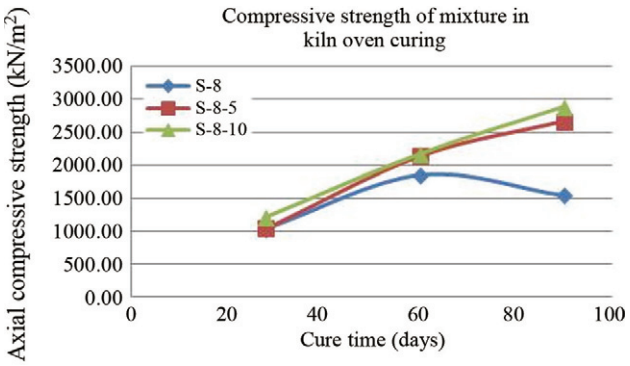

Figure 10 - Compressive strength of mixtures in kiln oven curing (kN/m^2).

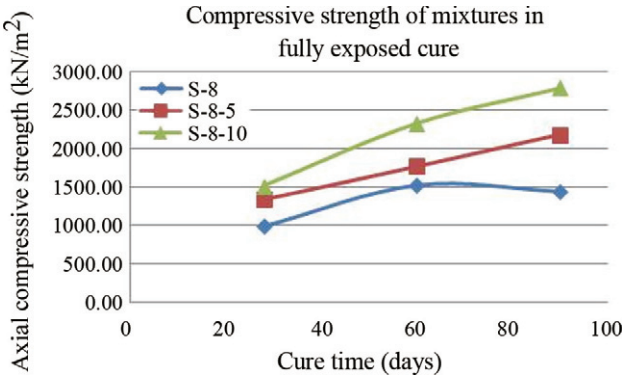

Figure 11 - Compressive strength of mixtures in fully exposed cure (kN/m^2).

The compressive strength values were approximately 50 to 70% lower than those shown in Alcântara *et al.* (2010), at 28, 60 and 90 days of cure, independent of the type of curing, considering that in the work of these authors, failure was for the specimens cured in a moist chamber with no water immersion. However, it was hoped that the results obtained in both works were not so dissimilar, and this fact could be related to the reactivity of lime, since even for the soil-lime mixture (8%), the decrease was also in the same order. However, comparing Figs. 10 to 12, it was observed that the types of mechanical strength curves generated were similar to those shown in Alcântara *et al.* (2010).

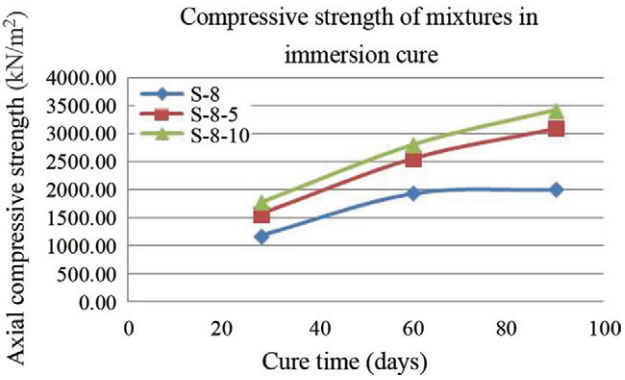

Figure 12 - Compressive strength of mixtures in immersion cure (kN/m^2).

Table 7 - Mean absorption and standard deviation of the specimens.

Curing absorption in a kiln oven (%)							
Mixture	Cure time (days)	28		60		90	
		μ	σ	μ	σ	μ	σ
S-8	Values (%)	20.33	0.44	15.01	0.53	15.21	0.38
S-8-5		22.09	0.35	18.13	0.28	16.82	0.22
S-8-10		21.03	0.4	18.44	0.35	17.22	0.5
Cure strength (with 24 h immersion)							
Mixture	Cure time (days)	28		60		90	
		μ	σ	μ	σ	μ	σ
S-8	Values (%)	20.9	0.32	15.44	0.52	14.72	0.78
S-8-5		20.64	0.6	17.43	0.55	15.68	0.32
S-8-10		23.43	0.33	18.89	0.31	16.82	0.43
Cure strength (with 24 h immersion)							
Mixture	Cure time (days)	28		60		90	
		μ	σ	μ	σ	μ	σ
S-8	Values (%)	20.74	0.56	16.01	0.8	15.59	0.55
S-8-5		22.05	0.34	17.97	0.2	16.75	0.46
S-8-10		21.57	0.54	18.51	0.63	17.93	0.51

Table 8 - Relative strength between soil-lime-ash (levels of 5% and 10% of ash) and soil-lime mixtures.

Relative strength for kiln oven curing				
Mixture	Cure time (days)	28	60	90
S-8-5	Values (%)	102.99	115.30	172.90
S-8-10		119.08	118.63	187.28
Relative strength for fully exposed curing				
Mixture	Cure time (days)	28	60	90
S-8-5	Values (%)	134.91	116.33	151.43
S-8-10		152.85	152.99	193.55
Relative strength for immersed curing				
Mixture	Cure time (days)	28	60	90
S-8-5	Values (%)	132.62	132.24	154.31
S-8-10		150.62	145.26	170.70

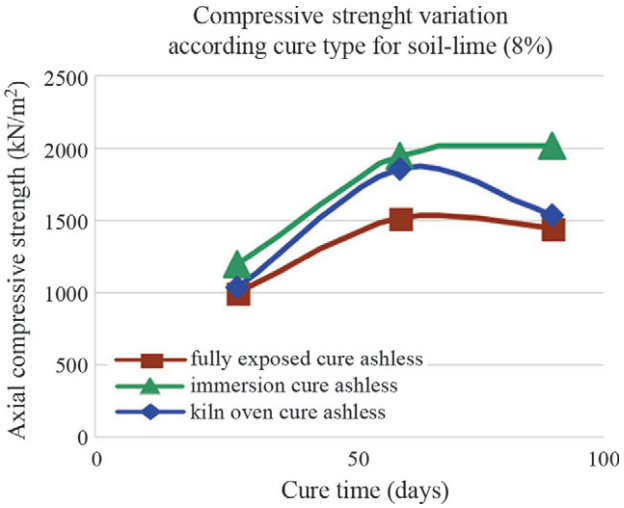

Figure 13 - Compressive Strength Variation according cure type for soil-lime (8%), (kN/m^2).

For a better visualization of the relationship between the type of cure and the mechanical strength variation, Figs. 13 to 15 show the mechanical strength variations in the mixtures used; soil-lime (8%), soil-lime (8%), ash (5%) and soil-lime (8%) ash (10%).

Figures 13 to 15 show more clearly the relationship between the type of exposure and mechanical strength of the specimens of the soil-lime-ash mixtures over time, confirming that the best curing condition was the one under water immersion, followed by curing in a kiln oven, and lastly the cure fully exposed to the elements. Table 9 shows the approximate angular coefficients for the curves that express the development of mechanical strength for the parts relating to the curing periods of 28 to 60 days and 60 to 90 days. These express the change rates for the strength values.

It can then be observed that for ages 28 to 60 days, there are higher values for the immersed and kiln oven cures, and lower values for fully exposed cures. For 60 to 90 days of cure, the values generally tend to be lower than for those of 28 to 60 days, and higher for immersed cure and for cases where the ash content is higher. As for the mixtures without ash, negative values can be seen in the angular

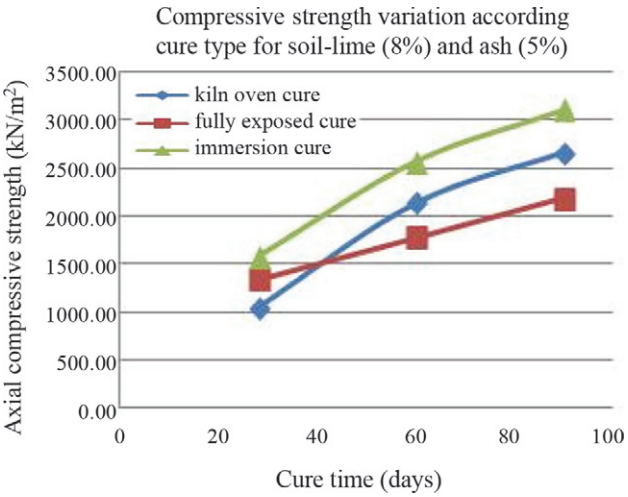

Figure 14 - Compressive Strength Variation according cure type for soil-lime (8%) and ash (5%), (kN/m^2).

coefficients, due to the decrease in strength with the curing time, and in the case of fully exposed cure and with ashes, there is an upwards displacement of the curve, increasing the ash content, indicating that there may be an improved

Table 9 - Approximate angular coefficients for the curves regarding mechanical strength gains in the various curing times and exposure conditions.

	Types of exposure conditions					
	Immersed cure		Kiln oven cure		Fully exposed cure	
	Curing periods (days)					
Mixtures	28-60	60-90	28-60	60-90	28-60	60-90
S-8	0.24	0.002	0.27	-0.11	0.17	-0.03
S-8-5	0.32	0.18	0.35	0.18	0.14	0.14
S-8-10	0.33	0.18	0.31	0.23	0.26	0.16

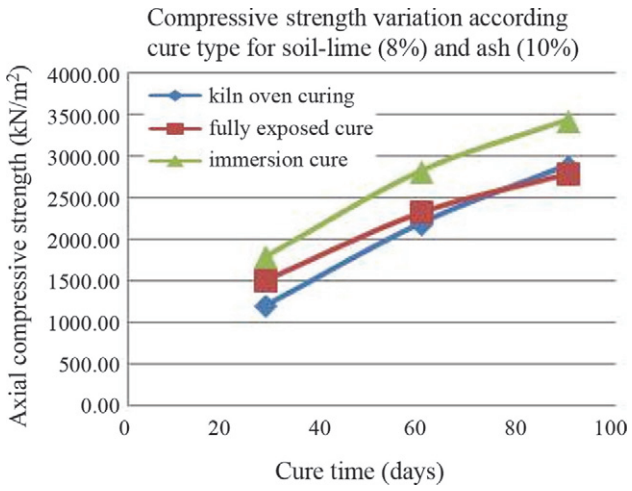

Figure 15 - Compressive Strength Variation according cure type for soil-lime (8%) and ash (10%), (kN/m^2).

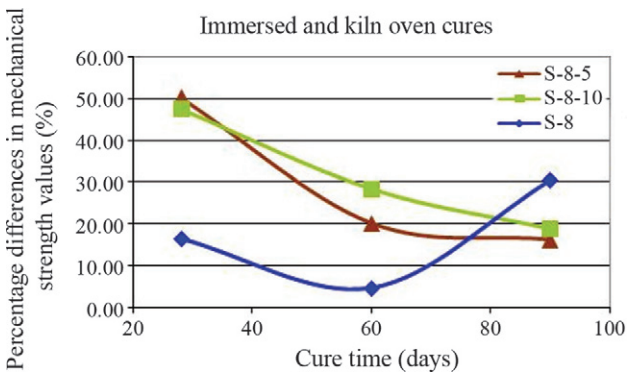

Figure 16 - Percentage differences of the mechanical strength values when compared to the immersed and kiln oven cures.

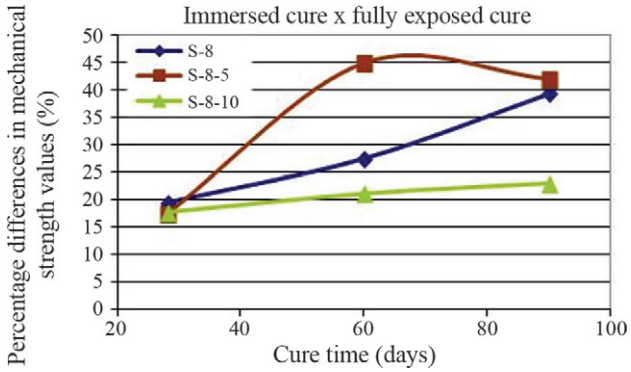

Figure 17 - Percentage differences of the mechanical strength values when compared to the immersed and fully exposed cures.

performance of the material due to the exposure conditions with the incorporation of ash.

Table 10 shows the differences in strength values, given in absolute values and percentages, when considering the types of immersion and kiln oven cures, and by immersion and fully exposed cures. For the first case, the absolute differences of values were enhanced by the presence of ash. Although the absolute differences show little change when the different curing ages are considered, in which case the percent values were always lower over time for the mixtures with ash since the base values increased, as seen in the data in Table 10 and Fig. 16. As for the mixture without ash, there is a return to the percentage increase at 90 days, due to the decreasing strength value of the ash mixture in a kiln oven. According to the data in Table 10 and Fig. 17, when comparing the immersed and fully exposed cures, the absolute differences and percentages increased, since the increase of the strength rates was higher for the immersed cures. Apparently the presence of ash may have greater efficacy in the immersed cure, and for the exposed cures, they are benefitted by the increasing ash content.

It is believed that the best curing performance is under immersion, when compared to the other modalities. This could be due to the fact that in this condition the specimens are protected from the effects of expansion and thermal contraction cycles and of absorption and drying, which may induce the microcracking of the material. The cure exposed to the contraction and shrinkage effects on the specimens of the mixtures were significantly higher, due to diurnal temperature variations and wetting and drying cycles promoted by

Table 10 - Values of the absolute and percentage differences for the mechanical strength increase compared to the immersed curing condition and kiln oven curing and fully exposed curing.

		Days of curing					
		28		60		90	
		Absolute	%	Absolute	%	Absolute	%
Immersed and kiln oven cures	S-8	1.73	16.7	0.93	4.9	4.79	30.47
	S-8-5	5.37	50.23	4.43	20.34	4.47	16.45
	S-8-10	5.88	47.57	6.38	28.47	5.57	18.92
Immersed cure and fully exposed cure	S-8	1.97	19.43	4.27	27.43	5.79	39.33
	S-8-5	2.38	17.40	8.12	44.89	9.36	41.00
	S-8-10	2.74	17.69	5.0	21.02	6.32	22.89

rain, followed by sunny days, which can negatively influence the development of mechanical strength. The immersed cure, as can be seen, is the only one that showed no increased negative resistance at 90 days of cure, for mixtures without ash. Another aspect is that this apparently favors the pozzolanic activity exerted by lime and ash and the active components in the soil, possibly due to the existence of an ever-present soil solution in the pores, which helps to facilitate ionic migration and the interaction of lime with the soil, with the formation of cementitious composites.

The saturation influence prior to compression strength can be seen with the data presented in Table 11, which shows the percentage relationship between the mechanical strength of the specimens of the mixtures obtained after saturation for 24 h prior to failure and those determined without saturation. The data in Table 11 shows that the saturation systematically reduced the mechanical strength of the specimens of the mixtures. Considering the cure times or the addition of ash, as well as the content incorporated, some changes can be observed in the values or in the stabilization tendencies. However there is an indication that the relative strength increases with the cure time and with the ash content incorporated. For the immersed and kiln oven cures, the values increase with cure time and with ash content at 60 days, as for the cure fully exposed to the elements, there are oscillations for the cure period and ash content. For the cure period of 28 days, the results oscillate for all types of cure.

As for the absorption values, the results in Table 12 indicate that these generally increase, particularly when ash was incorporated, and also increased with their content. This is in agreement with the hygroscopic nature that can be attributed to the ashes. However, the decrease or stabilization tendency with curing time can be observed, according to Figs. 18, 19 and 20, which illustrate the results shown in Table 7 for kiln oven, fully exposed and immersion cures, respectively. For 60 and 90 days of cure, it was seen that

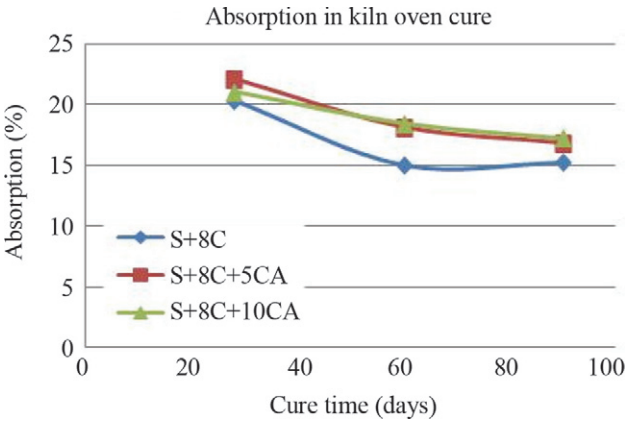

Figure 18 - Absorption in kiln oven cure (%).

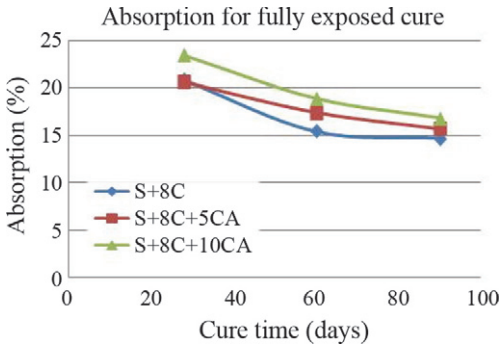

Figure 19 - Absorption for fully exposed cure (%).

Table 11 - Relative strength between rupture prior to immersion of 24 h and without immersion of 24 h.

Relative strength between rupture prior to immersion of 24 h and without immersion of 24 h. Moist-chamber cure				
Mixture	Cure time (days)	28	60	90
S-8	% of strength achieved at mean value	55.39	50.50	56.68
S-8-5		52.39	65.24	58.28
S-8-10		64.00	67.65	70.72
Relative strength between rupture prior to immersion of 24 h and fully exposed cure.				
Mixture	Cure time (days)	28	60	90
S-8	% of strength achieved at mean value	38.56	58.20	51.43
S-8-5		30.70	74.63	73.58
S-8-10		44.26	55.57	57.60
Relative strength between rupture prior to immersion of 24 h and without immersion of 24 h.				
Mixture	Cure time (days)	28	60	90
S-8	% of strength achieved at mean value	61.19	49.09	53.29
S-8-5		33.44	55.51	59.12
S-8-10		39.64	65.20	73.58

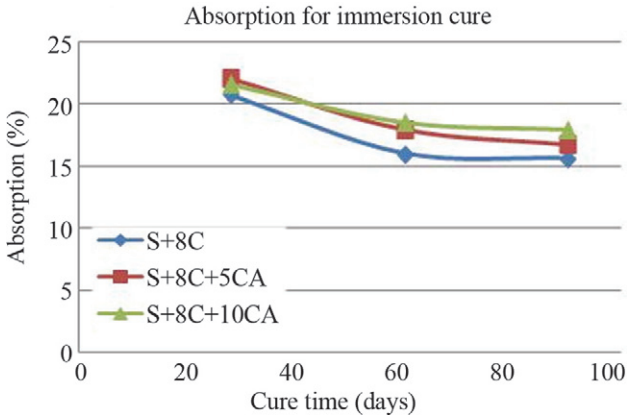

Figure 20 - Absorption for immersion cure (%).

Table 12 - Mean absorption values, in percentage, for mean relative strength values for all types and cure ages.

Kiln oven cure			
Days of cure	28	60	90
Absorption (%)	21.15	17.19	16.42
Relative strength (%)	57.26	61.13	62.03
Fully exposed cure			
Absorption (%)	21.36	17.25	15.74
Relative strength (%)	37.84	62.8	60.19
Immersed cure			
Absorption (%)	21.45	17.5	16.76
Relative strength (%)	44.76	56.6	62.00

while the mixes without the addition of ash appear to be stabilized with respect to absorption values, the ash mixes show they are still subject to more significant reduced values. The absorption behavior with time is different than that shown in Alcântara *et al.* (2011), because in that case the values increase over curing time and in this case the final values shown are lower, however the degree of compression was lower, about 95%, than the normal Proctor.

In order to associate the absorption values in the presence of voids due to microcracking, a correlation between the absorption values was set with the relative strength values, in percentage. The data in Table 12 shows that there is a tendency that the mean values of the relative resistance will grow inversely proportional to the mean absorption values. This appears to be consistent with the possibility for internal microcracking of the specimens and voids. On the other hand, according to the data in Table 13, it can be seen that even with the absorption increase due to the addition of ash, the relative strength values can increase, possibly due to the cementing achieved.

Figure 21 shows the variation of the mean relative strength value with the mean absorption value, decreasing, compared to the absorption values, independent of the cure time.

It was expected that there would be a significant difference between the absorption of the specimens cured in a

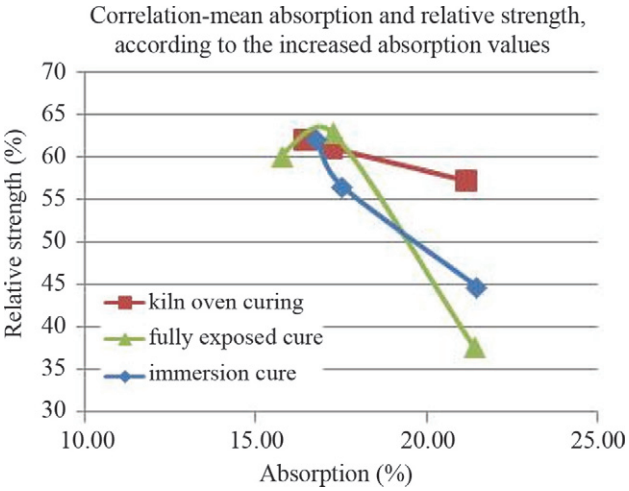

Figure 21 - Correlations between the mean absorption values and the relative strength, according to the increased absorption values.

Table 13 - Mean absorption values, in percentage, for mean relative strength values for the compositions, types and cure age.

Kiln oven cure									
Days	28			60			90		
Mixtures	S-8	S-8-5	S-8-10	S-8	S-8-5	S-8-10	S-8	S-8-5	S-8-10
Absorption (%)	20.33	22.09	21.03	15.01	18.13	18.44	15.21	16.82	17.22
Relative strength (%)	55.39	52.39	64.00	50.5	65.24	67.65	56.68	58.68	70.72
Fully exposed cure									
Absorption (%)	20	20.64	23.43	15.44	17.43	18.89	14.72	15.68	16.82
Relative strength (%)	38.56	30.7	44.26	58.2	74.63	55.57	51.43	73.58	57.6
Immersed cure									
Absorption (%)	20.74	22.05	21.57	16.01	17.97	18.51	15.59	16.76	17.93
Relative strength (%)	61.19	33.44	39.64	49.09	55.51	65.2	53.29	59.12	73.58

kiln oven and under immersion, compared to the fully exposed cured ones, due to the higher cracking produced in the latter case. However, what was seen in this case was a lower absorption. However, it showed a higher sensitivity to saturation with decreasing relative strength, as illustrated in Fig. 21, with the best cure performance, in this regard, achieved in a kiln oven.

5. Conclusions

Based on the results already presented and discussed in this work, in general it can be seen that the results show the advantages of using ash as an auxiliary additive in soil-lime mixtures, increasing value with the ash content, particularly promoting mechanical strength increase and maintaining this value in the long-term, including the reduced influence of the saturation conditions on the compressive strength. Curing by immersion was the one that best promoted mechanical strength increase. The water absorption values increased with the incorporation of increasing amounts of ash and curing time. Specifically conclusions are, as follows:

- The addition of rice husk ash produced a compressive strength increase, up to the 90-day curing period analyzed, in all cure forms studied;
- The immersion cure of the specimens of the mixes was the best out of those tested, improving their performance with the addition of ashes;
- Adding the ash to the soil-lime mixture influenced the water absorption, with a direct relationship between increasing the value of this parameter and increasing the ash content and the curing time of the mixtures, for all the cure conditions tested;
- Adding 10% of ash into the mixture was more effective to increase the mechanical strength than for the cases without addition and with the addition of 5% ash, for all the cure types analyzed; and
- The addition of ash contributed to improving the mechanical strength against saturation conditions, thereby minimizing performance loss, by increasing the ash content applied and with the increasing cure time and the ensuing development of cementation reactions.

References

Abiko, A.K. (1984) Tecnologias Apropriadas: Tijolos e Paredes Monolíticas de Solo-Cimento. Dissertação de Mestrado em Construção Civil, Escola Politécnica, Universidade de São Paulo, 115 pp.

Akasaki, J.L. & Silva, A.P. (2001) Estudo de composições do solo estabilizado com cal e resíduos agroindustriais. Proc. Congresso Brasileiro de Engenharia Agrícola, Foz do Iguaçu. SBEA, Foz do Iguaçu, CD-Rom.

Alcântara, M.A.M. (1995) Estabilização Química de Solos para Fins Rodoviários: Técnicas Disponíveis e Estudo de Caso Dirigido à Estabilização Solo-Cal de Três Solos de Ilha Solteira-SP. Tese de Mestrado, Universidade Federal de Viçosa, Viçosa, 91 pp.

Alcantara, M.A.M.; Silva, S.A.M.; Aguillar, D.F. & Segantini, A.A.S. (1996) Estabilização de solos com cal em construções rurais. Proc. Congresso Brasileiro de Engenharia Agrícola, 25, Bauru, CD-Rom.

Alcantara, M.A.M; Santos L.P. & Lima,. D.C. (2010) Evolution of mechanical properties of a tropical soil stabilized with lime and ash of rice rind. Soil and Rocks, v. 33:2, p. 97-102.

Alcantara, M.A.M.; Santos L.P.; Lima, D.C.; Akasaki, J.L. & Segantini, A.A.S. (2011) O uso de cinzas de casca de arroz como aditivo auxiliar na produção de tijolos de solo-cal. Revista Eletrônica de Engenharia Civil - REEC, v. 1:3, p. 1-11.

ABNT (1986) Solo - Ensaio de Compactação, NBR 7182. Rio de Janeiro, Brazil, 10 pp.

ABNT (1984a) Tijolo Maciço de Solo-Cimento - Especificação, NBR 8491. Rio de Janeiro, Brazil, 4 pp.

ABNT (1984b) Tijolo Maciço de Solo-Cimento - Determinação da Resistência À Compressão e da Absorção dÁgua - Método de Ensaio, NBR 8492. Rio de Janeiro, Brazil, 5 pp.

ABNT (1984c) Cal Hidratada para Argamassas, NBR 7175. Rio de Janeiro, Brazil, 3 pp.

ABNT (1989) Fabricação de Tijolo Maciço de Solo-Cimento com a Utilização de Prensa Manual. Procedimento, NBR 10832. Rio de Janeiro, Brazil, 3 pp.

Barbosa, M.B. (2006) Utilização de Resíduos de Cinzas de Casca de Arroz e Borrachas de Pneus em Concreto de Elevado Desempenho. Dissertação de Mestrado, Faculdade de Engenharia de Ilha Solteira, Ilha Solteira, 147 pp.

Cincotto, M.A. & Kaupatez, R.M.Z. (1984) Seleção de materiais quanto a atividade pozolânica, tecnologia de edificações, IPT/PINI. A Construção, v. 37:1905, p. 15-18.

DNIT (2006) Manual de Pavimentação, Publication IPR-719. Departamento Nacional de Infra-Estrutura de Transportes, DNIT, Rio de Janeiro, Brazil, 274 pp.

Embrapa (2006) Sistema Brasileiro de Classificação de Solos. 2ª edição. Embrapa, Rio de Janeiro, 306 pp.

Milani, A.P.S. (2005) Avaliação Físico-Mecânica de Tijolos de Solo-Cimento e de Solo-Cal Adicionados de Casca de Arroz. Dissertação de Mestrado, Universidade Estadual de Campinas, Campinas 131 pp.

Saeid, A; Amin, C. & Nikraz, H. (2012) A review on the lime and ash application in soil stabilization. International Journal of Biological, Ecological and Environmental Sciences, v. 1:3, p. 124-126.

Sharma, N.K.; Swain, S.K. & Sahoo, U.C. (2012) stabilization of a clayey soil with ash and lime: a micro level investigation. Geotech Geo Eng, v. 30, p. 1197-1205.

Silva, E.J.S. (2009) Contribuição para a Utilização da Cinza de Casca de Arroz na Construção Civil. Dissertação de Mestrado, Faculdade de Engenharia de Ilha Solteira, Ilha Solteira, 118 pp.

Dispersion Potential of a Clay Soil Stabilized by Alum. A Case Study

H.R. Jafari, M. Hassanlourad, M.R. Hassanlou

Abstract. In this paper modification potential of dispersive clay by white natural alum is evaluated. The studied clay is taken from basin of a constructing dam, called "Mirzakhanloo", located in Zanjan province, northwest of Iran. Dispersion potential of soil and its modifiability were evaluated using pinhole, single and double hydrometric, chemistry and standard compaction tests. The influence of alum on the Atterberg limits of soil was also studied. Tests results indicated that adding the alum and curing time up to 28 days, under hydraulic gradients up to 26.84, decreases the dispersivity of the modified soil. Increasing the alum content increases the plasticity limit. Liquid limit, plasticity index and pH of the soil were increased by adding the alum up to 0.6%, and then decreased. Both the plasticity and liquid limits were decreased by curing time, however the plasticity index variations were limited. Electrical conductivity (EC), and Sodium absorption ratio (SAR) of the soil were increased and total suspended solids (TSS) in the leached water were decreased by increasing the alum content and curing time. Generally, addition of 3% alum stabilized the used soil knowing that maximum dry density and optimum moisture content were obtained at 1% of alum.

Keywords: dispersive clay, stabilization, alum, pinhole test, chemical test, hydrometric test.

1. Introduction

Ions type of clay soils is one of the important issues which must be always considered when encountered as barrow resources of earth dams and so on. Past experiences indicated that ignoring this for implementing the water structures made many problems and caused structural damages. Erosion and changes in the structure, physical and mechanical properties of the soil are the most important reported problems of these soils (Asgari & Fakher1994).

Dispersive soils are related to clays particles that can be easily washed by waters with low salt contents. Such clays usually contain high content of sodium ions in their absorptive ions. Dispersion is a progressive phenomenon beginning from a point with high water concentration which gradually develops. Cracks from condensation, differential settlements and hydraulic gradient could result in dispersion. Dispersive phenomena knowledge is very important in the projects involving earth dams and water canals design and construction. Dispersive soils are abundant in different climates and regions through the world, such as Australia, Brazil, Iran and USA (Vakili et. al, 2009a, b).

The dispersive soils may not be recognized by regular soil classification tests. Therefore it is usually recommended to simultaneously use four tests to recognize them, including Pinhole, Kramb, chemical and double hydrometric tests (Ryker, 1977 and Sherard & Decher, 1977).

Dispersive phenomenon has usually a physical- chemical nature influenced by the type of soil's minerals and chemical properties of pore water. When a dispersive soil is exposed to the seepage, the clay particles are likely to separate from each other and be suspended. This results in the formation of piping phenomena in the earth dams together with erosion and demolition of roads and water canals as well as destruction of structure's foundation (Ouhadi & Goodarzi, 2006 and Sherard *et al.*, 1972). In the past, it was being severely stressed on not increasingly usage of such type of soils, but today it has been paid more attention to improve and use these soils. The most important factors influencing the improvement ability include: type and concentration of pore water ions, chemical properties of runoff and seepage water, cracking, and clay particles (Asgari & Fakher, 1994).

In this study the white natural alum, $Al_2(SO_4)_3.18H_2O$, was used for stabilizing a dispersive clay soil, in which, sodium cation (Na^+) is replaced with aluminum cation (Al^{3+}). In such replacement, the soil structure is changed from dispersive to flocculated state, reducing the repulsion force between the particles and then the dispersive potential of soils (Heidarian, 1993).

$$Al_2(So_4)_3 + Clay \rightarrow Al[Clay] + 3(H_2So_4)$$

and

$$Al^3 + OH^- \rightarrow Al(OH)^{++} \quad (1)$$

$$Al(OH)^{++} + OH^- \rightarrow Al(OH)_2 + \text{(Aluminum hydroxyl ions)}$$

The effects of adding different percentages of aluminum sulfate and curing times on a dispersive soil were evaluated using double hydrometric, pinhole and chemical tests. Atterberg limits test was also used for studying the in-

Hamid Reza Jafari, MSc. in Soil Mechanics,Young Researchers Club, Zanjan Branch, Islamic Azad University, Zanjan, Iran. e-mail: hamidrezajafari1@yahoo.com.
Mahmoud Hassanlourad, PhD. Assisstant Prof. of Soil Mechanics, Imam
Khomeini International University, Qazvin, Iran. e-mail: hassanlou@eng.ikiu.ac.ir.
Mohammad Reza Hassanlou, PhD. Assisstant Prof. of Soil Mechanics, Zanjan Branch, Islamic Azad University, Zanjan, Iran. e-mail: Mhasanlo@yahoo.com.
Submitted on November 13, 2012; Final Acceptance on July 30, 2013; Discussion open until December 31, 2013.

fluence of alum on the plasticity limits. Standard compaction test was used for studying the effect of alum on the maximum dry unit weight and optimum moisture content.

2. Material and Methods

The soil used in this study was obtained from a site of dispersive clays present in the basin of an earth dam called Mirzakhanloo 2, Gohar, located in in Zanjan province, North West of Iran.

Dispersion specifications and chemical properties of the used soil are summarized in Tables 1 and 2, respectively. Based on these Tables it is concluded that the used soil is classified in the category of wholly dispersive soils with highly vulnerable to erosion. Particle size distribution using single and double hydrometric tests is shown in Fig. 1. The used soil was classified by two soil classification systems of Unified and ASHTO as CH and A-7-5, respectively. Also, specific gravity of soil particle was 2.76 (Table 3).

2.1. Sample preparation and test programming

First compaction test was performed on the soil. For stabilization process, all samples were prepared at optimum moisture content and then cured. The additive content of alum included 0.6, 1, 3, 5 and 10 percent of soil dry weight. Prepared samples were cured up to 1, 7, 14 and 28 days. Pinhole, chemical and hydrometric tests were done for studying the soil dispersion and its modification process. All tests were conducted according to ASTM standards.

2.1.1. Pinhole tests

Pinhole test was introduced by (Sherard *et al.*, 1972). In this test, which is also called Sherard Test, the dispersion rate of fine-grained soils is measured by directly passing the water from a hole (with 1 mm in diameter) made in the soil sample. The leached water from dispersive soils sample is muddy containing colloids; nevertheless, in non-dispersive sample, it is clear. In this research, pinhole tests conducted on samples with length of 38 under the water heads of 50, 180, 380 and 1020 mm (hydraulic gradient of 1.32, 4.73, 10 and 26.84) by three methods of A, B and C (ASTM D4647). Figure 2 shows a picture of the pinhole test. The results are shown as water discharge, clarity of the

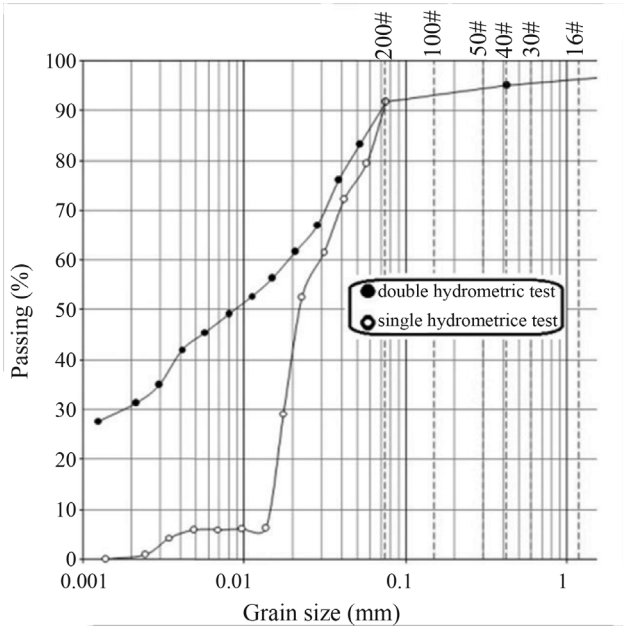

Figure 1 - Particle size distribution based on the single and double hydrometric test.

Table 1 - Dispersive properties of the used clay.

Classification based on pinhole test	Classification based on double hydrometric test	Dispersion percent in double hydrometric test
Wholly dispersive D1	Wholly dispersive	59.20

Table 2 - Chemical properties of the used soil.

$(SO_4)^{2-}$ (meq/L)	Cl^- (meq/L)	TDS (%)	EC (ms/cm)	Mg^{2+} (meq/L)	Ca^{2+} (meq/L)	K^+ (meq/L)	Na^+ (me1/L)	pH
38.90	10.22	0.6	96.00	13.90	34.8	9.00	174.30	7.2

Table 3 - Aggregation properties of the used soil.

D10 (mm)	D30 (mm)	D60 (mm)	Passing #200	Pas. 0.005(S)	Pas. 0.005(D)	Gs	UNIFIED Cl.	AASHTO Cl.
-	0.200	0.019	91.62	43.96	* 5.92	2.76	CH	A-7-5

*double hydrometric test.

leached water and hole diameter after test (Heidarian, 1993 and ASTM D698- A).

2.1.2. Double hydrometric tests

During these tests, the soil particle size distribution is initially determined by common method of hydrometric test, i.e. using mechanical agitator and dispersing chemical additive. Then it is repeated with another hydrometric test with another sample of the same soil without using mechanical agitator and dispersing chemical additive (ASTM D4221). The percentage of particles finer than 0.005 mm is determined in both tests. Dispersion percentage is defined as the ratio of percentage of particles finer than 0.005 mm in the second test to the first test.

2.1.3. Chemical tests

Dispersion is usually a physical - chemical phenomenon, and chemical properties of soils have important effect on the soils dispersion, particularly type and amount of cations and pore water. Therefore, different criteria have introduced for recognizing the dispersion potential for instance electrical conductivity (EC), pH value, sodium absorption ratio (SAR) and total suspended solids (TSS) (Rahimi, 1989).

2.1.4. Atterberg limit tests

Atterberg limit tests were conducted on samples with the mentioned alum contents as well as other tests (ASTM D4318) and at curing times of 1 to 28 days.

2.1.5. Compaction tests

The influence of maximum dry unit weight and moisture content on soils dispersion potential is not well understood. In some cases, reduction of moisture content results in decrease of soil dispersion and vice versa, and in some cases reduction of moisture content has added increased the soil dispersion. The reason for such incongruity has not been yet determined. Studies have indicated that the way of influencing both factors depends on other factors, such as type of soil, its chemical properties, concentration and type of ions in pore water, soil saturation and compaction energy (Asgari & Fakher1994). For studying the influence of additive content and curing time on the maximum dry unit weight as well as optimum moisture content, compaction tests were performed on the soil samples (ASTM D698).

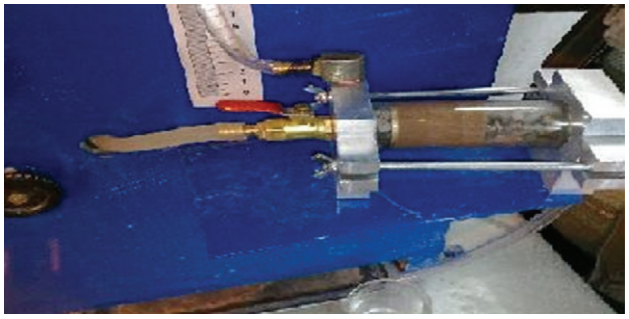

Figure 2 - Pinhole test.

3. Results and Discussions

3.1. Pinhole test results

The hole diameter in the natural soil sample without stabilizer increased for about four times and the leached water color turned to muddy and very muddy indicating the higher dispersion potential (Figs. 3 and 4, respectively). Dispersion rate of samples were considerably decreased by addition of 0.6% alum, such that the diameter of sample internal hole was about half of the natural soil with water color clearer than before (Fig. 5). Water discharged was also reduced in comparison with natural soil. The stabilized soil was categorized as the dispersion class of ND3, meaning low dispersion (In fact, ND3 means a soil slightly

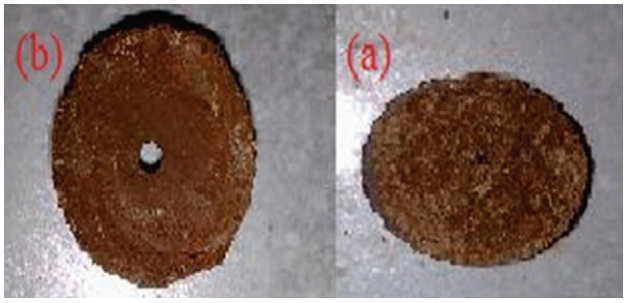

Figure 3 - (a) Non dispersive soil, and (b) Fourfold increase in the hole diameter of dispersive soil.

Figure 4 - The sample of the discharged water from pinhole test for dispersive and non dispersive soils.

Figure 5 - Changes in the dispersive and non-dispersive soils discharged water.

dispersive, suggesting high uncertainty about the existence of significant problems in the design). Continuously, soil was more improved at 1% of additive content. Adding alum from 3 to 10% fully causes the soil to be non-dispersive, the discharged water becomes more clear with no fundamental changes in the diameter of internal hole indicating lack of internal erosion (Fig. 6).

As shown in Figs. 7 to 10, discharged water increases *vs.* water head difference between input and output of the sample. Also, increasing the additive content in a specific water head difference reduces the discharged water. It was observed that increasing the curing time, the soil dispersion is reduced, because it has more opportunity for replacement and ion exchange by time.

As mentioned before, at all percentages of alum, soil's dispersion potential was reduced by increasing the curing time including the clarity of leached water, discharged water and diameter of eroded (Figs. 6 to 10). However, decrease of dispersion was more effective during the first 7 days. Also, for higher percentages of additives, there was non-dispersive soil even in at lower curing times. After 7 days, the rate of dispersion was decreased. Adding of 3 to 5% of alum for initial curing times and of 2 to 3% for 14 to 28 days curing times was considered to be resulted in fully non dispersion soil. Tables 4 to 6 indicate clarity of the leached water from the samples, illustrating the soil improvement trend.

3.2. Double hydrometric test results

Tests results indicated that it is more likely to erode and wash the clay particles with dispersion percentage more than 40. This limit also depends on the type of soil. Decker recommended that this limit is about 40% for the inorganic clay and it is considered about (25 to 30)% in the low plastic mud , clayey and muddy sand (Asgari & Fakher, 1994).

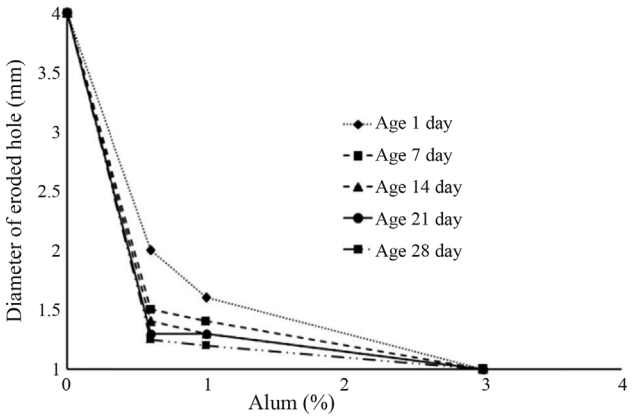

Figure 6 - Diameter of hole *vs.* alum content at water head of 50 mm.

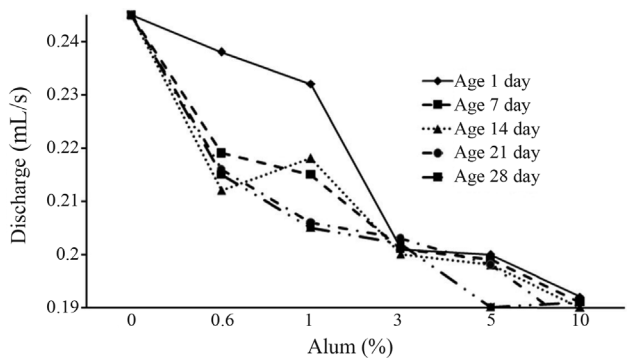

Figure 7 - Discharged water *vs.* alum additives at water head difference of 50 mm.

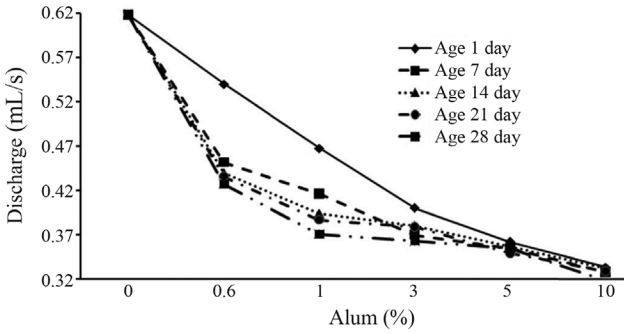

Figure 8 - Discharged water *vs.* alum additives at water head difference of 180 mm.

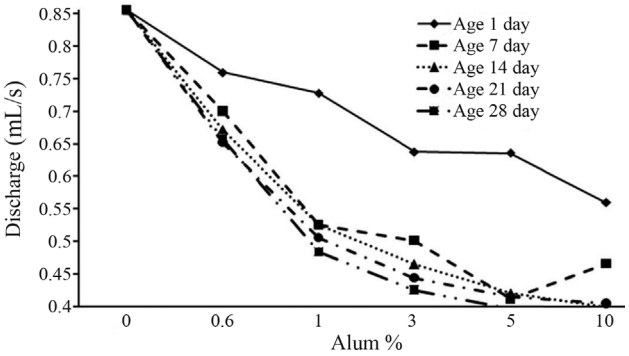

Figure 9 - Discharged water *vs.* alum additives at water head difference of 380 mm.

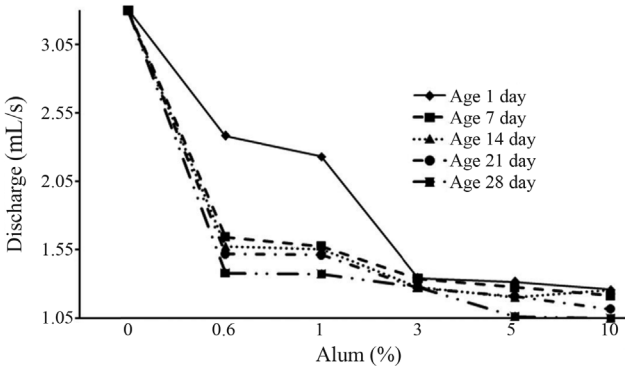

Figure 10 - Discharged water *vs.* alum additives at water head difference of 1020 mm.

Table 4 - Clarity of the leached water at different curing times, alum additive and water head of 50 mm.

Curing time	Additive (%)					
	0	0.6	1	3	5	10
1 day	A little turbidity	An effect of turbidity	Fully clear	Fully clear	Fully clear	Fully clear
7 days	A little turbidity	An effect of turbidity	Fully clear	Fully clear	Fully clear	Fully clear
≥ 14 days	A little turbidity	An effect of turbidity	Fully clear	Fully clear	Fully clear	Fully clear

Table 5 - Clarity of the leached water at different curing times, alum additive and water head of 380 mm.

Curing time	Additive (%)					
	0	0.6	1	3	5	10
1 day	Averagely turbidity	A little turbidity	An effect of turbidity	Fully clear	Fully clear	Fully clear
7 days	Averagely turbidity	A little turbidity	An effect of turbidity	Fully clear	Fully clear	Fully clear
≥ 14 days	Averagely turbidity	A little turbidity	An effect of turbidity	Fully clear	Fully clear	Fully clear

Table 6 - Clarity of the leached water at different curing times, alum additive and water head of 1020 mm.

Curing age	Additive (%)					
	0	0.6	1	3	5	10
1 day	Very turbidity	A little turbidity	An effect of turbidity	Fully clear	Fully clear	Fully clear
7 days	Very turbidity	A little turbidity	An effect of turbidity	Fully clear	Fully clear	Fully clear
≥ 14 days	Very turbidity	A little turbidity	An effect of turbidity	Fully clear	Fully clear	Fully clear

Increasing of alum and curing time considerably reduced the dispersion potential such that for 1 and 21 days curing time, the dispersion potential became zero for the additive percentages of 3 and 1% respectively (Fig. 11). As indicated in this figure, addition of even 0.6% alum severely reduced the dispersion potential. Experiences have indicated that the results of this test have an accuracy of about 85% when predicting the dispersion of soils. On the other hand, dispersive soils have dispersion percentage higher than 30% (Heidarian, 1993).

3.3. Chemical test results

As illustrated in Fig. 12, addition of alum as well as increasing curing time results in increased EC. This is because of displacement of ionic followed by soil stabilization. According to Fig. 13, adding the alum up to 0.6% increases the pH value and then decreases it. The reason for such increase is producing some acid resulted from ionic displacements. Ignoring the initial values, increasing the alum and curing time generally decreases pH value. Total suspended solid (TSS) in the leached water is reduced by

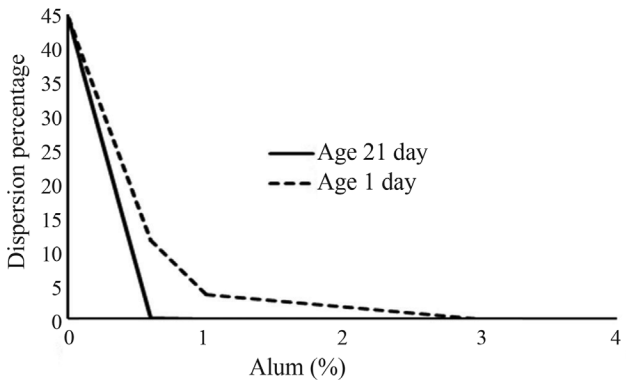

Figure 11 - Dispersion percentage for curing times of 1 and 21 days *vs.* alum using single and double hydrometric tests.

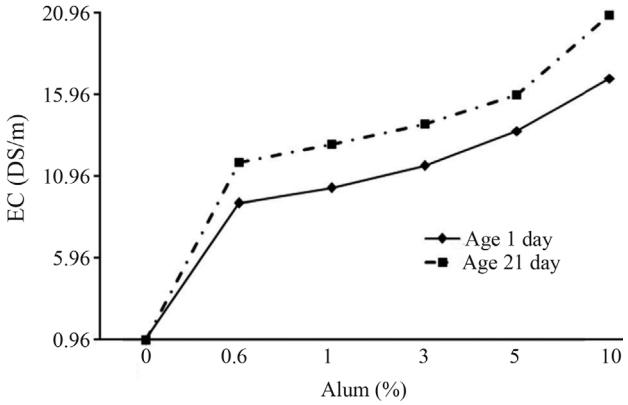

Figure 12 - Electrical conductivity *vs.* alum for curing times of 1 and 21 days.

increasing of alum content and curing time due to preventing of soil particles from escaping and washing (Fig. 14). Finally, according to Fig. 15, replacements of sodium with aluminum cations increases by increasing of alum content and curing time; however, the alum content is apparently more effective in comparison with curing time. Among these, increase of EC and decrease of TSS are considered as the more important criteria for reducing the dispersion (Asgari & Fakher1994).

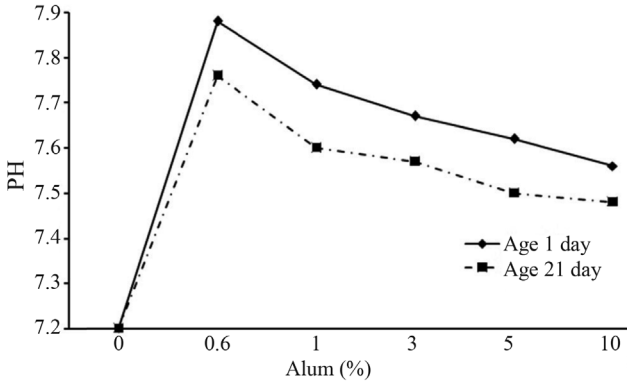

Figure 13 - PH values *vs.* alum for curing times of 1 and 21 days.

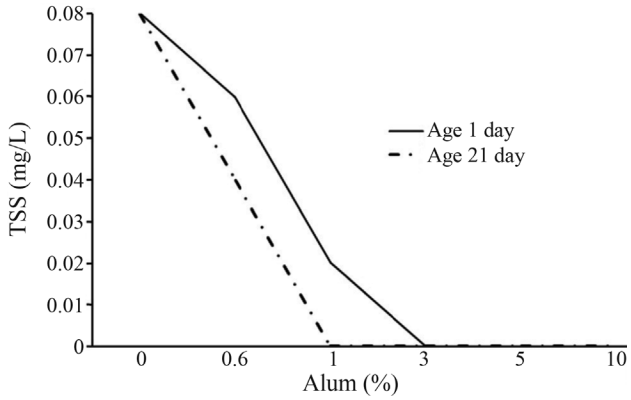

Figure 14 - TSS value in the leached water *vs.* alum for curing times of 1 and 21 days.

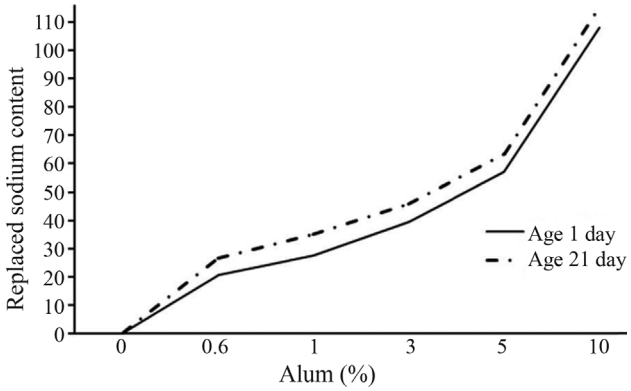

Figure 15 - Ionic exchanges *vs.* alum for curing times of 1 and 21 days.

3.4. Atterberg limit test results

Tests results shown in Figs. 16, 17 and 18 indicate that increasing the alum content and curing time have a regular trend on the stabilized soil. Generally, liquid limit and plasticity index are increased up to 0.6% of additive content and then decreased and plasticity limit indicates an ascending trend. It is seen more changes for plastic limit up to curing times of 7 days, but then, the closer is the changes trend. It was seen observed that increasing curing time decreases the liquid and plastic limits. However, there is no specific relation between soil dispersion and Atterberg limits (Asgari & Fakher, 1994).

3.5. Compaction tests results

Test results as revealed in Fig. 19 and 20 indicate that the changes trend is not very regular but at a glance, adding the alum increases and decreases the maximum dry unit weight (for about 6.2%) and optimum moisture content (for about 11%), respectively, up to alum content of 1%. Then the trend is reversed. Therefore, considering of these two parameters, the best alum additive content is about 1%.

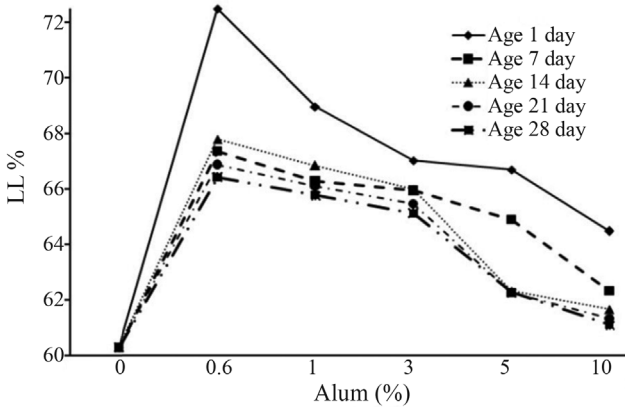

Figure 16 - Changes in liquid limits (LL) for different percentages and curing times.

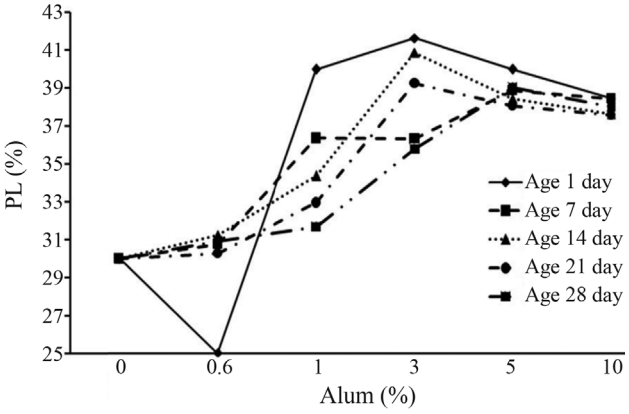

Figure 17 - Changes in plasticity limit (PL) for different percentages and curing times.

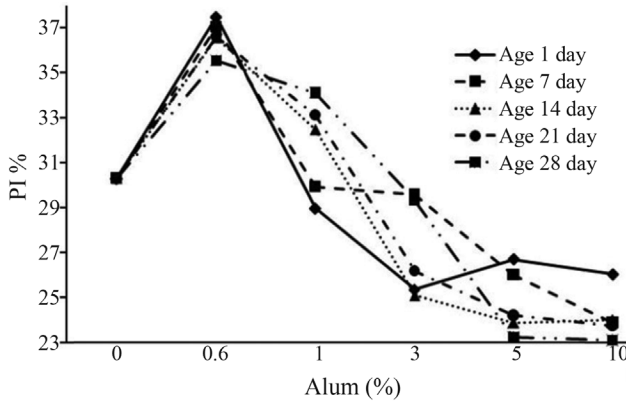

Figure 18 - Changes in plasticity index (PI) for different percentages and curing times.

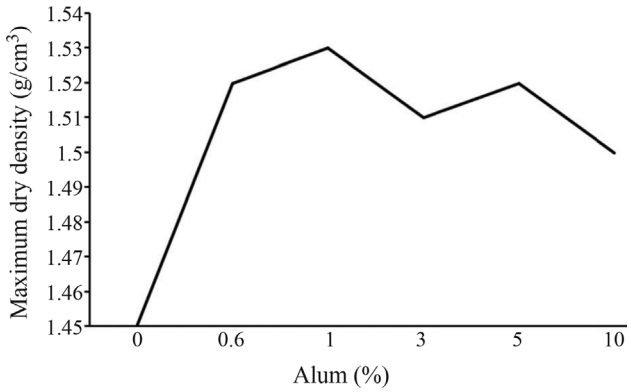

Figure 19 - Maximum dry unit weight *vs.* alum content for curing time of 21 days.

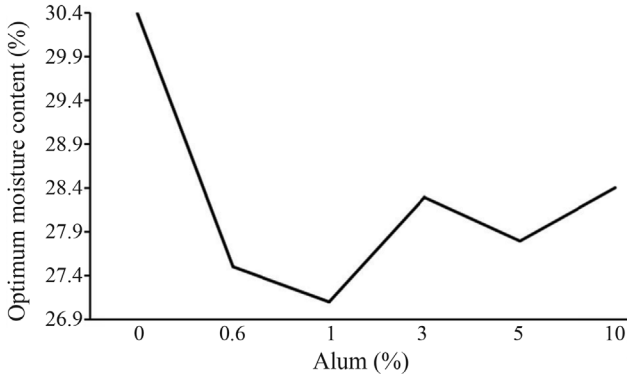

Figure 20 - Optimum moisture content *vs.* alum content for curing time of 21 days.

4. Conclusion

Addition of white alum to a dispersive clay results in adsorption of aluminum ions surrounding the clay particles. Dispersion potential of soil and its modifiability were evaluated using pinhole, single and double hydrometric, chemistry and standard compaction tests. The influence of alum on the Atterberg limits of soil was also studied. Tests results indicated that:

- Pinhole tests indicated that adding the alum and increasing the curing time up to 28 days, under hydraulic gradients up to 26.84, dispersion potential of the investigated soil was decreased.
- For curing time over than 14 days, addition of the alum of about 2-3% of dry weight of soil completely stabilized the dispersion potential of the soil. However, addition of 3% of alum by 3% of soil dry weight turns the soil to a fully non dispersive soil.
- Results of chemical, hydrometric tests indicated a completely positive performance for the process of soil stabilization and improvement.
- Adding the alum and curing time increased the electrical conductivity of the soil and replacement of sodium ion as well, and decreased the suspended materials in the leached water from soil.
- Adding the alum up to 0.6% of dry weight of soil increased the liquid limit and plasticity index and then decreased them. Changes in pH value of the modified soil also indicated a similar trend. Plasticity and liquid limits both were reduced by curing time; however, plasticity index slightly indicated some variations.
- Both the maximum dry unit weight and optimum moisture content indicated relatively irregular changes *vs.* the alum content. Nevertheless, optimum values of the mentioned parameters were obtained at 1% of alum.

References

Asgari, F.A. & Fakher, A. (1994) Soil Swelling and Dispersion from a Geotechnical Engineers Point of View. Jihad Daneshgahi Publications, Tehran University, 245 pp.

ASTM (1998) Standard Test Method for Identification and Classification of Dispersive Clay Soils by the Pinhole Test. D4647. ASTM International, West Conshohocken, Pennsylvania, USA, 11 pp.

ASTM (1999) Standard Test Method for Dispersive Characteristics of Clay Soils by Double Hydrometer Test. D4221. ASTM International, West Conshohocken, Pennsylvania, USA, 3 pp.

ASTM (2000) Standard Test Method for Laboratory Compaction Characteristic of Soil Using Standard Effort (600 kN.m/m^3). D698. ASTM International, West Conshohocken, Pennsylvania, USA, 11 pp.

ASTM (2005) Standard Test Method for Liquid limit, Plastic limit and Plasticity Index of Soils. D4318. ASTM International, West Conshohocken, Pennsylvania, USA, 16 pp.

ASTM (2007) Standard Test Method for Particle size Analysis of Soils. D422. ASTM International, West Conshohocken, Pennsylvania, USA, 8 pp.

Heidarian, H. (1993) Standard Methods of Soil Mechanics Laboratory Tests. Avand Andishe Publications, Tehran, pp. 64-70.

Ouhadi, V.R. & Goodarzi, A.R. (2006) Assessment of the stability of a dispersive soil treated by alum. Engineering Geology, v. 8, p. 91-101.

Rahimi, H. (1989) Water structural problems in salty and chalky soils (Case Study - irrigation system of Gotvand project). Iranian Journal of Agricultural Sciences, v. 21, p. 93-109.

Ryker, N.L. (1977) Encounting dispersive clays on soil conservation service projects in Oklahama. ASTM STP, v. 623, p. 370-389.

Sherard, J.L.; Decker, R.S. & Ryker, N.L. (1972) Piping in earth dams of dispersive clay. Proc. of Specialty Conf. on performance of earth and earth supported structures. ASCE, v. 1, Part 1, pp. 589-626.

Sherard, J.L. & Decher, R.S. (1977) Summary - Evaluation of symposium on dispersive clays. ASTM STP, v. 623, p. 467-479.

Vakili, A.H.; Zomorrodian, M.A & Vakili, A. (2009a) Evaluating dispersion potential of dispersion clays, stabilized by pozzolans. Proc. 8th International Congress of Civil Engineering, Shiraz University pp. 141-148.

Vakili, A.H.; Zomorrodian, M.A.; Vakili, A & ARAM, M. (2009b) Evaluating dispersion potential and physical-mechanical stabilized by lime and pozzolan. Proc. 8th International Congress of Civil Engineering, Shiraz University, pp. 232-240.

List of Symbols

CH: High plastic clay
pH: power hydrogen
EC: Electrical conductivity
SAR: Sodium absorption ratio
TSS: Total suspended solids in the leached water
Gs: Specific gravity
Cl: Clay
TDS: Total dissolved solids
ASTM: American society for testing and materials
LL: Liquid limit
PL: Plastic limit
PI: Plasticity index

Technical Note

Soils and Rocks
v. 36, n. 2

Scale Laboratory Model for Studying the Behavior of Pipe Umbrella in Sandy Soil

D. Galetto, J.C.B.J. Silva, D. Peila, A. Assis

Abstract. Steel pipe umbrellas have been used to tunnel in difficult conditions or in weak rock masses and/or soils. Despite the large number of applications around the world, there are still some doubts concerning how pipe umbrellas behave under loading when the tunnel face advances. For this reason, a scale laboratory model of pipe umbrella reinforced tunnel heading in a sandy soil was set up with the aim of understanding tunnel boundary deformation mechanisms in order to understand and define which is the best pipe umbrella design. The laboratory tests were performed using a box (1.5 m x 2.0 m x 1.8 m) in which the excavation of a 50 cm diameter tunnel at a low depth was simulated. The behavior of the ground and of some pipes of the umbrella was monitored during the test and the results were compared with FLAC 3D program modeling results. The paper reports the preliminary results of the first set of tests which, however, demonstrated the great efficiency of the pipe umbrella system, even for heading of half of the tunnel diameter, that the behavior of the tunnel face is a key parameter in the deformation scheme and that this support technique can be modeled using a three-dimensional code.

Keywords: tunnel, pipe umbrella, numerical modeling, portal.

1. Introduction

When adverse geotechnical conditions are encountered in tunnelling and the free span and self supporting times are short, the technological possibilities for the designer are: to reduce the size of the excavation sections, and increases the number of working attacks; to improve the rock mass quality or reinforce it or to pre-support the excavation to apply a pressure to the tunnel face. Among the different ways of pre-supporting a tunnel ahead of the tunnel face, steel pipe umbrellas have been widely used (Anagnostou & Serafeimidis, 2007). The umbrella method, which consists of a closely spaced, usually grouted, canopy of steel tubes, installed at the tunnel extrados, is effective in controlling deformations and volume losses for a wide range of ground conditions as it improves face stability and increases the stand-up time (Fig. 1). Steel pipes are usually installed with a 5°-10° dip (with reference to the horizontal) in such a way as to form an umbrella of pipes, with a size that ranges between 80 mm and 220 mm. The umbrella has a truncated cone shape which allows two adjacent umbrellas to overlapped thus covering advancement lengths of 12-15 m of which 9-12 m are of excavation. The diffusion of this method has been facilitated by the technological improvements on the installation machines.

This technique has been used for: the construction of shallow tunnels in soft ground where a good control of the ground displacements is necessary to reduce surface subsidence, the construction of tunnel portals because of low overburdens; the construction of tunnels through weak ground with high overburdens or through fault zones, and the crossing zones where the tunnel has already collapsed (Barisone *et al.*, 1982; Pelizza & Peila, 1993; Shirakawa *et al.*, 1999; Carrieri *et al.*, 2004; Volkmann *et al.*, 2007). Despite the large number of applications there are still no generally accepted methods or reliable means for designing a steel pipe umbrella. Among the other factors it is difficult to take into account: the high number of the involved geotechnical parameters, the three dimensional shape of the tunnel near the face, the effect of the overlapping of the umbrella pipes and their connection to the steel sets, the stiffness of the steel sets in comparison to the vertical loads and the geotechnical characteristics of the ground at the excavation face and finally the influence of the position of the face during the excavation process. Some researches have supposed that the pipes act by forming a shell around the tunnel boundary that reduces the stresses acting on the rock core ahead of the advancing tunnel face and that a two-dimension numerical model can also "model the physical behaviour of the reinforced tunnel in a realistic manner" (Hoek, 2001). Other authors believe that there is no significant mutual interaction between the singles pipes, thus each must be individually designed taking into account their longitudinal direction (Max & Mattle, 2002; Oreste & Peila, 1998; Peila & Pelizza, 2003), while others authors have used three-dimension numerical models to take into account the three dimensional shape of the tunnel face and the presence of the pipes and face reinforcement (Peila, 1994; Uhtsu *et al.*, 1995; Eclaircy-Caudron *et al.*, 2005) and finally some

D. Galetto, Engenheiro Civil, Politecnico di Torino, Torino, Italy. e-mail: didi_dws@hotmail.com.
J.C.B.J. da Silva, Associate Professor, PhD, Universidade Federal da Bahia, Universidade Estadual da Feira de Santana, BA, Brazil. e-mail: jcarlos@ufba.br.
D. Peila, PhD, Associate Professor, DITAG, Politecnico di Torino, Torino, Italy. E-mail: daniele.peila@polito.it.
A.P. Assis, PhD, Ful Professor, Universidade de Brasilia, DF, Brazil. e-mail: aassis@unb.br.
Submitted on May 6, 2011; Final Acceptance on July 23, 2013; Discussion open until December 31, 2013.

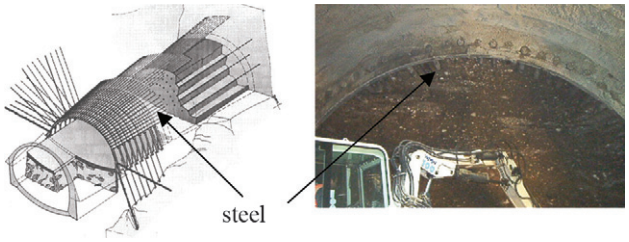

Figure 1 - Scheme of a steel pipe umbrella intervention for an excavation head and bench with face reinforcement and underpinning of the steel stets (courtesy Geodata SpA, Turin) (left) and photo of an application in a granular soil (Turin metro excavation) (right).

authors have carried out physical modelling to understand pipe behaviour more clearly or measurements in real tunnels (Volkmann *et al.*, 2007; Ocak, 2008).

A scale laboratory test can be an useful tool to better understand the global behavior of this pre-support during tunnel advancement as already developed by some researchers (Kim *et al.*, 2004; Takechi *et al.*, 2000; Yoo & Yang, 2001; Shin *et al.*, 2008) since measurements in real tunnels (Volkmann *et al.*, 2007; Ocak, 2008; Shirakawa *et al.*, 1999; Shin *et al.*, 2007) are particularly difficult to interpret due to the fact that the pipes are often overdesigned (because of the adopted safety factors) and therefore no significant deformations can be recorded and if collapse occurs, it is often very difficult to understand its real cause and its development.

2. Materials and equipment to simulate a tunnel excavation

A half-tunnel with 0.5 m diameter was excavated in a wooden 1.5 m wide, 2.0 m high and 1.8 m long box (Fig. 2). The box was filled with silty-sand, whose geotechnical parameters are summarized in Table 1. This paper presents the preliminary results obtained by the first set of experiments.

The sand was poured into 15 cm layers with its natural water content and the box filling was limited to one tunnel diameter of overburden, that is, 0.50 m over the tunnel crown.

The pipe umbrella was made with 18 fiber-glass (E = 27 GPa) 1.2 m long bars (Fig. 3) with a 10 mm x 3 mm section (Inertia modulus of $2.3*10^{-11}$ m^4). This type of elements, with different shape from the real ones, was chosen to have a more flexible support structure in order to permit

Figure 2 - Photograph of the test box where the position of the half-tunnel and holes for reinforcing elements can be observed.

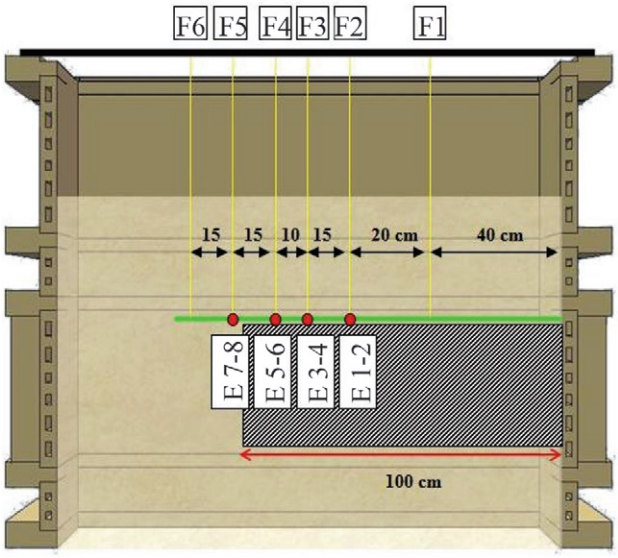

Figure 3 - Photograph of the fiber glass pipe umbrellas during installation.

deflection, even at low level of applied loads, so that the model could be used to understand the deformation shape expected ahead of the tunnel face.

The system has been monitored with (Fig. 4):

- Inspection windows located above the tunnel crown, where a 3 cm thick layer of sand, with different color

Table 1 - Geotechnical parameters of the silty-sand used for the test.

Sand content [%]	Silt content [%]	Water content (w) [%]	Dry unit weight (δ_d) [kN/m^3]	Total unit weight (δ_t) [kN/m^3]	Cohesion (c) [kN/m^2]	Friction angle (ø) [°]	Deformation modulus (E) [MPa]	Poisson modulus (ν)
90	10	4.6	16	17	1	32	25	0.40

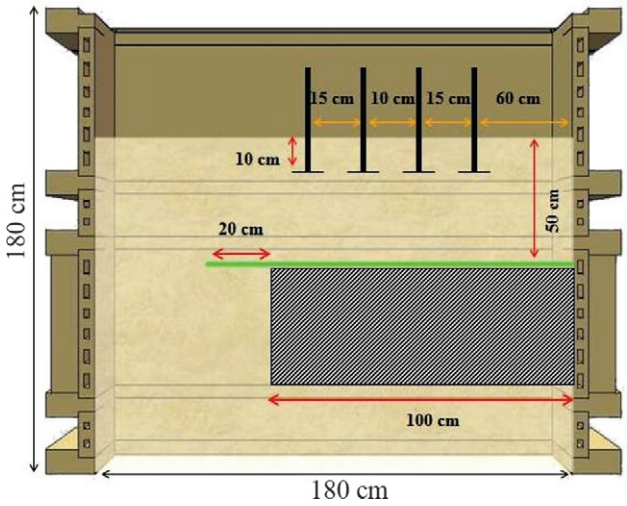

Figure 4 - Instrumentation scheme used in the test (upper figure *E* = strain-gauge; *F*= flexible wires that transmit the displacement outside the box) and topographic fixed points on ground level (lower figure).

from the sand used for filling, was created. The deformation of the layer was registered optically;

- A bar instrumented using 8 strain-gauges that was installed as a third beam from the tunnel axis;
- A bar instrumented using 6 flexible wires to measure its displacements that was installed as a fourth beam from the tunnel axis;
- 8 topographically fixed points situated about 10 cm below the ground level.

The excavation was done by hand in four stages (Fig. 5) and the advancement steps are reported in Table 2. An overload equal to the overburden (8.4 kPa) was applied to the surface at the end of the last excavation step. In the first preliminary test, during the excavation, the tunnel was kept unsupported.

3. Results of the Test

Vertical displacements measured on ground level were practically nil without the application of the overload, since the pipe umbrella was able to absorb completely the ground load. When the overload was applied it was necessary to withdraw the fixed measurement points thus making it impossible to obtain any further ground subsidence data

Figure 5 - Tunnel excavation by hand.

Figure 6 - Photograph of the inner part of the tunnel after excavation and application of the overload on the surface (step 5). It is possible to observe that a local arch is created between adjacent reinforcing elements, preventing material flowing.

(Fig. 6). Although it has not been possible to precisely quantify the displacement values observed through the observation windows above the tunnel crown, they permitted some qualitative evaluations that is that displacements have the same shape and similar values as those measured on the instrumented pipes. Therefore, it can be said that, in soft soils, the instrumented pipe displacements are closely

Table 2 - Excavation steps.

Step	Excavation length (mm)	Position of the face from the entrance (mm)	Note
1	350	350	Excavation
2	200	550	Excavation
3	200	750	Excavation
4	200	950	Excavation
5	-	950	Overload application

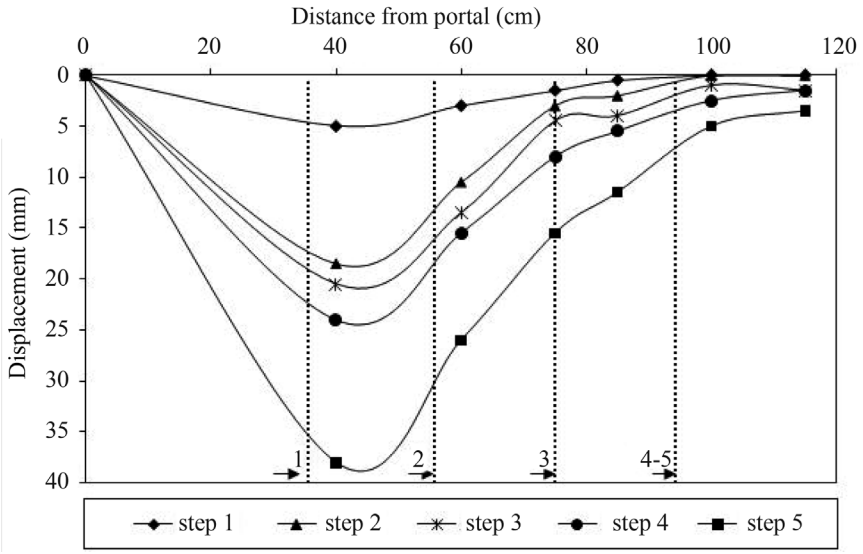

Figure 7 - Displacements observed in the fourth pipe from the tunnel axis for each excavation step.

linked to the surrounding soil displacements and are summarized in Fig. 7.

From Fig. 7 it can also be observed that the displacement of the reinforcing element ahead of the face, in this type of soil, is not negligible and reaches about the 30% of the excavated length (values similar to those found by Shin *et al.*, 2008).

Considering an advancing working face of 35 cm (0.7D), the value of the maximum displacement on the pipe umbrellas is 5 mm, which is 1% of the tunnel diameter. However, when the advancing working face reaches 1 D, the maximum displacement rises to 18.5 mm, (3.8% of the tunnel diameter). The test demonstrates a high efficiency of the pile umbrella system until an advancing working face of half of the tunnel diameter was reached. For an advancing work face of 95 cm, the observed maximum displacement in the pile umbrella is 26.5 mm (5.3% of the tunnel diameter) and when the overload equivalent was applied, the maximum displacement of the beam reached 40 mm.

4. Numerical Modeling

In order to verify the test obtained results during test, a numerical model of the small scale tunnel has been set up. The model was implemented using the Flac 3D code (Ver. 3.1) and all the individual reinforcing elements were singularly modeled using beam element. The whole model was described by a mesh with 8584 nodes and 7524 elements (Fig. 8).

The comparison between the displacements values measured in laboratory test on the monitored reinforcing element and the FLAC 3D results (Fig. 9) have show a very good agreement (Figs. 10 and 11).

From an analysis of the tunnel boundary displacements it emerges that the 3D codes give that the vertical displacement is mainly concentrated in the free span length

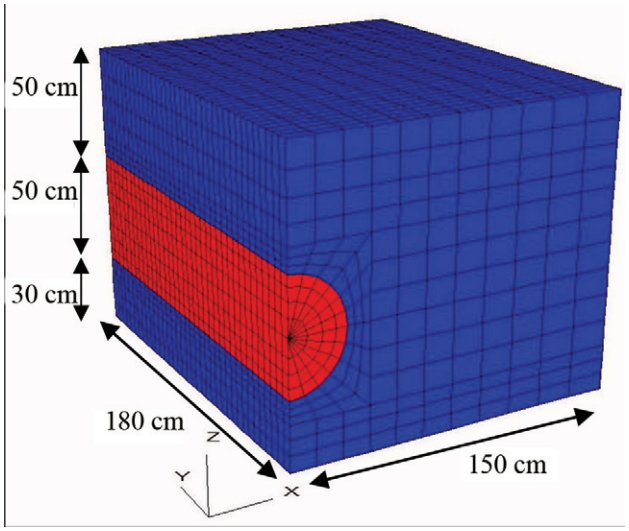

Figure 8 - Geometry of the Flac 3D model.

and that the reinforcing elements ahead of the face control the stability of the soil since few displacements are observed (Fig. 12).

5. Conclusion

Many different approaches have been used in the literature for steel pipe umbrella design and this problem is more relevant near the tunnel portal where low tunnel depths are faced and taken into account. For this reason, a simple scale laboratory test was developed aiming to better understand how this type of pre-support behaves during tunnel excavation, particularly ahead of the face.

The physical model allowed to observe that pre-supports installed ahead of the face permitted a stress transfer in the longitudinal direction until the region beyond the tunnel heading is reached (not yet excavated), thus mini-

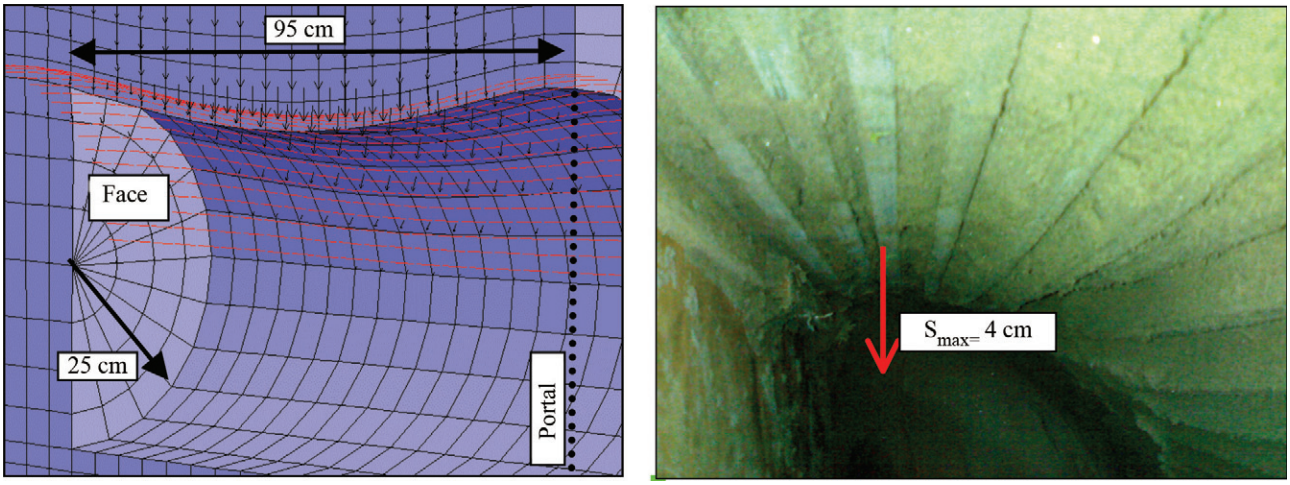

Figure 9 - Computed displacement using FLAC 3D code compared with the physical model results after step 5 (the arrow in the left figure shows the maximum measured displacement while the FLAC 3D shows the computed deformed mesh with deformation amplification factor equal to 1).

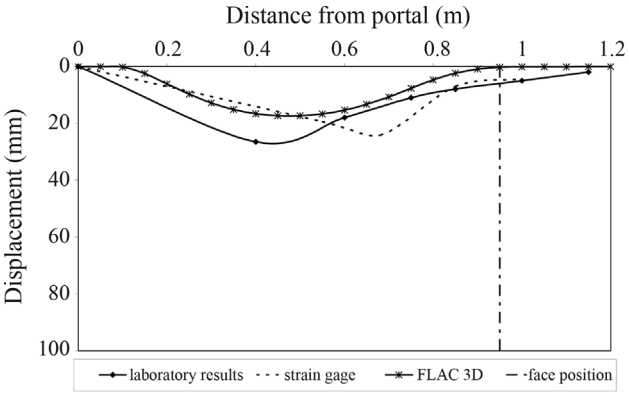

Figure 10 - Displacement for stage 4 (95 cm).

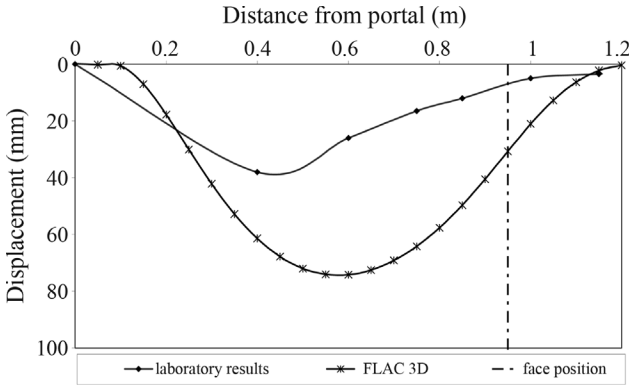

Figure 11 - Displacement after the overload (strain gauges damaged).

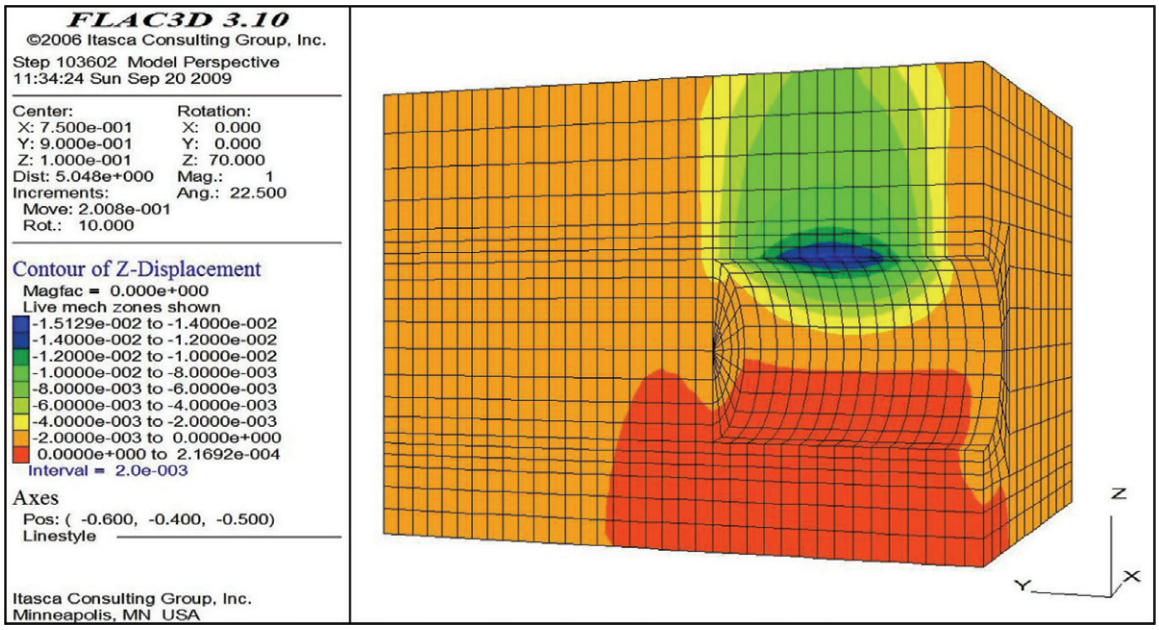

Figure 12 - Computed vertical displacements after step 3 (it is possible to see that the vertical displacement is mainly concentrated in the free span length and that the reinforcing elements ahead of the face control the stability of the soil since few displacements are observed).

mizing the global deformations of the tunnel boundary. It was also been highlighted that the displacement of the support element starts ahead of the face with a distance that, in the physical model case, was about 0.5D, which is also confirmed by the numerical 3D computation.

References

Anagnostou, G. & Serafeimidis, K. (2007). The dimentioning of tunnel face reinforcement. underground space – Proc. The 4th Dimension of Metropolises, WTC 2007, ITA, Prague, Czech Republic, pp. 289-296.

Barisone, G.; Pelizza, S. & Pigorini, B. (1982) Umbrella arch method for tunnelling in difficult conditions - Analysis of Italian cases. Proc. IV International Congress of I.A.E.G., New Delhi, pp. 15-27.

Carrieri G., Grasso P., Fiorotto R. & Pelizza S (2004). Venti Anni di Esperienza Nell'uso del Metodo Dell'ombrello di Infilaggi Come Sostegno per lo Scavo di Gallerie. Gallerie e Grandi Opere Sotterranee, v. 72, p. 41-61.

Eclaircy-Caudron, S., Dias, D., Kastner, R. & Chantron, L. (2005). Numerical Modelling of a Reinforcement Process by Umbrella Arch. Proc. Numerical Modelling of Construction Process in Geotechnical Engineering for Urban Environment, Paris, France, pp. 1-15.

Hoek, E. (2001). Big tunnels in bad rock. Journal of Geotechnical and Geoenvironmental Engineering, ASCE, v. 131:5, p. 726-740.

Kim, C., Kim, K., Hong, S., Bae, G. & Shin, H. (2004). Interpretation of field measurements and numerical analyses on pipe umbrella method in weak ground tunneling. Proc. Eurock 2004, Salzburg, v. 1, pp. 167-170.

Max, J. & Mattle, B. (2002). Design of Tube Umbrellas. Tunnel, v. 3, p. 4-11.

Marchino, C.; Borio, L. & Peila, D. (2010) Analisi mediante modellazione numerica e modelli analitici di un presostegno con infilaggi in gallerie superficiali. Geoingegneria Ambientale E Mineraria, v. XLVII:3, p. 69-74.

Ocak, I. (2008). Control of Settlements With Umbrella Arch Method in Second Stage Excavation of Istanbul Metro. Tunnelling and Underground Space Technology, v. 23, p. 674-681.

Oreste, P.P. & Peila, D. (1998). A new theory for steel pipe umbrella design in tunneling. Proc. Tunnel and Metropoles, São Paulo, SP, v. 1, p. 1033-1040

Peila, D. & Pelizza, S. (2003) Ground Reinforcing and Steel Pipe Umbrella System in Tunnelling, Rational Tunnelling. Logos Verlag, Berlin, pp. 93-132.

Peila, D. (1994). A Theoretical study of reinforcement influence on the stability of tunnel face. Geotechnical and Geological Engineering, v. 12, p. 145-168.

Pelizza, S. & Peila, D. (1993). Soil and rock reinforcements in tunnelling. Tunnelling and Underground Space Technology, v. 8, p. 357-372.

Shin, J.H.; Choi, S.H.; Woo, S.B. & Choi, Y.K. (2007) Reinforcing effects around tunnel face by crown and face reinforcing. underground space - The 4th dimension of metropolises. Bartak, Hrdina, Romancov and Zlamal (eds) Taylor and Francis Group, London, pp. 345-325.

Shin, J.; Choi, Y.; Kwon, O. & Lee, S. (2008) Model testing for pipe-reinforced tunnel heading in a granular soil. Tunnel and Underground Space Technology, v. 23, p. 241-250.

Shirakawa, K.; Aoki, T.; Fujii, Y. & Nakao, T. (1999) Excavation through semicircular-shaped shell formed by umbrella method at fault fracture zone beneath densely residential area, Challenge for the 21th century. ITA-AITES, Balkema, Oslo, pp. 441-452.

Takechi H., Kavakami K., Orihashi T. & Nakagawa K. (2000). Some considerations on effect of the long-forepiling-method. Proc. Tunnels Under Pressure, SAIMM, Durban, pp. 395-398

Uhtsu, H.; Hakoishi, Y.; Nago, M. & Taki, H. (1995) A prediction of ground bearing due to tunnel excavation under shallow overburden with long-length forepilings. South East Asian Symposium of Tunneling and Underground Space Development, JTA, Bangkok, pp. 157-165.

Volkmann, G.M.; Button, E. & Schubert, W. (2007) Pipe umbrella support systems and installation methods. Proc. 2nd Symposium on Underground Excavations for Transportation, Istanbul, pp. 395-402.

Yoo, C. S. & Yang, K. H. (2001). Laboratory Investigation of Behaviour of Tunnel Face Reinforced with Longitudinal Pipes. Proc. Progress in Tunnelling after 2000, Patron, Bologna, Milano, pp. 757-764.

SOILS and ROCKS
An International Journal of Geotechnical and Geoenvironmental Engineering

Publication of
ABMS - Brazilian Association for Soil Mechanics and Geotechnical Engineering
SPG - Portuguese Geotechnical Society
Volume 36, N. 2, May-August 2013

Author index

1. Mangaratiba RJ
2. Botafogo RJ
3. Copacabana, RJ

Recorde Mundial: impacto de 20 toneladas métricas à 103km/h contido!

A nova barreira para queda de rochas modelo GBE 8000A estabeleceu novo recorde mundial em teste realizado em Outubro,2011 no campo de testes verticais em Wallenstadt na Suíça. Teste certificado realizado e resultados certificados obtidos de acordo com a norma do ETAG 027 :

- 8,000kj de energia de impacto
- 8.5 metros de deflexão da barreira
- 85% de altura residual da barreira

A barreira modelo GBE-8000A protege contra queda de grandes blocos de rocha que produzem altas cargas de energia cinética, são aplicáveis onde as barragens de retenção não são possíveis e excedem a capacidade de absorção da maioria das galerias de concreto.

Assista ou escaneie o filme do teste em:
www.geobrugg.com/GBE-8000A

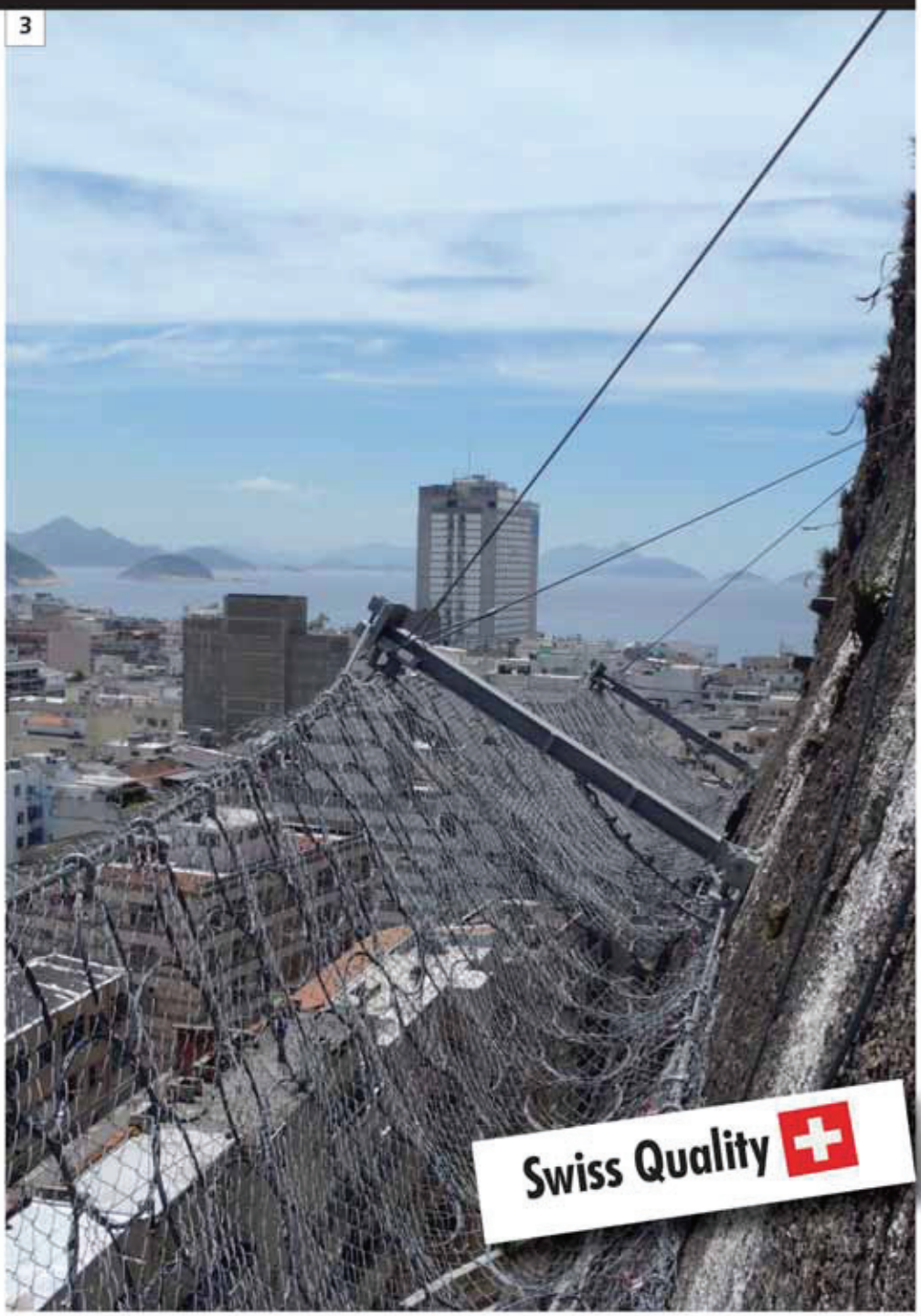

GEOBRUGG
BRUGG

Geobrugg AG
Geohazard Solutions
Rua Visconde de Pirajá, 82 sl.606
Ipanema - Rio de Janeiro • 22410-003
Fone: +55 21 3624.1449
Cel: +55 21 9979.1288
info@geobrugg.com • www.geobrugg.com

» We're known for our strength «

Fortrac®
High tensile stiffness geogrid for soil reinforcement

HaTelit®C
Flexible grid for asphalt reinforcement

Fornit®
Flexible geogrid for base reinforcement

HaTe®
Fabric for separation, stabilization and filtration

Ringtrac®
Ring reinforcement for granular columns on soil improvement

Stabilenka®
High strength woven geosynthetic for soil reinforcement

NaBento®
Geosynthetic clay liner for sealing

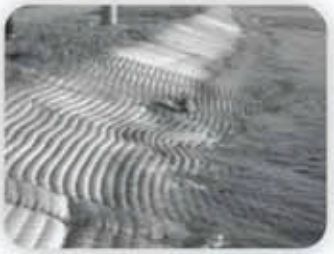

Incomat®
Construction system for slope and bed protection

HUESKER
Engineering with Geosynthetics

Tel.: +55 (12) 3903-9300 **www.huesker.com** huesker@huesker.com.br

SOLOS MOLES?

ENGEGRAUT
www.engegraut.com.br

CPR®

CONSOLIDAÇÃO PROFUNDA RADIAL

O MAIS RÁPIDO E EFETIVO TRATAMENTO PARA SOLOS MOLES

Processo de adensamento de solo mole, eficientemente controlado, monitorando-se o grau de consolidação desejado.

TÉCNICA DE TRATAMENTO DE SOLO MOLE POR CONSOLIDAÇÃO
METODOLOGIA PREMIADA PARA TRATAMENTO DE SOLO MOLE

Vantagens do CPR

- 100% específico para solos moles;
- Mobilização rápida;
- Ausência de transtornos à obra;
- Ampla gama de aplicações;
- Ausência de aterros, refugos e lama;
- Técnica não destrutiva;
- Alternativa super econômica, além de prazos extremamente curtos em relação à substituição de solos, aterros temporários, colunas granulares e estaqueamentos;
- Alcança profundidades de tratamento onde técnicas clássicas são limitadas;
- Acesso a locais restritos, limitados e difíceis, sem interferência com a rotina do cliente;
- Melhor custo benefício;
- Perfeito para reforço de fundação.

www.engegraut.com.br

Para maiores informações, entre em contato com nosso departamento de geotecnia. A marca CPR® e a tecnologia Consolidação Profunda Radial são patentes da ENGEGRAUT.

SOILS AND ROCKS PROBLEMS?
WE HAVE THE SOLUTION

BRASIL
Phone: 55 (11) 4525-5000
Fax: 55 (11) 4599-4275
maccaferri@maccaferri.com.br
www.maccaferri.com.br

PORTUGAL
Phone: (351) 218 968 282
Fax: (351) 218 968 078
portugal@abianchini.pt
www.abianchini.es

MACCAFERRI

Engineering a better solution

Tecnasol

Geotechnics and Foundation Engineering

Diaphragm Walls

Piles

Micropiles

Retaining Walls

Anchors

Soil nails

Monitoring

Repair Stuctures

Post tensioning

Grouting

Jet Grouting

Compensation Grouting

Tunnelling and

Underground Works

Sealing and

Waterproofing Systems

Site Investigations

Slope Stabilization

HEAD OFFICE
Edifício Edifer
Estrada do Seminário , 4 - Alfragide
2610 - 171 Amadora - PORTUGAL
Tel. 00 351 21 475 90 00 / Fax 00 351 21 475 95 00

Madrid
Calle Rodríguez Marín, Nº 88 1º Dcha
28016 Madrid – ESPANHA
Tel. 00 34 91 745 03 64 / Fax 00 34 91 411 31 87

Angola
Rua Alameda Van-Dúnem, n.º 265 R/c
Luanda - ANGOLA
Tel. 00 244 222 443 559 / Fax 00 244 222 448 843

Porto
Rua Eng. Ferreira Dias, nº 161 2º Andar
4100-247 Porto – PORTUGAL
Tel. 00 351 22 616 74 60 / Fax 00 351 22 616 74 69

Barcelona
Calle Comte d' Urgell, 204-208 6.º A
08036 Barcelona – ESPANHA
Tel. 00 34 93 419 04 52 / Fax 00 34 93 419 04 16

Madeira
Rampa dos Piornais, n.º 5 - Sala 1
9000-248 Funchal – PORTUGAL
Tel. 00 351 291 22 10 33 / Fax 00351 291 22 10 34

Sevilha
Polígono Industrial de Guadalquivir, C/ Artesanía, 3
41120 Gelves (Sevilla) - ESPANHA
Tel. 00 34 955 762 833 / Fax 00 34 955 76 11 75

www.tecnasolfge.com

TEIXEIRA DUARTE
ENGENHARIA E CONSTRUÇÕES, S.A.

- Head Office
  Lagoas Park – Edifício 2
  2740-265 Porto Salvo - Portugal
  Tel.:(+351) 217 912 300
  Fax: (+351) 217 941 120/21/26

- Algeria
  Parc Miremont – Rua A, Nº136 - Bouzareah
  16000 Alger
  Tel.:(+213) 219 362 83
  Fax: (+213) 219 365 66

- Spain
  Avenida Alberto Alcocer, nº24 – 7º C
  28036 Madrid
  Tel.:(+34) 915 550 903
  Fax: (+34) 915 972 834

- Angola
  Alameda Manuel Van Dunen 316/320 - A
  Caixa Postal 2857 - Luanda
  Tel.:(+34) 915 550 903
  Fax: (+34) 915 972 834

- Brazil
  Rua Iguatemi, nº488 – 14º - Conj. 1401
  CEP 01451 - 010 - Itaim Bibi - São Paulo
  Tel.: (+55) 112 144 5700
  Fax: (+55) 112 144 5704

- Mozambique
  Avenida Julyus Nyerere, 130 – R/C
  Maputo
  Tel.:(+258) 214 914 01
  Fax: (+258) 214 914 00

www.teixeiraduarte.pt

> Prospecção Geotécnica
Site Investigation
> Consultoria Geotécnica
Geotechnical Consultancy
> Obras Geotécnicas
Ground Treatment-Construction Services
> Controlo e Observação
Field Instrumentation Services and Monitoring Services
> Laboratório de Mecânica de Solos
Soil and Rock Mechanics Laboratory

Certificada ISO 9001 por

BVQi

Geocontrole

Parque Oriente, Bloco 4, EN10
2699-501 Bobadela LRS
Tel. 21 995 80 00
Fax. 21 995 80 01
e.mail: mail@geocontrole.pt
www.geocontrole.pt

Geocontrole
Geotecnia e Estruturas de Fundação SA

tgeotecnia

in the origin
of construction

dstgroup

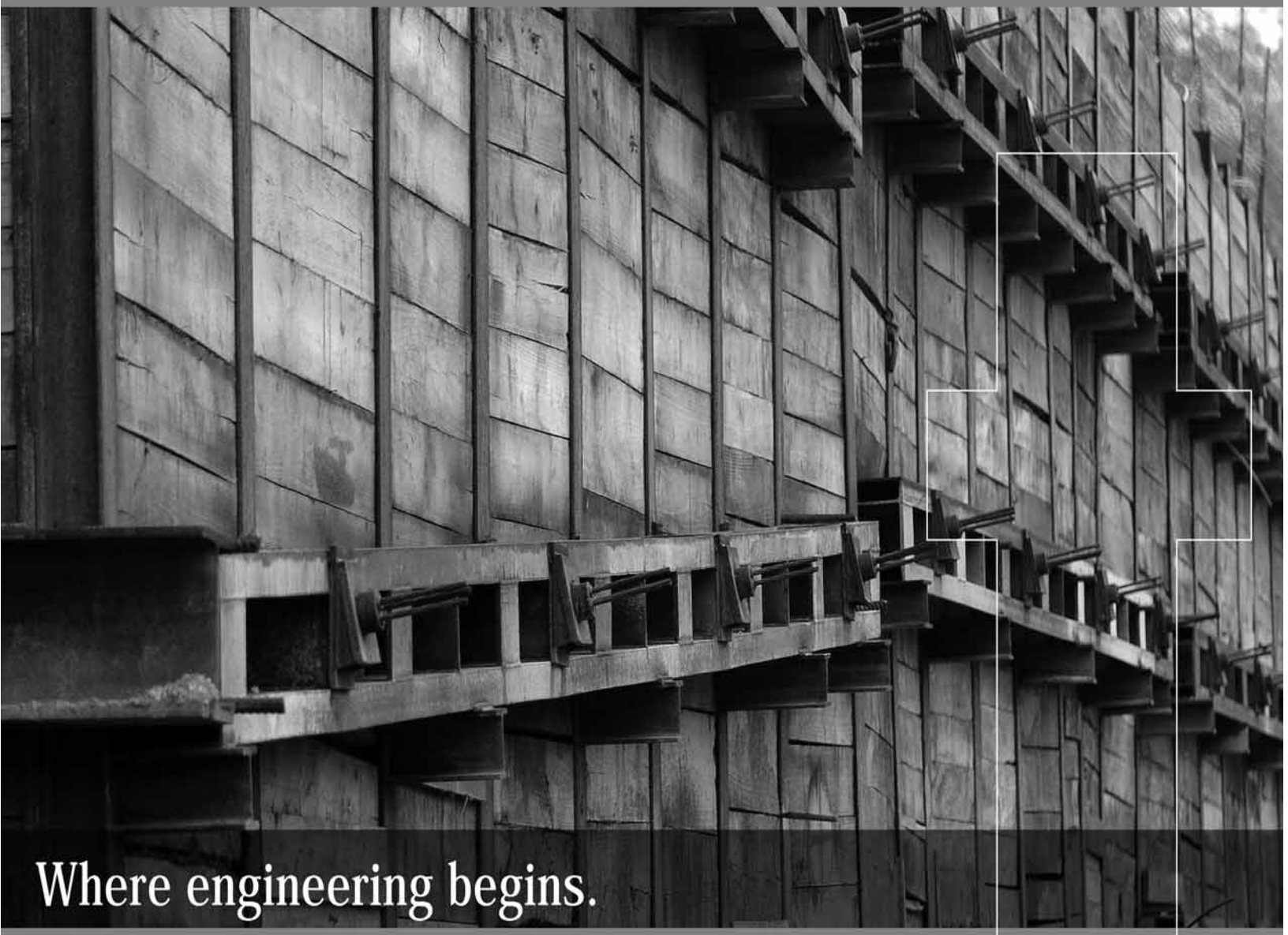

Where engineering begins.

Behind a great work there's always a great company.
tgeotecnia enters in national and Spanish market with a wide range of solutions, with state of the art technology and qualified means necessaries to engage geotechnical studies, projects and works.
Currently, tgeotecnia is specialised in all kinds of work, from geologic-geotechnical studies and project development to slope stabilisation, reinforcement, soil treatment and special foundations.
The works carried out and client satisfaction, as well as the growing number of projects, are the proof that it is worth making innovation the lever of development.

tgeotecnia
In the origin of construction

a dst group company

ph + 351 253 307 285 | geral@tgeotecnia.pt | www.dstsgps.com

ENGINEERING AND ENVIRONMENTAL CONSULTANTS


COBA


GEOLOGY AND GEOTECHNICS

Hydrogeology • Engineering Geology • Rock Mechanics • Soil Mechanics • Foundations and Retaining Structures • Underground Works • Embankments and Slope Stability Environmental Geotechnics • Geotechnical Mapping

Water Resources Planning and Management
Hydraulic Undertakings
Electrical Power Generation and Transmission
Water Supply Systems and Pluvial and Wastewater Systems
Agriculture and Rural Development
Road, Railway and Airway Infrastructures
Environment
Geotechnical Structures
Cartography and Cadastre
Safety Control and Work Rehabilitation
Project Management and Construction Supervision

PORTUGAL
CENTER AND SOUTH REGION
Av. 5 de Outubro, 323
1649-011 LISBOA
Tel.: (351) 210125000, (351) 217925000
Fax: (351) 217970348
E-mail: coba@coba.pt
www.coba.pt

Av. Marquês de Tomar, 9, 6º.
1050-152 LISBOA
Tel.:(351) 217925000
Fax:(351) 213537492

NORTH REGION
Rua Mouzinho de Albuquerque, 744, 1º.
4450-203 MATOSINHOS
Tel:(351) 229380421
Fax:(351) 229373648
E-mail: engico@engico.pt

ANGOLA
Praceta Farinha Leitão, edifício nº 27, 27-A - 2º Dto
Bairro do Maculusso, LUANDA
Tel./Fax: (244) 222338 513
Cell: (244) 923317541
E-mail: coba-angola@netcabo.co.ao

MOZAMBIQUE
Pestana Rovuma Hotel. Centro de Escritórios.
Rua da Sé nº114. Piso 3, MAPUTO
Tel./Fax: (258) 21 328 813
Cell:(258) 82 409 9605
E-mail: coba.mz@tdm.co.mz

ALGERIA
09, Rue des Frères Hocine
El Biar - 16606, ARGEL
Tel.: (213) 21 922802
Fax: (213) 21 922802
E-mail: coba.alger@gmail.com

BRAZIL
Rio de Janeiro
COBA Ltd. - Rua Bela 1128
São Cristóvão
20930-380 Rio de Janeiro RJ
Tel.: (55 21) 351 50 101
Fax: (55 21) 258 01 026

Fortaleza
Av. Senador Virgílio Távora 1701, Sala 403
Aldeota - Fortaleza CEP 60170 - 251
Tel.: (55 85) 3261 17 38
Fax: (55 85) 3261 50 83
E-mail: coba@esc-te.com.br

UNITED ARAB EMIRATES
Corniche Road – Corniche Tower - 5th Floor - 5B
P. O. Box 38360 ABU DHABI
Tel.: (971) 2 627 0088
Fax: (971) 2 627 0087

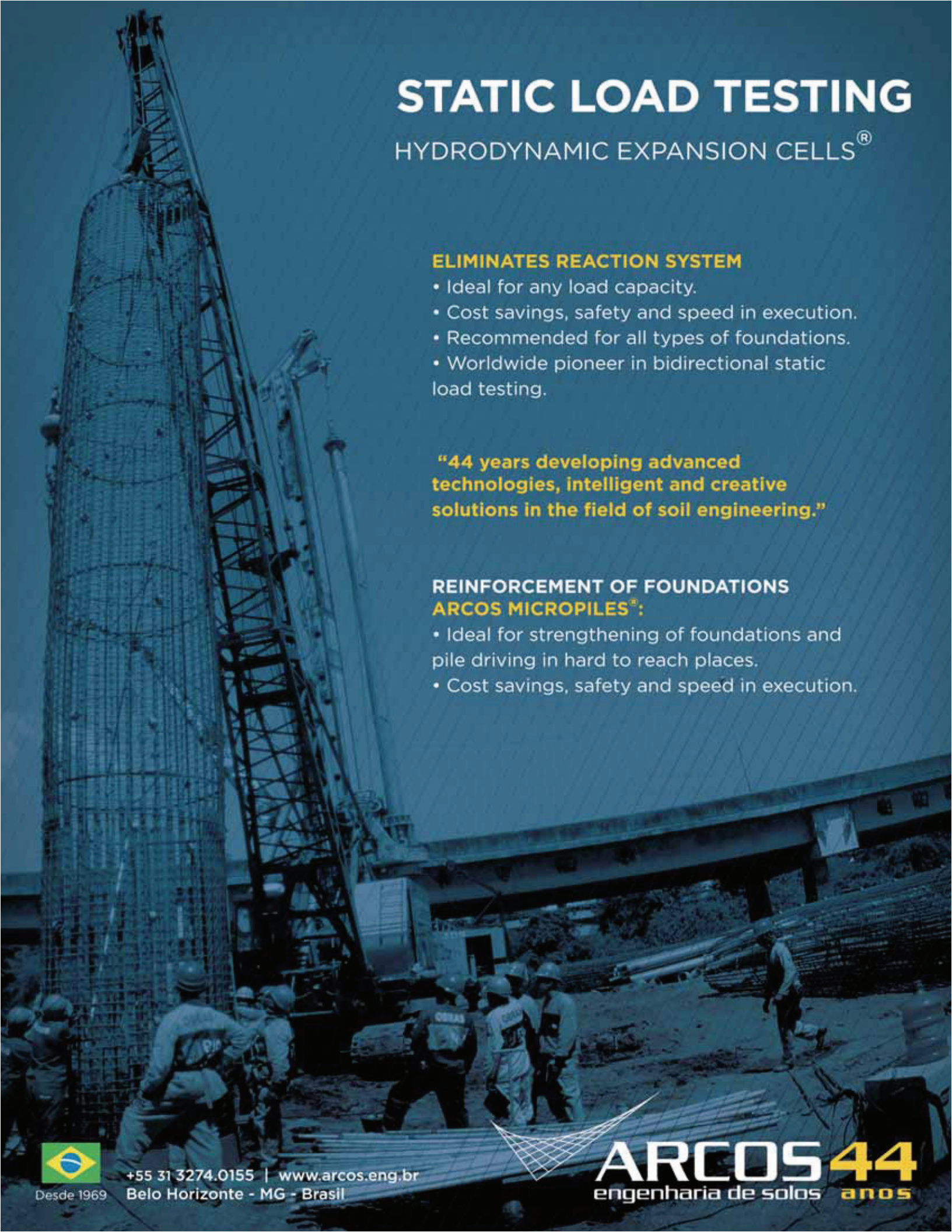
STATIC LOAD TESTING
HYDRODYNAMIC EXPANSION CELLS®
ELIMINATES REACTION SYSTEM
• Ideal for any load capacity.
• Cost savings, safety and speed in execution.
• Recommended for all types of foundations.
• Worldwide pioneer in bidirectional static load testing.
"44 years developing advanced technologies, intelligent and creative solutions in the field of soil engineering."
REINFORCEMENT OF FOUNDATIONS
ARCOS MICROPILES®:
• Ideal for strengthening of foundations and pile driving in hard to reach places.
• Cost savings, safety and speed in execution.
Desde 1969
+55 31 3274.0155 | www.arcos.eng.br
Belo Horizonte - MG - Brasil
ARCOS 44
engenharia de solos anos

Instructions to Authors

Category of the Papers

Soils and Rocks is the scientific journal edited by the Brazilian Association for Soil Mechanics and Geotechnical Engineering (ABMS) and the Portuguese Geotechnical Society (SPG). The journal is intended to the divulgation of original research works from all geotechnical branches.

The accepted papers are classified either as an Article paper, a Technical Note, a Case Study, or a Discussion according to its content. An article paper is an extensive and conclusive dissertation about a geotechnical topic. A paper is considered as a technical note if it gives a short description of ongoing studies, comprising partial results and/or particular aspects of the investigation. A case study is a report of unusual problems found during the design, construction or the performance of geotechnical projects. A case study is also considered as the report of an unusual solution given to an ordinary problem. The discussions about published papers, case studies and technical notes are made in the Discussions Section.

When submitting a manuscript for review, the authors should indicate the category of the manuscript, and is also understood that they:

a) assume full responsibility for the contents and accuracy of the information in the paper;

b) assure that the paper has not been previously published, and is not being submitted to any other periodical for publication.

Manuscript Instructions

Manuscripts must be written in English. The text is to be typed in a word processor (MS Word or equivalent), using ISO A4 page size, left, right, top, and bottom margins of 25 mm, Times New Roman 12 font, and line spacing of 1.5. All lines and pages should be numbered. The text should be written in the third person.

The fist page of the manuscript is to include the title of the paper in English, followed by the names of the authors with the abbreviation of the most relevant academic title. The affiliation, address and e-mail is to be indicated below each author's name. An abstract of 200 words is to be written in English after the author's names. A list with up to six keywords at the end of the abstract is required.

Although alteration of the sequence and the title of each section may be required, it is suggested that the text contains the following sections: Introduction, Material and Methods, Results, Discussions, Conclusion, Acknowledgements, References and List of Symbols. A brief description of each section is given next.

Introduction: This section should indicate the state of the art of the problem under evaluation, a description of the problem and the methods undertaken. The objective of the work is to be clearly presented at the end of the section.

Materials and Methods: This section should include all information needed to the reproduction of the presented work by other researchers.

Results: In this section the data of the investigation should be presented in a clear and concise way. Figures and tables should not repeat the same information.

Discussion: The analyses of the results should be described in this section. **Conclusions**: The text of this section should be based on the presented data and in the discussions.

Acknowledgenments: If necessary, concise acknowledgements should be written in this section.

References: References to other published sources are to be made in the text by the last name(s) of the author(s), followed by the year of publication, similarly to one of the two possibilities below:

"*while Silva & Pereira (1987) observed that resistance depended on soil density*" or "*It was observed that resistance depended on soil density (Silva & Pereira, 1987).*"

In the case of three or more authors, the reduced format must be used, *e.g.*: Silva *et al.* (1982) or (Silva *et al.*, 1982). Two or more citations belonging to the same author(s) and published in the same year are to be distinguished with small letters, *e.g.*: (Silva, 1975a, b, c.). Standards must be cited in the text by the initials of the entity and the year of publication, *e.g.*: ABNT (1996), ASTM (2003).

Full references shall be listed alphabetically at the end of the text by the first author's last name. Several references belonging to the same author shall be cited chronologically. Some examples are listed next:

Papers: Bishop, A.W. & Blight, G.E. (1963) Some aspects of effective stress in saturated and unsaturated soils. Géotechnique, v. 13:2, p. 177-197.

Books: Lambe, T.W & Whitman, R.V. (1979) Soil Mechanics, SI Version, 2nd ed. John Wiley & Sons, New York, p. 553.

Book with editors: Sharma, H.D.; Dukes, M.T. & Olsen, D.M. (1990) Field measurements of dynamic moduli and Poisson's ratios of refuse and underlying soils at a landfill site. Landva A. & Knowles, G.D. (eds) Geotechnics of Waste Fills - Theory and Practice, American Society for Testing and Materials - STP 1070, Philadelphia, p. 57-70.

Proceedings (printed matter or CD-ROM): Jamiolkowski, M.; Ladd, C.C.; Germaine, J.T & Lancellotta, R. (1985) New developments in field and laboratory testing of soils. Proc. 11th Int. Conf. on Soil Mech. and Found. Engn., ISSMFE, San Francisco, v. 1, pp. 57-153.(specify if CD – ROM)

Thesis and dissertations: Lee, K.L. (1965) Triaxial Compressive Strength of Saturated Sands Under Seismic Loading Conditions. PhD Dissertation, Department of Civil Engineering, University of California, Berkeley, 521 p.

Standards: ASTM (2003) Standard Test Method for Particle Size Analysis of Soils - D 422-63. ASTM International, West Conshohocken, Pennsylvania, USA, 8 p.

Internet references: Soils and Rocks available at http://www.abms.com.br.

On line first publications must also bring the digital object identifier (DOI) at the end.

Figures shall be either computer generated or drawn with India ink on tracing paper. Computer generated figures must be accompanied by the corresponding digital file (.tif, .jpg, .pcx, etc.). All figures (graphs, line drawings, photographs, etc.) shall be numbered consecutively and have a caption consisting of the figure number and a brief title or description of the figure. This number should be used when referring to the figure in text. Photographs should be black and white, sharp, high contrasted and printed on glossy paper.

Tables shall be numbered consecutively in Arabic and have a caption consisting of the table number and a brief title. This number should be used when referring to the table in text. Units should be indicated in the first line of the table, below the title of each column. Abbreviations should be avoided. Column headings should not be abbreviated. When applicable, the units should come right below the corresponding column heading. Any necessary explanation can be placed as footnotes.

Equations shall appear isolated in a single line of the text. Numbers identifying equations must be flush with the right margin. International System (SI) units are to be used. The symbols used in the equations shall be listed in the List of Symbols. It is recommended that the used symbols

be in accordance with Lexicon in 8 Languages, ISSMFE (1981) and the ISRM List of Symbols.

The text of the submitted manuscript (including figures, tables and references) intended to be published as an article paper or a case history should not contain more than 30 pages formatted according to the instructions mentioned above. Technical notes and discussions should have no more than 15 and 8 pages, respectively. Longer manuscripts may be exceptionally accepted if the authors provide proper explanation for the need of the required extra space in the cover letter.

Discussion

Discussions must be written in English. The first page of a discussion paper should contain:

• The title of the paper under discussion in the language chosen for publication;

• Name of the author(s) of the discussion, followed by the position, affiliation, address and e-mail. The discusser(s) should refer himself (herself, themselves) as "the discusser(s)" and to the author(s) of the paper as "the author(s)".

Figures, tables and equations should be numbered following the same sequence of the original paper. All instructions previously mentioned for the preparation of article papers, case studies and technical notes also apply to the preparation of discussions.

Editorial Review

Each paper will be evaluated by reviewers selected by the editors according to the subject of the paper. The authors will be informed about the results of the review process. If the paper is accepted, the authors will be required to submit a version of the revised manuscript with the suggested modifications. If the manuscript is refused for publication, the authors will be informed about the reasons for rejection. In any situation comprising modification of the original text, classification of the manuscript in a category different from that proposed by the authors, or refusal for publication, the authors can reply presenting their reasons for disagreeing with the reviewers' comments

Submission

The author(s) must submit for review:

1. A hard copy of the manuscript to Editors - Soils and Rocks, Av. Prof. Almeida Prado, 532 – IPT, Prédio 54 – DEC/ABMS, 05508-901 - São Paulo, SP, Brazil. The first page of the manuscript should contain the identification of the author(s), or

2. The digital file of the manuscript, omitting the authors' name and any information that eventually could identify them, should be sent to **abms@ipt.br**. The following must be written in the subject of the e-mail message: "*Paper submitted to Soils and Rocks"*. The authors' names, academic degrees and affiliations should be mentioned in the e-mail message. The e-mail address from which the digital file of the paper was sent will be the only one used by the editors for communication with the corresponding author.

Follow Up

Authors of manuscripts can assess the status of the review process at the journal website (www.soilsandrocks.com.br) or by contacting the ABMS secretariat.

Volume 36, N. 2, May-August 2013

Table of Contents